SHEAR LAYER INSTABILITIES AND FLOW-ACOUSTIC COUPLING IN VALVES: APPLICATION TO POWER PLANT COMPONENTS AND CARDIOVASCULAR DEVICES

by

Oleksandr Barannyk

M.A.Sc., University of Victoria, 2009

M.Sc. in Applied Mathematics, New Jersey Institute of Technology, 2003

A Dissertation Submitted in Partial Fulfillment

of the Requirements for the Degree of

DOCTOR OF PHILOSOPHY

in the Department of Mechanical Engineering

University of Victoria

SUPERVISORY COMMITTEE

SHEAR LAYER INSTABILITIES AND FLOW-ACOUSTIC COUPLING

IN VALVES:

APPLICATION TO POWER PLANT COMPONENTS AND

CARDIOVASCULAR DEVICES

by

Oleksandr Barannyk
M.A.Sc., University of Victoria, 2009
M.Sc. in Applied Mathematics, New Jersey Institute of Technology, 2003

Supervisory Committee

Dr. Peter Oshkai (Department of Mechanical Engineering)
Supervisor

Dr. Brad Buckham, P.Eng. (Department of Mechanical Engineering)
Departmental Member

Prof. David Sinton, P.Eng. (Department of Mechanical Engineering)
Departmental Member

Prof. Reinhard Illner (Department of Mathematics and Statistics)
Outside Member

ABSTRACT

Supervisory Committee

Dr. Peter Oshkai (Department of Mechanical Engineering)

Supervisor

Dr. Brad Buckham, P.Eng. (Department of Mechanical Engineering)

Departmental Member

Prof. David Sinton, P.Eng. (Department of Mechanical Engineering)

Departmental Member

Prof. Reinhard Illner (Department of Mathematics and Statistics)

Outside Member

In the first part of this dissertation, the phenomenon of self-sustained pressure oscillations due to the flow past a circular, axisymmetric cavity, associated with inline gate valves, was investigated. In many engineering applications, such as flows through open gate valves, there exists potential for coupling between the vortex shedding from the upstream edge of the cavity and a diametral mode of the acoustic pressure fluctuations. The effects of the internal pipe geometry immediately upstream and downstream of the shallow cavity on the characteristics of partially trapped diametral acoustic modes were investigated numerically and experimentally on a scaled model of a gate valve mounted in a pipeline that contained convergence-divergence sections in the vicinity of the valve. The resonant response of the system corresponded to the second acoustic diametral mode of the cavity. Excitation of the dominant acoustic mode was accompanied by pressure oscillations, and, in addition to that, as the angle of the converging-diverging section of the main pipeline in the vicinity of the cavity increased, the trapped behavior of the acoustic diametral modes diminished, and additional antinodes of the acoustic pressure wave were observed in the main pipeline.

In addition to that, the effect of shallow chamfers, introduced at the upstream and/or downstream cavity edges, was investigated in the experimental system that contained a deep, circular, axisymmetric cavity. Through the measurements of unsteady pressure and associated acoustic mode shapes, which were calculated numerically for several representative cases of the internal cavity geometry, it was possible to identify the configuration that corresponded to the most efficient noise suppression. This arrangement also allowed calculation of the azimuthal orientation of the acoustic modes, which were classified as stationary, partially spinning or spinning. Introduction of shallow chamfers at the upstream and the downstream edges of the cavity resulted in changes of azimuthal orientation and spinning behaviour of the acoustic modes. In addition, introduction of splitter plates in the cavity led to pronounced change in the spatial orientation and the spinning behaviour of the acoustic modes. The short splitter plates changed the behaviour of the dominant acoustic modes from partially spinning to stationary, while the long splitter plates enforced the stationary behaviour across all resonant acoustic modes.

Finally, the evolution of fully turbulent, acoustically coupled shear layers that form across deep, axisymmetric cavities and the effects of geometric modifications of the cavity edges on the separated flow structure were investigated using digital particle image velocimetry (PIV). Instantaneous, time- and phase-averaged patterns of vorticity provided insight into the flow physics during flow tone generation and noise suppression by the geometric modifications. In particular, the first mode of the shear layer oscillations was significantly affected by shallow chamfers located at the upstream and, to a lesser degree, the downstream edges of the cavity.

In the second part of the dissertation, the performance of aortic heart valve prosthesis was assessed in geometries of the aortic root associated with certain types of valve diseases, such as aortic valve stenosis and aortic valve insufficiency. The control case that corresponds to the aortic root of a patient without valve disease was used as a reference. By varying the aortic root geometry, it was possible to investigate corresponding changes in the levels of Reynolds shear stress and establish the possibility of platelet activation and, as a result of that, the formation of blood clots.

TABLE OF CONTENTS

LIST OF TABLES

LIST OF FIGURES

ACKNOWLEDGMENTS

Completing my Ph.D. degree is probably the most challenging activity during my entire life as a graduate student. Many wonderful people shared the best and worst moments of my doctoral journey. It has been a great privilege to spend several years in the Department of Mechanical Engineering at the University of Victoria and at the Institute for Integrated Energy Systems; their members will always remain dear to me.

First of all, I wish to thank my wife, Vasylyna, my son, Dimitri, and my daughter, Zlata, as well as my dad, my mom, and my sister, Lyudmyla, who have always been supportive throughout my entire graduate study. Completion of this dissertation was simply impossible without them.

I would like to express my sincere gratitude and deep appreciation to my adviser, Dr. Peter Oshkai, for mentorship, patient guidance, and enthusiasm he provided to me, all the way from when I first inquired about applying to the Ph.D. program in Department of Mechanical Engineering, through the completion of my dissertation. He has been a strong and supportive adviser to me throughout my graduate school career, but he has always given me great freedom to pursue independent work.

Members of Fluid Mechanics Laboratory also deserve my sincerest thanks, their friendship and assistance has meant more to me than I could ever express. I could not complete my work without invaluable friendly assistance of Dr. Satia Karri of *W.L. Gore and Associates* for introducing me to the whole new world of cardiovascular engineering and allowing me to be a part of a great professional community.

Last but not least, I wish to thank the Atomic Energy of Canada Limited (AECL) for providing the original experimental model of the gate valve, ViVitro Labs Inc. for

providing access to their laboratory and equipment, and the Natural Sciences and Engineering Research Council of Canada (NSERC) for providing funding for financial support during my entire Ph.D. program.

DEDICATION

This dissertation is dedicated to my family for their love, endless support and encouragement.

CHAPTER 1

INTRODUCTION

1.1 MOTIVATION

In this work the phenomenon of shear layer instabilities occurring in the flow through valves was investigated experimentally in two different cases. The first case was represented by a circular axisymmetric cavity, associated with inline gate valves, typically present in the steam pipelines of nuclear or fossil-fuel power plants. The second system is associated with cardiovascular devices and was represented by an artificial heart valve coupled with the model of an ascending aorta.

The flow physics associated with the first system represents a coupling between the acoustic pressure fluctuations (acoustic field) in the circular axisymmetric cavity and the velocity fluctuations (hydrodynamic field) in the separated shear layers formed at the upstream edge of the cavity with the focus on acoustic tone generation. Generation of flow-tones is closely connected to formation of coherent structures in the shear layers and their development along the cavity length. An important feature of such vortices is that the frequency with which they are shed from the upstream edge of the cavity is directly related to the frequency of the flow tone. There are many industrial problems associated with the destructive aftermath of the flow-acoustic coupling. For instance, the development of a self-sustained, flow dominant lock-on inside of a gate valve of a cold-reheat steam line not only can lead to a premature wear of the steam delivery line itself, but also to its fracture and uncontrolled re-

lease of the high-pressure, high-temperature steam. As such, by imaging flow patterns across the cavity, one can identify the onset of flow tones and guide the design of the cavity towards suppression of unwanted flow oscillations.

The flow physics associated with the second case represents the development of shear layer instabilities downstream of the heart valve placed into the anatomically correct model of an ascending aorta. The focus in this study is on the formation of abnormal flow patterns and the associated levels of turbulent shear stresses. The operation of the artificial heart valve during the cardiac cycle gives rise to the formation of coherent vortical structures, shed from the leaflets of the valve and, in some cases, from the valve housing. Those vortical structures play an important role in the growth of a noticeable vorticity oscillation that eventually induces the instability and break down of the leaflet shear layers. The shear forces, induced by unstable shear layers, can act destructively on the blood elements such as platelets and, in certain cases can induce a hemolysis and/or lead to thrombus formation. The ability to visualize flow structures induced by the flow through an artificial heart valve and quantify the levels of turbulent shear stresses allows one to determine if the particular design of the artificial heart valve is safe and can operate within the requirements of a regulatory board (ISO, 2013).

These two cases share important fundamental similarities, which are the unsteady development of shear layer instabilities and generation of coherent vortical structures. In both systems the development and growth of coherent vortical structures is due to a two-way coupling between hydrodynamic instabilities formed at the upstream edge of the cavity with the acoustic flow field in the first case and, in the second case, between the confined, circular jet formed by the heart valve leaflets, when it attempts to attach downstream, on the wall of the ascending aorta. The formation of the shear layer at the interface between the jet and the sur-

rounding fluid is accompanied by an entrainment process from the downstream region. As the jet expands it attaches and breaks from the walls of the ascending aorta, which leads to the oscillation of the surrounding fluid, which, in turn, affects greatly the character of the shear layer and the scale of the coherent structures. The present work indicates that self-sustained periodic flow oscillations accompanied by generation of large-scale vortical structures due to flow-acoustic coupling and periodic fluctuations caused by the movement of large-scale vortical structures subject to a forced, pulsatile jet-like flow through heart valve share many common features. Such commonalities between those two cases indicate that they can be fruitfully explored in the future.

1.2 FLOW-INDUCED VIBRATION IN POWER PLANT COMPONENTS

The aero-acoustic coupling in a thermal power plant's steam delivery system that consists of multiple pipes, gate valves and high pressure orifices that disrupt the smooth flow is a dangerous issue that can lead to premature wear of mechanical components, high levels of noise, and shutdown of certain sections of the plant itself (Heller et al., 1971, Michaud et al., 2001, Tonon et al., 2011, Ziada, 2010, Ziada and Lafon, 2013).

Gate valves, in particular, are associated with coupling of flow oscillations with the acoustic modes of the internal valve and pipeline geometry. The impact of high levels of flow-induced noise and vibrations on the operation cycle of the power plant can range from creating an environmental hazard for plant personnel (Smith and Luloff, 2000) to a serious disruption in the operation cycle such as an 80% reduction of nominal power that occurred in Unit 3 of the Chernobyl nuclear power plant (Ukraine) due to intensive vibrations of the main

steam pipelines (Fomin et al., 2001). Detailed reviews of the generation of noise and vibrations can be found, for example, in (Tonon et al., 2011, Rockwell and Naudascher, 1978, Ziada and Buhlmann, 1992, Bruggeman et al., 1989, Kriesels et al., 1995, Ziada and Lafon, 2013).

The problem considered in this dissertation is motivated by the issue that originated in the Reliant Energy's Seward coal-fired power plant, which experienced significant vibration and some branch line failures in the cold-reheat (CRH) steam lines. As one of the possible solutions to address this issue, it was decided that if a new seat design could be developed to solve the problem, the company would replace the original seats with newly fabricated ones.

References (Janzen et al., 2008, Smith and Luloff, 2000) reported the results of a scale-model investigation of reducing the steam line noise and vibration at a thermal power plant. During the preliminary tests, performed by the Atomic Energy of Canada Limited (AECL), it was confirmed that the source of the acoustic excitation leading to excessive pipe vibration in the cold reheat steam lines (CRH) of the power plant was the vortex shedding related directly to the geometry of the cold-reheat gate valves. Based on the measurements conducted at the site, it was concluded that the inline gate valves were the most probable source of the problem. A variety of practical cavity, gate and seat modifications were tested in a 0.108-scale model using air as the working fluid. During the tests, it was shown that the model reproduced the tonal noise generation observed in the plant and that modifying the upstream and downstream valve seats can be effective in eliminating this noise. The noise generation mechanism was found to be associated with the vortex shedding over the valve seat cavity coupled with an acoustic mode in the valve throat.

1.2.1 Generation of sound by fluid flow over the cavity

When steam or air flow at high Reynolds numbers passes over the cavity formed by the seat of a gate valve mounted in a circular pipe, flow separation leads to formation of an unsteady shear layer over the opening of the cavity, as shown in Figure 1.1. Coupling of the shear layer oscillations with the acoustic modes of the cavity often leads to a flow-excited resonance accompanied by generation of noise and high levels of pipe vibration (Janzen et al., 2008, Smith and Luloff, 2000). Since this phenomenon is associated with vortex shedding, the vorticity in the flow is directly related to the generation of the sound (Powell, 1964, Howe, 1975). This type of the excitation mechanism of the acoustic resonance, where the resonant sound field, associated with the acoustic modes of the cavity, is in charge of sustaining the oscillations at the upstream cavity edge, is referred to as fluid-resonant (Rockwell and Naudascher, 1978).

In the flow-excited acoustic resonance, schematically shown in Figure 1.1, the feedback event at the upstream corner, introduced by the acoustic particle velocity of the resonant acoustic mode plays a crucial role by inducing velocity perturbations in the unstable separated flow. At the upstream edge of the cavity, as it was shown in (Blevins, 1985, Hall et al., 2003), sound can shift the frequency of the vortex shedding from the natural frequencies and enhance the development of the organized, large-scale vortical structures. Initially, small-scale vortical structures, formed at the upstream cavity edge, travel downstream while interacting with the acoustic modes and the shear layer oscillations. As a result of this interaction, large-scale vortices are formed and convected downstream where they eventually interact with the downstream corner of the cavity and transfer part of their energy to the acoustic field. This energy sustains the resonance of the acoustic mode and contributes to the increase

of the amplitude of the acoustic oscillations and, in turn, to the radiated noise. The state of knowledge in the field of flow-excited acoustic resonance can be found in (Tonon et al., 2011, Ziada and Lafon, 2013).

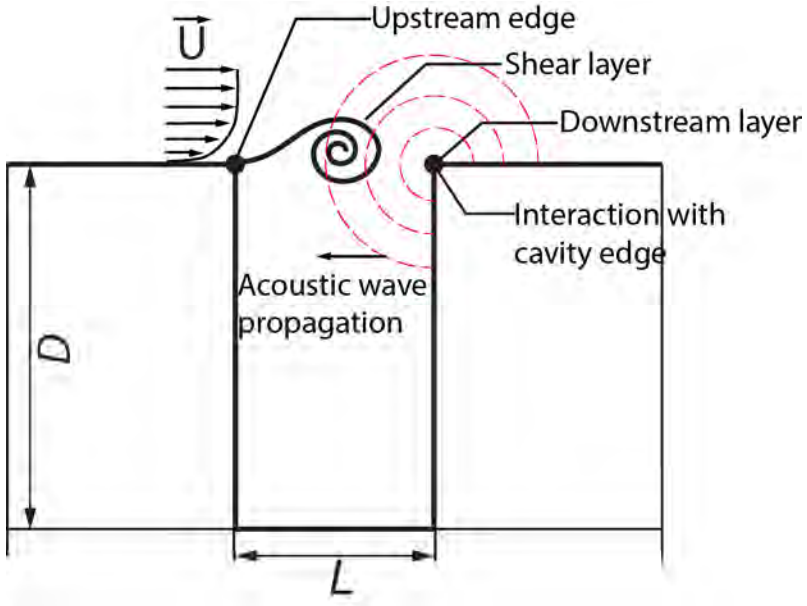

Figure 1.1 Principal elements of self-sustaining oscillation of turbulent flow past cavity where *L* is a cavity length, and *D* is the cavity depth.

The relationship between sound generation and vortex shedding in the case of free field conditions was formally established in (Powell, 1964), and later generalized in (Howe, 1975, Howe, 1980, Howe, 1981). In particular, in (Howe, 1980) vorticity was identified as a source of sound and it was also proposed that the instantaneous acoustic power *P*, generated by vorticity $\boldsymbol{\omega}$, within a volume *V* can be obtained as follows,

$$P = -\rho_0 \iiint_V (\boldsymbol{\omega} \times \boldsymbol{V}) \cdot \boldsymbol{u}_{ac} dV \,, \tag{1.1}$$

where ρ_0 is the fluid density, $\boldsymbol{V}$ is the fluid velocity and $\boldsymbol{u}_{ac}$ is the acoustic particle velocity, defined as a local displacement of particles of air volume around their equilibrium position,

subject to an acoustic field. The sign of the triple product $(\boldsymbol{\omega} \times \boldsymbol{V}) \cdot \boldsymbol{u}_{ac}$ determines whether vorticity acts as an acoustic source or sink. If the integral of instantaneous acoustic power over one acoustic cycle is positive, the acoustic resonance is self-sustained. This, in turn, imposes a phase condition on the timing of vortex convection within the resonant sound field so that at the beginning phase of the acoustic cycle the acoustic particle velocity is directed downwards, which results in the absorption of the acoustic energy by the growing vortex. On the contrary, at the later phase of the acoustic cycle, the acoustic particle velocity is directed upwards, which results in the generation of the acoustic energy (Oshkai and Velikorodny, 2013, Ziada, 2010).

1.2.2 Acoustic diametral modes of circular axisymmetric cavities

In many cases, flow-tone generation in the thermal power plant's steam delivery system is due to air flow through control gate valves that contain circular or near-circular cavities (Ziada, 2010, Smith and Luloff, 2000, Weaver et al., 2000). The circular cavities are associated with an infinite number of diametral acoustic modes, which can potentially be excited by the separated flow across the cavity (Duan et al., 2007, Hein and Koch, 2008, Aly and Ziada, 2010, Aly and Ziada, 2012). These studies were aimed at understanding the excitation mechanism of the trapped acoustic diametral modes, as well as their azimuthal behavior. It was shown by the authors, that for all tested configurations, flow coupling with acoustic diametral modes was a dominant phenomenon at relatively low Mach numbers. It was found that the pulsation amplitude during resonance was increased as the cavity was made deeper or shorter. The authors also concluded that the acoustic diametral modes, coupled with the flow, were likely to spin when the cavity-duct system has a perfectly axisymmetric geometry and switch to a partially spinning regime when the cavity geometry is no longer axisymmetric

(Keller and Escudier, 1983).

These so-called trapped acoustic diametral modes are generally confined to the cavity and its immediate vicinity and are associated with negligible acoustic radiation losses. Existence of trapped modes in a system is of great importance for practical applications, because these modes can typically be easily excited by external forcing. The application of the modified residue-calculus method for establishing the existence of the trapped modes in an acoustic medium was originally presented in (Evans et al., 1993) for the case of a thin, finite-length strip, placed between and parallel to two boundaries. The technique was further extended to more complicated problems in (Linton and McIver, 1998, Linton et al., 2002) where the existence of one propagating mode and set of trapped modes was established. In (Linton and McIver, 1998), the existence of an infinite sequence of trapped modes was proven for cylindrical ducts. The authors in (Duan et al., 2007) compared numerically-obtained resonant responses of several model configurations with analytically calculated trapped modes. The lock-on in two-dimensional models of a butterfly and ball-type valves were also investigated.

1.2.3 Shear layer modes and their prediction

The high Reynolds number flow over a cavity typically generates self-sustained hydrodynamic oscillations of the cavity shear layer and induces high amplitude pressure fluctuations for a particular range of Strouhal numbers. Flow structures that are present in the cavity shear layer, once formed at the leading edge of the cavity, are growing within the shear layer and, consequently, get convected towards the trailing edge of the cavity with a characteristic velocity u_c. In order to describe the transverse oscillation of the cavity shear layer that in-

cludes convection of vortices and their impingement on the downstream edge, (Rossiter, 1964) came up with the following semi-empirical model,

$$\frac{fL}{U} = \frac{n - \frac{1}{4}}{1/\kappa + \mathrm{M}}, \tag{1.2}$$

where L is the cavity length (see Figure 1.1), f is the frequency of the vortex shedding, U is the velocity of the fluid, n is the shear layer mode number, κ = 0.57 is the convection coefficient, which is often considered as empirical and taken as a constant value (Kegerise et al., 2004, Hirahara et al., 2007), -1/4 represents the end correction (Rockwell et al., 2003), and M is the Mach number. While the the Equation (1.2) would not have much physical relevance in the problem investigated in this dissertation, as the acoustic feedback is provided by the almost uniform acoustic flow in the direction normal to the main flow vs. only downstream cavity edge, originally proposed by the Rossiter, as it would be shown in the Chapter 4, this formula can provide a quick and rather accurate estimate where the locked-on flow states would occur.

A slightly simplified, although still capable in theoretical approximations of the modes of the transverse shear layer oscillations, is the following semi-empirical model of the Strouhal modes (Rockwell et al., 2003),

$$\frac{fL}{U} = 0.52(n - \frac{1}{4}). \tag{1.3}$$

The empirical constant 0.52 represents the ratio of the average convective speed of the vortical structures across the cavity to the inflow.

As it will be shown in the Chapter 4, Equation (1.3) generally under-predicts the values of the inflow velocity U, at which the lock-on occurred. On the other hand, Equation (1.2)

which accounts for the effect of the acoustic field on the convection speed of vortical structures, which increases significantly at larger flow velocities, provides similarly good fit at low flow velocity, but improved performance at higher flow speeds.

Few models, alternative to Rossiter's Equation (1.2), were proposed. Specifically, (Bilanin and Covert, 1973, Tam and Block, 1978) provided robust descriptions that accounted for the depth of the cavity and showed a good agreement with experimental data. The drawback of these models is the fact that they both considered a two-dimensional domain and did not account for the cavity width as in the case of (Rossiter, 1964). These two models also used the concept of a monopole presence to simulate the pressure pulses generated at the downstream edge. However, since a substantial pressure pulsation might not be present at low Mach number flows, an alternative approach that does not rely on the monopole concept might provide better results for low Mach number flows.

1.2.4 Control strategies for suppression of flow induced oscillations

There exists a large body of work dedicated to understanding and control of shear flows over cavities in walls and external cavities in axisymmetric bodies of revolution (Erdem et al., 2003, Michaud et al., 2001, Rockwell et al., 2003, Verdugo et al., 2012, Ziada, 2010). Because of the inherent instability of the free shear layer, small disturbances at the upstream edge of the cavity result in the formation of large-scale vortices in the shear layer over the cavity. Each vortex will convect downstream until it impinges on the downstream edge of the cavity where it causes a pressure perturbation. This pressure perturbation will then be acoustically transmitted back to the upstream edge where it can initiate the formation of another vortex. The time required for the vortex to move across the mouth of the cavity plus the time required to transmit the pressure back to initiate the formation of a new vortex will de-

termine the preferred vortex shedding frequencies.

Several reports (Blevins, 1990, Rockwell and Knisely, 1979, Willmarth et al., 1978) indicated that the flow instabilities over a cavity can be significantly reduced if the flow is prevented from impinging on the downstream edge of the cavity either by moving the downstream edge out of the shear flow region or by deflecting the flow at the upstream edge. Alternatively, geometric modifications of the upstream and/or the downstream cavity edges can also lead to effective reduction of the pressure oscillations (Franke and Carr, 1975, Smith and Luloff, 2000, Ethembabaoglu, 1973). These approaches were examined for the gate valve geometry in (Janzen et al., 2008), where downstream seats that had rounded or chamfered corners were implemented. In addition to that, it has been previously shown that introduction of chevron-shaped spoilers or vortex generators to the upstream edge of the cavity can lead to suppressing of strong acoustic resonance, as it affects the boundary layer structure directly (Bolduc et al., 2013). Finally, one can minimize or completely mitigate the development of the disturbances by introducing an obstacle within the flow, which will induce and amplify the flow's three-dimensionality. These obstacles are usually referred as vortex generators or splitter plates, and as it was shown by several researchers (Karadogan and Rockwell, 1983, Velikorodny et al., 2010, Arthurs et al., 2007) can substantially decrease sound pressure in the resonant system.

In contrast to the passive control strategies mentioned above, there are a number of active control strategies, which are applicable to cavity flows (Cattafesta et al., 2003, Vakili and Gauthier, 1994, Ziada, 2003). Specifically, the possibility of suppression of self-sustained oscillations through the introduction of synthetic jets, generated by loudspeakers, placed at the location of the flow separation, was investigated in (Ziada, 2003). The introduction of

synthetic jets showed to be very effective technique as it suppressed the oscillation amplitudes up to 35 dB. Although successful in many applications, these active techniques typically require introduction of additional hardware, which is not always practical. In this work, the focus is on the passive control strategies based on geometrical changes of certain parts of the cavity.

1.3 SHEAR LAYER INSTABILITIES IN CARDIOVASCULAR SYSTEMS

The heart is probably the most important muscle in the human body. It receives energy from blood rich in oxygen and nutrients. Having a constant supply of blood keeps the heart working properly, as such, the flawless operation of the whole cardiovascular system is essential. Unfortunately our technological progress has directly and indirectly led to the whole spectrum of human cardiac diseases either due to decrease in the everyday physical activities or due to development of unhealthy eating habits. A broad range of disorders, including myocardial ischemia, valvular disease, diastolic dysfunction, has caused serious disruption of the blood flow in the cardiovascular system and, in many cases, surgical replacement of the heart valves and/or section of the ascending aorta, referred to as the aortic root reconstruction, is the only remedy (Aazami and Schäfers, 2003). Any future advances in cardiovascular surgery have to deal with the fact that each implanted prosthetic valve should not cause thromboembolic complications. Therefore, the proper design of aortic valve prostheses with disturbance-free velocity field and low pressure drop is of great importance (Bellhous.Bj, 1972, Funder et al., 2010).

Prosthetic heart valves have been successfully used in heart valve replacement over

many decades. Heart valve prostheses can be classified into three major categories: mechanical (MHV), polymeric (PV) and tissue valves (TV). Successful analysis of the flow through prosthetic heart valves depends on effective understanding of the conditions under which natural valves function. Most disorders of the heart initiate within the left ventricle, shown in Figure 1.2, as this chamber is subjected to the highest mechanical loads. The flow through the left ventricle is regulated by the mitral and the aortic valves, which influence the inflow and the outflow conditions, respectively (McDonald, 1974). The mitral and the aortic valves are the most commonly affected heart valves in a diseased heart, and they are responsible for 34% and 44% of morbidity (Iung et al., 2003, Yoganathan et al., 2004), respectively.

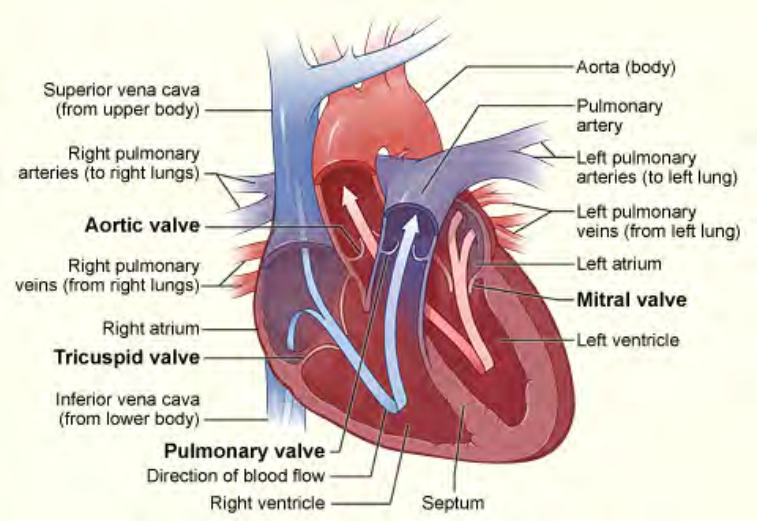

Figure 1.2: Flow past the heart valves (source: National Heart, Lung, and Blood Institute; National Institutes of Health; U.S. Department of Health and Human Services).

The left ventricle (LV) is responsible for pumping oxygenated blood into the primary circulation. This part of the heart typically operates under high load and is critical in the process of effective blood flow. It is also serves as a good indicator of proper heart function. During systole phase (LV contraction), the pressure difference required to drive the blood

through the aortic valve is not very high, usually about few millimeters of mercury. On the other hand, the diastolic pressure differences across the aortic valve are much larger than systolic, usually being about 80 mmHg (Yoganathan et al., 2004).

Pressure drop and recovery through prosthetic valves strongly impact the pressure distribution within the LV. A larger pressure drop across a prosthetic valve requires a larger systolic pressure in the left ventricle to drive the flow through the circulation. Since LV pressure is the primary determinant of myocardial oxygen consumption, the minimization of pressure levels in the LV is essential for a prosthetic heart valve to operate properly.

The rigidity of the MHVs often leads to inability to form tight seals during the closed phase, which results in leakage or the presence of so-called regurgitant jets under normal operating conditions. Some of the MHV designs, such as Medtronic's Hall MHV, have a small central orifice, which promotes the formation of the regurgitant jets during closed phase. While the regurgitant volume caused by mechanical valves is usually higher than that for polymeric or tissue valves, the presence of valve disease can lead to significant deformation of polymeric or tissue valves, and eventually to a substantial regurgitation when they malfunction.

1.3.1 Shear stresses as indicators of the proper valve choice and its operation

Good understanding of the hemodynamics (blood flow motion) is essential to the development of novel methods in cardiovascular implant surgery (Reul et al., 1990b). The blood flow through the heart valve is driven by the periodic contractions of the heart muscles (McDonald, 1974). As the result, the statistically time-periodic, pulsatile blood flow is highly complex. In particular, during a cardiac cycle, it undergoes a transition from a laminar to a turbulent phase (Dasi et al., 2007). Moreover, the fluid mechanical stresses that result from

the complex blood flow regime can lead, through transduction mechanisms, to biomechanical responses causing cardiovascular disease (Goncalves et al., 2005). Within the heart, the blood flow dynamics also plays an important role regulating the efficient working of the heart. So, naturally, the problems associated with the blood flow through the heart valve are of great importance.

Much progress had been done in the development of artificial heart valves (Vongpatanasin et al., 1996, Yoganathan et al., 2005). Nevertheless, serious problems still exist due to abnormally high velocity gradients that are present within the jets that emanate from these prosthetic valves. These gradients result in elevated shear stresses, which may cause red blood cell damage, platelet activation and thrombus formation (Leverett et al., 1972, Lu et al., 2001), which in turn lead to thromboembolism, hemorrhage and tissue overgrowth. Flow-induced stresses in blood, acting on a cellular level, have been known in causing thrombus initiation within the components of the mechanical valve prostheses (Ge et al., 2008). Regions of elevated stresses during the complex motion of the leaflets in some cases lead to structural failure of the mechanical heart valves (MHV). In vivo and in vitro experimental studies have yielded valuable information on the relationship between hemodynamic stresses and the problems associated with the implants (Dasi et al., 2007, Yoganathan et al., 2004).

1.3.2 Application of PIV to the investigation of flow-induced stresses in blood

When studying such complex phenomenon as blood flow through the heart valve, the choice of the methodology is very important. Among several experimental methods that allow flow visualization, digital particle image velocimetry (PIV) is particularly useful, as it is able to deliver global, quantitative flow images with high spatial and temporal resolution. The

authors of (Lim et al., 1994) were among the first to apply PIV methodology to study flow through an artificial heart valve and they outlined experimental challenges associated with it. Among many challenges typically encountered when applying 2D PIV to pulsatile flow problems, correct tracer particle choice, optical distortions, loss of important flow characteristics that involve out-of-plane fluid movement are the most important. The PIV technique was subsequently extended to flows involving various types of heart valves, cardiac conditions and biomedical devices, including a porcine tissue heart valve (Lim et al., 1998, Lim et al., 2001), symmetric stenotic arteries (Karri and Vlachos, 2010), and pediatric ventricular assist devices (Roszelle et al., 2010).

Most of the previous studies (Bellhous.Bj, 1972, Brucker et al., 2002, Dasi et al., 2007, Funder et al., 2010) were concentrated on biomechanical characteristics of various valve materials, the performance of particular valve designs in terms of potential for thromboembolism, and hydrodynamic investigations aimed at flow characteristics and durability of valves and their elements. Turbulent characteristics of the flow through a polymeric trileaflet heart valve and verification if the deformation in the aortic root geometry leads to the elevated levels of the turbulent shear stresses has not been considered. The application of PIV, in conjunction with a pulsatile flow duplicator and blood-analog fluid yielded physiologically realistic velocity data (Dasi et al., 2007) (i) everywhere within the experimental chamber, including close proximity to the aortic walls, (ii) with a high temporal resolution, by employing phase-locked measurements, (iii) for the polymeric trileaflet heart valve at two orthogonal planes, at the same phase of the cardiac cycle and under identical experimental conditions.

1.4 OBJECTIVES

The objective of the first part of this dissertation was to develop a methodology for efficient control of flow-induced noise and vibration caused by gate valves in a wide variety of piping systems. The specific emphasis was on characterization of the key geometric parameters, such as the angle of convergence-divergence of the main pipeline in the immediate vicinity of the valve and the design of the upstream and downstream edges of the cavity, formed by the seat of the valve. These geometric modifications are expected to have a strong influence on the occurrence of locked-on states.

In order to identify conditions under which the locked-on states can occur, the acoustic mode shapes and the associated frequencies were first calculated numerically by solving a Helmholtz equation in the three-dimensional volume. The details are provided in Chapter 3. In addition, a series of experiments was performed using two experimental systems: a simplified scaled model with relatively shallow cavity of the actual inline gate valve of the thermal power plant (Chapter 3) and a model with a deep, circular, axisymmetric cavity (Chapter 4). The second type of cavity is an idealized case that is related to circular, axisymmetric cavities of the gate valves that are present in the steam delivery system of a power plant.

It should be mentioned that gate valves are typically associated with relatively shallow cavities, while deeper circular cavities are associated with annular combustion applications and high speed axial compressors (Hellmich and Seume, 2008, Sensiau et al., 2009). The academic reason for selecting the geometry of Chapter 4 was to increase the degree of confinement of the diametral modes in the vicinity of the cavity. As it was demonstrated in earlier studies (Blevins, 1979, Lafon et al., 2003), the strength of the lock-on increases as the

partially trapped modes become more confined, and as the cavity becomes deeper and narrower relative to the main pipe diameter (Aly and Ziada, 2010).

The objective of the second part of the dissertation was to establish a practical methodology for investigating the performance of a prosthetic heart valve, implanted in the patient who had developed a certain type of valvular disease prior to the surgery. This objective was achieved through series of experiments on a polymeric heart valve coupled with anatomically correct models of the aortic root by means of flow visualization.

Implanting a heart valve without investigating potential side effects caused by valve diseases such as *severe insufficiency* (weakening and ballooning that prevents the valve from closing tightly) or *severe stenosis* (narrowing of the valve opening area) may lead to serious complications in the performance of the heart valve (Reul et al., 1990a). By replicating the aortic root geometry, and by performing a series of experiments with a polymeric heart valve, it was possible to establish how the change in the aortic root geometry affects general flow characteristics, shear stress distribution and turbulence intensities and, consequently, the performance of the heart valve.

The study of heart valves through fluid dynamics testing poses certain inherent challenges. This work aims to address the problem of application of experimental methods based on quantitative flow imaging to the investigation of the effect of aortic root geometry on the heart valve performance. Given the complex nature of the problem, fluid dynamics testing of flow through the prosthetic heart valve requires well-defined, and accurately established experimental techniques.

1.5 DISSERTATION OVERVIEW

In Chapter 2, the flow facility, experimental apparatus and the range of parameters studied are discussed in order to provide the reader with a good understanding of how the experiments were conducted. The experimental procedures are introduced along with applicable hardware setup and software pre- and post-processing. The accuracy of the equipment used and the overall error in the measurements are discussed.

Chapter 3 to Chapter 6 present experimental results and analysis for acoustically coupled flows over both shallow and deep circular axisymmetric cavities.

In Chapter 7, the performance of aortic heart valve prosthesis in different geometries of the aortic root is investigated experimentally. The objective of this investigation was to establish a set of parameters, which are associated with abnormal flow patterns due to the flow through a prosthetic heart valve implanted in patients that had certain types of valve diseases prior to the valve replacement.

Finally, in Chapter 8, the conclusions of this dissertation are summarized and the recommendations for the future research are presented.

1.6 CONTRIBUTIONS

This dissertation contributes to the area of fluid-structure interaction. Specifically, it addresses industrially relevant problems of flow-acoustic coupling, and their associated shear layer instabilities, in the steam delivery components of the power plants along with destructive aftermath of shear layer instabilities in the human cardiovascular system. Despite the advances made in the areas mentioned above, there are still a number of issues that need to be addressed. The primary contributions from the first part of the dissertation are related to bet-

ter understanding of the behaviour of the trapped acoustic diametral modes, which are often encountered in industrial applications, in particular, in steam line gate valves. The flow-acoustic coupling for both shallow and deep, circular axisymmetric cavities was investigated using a combined approach that involved numerical simulation of the resonant acoustic mode shapes, measurements of acoustic pressure and quantitative flow imaging, which provided quantitative insight into the physics of the phenomenon.

Specific contributions related to the first part of the dissertation, are listed below:

1) The results based on the experimental work associated with a shallow axisymmetric cavity presented a detailed quantitative description of the effect of convergence-divergence angle of the pipeline section on the partially trapped acoustic modes of the cavity. The acoustic response of the experimental system demonstrated mode switching at low inflow velocity between longitudinal and diametral acoustic modes, and, at higher inflow velocities, a simultaneous excitation of those two groups of acoustic modes. The experimental results also revealed a possibility of simultaneous excitation of multiple acoustic diametral modes by different azimuthal portions of the cavity shear layer, corresponding to the different locations of the pressure transducers (Barannyk and Oshkai, 2014b).
2) This work represents the first extensive description of flow-acoustic resonance in a deep, circular, axisymmetric cavity and the effect of cavity edge geometry on the occurrence and strength of the locked-on flow states. In particular, several important issues related to their understanding of trapped acoustic diametral modes, and the associated mechanism of flow-acoustic coupling have been addressed in this work:

a. In contrast to the earlier work associated with a shallow axisymmetric cavity (Aly and Ziada, 2011), the acoustic response of the cavity-pipeline system in the present study manifested as high-amplitude, self-sustained pressure oscillations corresponding to the first, the fourth and the seventh diametral acoustic modes of the cavity, with consequent excitation of several other high frequency acoustic diametral modes. For the first time, it was shown that the occurrence and the behaviour of locked-on flow states, and their associated acoustic diametral modes, was influenced by the introduction of chamfers to the upstream and/or downstream cavity edges. Among the considered cavity geometries, the configuration that corresponded to the most efficient noise suppression was identified (Barannyk and Oshkai, 2014a).

b. This work contributes to the better understanding of spinning behaviour of acoustic diametral modes associated with self-sustained flow oscillations. In particular, for the first time the acoustic diametral modes were investigated in a deep, circular, axisymmetric cavity with chamfers. This arrangement allowed investigation of the azimuthal orientation of the acoustic modes, which were classified as stationary, partially spinning or spinning. Introduction of shallow chamfers to the upstream and the downstream edges of the cavity resulted in changes of azimuthal orientation and spinning behaviour of the acoustic modes. In addition, introduction of splitter plates in the cavity led to a pronounced change in the spatial orientation and the spinning behaviour of the acoustic modes. The short splitter plates changed the behaviour of the dominant acoustic modes from partially spinning to

stationary, while the long splitter plates enforced the stationary behaviour across all resonant acoustic modes (Barannyk and Oshkai, 2014c).

c. The evolution of fully turbulent, acoustically coupled shear layers that form across deep, axisymmetric cavities were quantitatively investigated in a deep, circular, axisymmetric cavity for the first time using digital particle image velocimetry. One of the novel experimental techniques in this study was the usage of a borescope for non-intrusive optical access to the cavity. This technique allowed illumination and optical recording of flow tracers inside the cavity. Instantaneous, phase- and time-averaged patterns of velocity and vorticity provided insight into the flow physics during flow tone generation and noise suppression by the geometric modifications. In particular, the first mode of the shear layer oscillations was significantly affected by shallow chamfers located at the upstream and, to a lesser degree, the downstream edges of the cavity. Specifically, the introduction of the chamfers affected the phase and the location of formation of large-scale vortical structures in the shear layer, which is associated with a maximum of the vorticity thickness across the cavity opening. In turn, these changes in the flow structure affected the amplitude of acoustic pressure pulsations (Oshkai and Barannyk, 2014).

Specific contributions, which are related to the second part of the dissertation, are listed below:

1) Qualitative and quantitative flow visualization study was conducted for the case of a biomimetic pulsatile flow through an artificial heart valve placed into a physiologi-

cally accurate model of an aortic root with sinuses of Valsalva. For the first time, the dependence between abnormal flow patterns due to the flow through a prosthetic heart valve implanted in patients that had certain types of valve diseases, mainly aortic valve stenosis and aortic valve insufficiency, and the actual geometry of the aortic root was identified.

2) The presence of the elevated levels of Reynolds shear stress in the diseased model of an aortic root has not been previously addressed. In this study, cases that corresponded to abnormally high levels of Reynolds shear stress, which could potentially lead to platelet activation and, as a result of that, the formation of blood clots, were identified (Barannyk et al., 2013).

CHAPTER 2

EXPERIMENTAL SYSTEM AND TECHNIQUES

2.1 EXPERIMENTAL SET-UP

The steam in the Reliant Energy's Seward cold reheat (CRH) lines comes in through a 667 mm CRH line, through a gate valve, shown in Figure 2.1 and through a proportioning control valve. The inline gate valve is a valve that opens by lifting a round gate out of the path of the fluid. This type of valves is typically used when a straight-line flow of fluid and minimal restriction is desired. The CRH valves are oriented with the actuators at the top. The CRH lines vibrate sufficiently at certain conditions to have damaged small-diameter branch lines.

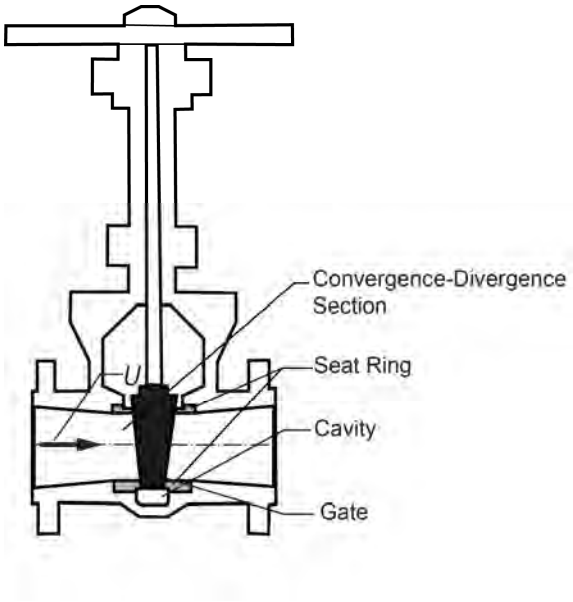

Figure 2.1: Cross section of the inline gate valve.

2.1.1 Shallow circular axisymmetric cavity

The flow system, which is shown schematically in Figure 2.2, consisted of two 1 m-long PVC pipe sections of circular cross-section connected to the valve model, a simplified version of the gate valve shown in Figure 2.1. Figure 2.3 illustrates the internal geometry of the model.

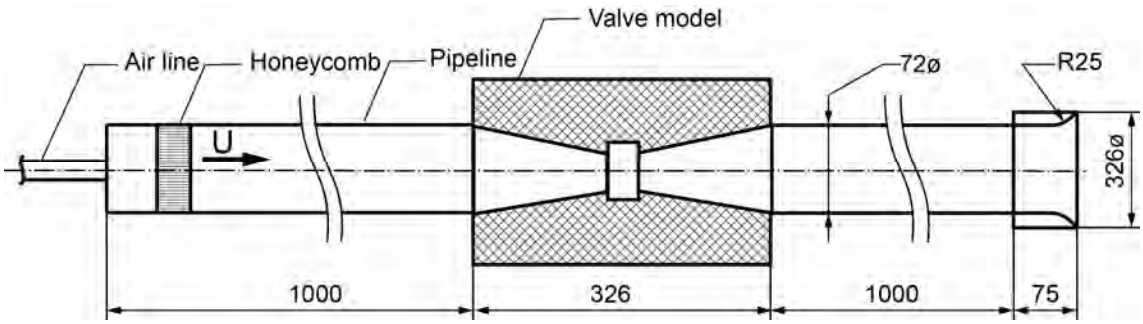

Figure 2.2: Schematic of the experimental system (dimensions in mm).

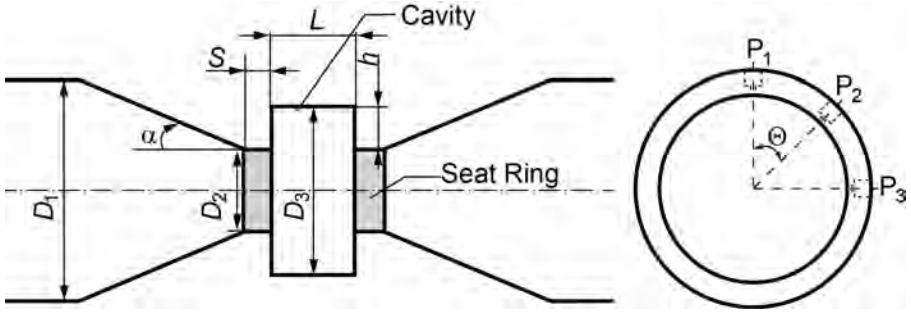

Figure 2.3: Characteristic parameters of the valve geometry.

A superheated (dry) steam is a type of steam that exits a high power section of the turbine and is redirected to a typical CRH line. It is important to understand that typically steam (not superheated) contains liquid droplets and as such is incompressible. When this type of steam doing work on a turbine the water droplets entrained in the fluid flow will strike the mechanical parts of the turbine, with enough force to damage them. Superheating of

steam ensures that the steam flow will not damage the internal moving parts of the turbine through which the steam passes. As superheated steam can be approximated by the air, it was decided to use air as the working fluid. It was supplied by a compressor located in a separate room. The test section was isolated from the flow pulsations induced by the compressor by employing a long connecting hose that served as a damper for the incoming flow oscillations. The inlet chamber was located upstream of the experimental apparatus and incorporated honeycomb flow straighteners in order to provide well-conditioned inflow to the test section. The outlet pipe was outfitted with a diffuser. The air compressor was able to provide a constant air supply at 410 kPa, which corresponded to a maximum velocity U = 30 m/s, measured at the centerline of the pipeline, immediately upstream of the cavity.

The model shown schematically in Figure 2.3 is a variation of the experimental apparatus that was used in the previous studies by Atomic Energy of Canada Limited (AECL) (Janzen et al., 2008, Smith and Luloff, 2000) where the maximum flow rate was equal to 530 g/s with the maximum constant pressure of 500 kPa.

The model contained three major parts: an upstream converging section, a downstream diverging section, machined from a single PVC rod, both with the same convergence-divergence angle α and a central insert that represented the valve seat cavity. All three parts were interfaced with O-rings and were tightly clamped together by four threaded rods. Three different values of the convergence-divergence angle were considered in the present study: α = 5°, α = 8°, α = 11.2°. The valve seat cavity had the length-to-depth ratio of L/h = 6 with L = 21.3 mm and h = 3.55 mm. Brass seat rings with the internal diameter D_2 = 47.2 mm and width S = 6.2 mm were located immediately upstream and downstream of the cavity. In all cases, the following parameters were kept constant: D_1 = 72 mm, D_3 = 54.3 mm.

2.1.2 Deep circular axisymmetric cavity

The experimental apparatus, which is shown schematically in Figure 2.4, consisted of a circular cavity of diameter d_C = 203.2 mm mounted in an aluminum pipeline, which was L_P = 2000 mm long and that had an internal diameter d = 21.1 mm. At the downstream end of the pipeline, a diffuser L_D = 25.4 mm long and d_D = 38.1 mm wide was attached to mitigate the end effects. Air was used as a working fluid. The flow was provided by a compressor that was connected to the inlet of the pipeline by a long hose in order to minimize the inflow fluctuations. The compressor was able to provide a maximum pressure of 410 kPa, which corresponded to the maximum flow velocity magnitude U_{max} = 149 m/s immediately upstream of the cavity.

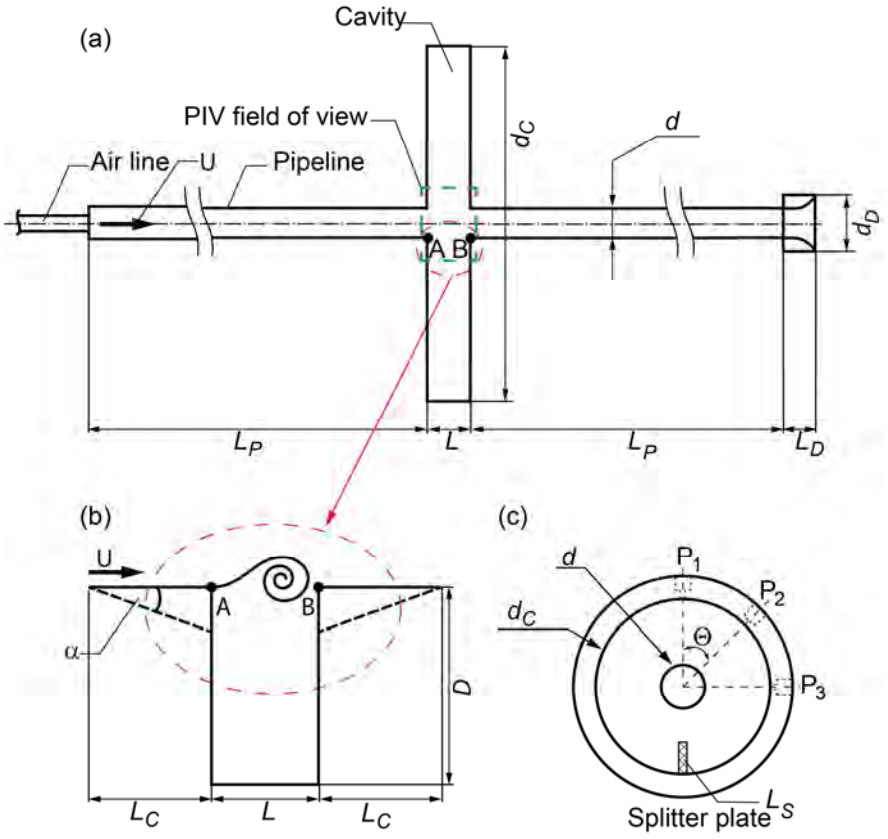

Figure 2.4: Schematic of the experimental system: (a) overview of pipeline-cavity system, (b) schematic of the cavity, (c) cross-sectional view of the cavity.

The circular cavity had a nominal length L = 25.4 mm and a depth D = 91.06 mm. In addition to the reference cavity geometry with the sharp 90° edges, three other configurations were investigated. In these modified configurations, the cavity corners indicated by points A and B in Figure 2.4 were removed by introducing chamfers (dashed lines in Figure 2.4 (b)) with the angle α = 15° to the upstream and/or the downstream edge. Three values of the chamfer length L_C were considered (L_C = 1.27 mm, 3.81 mm and 10.16 mm). For each chamfer length, three configurations were studied: 1) symmetric chamfers at the upstream and the downstream corners of the cavity, 2) chamfer at the downstream corner only, and 3) chamfer at the upstream corner only.

2.1.3 Pulsatile flow system

In Figure 2.5 and Figure 2.6, one can see the schematic of the experimental apparatus that allows testing of the heart valves in the aortic configuration. The ViVitro pulse duplicator is a heart model that incorporates the functional capability to test two heart valve substitutes simultaneously in left or right heart configurations while assessing their performance and function under simulated cardiac conditions.

The pulse duplicator was powered by a piston-in-cylinder pump driven by a motor connected to the ViViTest data acquisition and control block, which controlled the pump. This setup allowed for various ventricular waveform states and beat rates, while generating physiological pressures and flow regimes through the heart valve.

The present investigation was focused on the hemodynamics of a prototype trileaflet polymeric heart valve, which is shown in Figure 2.7 (b). The valve, which had a nominal

diameter of 19 mm, was mounted in a model of the aortic root with severe pathological changes of the aortic root geometry.

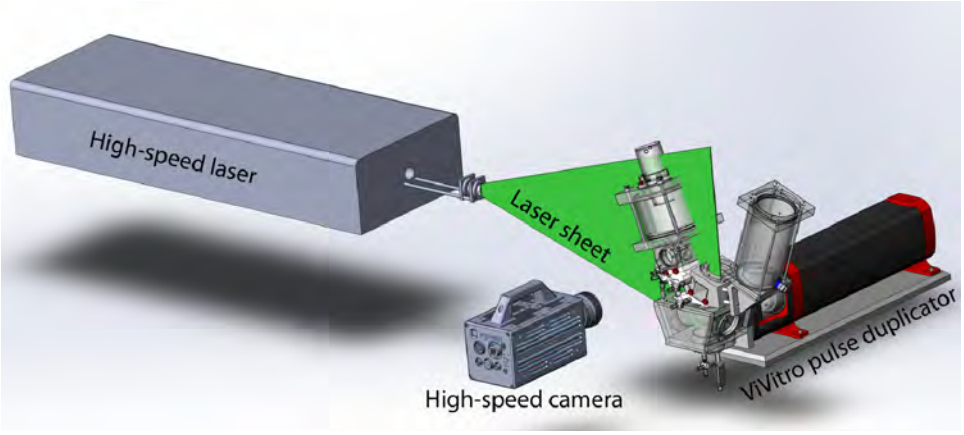

Figure 2.5: Schematic of the flow visualization setup (image courtesy of ViVitro Labs Inc.).

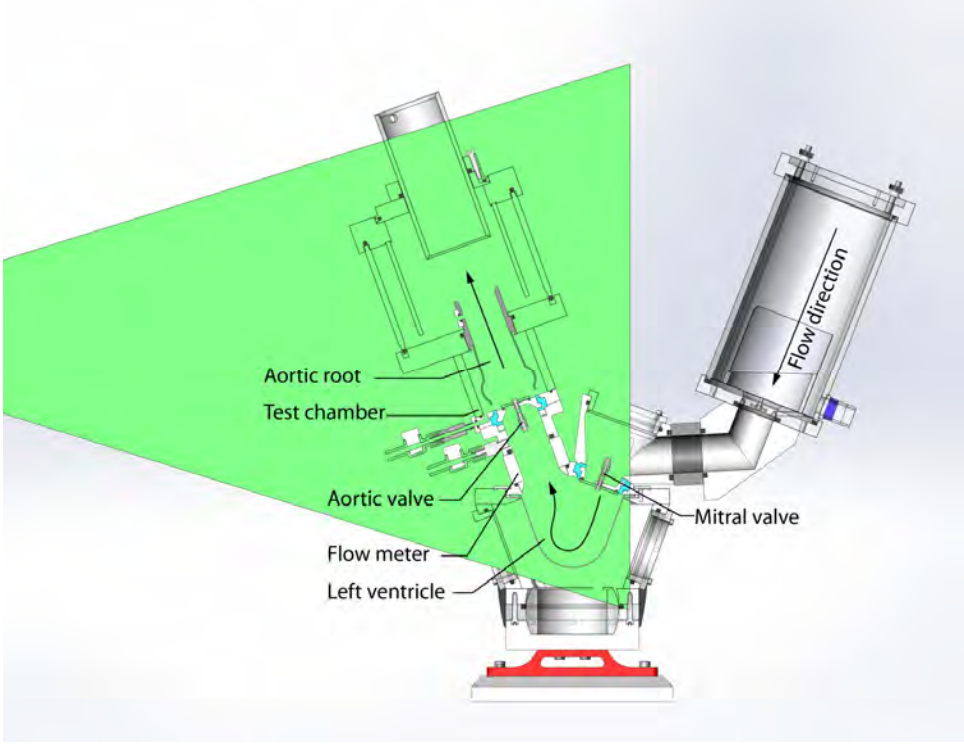

Figure 2.6: Schematics of the test chamber and the trileaflet aortic valve (image courtesy of ViVitro Labs Inc.).

For each of the aortic root types, the flow fields were collected in two perpendicular planes, as shown in Figure 2.7 (a). The start of the image capture was triggered by a

synchronization pulse from the pump controller. The PIV data were acquired at six representative phases of the cardiac cycle, indicated by black circles in Figure 2.8. These phases correspond to the opening acceleration phase (t/T = 0.05), the peak systole phase (t/T = 0.13), the deceleration phase (t/T = 0.22), the closing phase (t/T = 0.29), and the leakage phase (t/T = 0.69). Here, t denotes time and T = 860 ms is the period of the simulated cardiac cycle.

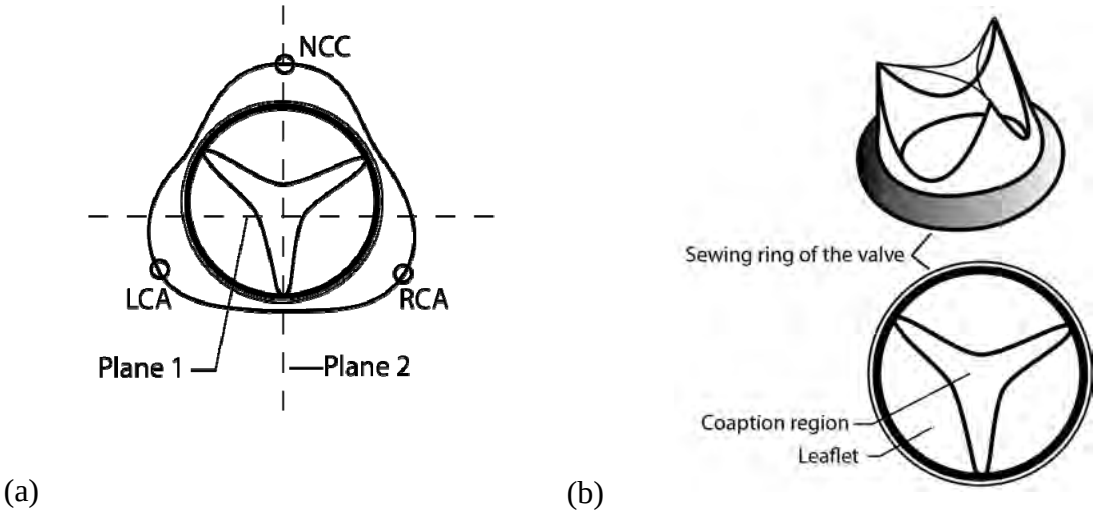

Figure 2.7: (a) Orientation of the valve with respect to the left coronary artery (LCA), the right coronary artery (RCA) and the noncoronary cusp (NCC) and the PIV data acquisition planes (dashed lines), (b) schematic of the prototype trileaflet polymeric valve.

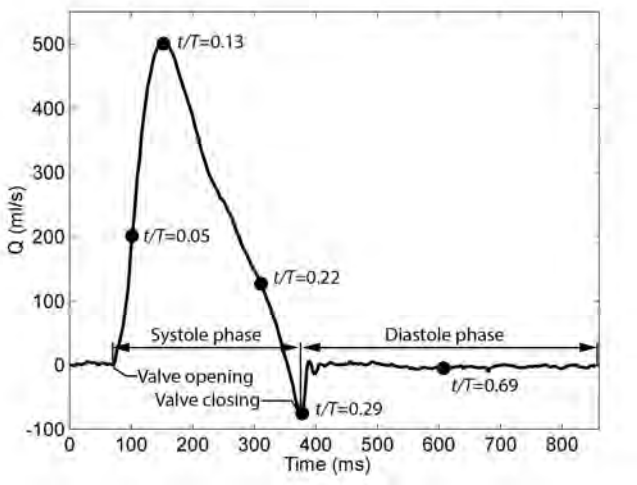

Figure 2.8: Variation of flow rate as a function of time during a typical cardiac cycle. Black circles correspond to the phases of the cardiac cycle, at which PIV data were obtained.

2.1.3.1 *Aortic root geometry*

The aortic root is a part of the ascending aorta, shown in Figure 2.9, with a combined length $h \cong 80$ mm (McDonald, 1974, Reul et al., 1990a). The anatomically accurate geometry of the aortic root is essential in replicating the internal flow field correctly (Bellhous.Bj, 1972, Reul et al., 1990a). During just one cardiac cycle that includes the systole and the diastole phases, several complex flow events occurred within the aortic root. The opening and the closing motions of the valve are supported through vortex formation within the aortic sinuses. In addition, when the valve is closed, previously formed sinus vortices are responsible for washout of the sinus cavities, so that the thrombotic deposition does not occur.

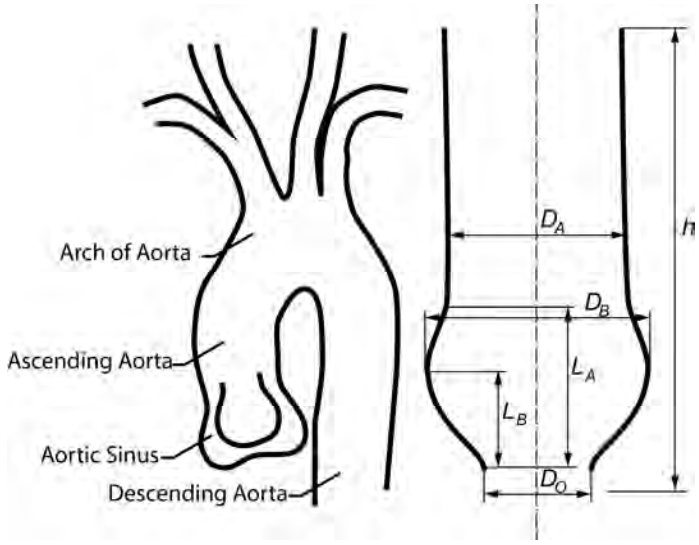

Figure 2.9: Major parts of aorta and principal dimensions of the aortic root sinuses (Reul et al., 1990b).

The importance of studying aortic root geometry associated with a specific clinical case in conjunction with a valve prosthetic in a single study was stressed in (Reul et al., 1990a). The authors demonstrated a concise quantification of the aortic root geometry changes due to valvular diseases. Geometric parameters and algebraic quotients were derived from 604 independent angiographic films collected from patients with various types and degrees of valvular diseases.

These derived quantities were used in the present work in such way that the resulting aortic root geometry was complaint with the existing ViVitro pulse duplicator system. By setting the orifice diameter to D_O = 24 mm, and the wall thickness to Δ = 1.5 mm, the dimensions listed in were derived from relationships originally presented in (Reul et al., 1990b). Here, D_O is the diameter of the orifice, D_A is aortic diameter distal to sinus, D_B is the maximum projected sinus diameter, L_A is the length of the sinuses, and L_B is the distance between D_O and D_B.

Table 2.1 Principal dimensions of the aortic root associated with clinical cases of heart disease.

	D_O (mm)	D_A (mm)	D_B (mm)	L_A (mm)	L_B (mm)
Normal	24	29.76	37.2	24	8.16
Severe Stenosis	24	36	41.28	24.96	10.8
Severe Insufficiency	24	25.2	32.88	19.68	13.44

Based on the dimensions presented in , three types of geometries that represented aortic root and ascending aorta system were built through the process of stereolithography (SLA). DSM Somos Watershed© XC 11122 an optically clear resin with acrylonitrile butadiene styrene (ABS)-like properties, good temperature resistance, water resistance, and great durability was used as a base material. This material is also a Class VI Approved Medical Grade material making it suitable for any medical applications. DSM Somos Watershed© material has an index of refraction of 1.51, which is approximately equal to that of clear cast acrylic 1.52, used as a base product for the aortic root housing.

Matching the refraction indices of the experimental model was essential for avoiding optical distortions and achieving good image quality for flow visualization. The test fluid used in the current test was as mixture of NaI (sodium iodide) and H_2O (water) at the ratio of 1185 g to 697 g by weight. In addition, a small quantity of $Na_2S_2O_3$ (sodium thiosulphate) was used to render the solution colorless. The solution had a viscosity of 0.032 Pa·s, measured by a calibrated, laboratory grade viscometer Brookfield RVT, and a density of 1650 kg/m^3, which is comparable to the viscosity and the density of the blood of 0.03 Pa·s and a density of 1100 kg/m^3 respectively. The solution achieved an index of refraction of about 1.51, resulting in minimal optical distortion, as shown in Figure 2.10.

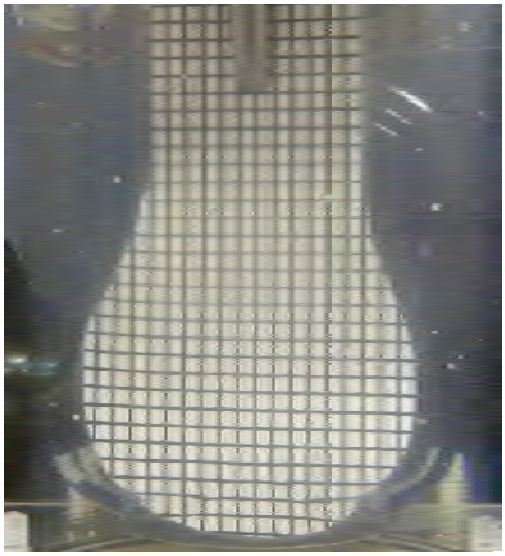

Figure 2.10: Grid pattern implemented to verify the absence of optical distortions for flow imaging.

2.1.4 Unsteady pressure measurements

The acoustic pressure measurements were obtained using three piezoelectric pressure transducers (PCB model 103A02), which were flush mounted into the bottom wall of the cavity. The details of the mounting arrangement are provided in (Peters, 1993). Particular attention was paid to ensuring that for the considered range of the flow velocities no acoustic resonance would be generated in the region between the face of a transducer and the edge of the pressure tap at the interior surface of the cavity wall. The transducers P_1, P_2 and P_3, shown in Figure 2.4, were separated from each other by angle $\Theta = 45°$ in the azimuthal direction. This arrangement allowed investigation of the azimuthal orientation of the trapped diametral modes (Aly and Ziada, 2010, Aly and Ziada, 2011). The analogue pressure signals were converted to digital form by a data acquisition board (National Instruments PXI-4472) with 24-bit resolution at a rate of 100 kHz.

2.2 DIGITAL PARTICLE IMAGE VELOCIMETRY

The technique of digital particle image velocimetry (PIV) belongs to the family of flow-visualisation tools that allow describing the qualitative and quantitative properties of the flow. Ludwig Prandtl was at the origin of application of flow visualization technique in the recirculation flow system in his investigation of the unsteady separated flows behind wings and various other objects (Prandtl, 1904). The results obtained from those experiments, allowed him to gain insights into various features of unsteady flow phenomena, although only qualitatively. Those early experiments by Ludwig Prandtl led to the development of the modern PIV technique, which has been used in its present form for more than 25 years.

Among the major advantages of the PIV technique is its non-intrusiveness and capability of delivering data with high spatial and temporal resolution. The uniqueness of PIV is its ability to extract velocity information from relatively large sections of flow fields in liquid or gaseous media (Raffel et al., 2007).

The popularity of using PIV technique as a primary flow visualization tool for various experimental studies led to accumulation of substantial number of research manuscripts, review articles and books on the subject: (Adrian, 2005, Adrian and Westerweel, 2011, Grant, 1997, Raffel et al., 2007, Westerweel, 1997). In this section, only a simple description of PIV, essential for proper understanding of the current work, will be provided.

2.2.1 Principles of PIV and its major components

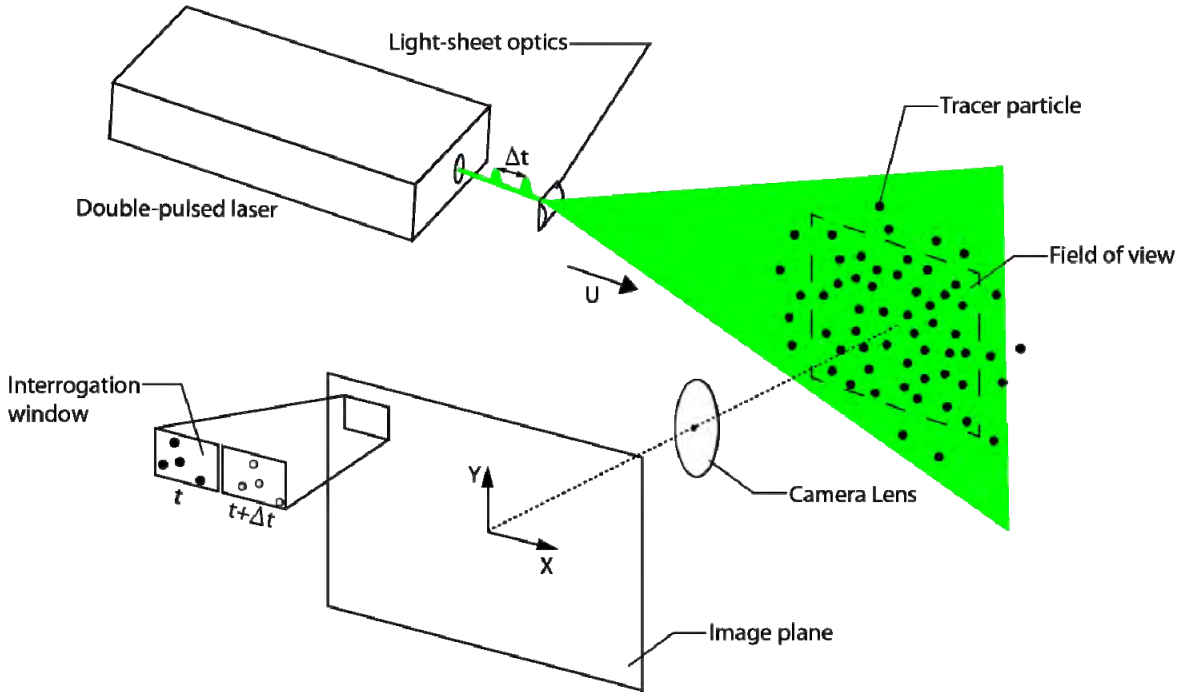

Figure 2.11: Schematic of a planar particle image velocimetry (PIV) system.

In Figure 2.11, one can see a typical experimental set-up for a planar PIV system, which consists of a reliable, high power dual cavity laser retrofitted with light sheet optics, that typically consist of spherical and cylindrical lenses, and a high resolution digital camera, equipped with high quality lens. Laser sheet thickness should be thin enough, typically about 1 mm or less, measured from the type 1895 linagraph laser burn paper, in order to avoid spatial averaging of the velocity (Hariharan et al., 2008).

During a typical PIV flow visualization experiment, the flow is seeded with the tracer particles. Within a relatively short time interval Δt, tracer particles are illuminated twice by the light sheet, generated by the laser. The scattered light obtained from the tracer particles in the plane of flow is recorded by the digital camera, as it is shown in Figure 2.11, which then

transfers all collected frames to the storage device, from which they can be used for further data post-processing and analysis.

It is assumed that particles are homogeneously distributed within the flow that the particles' specific gravity allows them to follow the flow freely and without influencing the flow itself, and finally, particles should have good light scattering efficiency in order to achieve sufficient contrast. Among many particle types that are commonly used in flow visualization studies, the following two types are the most common (Raffel et al., 2007): 1) Di-Ethyl-Hexyl-Sebacat (DEHS) droplets with the mean diameter of 1μm, predominately used in gaseous flows or 2) silver-coated hollow glass spheres, used in liquid flows, with mean diameter of 14 μm and specific gravity of 1.3 relative to water, used to study flow of liquids.

The proper particle size influences greatly their flow tracking ability and is associated with the Stokes number Sk, defined as a ratio of the particle relaxation time to the characteristic time of the velocity field, expressed as follows:

$$\mathrm{Sk} = \frac{\rho_p d_p^{\,2}}{18\mu}\frac{U}{L} \tag{2.1}$$

here, ρ_p, d_p are the density and the diameter of the tracer particle respectively, μ is the dynamic viscosity of the fluid; U, L are the characteristic velocity and the length scale of the flow (Raju and Meiburg, 1995, Tang et al., 1992). The particle' Stokes number should be substantially less then unity in order for particles to faithfully follow the flow (Melling, 1997, Raffel et al., 2007).

2.2.2 Optical challenges during PIV experiments and their resolution

PIV is a whole field, indirect and non-intrusive velocity measurement technique, which fundamental properties allow it to be applied in various flow scenarios, including high

speed flows with shocks and flows with thin boundary layers that otherwise will be disturbed by the presence of a probe. However, these same properties, that make PIV so attractive, impose one significant constraint on the experimental set-up, which is clear optical access to the plane of flow. Typically, in the flow visualization of internal flows the optical access is created by using either thin wall cut out section, like in the case of a cavity or pipe flow (Oshkai et al., 2005), by inserting a section made of an optical glass and accessing the region of interest (Raffel et al., 2007), by an external lens, or by matching the index of refraction (IoR) of a working fluid with the one of the test section (Hariharan et al., 2011). The biggest challenge during PIV measurements in the confined environment is the existence of the reflections when collecting data close to the boundaries. Typically, one can coat the walls with black matte paint in order to reduce certain amount of light reflected by the laser sheet from the interior walls, or match the IoR of the fluid with that of the test section. However, when a laser operates near its maximum power this approach does not work anymore. When IoR technique is not applicable, a thin coat of a fluorescent paint, like a mixture of Rhodamine-B with a clear acrylic coat used on the cavity walls, and the usage of a band-pass filter is the only remedy (Ide et al., 2010).

2.2.3 Backbone of PIV (cross-correlation, location of the displacement peak)

The type of recording during which the particle images exposed by a planar laser sheet and captured on the pair of frames of a digital camera over a time interval Δt is referred as a single-pulsed, double-frame recording (Adrian and Westerweel, 2011). In order to calculate the straight-line displacement of the particle images between two frames and, eventually, the velocity field, one needs to analyze the movement of localized groups of particles and

find the best match between images in two frames in a statistical sense. For that purpose, statistical methods that track the displacement of a small group of particles are implemented.

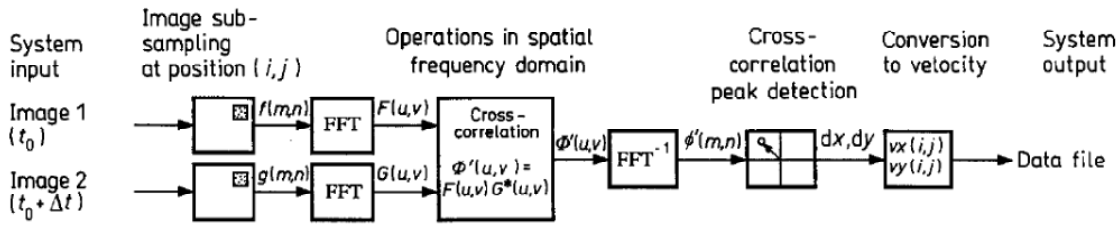

Figure 2.12: Schematics of the FFT based cross-correlation algorithm (Willert and Gharib, 1991).

In this work, a commercial software (Davis 8.1.3 by LaVision GmbH) that implements a discrete cross-correlation method (Willert and Gharib, 1991) was used in order to calculate the velocity field. The whole process is schematically illustrated in Figure 2.12. In its essence, the original frames are divided into small interrogation windows (IW), which are typically square. The cross-correlation technique is then applied to estimate the most probable displacement of the particles in each IW, which correspond to the highest peak in the cross-correlation plane. The displacement is then divided by the time interval Δt between two laser pulses to determine a local velocity vector for each IW.

In order to speed up the whole process, the cross-correlation technique relies on the correlation theorem, which equates the cross-correlation of two functions to a complex conjugate multiplication of their Fourier transforms which in practice is realized through a Fast Fourier Transform (FFT). The implementation of FFT reduces the number of operations from $O[N^2]$ to $O[N \log_2 N]$ (Raffel et al., 2007).

The usage of FFT is accompanied by its shortcomings that have to be dealt with. One of the most important shortcomings of FFT with respect to PIV is the limitation on the parti-

cle displacement range. Due to the Nyquist criterion associated with FFT, for the data of length *N* (size of the IW in pixels) the maximum displacement magnitude that can be accurately recovered has to be equal to *N/2*. During a typical PIV experiment, however, because of the rapid decrease of the correlation peak strength with the increase in displacement, a widely adopted limit is *N/4* (Raffel et al., 2007, Keane and Adrian, 1990). Another shortcoming of the FFT with respect to its implementation in cross-correlation is that correlation estimates are biased due to the imposed periodicity of the correlation data. In order to negate this issue, a proper weighting function needs to be implemented. When all of the above issues are properly addressed, one gets an efficient and reliable cross-correlation algorithm such as the one implemented in the Davis 8.1.3 software used in this study.

In order to increase the correlation signal-to-noise ratio and decrease the number of spurious vectors obtained during typical calculation of the vector field, two advanced interrogation techniques were implemented during data processing. First, the technique of correlation based correction (CBC) (Hart, 2000) in conjunction with fifty-percent overlap between adjacent IWs was applied to the PIV images. In its essence, the CBC technique corrects for errors resulting from insufficient data and errors caused by correlation anomalies due to the gradients in the flow, by multiplying two overlapping regions, which in turn amplifies the common correlation peaks. The CBC method improves the spatial resolution of the velocity field and effectively decreases the number of spurious vectors, which was about 10% in this study.

In addition to the CBC technique, the adaptive multipass interrogation technique (Westerweel, 1997) was applied to correct for the velocity bias. The velocity bias is resulted from large velocity gradients accompanied by unequal particle displacement causing one re-

gion of the IW to correlate at a significantly different location then another region. In the adaptive multipass technique, the image pair is interrogated such that in each subsequent pass the dimension of the IW is reduced and the interrogation grid is refined. This process is then repeated until the desired resolution is achieved. Each pass of the adaptive multipass interrogation technique is accompanied by the regional median filter, which detects and removes any spurious data. A typical error using adaptive multipass interrogation technique in PIV is on the order of 0.1 pixels (Huang et al., 1997, Westerweel et al., 1997), and a conservative estimate of 5% error in true particle displacement can be assumed. The final vector field is smoothed by a 3 × 3 smoothing filter to reduce noise.

2.2.4 PIV parameter choice for deep circular axisymmetric cavity flow system

The PIV system, implemented to acquire quantitative images of the air flow across the cavity opening, consisted of an Nd:YAG dual cavity laser (Solo PIV manufactured by New Wave Research), which provided illumination of the flow field. The flow was seeded with Di-Ethyl-Hexyl-Sebacat (DEHS) droplets with the mean diameter of 1μm. The Stokes number of the droplets was equal to 2.8×10^{-3}, which indicated that the droplets were sufficiently small to accurately follow the flow (Raffel et al., 2007). The images of the tracer particles (droplets) were recorded with a digital camera equipped with a Charge-Coupled Device (CCD) sensor that consisted of 1376×1040 pixels.

The dimensions of the cavity and the highly confined nature of the flow under consideration presented several challenges for implementation of PIV. In particular, optical access for the camera to the area of interest was limited due to the parallax effect produced by the high depth-to-length ratio of the cavity. Moreover, the curved walls of the cavity introduced a

significant amount of optical distortion to the particle images. The combination of these factors made conventional flow images unfeasible. In order to overcome these challenges, the camera was outfitted with a borescope, which optically projected the area of interest to the CCD sensor. The main components of the PIV system and their position with respect to the flow system are shown schematically in Figure 2.13. The inherent limitation of this imaging approach is the decreased in the amount of light that reached the CCD sensor due to optical losses inside the borescope. This constraint can be partially overcome by increasing the output power of the laser and attaching a lens with a low f-number to the camera. In the present study, an f/1.4 lens was employed.

In order to minimize the interference between the laser light reflected from the cavity walls and the light scattered by the tracer particles, the interior surfaces of the pipeline-cavity system were coated with a fluorescent paint in order to change the wavelength of the reflected light. A band-pass filter attached to the lens of the camera prevented the reflected light from reaching the CCD sensor. In these experiments, a mixture of Rhodamine-B with clear coat paint was used in conjunction with a 527 nm band-pass filter, which had a bandwidth of 10 nm.

Pairs of tracer images were collected at a rate of 4.9 image pairs per second. The beginning of image acquisition sequence was synchronized to a zero-crossing of the acoustic pressure signal at the state of flow-tone resonance, commonly referred to as a locked-on condition. The time interval *dt* between the images in each pair was interactively adjusted in order to optimize the accuracy of the calculated particle displacement. In the present study, values of *dt* between 5 μs and 25 μs were used. The images were processed in the Davis 8.1.3 software, which utilized a multipass cross-correlation algorithm to calculate the flow velocity

vectors based on the local displacement of the tracer particles. The initial pass of the algorithm employed 64 pixel × 64 pixel interrogation windows with 50% overlap in each direction. The final pass involved 16 pixel × 16 pixel interrogation windows with 50% overlap in each direction, which resulted in the 8 pixel spacing between individual velocity vectors.

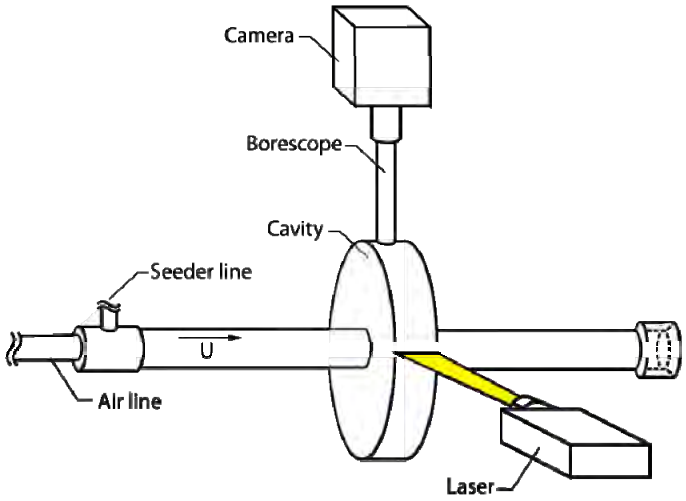

Figure 2.13: Schematic of the PIV set-up.

The field of view of the camera (shown in Figure 2.4 (a)) corresponded to an area of 26 mm x 40 mm, with a resolution of 6.45 μm/pixel. The data acquisition plane was oriented along the centerline of the pipeline. The origin (X = 0 mm, Y = 0 mm) corresponded to the center of the pipe cross-section at the upstream edge of the cavity.

2.2.5 Time-averaging of experimental data

As mentioned in the previous section, pairs of tracer images that were used to yield a velocity vector field were collected at a rate of 4.9 image pairs per second. Because the image sampling rate was substantially lower than the frequency of the first acoustic resonant mode, the set of acquired PIV images consisted of random samples that are independent from acous-

tically coupled flow, and which make them suitable for the calculation of time-averaged turbulent statistics. In order to determine the minimal number of images *N* required for time-averaged quantities such as streamwise and transverse velocity components, vorticity, RMS of the *u* and *v* component fluctuations, as well as Reynolds stress correlations to converge, the number of images was incrementally increased, and the results were compared for different sample sizes. For the present configuration of the experimental apparatus and the range of inflow velocities, a total number of 200 image pairs was found to be sufficient. Time-averaged flow quantities used in the present investigation, where *N* is a total number PIV images, are defined in Equations (2.2) through (2.7).

Time-averaged streamwise component of velocity:

$$< u >= \frac{1}{N}\sum_{n=1}^{N} u_n(x,y) \tag{2.2}$$

Time-averaged transverse component of velocity:

$$< v >= \frac{1}{N}\sum_{n=1}^{N} v_n(x,y) \tag{2.3}$$

Time-averaged vorticity:

$$< \omega >= \frac{1}{N}\sum_{n=1}^{N} \omega_n(x,y) \tag{2.4}$$

Root-mean-square of *u* component fluctuation:

$$u_{rms} = \left\{ \frac{1}{N}\sum_{n=1}^{N} \left[u_n(x,y) - < u(x,y) > \right]^2 \right\}^{1/2} \tag{2.5}$$

Root-mean-square of *v* component fluctuation:

$$v_{rms} = \left\{ \frac{1}{N}\sum_{n=1}^{N} \left[v_n(x,y) - < v(x,y) > \right]^2 \right\}^{1/2} \tag{2.6}$$

Averaged value of Reynolds shear stress (RSS) correlation:

$$< u'v' >= -\frac{\rho}{N}\sum_{n=1}^{N}\left[u_n(x,y) - < u(x,y) >\right]\left[v_n(x,y) - < v(x,y) >\right] \qquad (2.7)$$

2.2.6 Phase-averaging of experimental data

In addition to time-averaging, phase-averaging of the PIV images was performed. Following the methodology established in (Velikorodny et al., 2010, Geveci et al., 2003), the identification of the proper phase of the velocity field was successfully performed by analyzing the sinusoidal reference pressure signal which was collected in conjunction with the trigger signal to the laser (Q-switch).

In essence, as described in (Geveci et al., 2003), phase φ is defined as the phase difference between the occurrence of the zero crossing of the pressure signal from negative to positive and acquisition of the pair of images. In this study, the acoustic cycle was divided into a ten equally spaced phases, starting at φ = 36° and with an increment of $\Delta\varphi$ = 36°. In addition to that, the usage of the streamwise position of large-scale vortical structures along the cavity opening as an additional constraint in phase matching resulted in the increase in accuracy in determination of the phase. In the present study, at least 100 cross-correlated pairs of images for each pre-determined phase of the acoustic oscillation cycle were collected. Using this methodology, the resolution of the effective phase angle was ±1.5° (Geveci et al., 2003).

2.2.7 PIV parameter choice for cardiovascular flow system

The PIV system used in the cardiovascular flow experiments contained a Litron LDY 300 series diode pumped Nd:YLF dual cavity laser with a maximum energy output of 22.5

mJ at 1 kHz operating at a wavelength of 527 nm. The laser sheet with a thickness of 1 mm, measured from the type 1895 linagraph laser burn paper, was generated by a series of cylindrical and spherical lenses.

The flow was seeded with silver-coated hollow glass spheres with mean diameter of 14 μm and specific gravity of 1.3 relative to water. The Stokes number of the droplets was equal to 0.7×10^{-3}, which indicated that the droplets were sufficiently small to accurately follow the flow (Melling, 1997, Raffel et al., 2007). The images of the tracers were recorded using a Photron Complementary Metal Oxide Semiconductor (CMOS) camera with a sensor that consisted of 1024 × 1024 pixels, which was oriented parallel to the data acquisition plane shown in Figure 2.11.

The resolution of the images was 17 μm/pixel and a particle size of 2 pixels. The field of view was 70 mm × 30 mm, which represented a physical region extending $1.5D_O$ upstream and $3D_O$ downstream of the valve (see Figure 2.9). The origin (X = 0 mm, Y = 0 mm) corresponded to the center of the outflow area of the gasket holding the valve.

The images were recorded in a double frame/double exposure mode at a sampling rate 100 Hz and with the time interval between the frames in a pair of 500 μsec. The velocity vector fields were calculated using commercial PIV software (LaVision Davis 8.1.3). A multi-pass cross-correlation algorithm, with the initial pass of 64 pixel × 64 pixel interrogation windows with a 50% overlap between the adjacent windows in both X- and Y-directions, and the final pass of 16 pixel × 16 pixel interrogation windows with a 50% overlap in both directions was implemented. The resulting vector-to-vector spacing was equal to 8 pixels.

2.2.8 Ensemble-averaging of the data

In order to provide accurate description of various properties of the flow, the ensemble-averaging technique was implemented for adequate representation of each phase of the cardiac cycle. For each data acquisition plane, 10 randomly selected, statistically independent sets of data, where each set contained 32 periods of a typical cardiac cycle, were collected at a 100 Hz sampling rate. This sampling rate resulted in 86 phases over the typical period of a cardiac cycle. Combining together 10 independent data sets yielded a number of 320 ensembles of each of 86 phases of the cardiac cycle.

Following (Dasi et al., 2007, Leo et al., 2006), only 250 ensembles were used. In order to calculate the mean and the root-mean-square (RMS) values of the velocity vector fields at each phase for the cardiac cycle, the following formulas were implemented:

$$\overline{u}^{\varphi} = \frac{1}{N}\sum_{k=1}^{N} u_k{}^{\varphi}, \qquad u'^{\varphi} = u^{\varphi} - \overline{u}^{\varphi}, \qquad u^{\varphi}{}_{rms} = \left\{ \frac{1}{N}\sum_{k=1}^{N} \left[u'^{\varphi} \right]_k^{\,2} \right\}^{1/2};$$

$$\overline{v}^{\varphi} = \frac{1}{N}\sum_{n=1}^{N} v_k{}^{\varphi}, \qquad v'^{\varphi} = v^{\varphi} - \overline{v}^{\varphi}, \qquad v^{\varphi}{}_{rms} = \left\{ \frac{1}{N}\sum_{k=1}^{N} \left[v'^{\varphi} \right]_k^{\,2} \right\}^{1/2},$$

here, N is the number of samples that was used for the ensemble-averaging and φ represents a particular phase of the cardiac cycle and the bar denotes the average in time.

The Reynolds shear stresses (RSS) correlation was defined as the time average of the product of the fluctuating components of the velocity field. The mathematical definition of the ensemble-averaged Reynolds stresses is given in following equation:

$$-\rho\,\overline{u'v'}^{\varphi} = \frac{1}{N}\sum_{k=1}^{N} [u'^{\varphi} v'^{\varphi}]_k \tag{2.8}$$

The RSS values were used to provide a statistical measure of the influence on the averaged velocity field by turbulent fluctuations at a given location.

CHAPTER 3

INVESTIGATION OF DIAMETRAL ACOUSTIC MODES IN A MODEL OF A STEAM CONTROL GATE VALVE

3.1 NUMERICAL SIMULATION OF ACOUSTIC MODES

3.1.1 Governing equations and boundary conditions

Sound waves in a lossless medium, without dipole and monopole sources, are governed by the following equation for the pressure p,

$$\frac{1}{\rho c^2}\frac{\partial^2 p}{\partial t^2} + \nabla \cdot \left(-\frac{1}{\rho}\nabla p \right) = 0, \tag{3.1}$$

where ρ is the density of the medium, p is the acoustic pressure, t is time, and c is the speed of sound. Considering time-harmonic acoustic waves of angular frequency ω (rad/s), the pressure associated with this type of wave varies with time as

$$p(\mathbf{x},t) = p(\mathbf{x})e^{i\omega t}, \tag{3.2}$$

where $\mathbf{x}$ is the position vector. After substituting (3.2) into (3.1), one obtains a Helmholtz equation,

$$\nabla \cdot \left(-\frac{1}{\rho}(\nabla p) \right) - \frac{\omega^2 p}{\rho c^2} = 0. \tag{3.3}$$

By introducing the eigenvalues $\lambda = -i2\pi f = -i\omega$, Equation (3.3) can be treated as an eigenvalue problem, and the eigenfrequencies with the correspondent eigenmodes can be obtained. In the case of the pipeline-cavity system, the eigenvalues represent the resonant frequencies, and the corresponding eigenfunctions represent the acoustic mode shapes.

3.1.2 Domain discretization and mesh independence

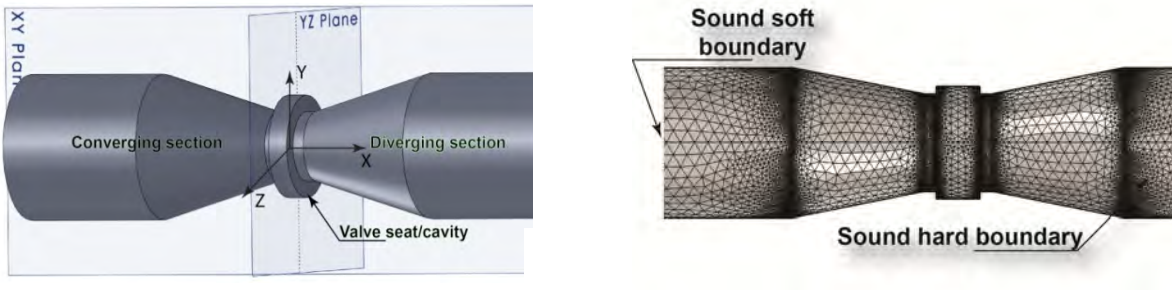

Figure 3.1: (a) Computational domain, (b) Computational grid.

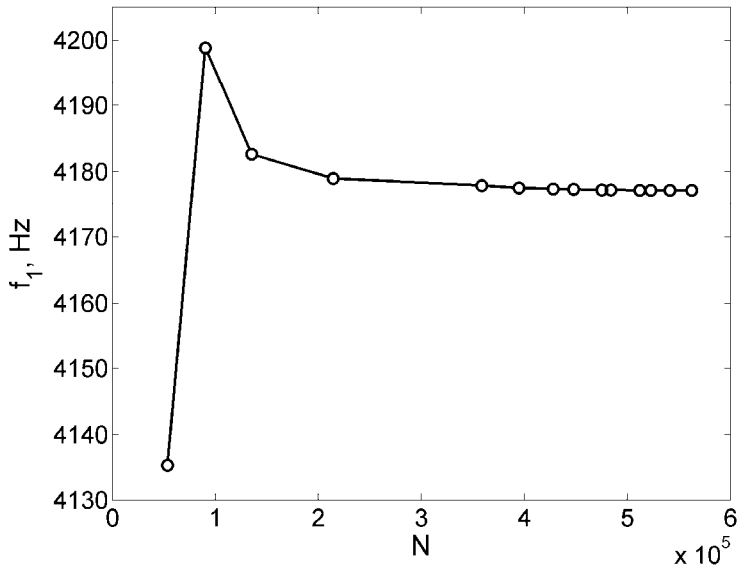

Figure 3.2: Frequency of the first diametral acoustic mode f_1 as a function of the number of mesh elements N.

Figure 3.1 (a,b) shows a schematic of the computational domain and the grid, respectively. The boundary conditions on all solid surfaces corresponded to the sound hard walls,

i.e. the normal derivative of the pressure was equal to zero on the boundaries. The inlet/outlet boundary conditions corresponded to the sound soft boundaries, i.e. to zero acoustic pressure. With this approach, the system was simulated as an open-ended duct with zero pressure gradient imposed on the surfaces. The finite-element package Comsol 4.2a was employed to solve the eigenvalue problem corresponding to the governing Equation (3.3). The resulting solution is a set of eigenvalues and eigenvectors of the geometry, samples of which are illustrated in Figure 3.3. The computational domain was discretized using a 4-node tetrahedral mesh with minimal element size of 1.2 mm, which yielded a total number of 522,766 elements. The singularities associated with the sharp edges of the cavity were removed by replacing the sharp corners with radii of 0.2 mm.

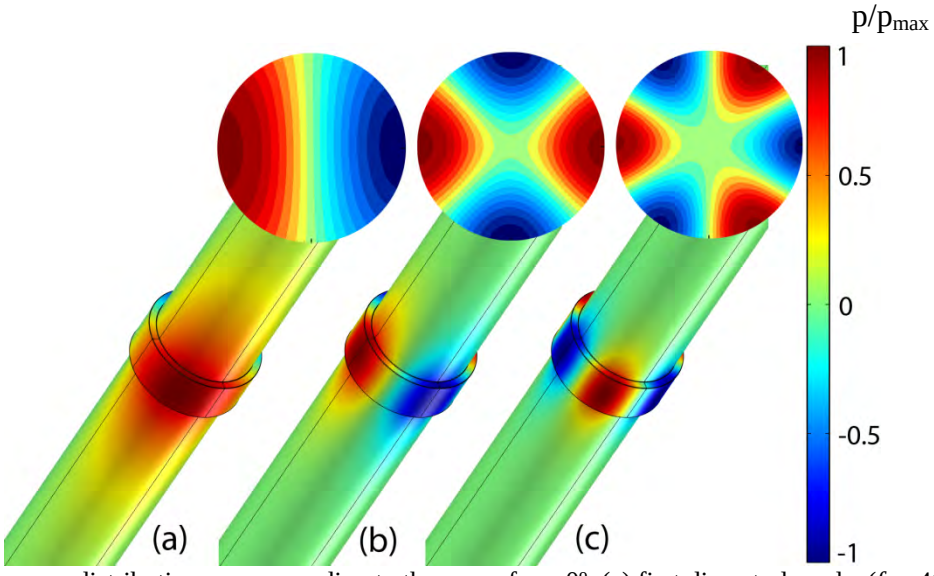

Figure 3.3: Pressure distributions corresponding to the case of α = 0º: (a) first diametral mode (f_1 = 4141 Hz); (b) second diametral mode (f_2 = 6665 Hz); (c) third diametral mode (f_3 = 8973 Hz).

The numerical solutions were tested for mesh independence by performing successive refinements of the grid and monitoring the numerical values of the simulated frequencies. The

acceptable convergence was achieved for grids with 522,766 elements and above. These grids corresponded to at least 30 elements per wave length associated with the maximum simulated frequency of approximately 9 kHz. The results of the mesh independence study are shown in Figure 3.2 in terms of the calculated frequency of the first diametral acoustic mode, f_1, for the case of $\alpha = 0°$.

Figure 3.3 shows the pressure amplitude distributions corresponding to the first three diametral acoustic modes for geometry corresponding to $\alpha = 0°$. The first three diametral modes were trapped in the vicinity of the cavity, i.e. the pressure levels in the main pipeline, away from the cavity, were negligible. This feature is in agreement with the published results (Aly and Ziada, 2010, Aly and Ziada, 2011). The higher modes were more concentrated around the cavity, compared to the lower modes. In other words, they corresponded to lower levels of radiation into the main pipeline.

For all modes, the maximum pressure amplitude occurred at the bottom wall of the cavity, at $x = 0$ (as defined in Figure 3.1(a)). The cross-sections of the mode shapes in the *YZ* plane, illustrated in Figure 3.3, located at $x = 0$ show that the pressure distribution at the bottom wall of the cavity, along its circumference, corresponded to a sinusoidal function with respect to the azimuthal position. These results follow the general trend observed in the earlier investigations (Aly and Ziada, 2010, Aly and Ziada, 2011). The numerical model presented in this section was further validated against experimental results corresponding to a shallow axisymmetric cavity model, presented in Table 3.1.

Table 3.1: Numerical and experimental frequencies of the diametral acoustic modes corresponding to different convergence-divergence angles α.

Geometry	f^{NUM}, Hz	f^{EXP}, Hz
$\alpha = 0°$	f_1 = 4141, f_2 = 6665, f_3 = 8973	N/A
$\alpha = 5°$	f_1 = 4125, f_2 = 6648, f_3 = 8984	f_1 = 4127, f_2 = 6636, f_3 = 8998
$\alpha = 8°$	f_1 = 4191, f_2 = 6644, f_3 = 8996	f_1 = 4113, f_2 = 6616, f_3 = 8964
$\alpha = 11.2°$	f_1 = 4181, f_2 = 6632, f_3 = 8985	f_1 = 4079, f_2 = 6662, f_3 = 9052

While the simulated frequencies were in good agreement with the experimental values, as it can be seen in Table 3.1, the difference between the numerical and experimental results increased with the increase in convergence-divergence angle α. This trend is due to the fact that the numerical procedure did not account for the presence of the flow and, in particular, for coupling between the fluctuating acoustic velocity in the cavity and the vorticity-bearing hydrodynamic velocity component in the separated shear layers. The change in the geometry of the upstream section of the pipe directly affected the development of the boundary layer in the vicinity of the cavity, which in turn led to changes in the flow-acoustic coupling. The changes in the properties of the shear layers induced by the converging-diverging section increased as the convergence-divergence angle α became larger.

3.2 EXPERIMENTAL RESULTS AND DISCUSSION

3.2.1 Effect of the inflow velocity

In this section, experimentally obtained pressure spectra are analyzed for a range of the inflow velocity 8 m/s $\leq U \leq$ 30 m/s with an increment ΔU = 0.5 m/s, measured at the centerline of the pipeline, immediately upstream of the cavity. The data correspond to three values of the convergence-divergence angles α = 5º, 8º, 11.2º. The measurements were obtained at the bottom wall of the cavity. Unless stated otherwise, the results presented here correspond to the pressure transducer P_1. Figure 3.4 shows typical features of the power spectrum of the acoustic pressure measured, in this case, for the geometry with convergence-divergence angles α = 5º and corresponding to the inflow velocity U = 21.5 m/s. To identify the acoustic modes, both numerical results and theoretically calculated cut-off frequencies (f_1^c = 4221 Hz, f_2^c = 7003 Hz, f_3^c = 9632 Hz) were used to identify the frequency ranges where particular acoustic modes were expected. The maxima in the experimentally obtained pressure spectra in those frequency ranges were subsequently identified.

In Figure 3.4 pronounced pressure peaks are evident and can be clearly classified into two major groups. The first group contains modes with relatively low amplitudes and the frequencies below 1000 Hz, corresponding to the longitudinal acoustic modes and their harmonics. The second group contains the predominant modes, corresponding to the first three partially trapped acoustic diametral modes with the characteristic frequencies f_1 = 4127 Hz, f_2 = 6636 Hz, f_3 = 8998 Hz, among several other acoustic modes excited in the cavity. Simultaneous excitation of multiple resonant modes is typical for the cases of turbulent flow in pipeline-cavity systems (Rockwell et al., 2003).

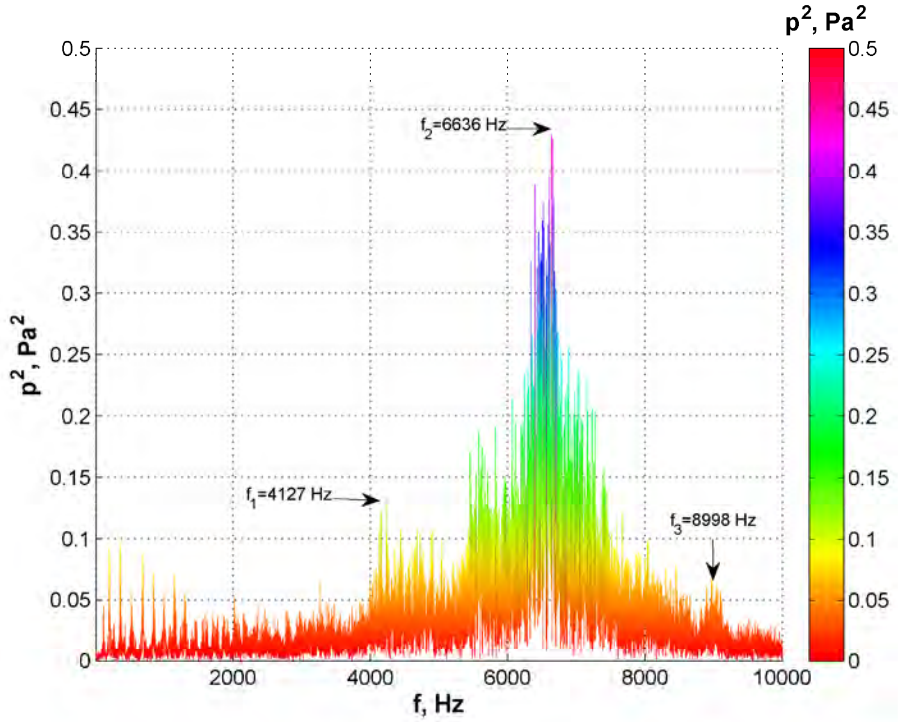

Figure 3.4: Pressure spectrum corresponding to the inflow velocity U = 21.5 m/s, for the case of α = 5º.

Figure 3.5 through Figure 3.7 show plots of 44 individual pressure spectra corresponding to three values of the convergence-divergence angles: α = 5º, 8º, 11.2º, respectively. All three plots show narrow-band noise peaks of elevated pressure amplitude that occurred within the range of tested inflow velocities. The maximum pressure amplitude changed as a function of the convergence-divergence angle α. The maximum value of the pressure amplitude was observed for the case of α = 5°. The maximum pressure amplitude decreased as the convergence-divergence angle α increased to α = 11.2°. In addition, simultaneous excitation of multiple modes at a given value of the inflow velocity U can be observed at all three values of the convergence-divergence angle α. This feature of the pressure spectra indicates the presence of a broadband noise source, generated by small-scale turbulence and large-scale flow separation (Gijrath et al., 2000).

While multiple acoustic modes were excited by the broadband source, the pressure peak with the highest amplitude in Figure 3.5 through Figure 3.7 corresponds to the second acoustic diametral mode of the cavity. It can be seen from these figures that the maximum pressure amplitude increased as the mean flow velocity increased up to U = 21.5 m/s, followed by a rapid decrease at U = 23 m/s. This attenuation of the predominant acoustic mode points out the physical mechanism of the acoustic mode excitation. Specifically, the acoustic response appears to be due to a combination of the broadband excitation by the turbulent pipe flow, the intermittent coupling between the acoustic velocity field and the periodic oscillations of the shear layer that forms across the opening of the shallow cavity, as observed in (Geveci et al., 2003). The maximum pressure amplitude increased again as the inflow velocity increased from U = 23.5 m/s to U = 30 m/s. The local maxima of the pressure amplitudes for the case of $\alpha = 5°$ were observed at the inflow velocities of U = 21.5 m/s and U = 30 m/s. The summary of the results obtained for all three geometries at critical values of inflow velocity, where the pressure fluctuations attained their maximum, are presented in Table 3.2.

Table 3.2: Summary of experimental results.

Geometry	p^2, Pa^2	f, Hz	U, m/s	St	Ma	Re
$\alpha = 5°$	0.491	6636	21.5	6.57	0.063	65000
	0.429	6507	30	4.62	0.088	90000
$\alpha = 8°$	0.487	6616	22	6.41	0.064	66000
	0.416	6500	29.5	4.69	0.087	89000
$\alpha = 11.2°$	0.455	6662	22	6.45	0.064	66000
	0.409	6465	29	4.75	0.085	87000

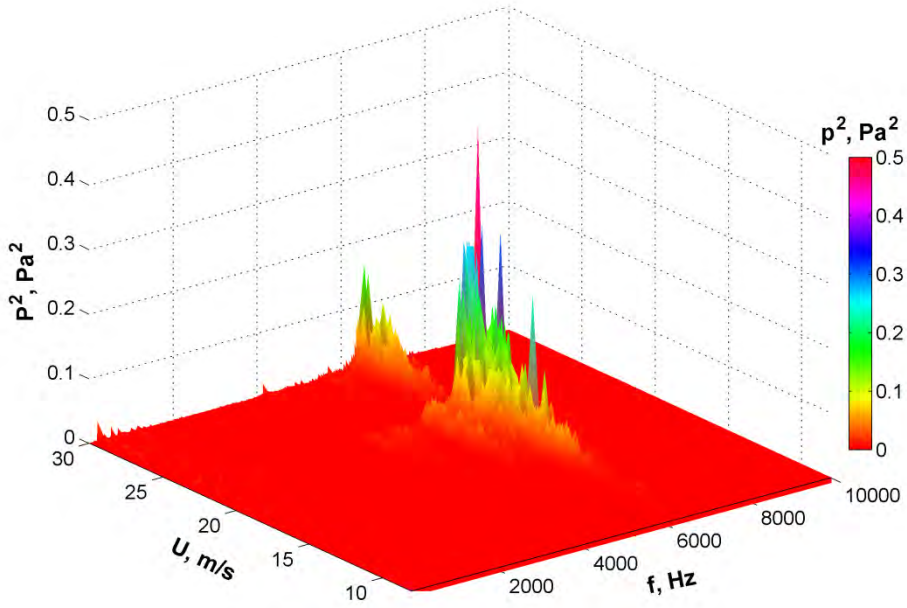

Figure 3.5: Waterfall plot of the pressure amplitude as a function of the frequency *f* and the inflow velocity *U* for the case of $\alpha = 5^{o}$.

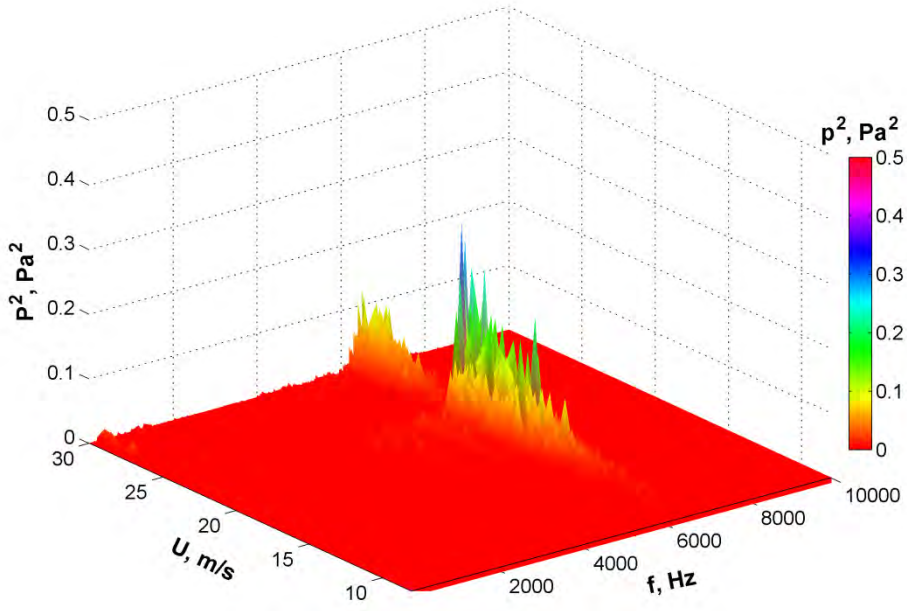

Figure 3.6: Waterfall plot of the pressure amplitude as a function of the frequency *f* and the inflow velocity *U* for the case of $\alpha = 8^{o}$.

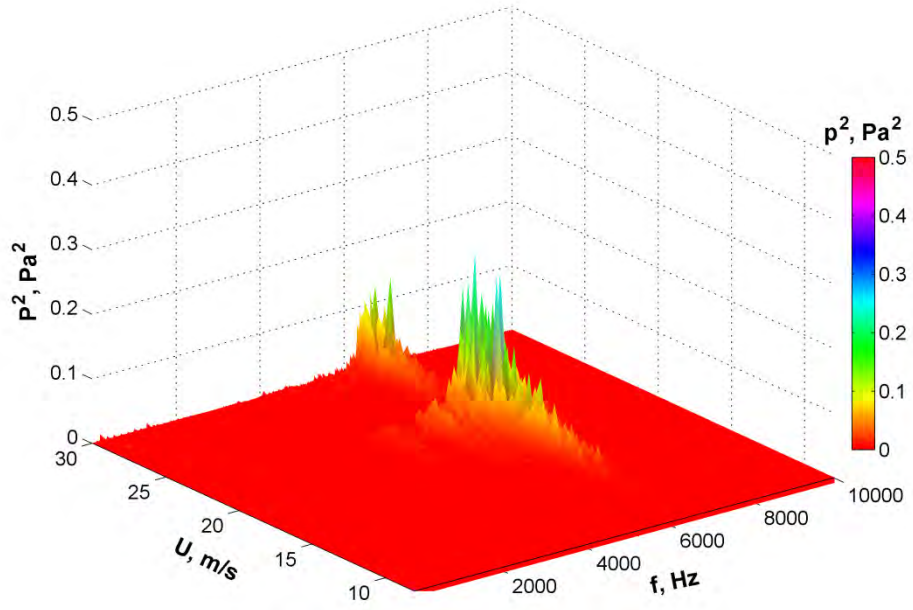

Figure 3.7: Waterfall plot of the pressure amplitude as a function of the frequency f and the inflow velocity U for the case of $\alpha = 11.2^{o}$.

For each geometrical configuration, the maximum value of the pressure amplitudes were listed along with the corresponding values of frequency f, inflow velocity U, the Strouhal number (St = fL/U), Mach number (Ma = U/c), and Reynolds number (Re = $\rho UD_2/\mu$).

3.2.2 Excitation of multiple acoustic modes

The major system dimensions such as the length L and the depth W of the cavity, the diameter of the inflow and outflow pipelines, as well as the range of the inflow velocities constitute the necessary set of parameters that can be used to describe the aero-acoustic response of the cavity-pipeline system. The axisymmetric cavity that was studied in this work had the aspect ratio, $L/W = 6$, which influenced greatly the evolution of cavity shear layers. In particular, such a shallow cavity did not allow the effective development of a large-scale vor-

tex over the cavity length which accounts for the absence of a significant lock-on (Geveci et al., 2003).

Another phenomenon that was observed during data analysis was simultaneous excitation of several acoustic modes. In Figure 3.8, one can see a plot of the frequencies that correspond to the maximum pressure amplitudes as the inflow velocity was varied in the vicinity of U = 20.5 m/s for the case of α = 5º. For example, at U = 20.5 m/s, the maximum pressure peaks, measured by the three pressure transducers P_1, P_2 and P_3 corresponded to the frequencies of 6513 Hz, 6649 Hz and 6972 Hz, respectively. This observation coincides with a similar result reported in (Aly and Ziada, 2011) and indicates a possibility of simultaneous excitation of multiple acoustic diametral modes by different azimuthal portions of the cavity shear layer (corresponding to the different locations of the pressure transducers).

Figure 3.9 shows variation of the peak acoustic pressure amplitude as a function of the inflow velocity. The plot shows relatively small difference in pressure amplitude between the three transducers P_1, P_2 and P_3. In conjunction with the corresponding frequency differences illustrated in Figure 3.8, these results indicate simultaneous excitation of several diametral modes of the cavity. Following the methodology established in (Aly and Ziada, 2011), superposition of the excited diametral modes can be interpreted as a spinning behavior of the second diametral mode (f_2 = 6648 Hz).

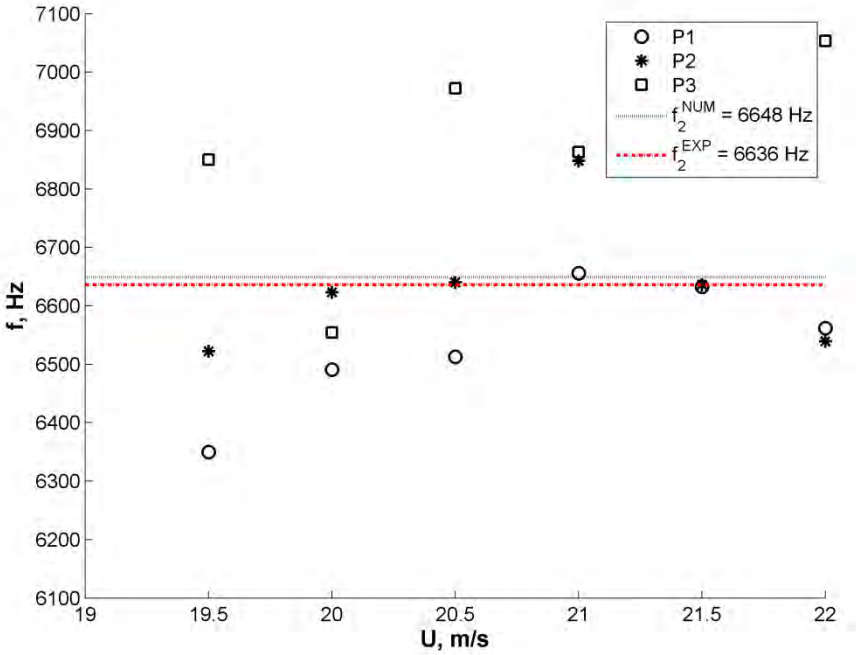

Figure 3.8: Frequency as a function of the inflow velocity and the azimuthal position for the case of α = 5º.

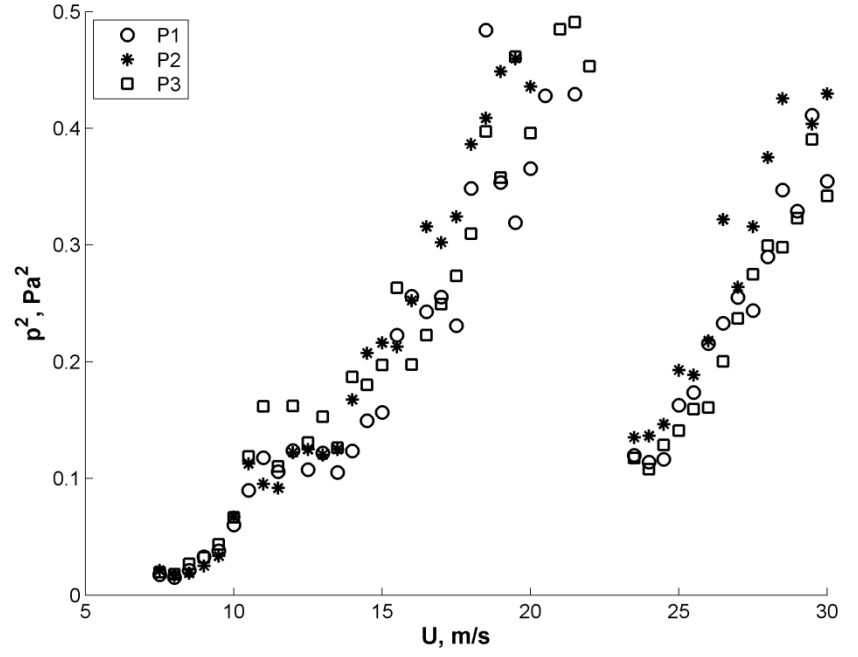

Figure 3.9: Pressure as a function of the inflow velocity and the azimuthal position for the case of α = 5º.

3.2.3 Effect of the convergence-divergence angle

In this section, the effect of the convergence-divergence angle of the pipeline, α, on the acoustic pressure distribution corresponding to the (partially-) trapped modes is discussed based on the results obtained from numerical simulations.

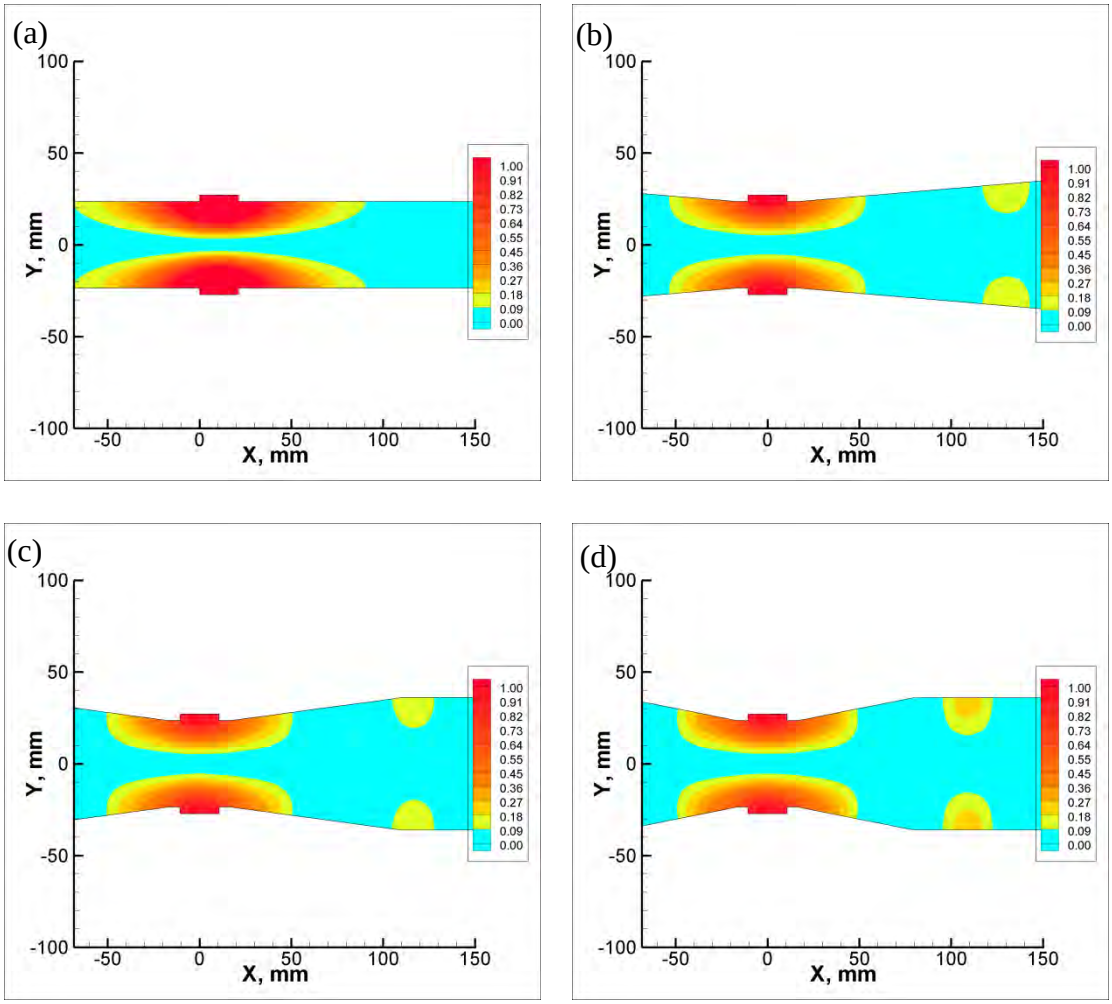

Figure 3.10: Mode shapes (p/p_{max}) of the second acoustic diametral mode in the case of (a) α = 0°, (b) α = 5°, (c) α = 8°, (d) α = 11.2°.

Figure 3.10 illustrates the effect of the geometry of the main pipeline in the vicinity of the cavity on the degree of confinement of the second diametral mode. As the characteristic angle α of the convergence-divergence pipe section was changed from 0° to 11.2°, the levels

of radiation of the acoustic pressure into the main pipeline increased. In other words, the degree of confinement of the second diametral mode diminished, which is described by noting the occurrence of the secondary pressure peaks in the main pipeline for the cases of higher α. This trend is similar for the higher-order diametral modes (not shown).

The degree of mode confinement or, inversely, the level of radiation of a mode was quantified in terms of the numerically calculated magnitude of the secondary peak closest to the cavity, P_0, relative to the experimentally measured magnitude of the primary peak P_{MAX}. The ratio P_0/P_{MAX}, as a function of α, is plotted in Figure 3.11. The decreased confinement of the diametral modes with the increasing convergence-divergence angle is in agreement with the experimental results presented in the previous section. Specifically, increasing α resulted in a decrease of the maximum acoustic pressure amplitude, illustrated in Table 3.2, which is an indication of the increased radiation losses.

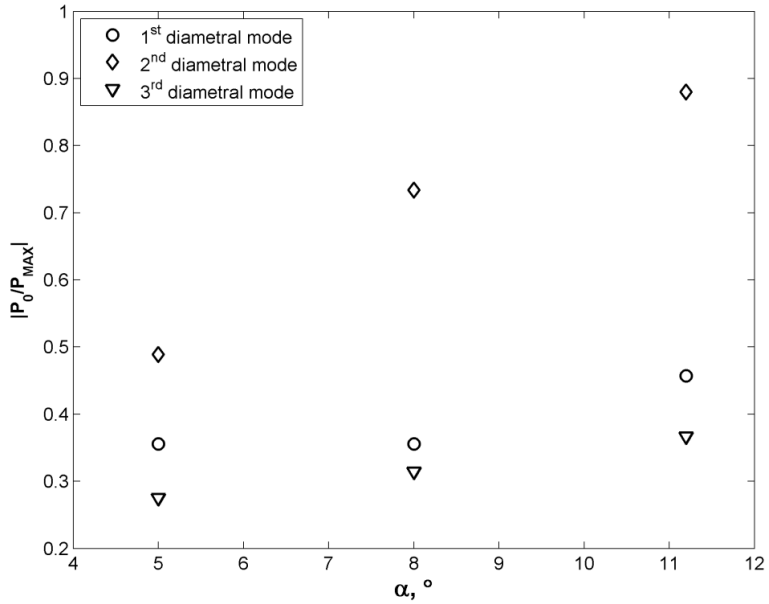

Figure 3.11: Relative magnitude of the secondary pressure peak as a function of the convergence-divergence angle of the main pipeline in the vicinity of the cavity for the first three diametral modes.

The experimentally observed acoustic response of the cavity-pipeline system for the cases of α = 8° and α = 11.2° (not shown) is qualitatively similar to that of the case of α = 5°, which is described in the previous section. The maximum pressure amplitude decreased by 45% at U = 21.5 m/s and by 4% at U =30 m/s as the convergence-divergence angle increased from α = 5° to α = 11.2°. This result indicates that increasing convergence-divergence angle in the vicinity of the cavity promoted radiation of the acoustic energy associated with the partially trapped diametral acoustic modes into the main pipeline, which reduced the strength of the associated flow tone.

3.2.4 Effect of seat width

In the previous section, it was shown that the increase in convergence-divergence angle α led to decreased confinement of the diametral acoustic modes and to the appearance of secondary pressure peaks outside of the cavity. In this section, the effect on another parameter, the seat width S (see Figure 2.3), on the degree of confinement of the first three diametral acoustic modes is presented. For the n^{th} acoustic mode f_n, the lowest value of the seat width S, for which a local maximum (secondary peak) of acoustic pressure did not appear in the main pipeline, i.e. the modes become fully trapped, is referred to as the critical value of the seat width and is denoted as S^*_n. Table 3.3 lists the critical seat width values for the first three diametral acoustic modes (n = 1, 2 and 3) corresponding to three different values of the convergence-divergence angle (α = 5°, 8° and 11.2°). For all three acoustic modes, the critical values of the seat width increased as α increased. Moreover, higher order acoustic modes become trapped at lower critical values of the seat width.

It can be concluded that while increasing the convergence-divergence angle promotes acoustic radiation into the main pipeline, this effect is only observed in the convergence-divergence section is located in the immediate vicinity of the cavity. Increasing the seat width (i.e. the length of the constant-diameter section of the pipe immediately upstream and downstream of the cavity) results in the trapped behavior of the acoustic modes. While this behavior is expected, it is interesting to note that the critical value of the seat width depends on the angle α.

Table 3.3: Numerically obtained critical values of the seat width (mm) corresponding to different convergence/divergence angles α.

Geometry	S_1^*	S_2^*	S_3^*
$\alpha = 5°$	96	80	18
$\alpha = 8°$	116	110	30
$\alpha = 11.2°$	126	114	35

CHAPTER 4

EFFECT OF THE EDGE GEOMETRY ON FLOW-ACOUSTIC COUPLING IN A DEEP AXISYMMETRIC CAVITY

4.1 ACOUSTIC MODE SHAPES

The frequencies of the diametral acoustic modes and the associated mode shapes were calculated numerically by solving the eigenvalue problem corresponding to the Helmholtz Equation (3.3) in the three-dimensional domain representing the internal geometry of the pipeline-cavity system. The details of the numerical procedure, including the domain discretization and the mesh independence study were presented in Section 3.1.2 for the case of a shallow cavity.

Figure 4.1 shows the numerically calculated pressure distributions corresponding to the diametral modes of the cavity, encountered during experiments. The corresponding calculated pressure oscillation frequencies were equal to f_1 = 992 Hz, f_2 = 1,642 Hz, f_4 = 2,891 Hz, f_7 = 4,618 Hz, f_{10} = 6,328 Hz and f_{15} = 9,152 Hz. The numerical procedure outlined in Section 3.1.2 yields the mode shapes and the associated frequencies for the case of the stagnant fluid (no-flow condition). In the case of moving air, the experimentally measured frequencies of the first three diametral acoustic modes were equal to f_1 = 989 Hz, f_4 = 2,885 Hz, and f_7 = 4,600 Hz.

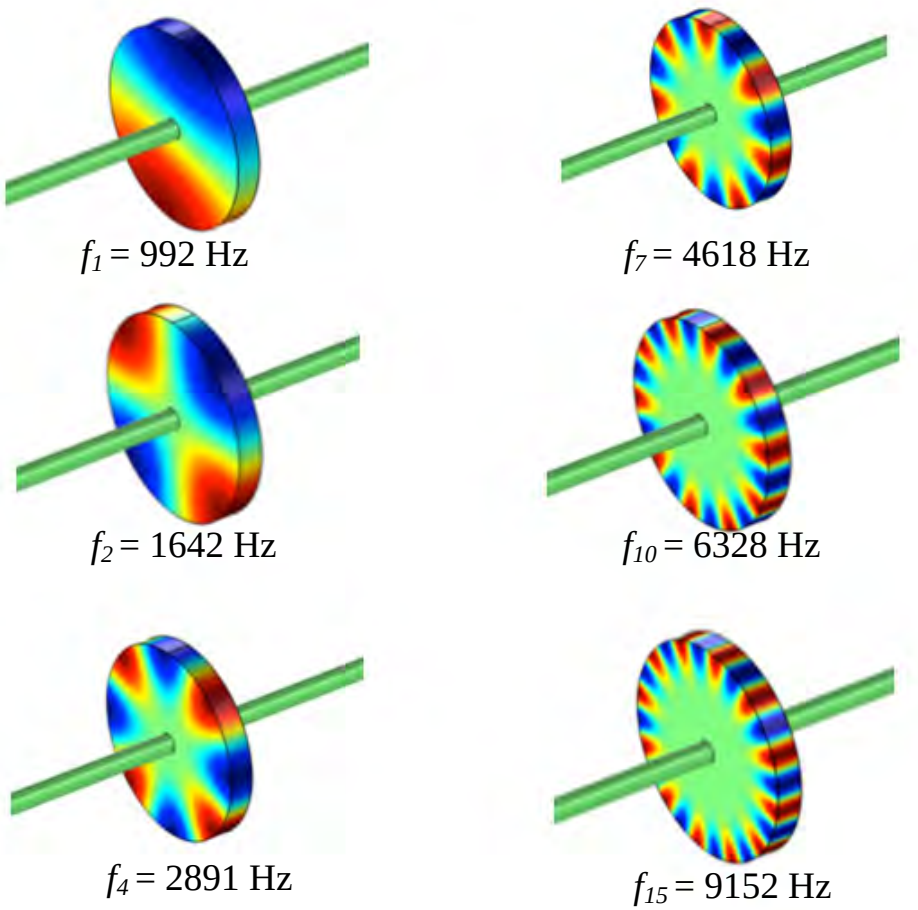

Figure 4.1: Mode shapes of major resonant diametral acoustic modes with their corresponding frequencies.

The experimental measurements revealed spinning behavior of the excited diametral modes, which was reported earlier for the case of shallow cavities (Aly and Ziada, 2011). In (Aly and Ziada, 2012) it was also shown that the mode shapes are affected by the inflow velocity, and the frequency of the acoustic mode decreases with the increase of the mean flow Mach number.

Simultaneous measurements of the acoustic pressure at three different azimuthal locations indicated in Figure 2.4 can be used to determine the orientation of the acoustic modes, and give an insight about the distribution of the acoustic particle velocity, at each phase of the acoustic oscillation cycle (Aly and Ziada, 2011).

4.2 EFFECT OF CHAMFER LENGTH ON THE ACOUSTIC RESPONSE

Unless indicated otherwise, the pressure data presented herein corresponds to the pressure transducer P_1 shown in Figure 2.4 (c). For each considered cavity geometry, pressure spectra were acquired for a range of the inflow velocities 14 m/s $\leq U \leq$ 149 m/s with an increment ΔU = 0.5 m/s, where U is the mean velocity magnitude, measured at the centerline of the pipeline, immediately upstream of the cavity.

4.2.1 Case 1: No chamfers

Figure 4.2(a) shows a plot of 272 individual pressure spectra corresponding to the reference case of the 90° cavity edges (without chamfers) as a function of the inflow velocity in a waterfall format. The plot shows multiple peaks of elevated pressure amplitude, which occurred for a wide range of the inflow velocities. The pressure peaks are clustered around approximately constant frequency values that correspond to the resonant acoustic modes of the cavity-pipeline system. This feature can also be observed in Figure 4.2(b), which shows a contour plot of the pressure amplitude as a function of the pressure oscillation frequency f and the inflow velocity U. In other words, the contour plot of Figure 4.2(b) is a top view of the 3D

surface shown in Figure 4.2(a). It should be noted that the predominant pressure peaks correspond to the first, fourth, seventh, tenth and fifteenth diametral acoustic modes of the cavity, which are shown in Figure 4.1.

Figure 4.2(b) also shows the theoretical approximations to the first three modes of the transverse shear layer oscillations (the Strouhal modes), which are labeled H_1, H_2 and H_3, respectively. The dashed lines represent a simplified semi-empirical model of the Strouhal modes defined in Equation (1.3), while the dash-dotted lines represent a semi-empirical model developed by Rossiter and defined in Equation (1.2).

It can be seen in Figure 4.2(b) that Equation (1.3) generally under-predicted the values of the inflow velocity *U*, at which the lock-on occurred. On the other hand, Equation (1.2), which accounts for the effect of the acoustic field on the convection speed of vortical structures that increases significantly at larger flow velocities, provides similarly good fit at low flow velocity, but improved performance at higher flow speeds. As the acoustic effects on propagation of vortices are neglected in the model given in Equation (1.3), this linear model deviates from the system response at higher flow speeds. In both models, the dominant pressure peaks were observed when the frequencies of the diametral acoustic modes matched those of the shear layer oscillation modes.

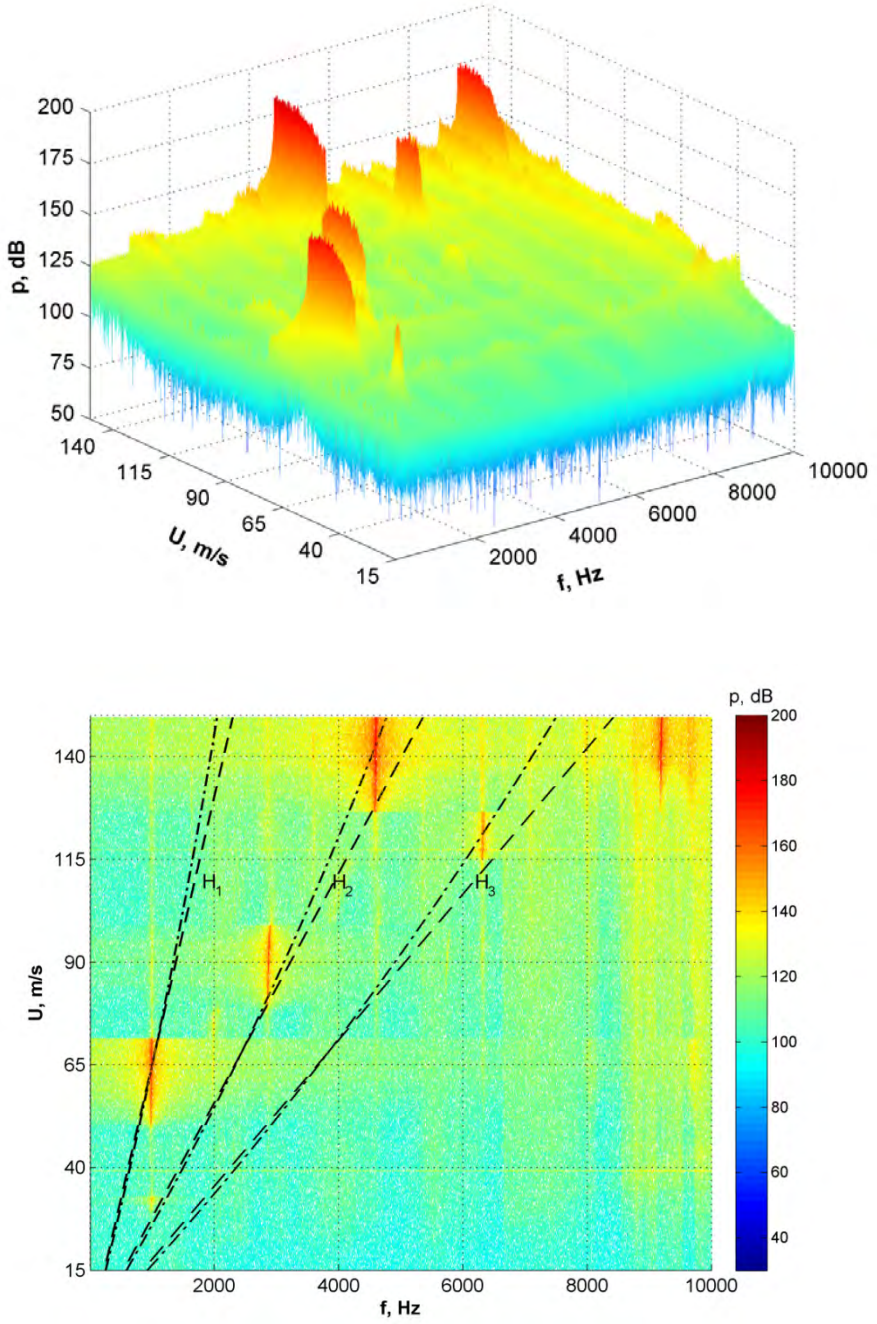

Figure 4.2: Pressure amplitude as a function of the frequency *f* and the inflow velocity *U* for the case of the 90° cavity edges (no chamfers): (a) waterfall plot, (b) contour plot. Shear layer oscillation modes:

$$---\ \frac{f_n L}{U} = 0.52(n - 1/4), -\cdot-\cdot\ \frac{f_n L}{U} = \frac{n - 1/4}{0.58 + M}.$$

As the inflow velocity increased to U = 30 m/s, a discernible peak of the pressure amplitude appeared above the background level. For the range of the inflow velocities 50 m/s $\leq U \leq$ 71 m/s, a locked-on state corresponding to the first diametral mode of the cavity (f_1 = 992 Hz) and the first hydrodynamic mode H_1 was observed.

As the inflow velocity increased, the predominant locked-on state consecutively shifted to the second hydrodynamic mode H_2 coupled with the 4th acoustic mode f_4 = 2891 Hz (for 78.5 m/s $\leq U \leq$ 100 m/s), the third hydrodynamic mode H_3 coupled with the 10th acoustic mode f_{10} = 6328 Hz (for 113.5 m/s $\leq U \leq$ 126.5 m/s) and again to H_2 coupled with f_7 = 4618 Hz and simultaneous excitation of f_{15} = 9152 Hz (for 126 m/s $\leq U \leq$ 149 m/s). Over the complete range of inflow velocities, the overall maximum pressure amplitude of 185.6 dB was attained during the lock-on state that corresponds to the 7th acoustic mode at U = 142.5 m/s. The maximum pressure amplitude of 178.8 dB, corresponding to the first diametral mode of the cavity was attained at U = 66 m/s.

Figure 4.3 shows patterns of the instantaneous velocity and the streamlines corresponding to the first hydrodynamic mode at U = 67 m/s, i.e. the Strouhal number St = fL/U = 0.37. The area of the plots represents the opening of the cavity. The flow in the main pipeline is from left to right, and the cavity extends in the vertical direction. Two shear layers form between the fast flow in the middle of the pipeline and the slowly moving flow inside the cavity. The first hydrodynamic oscillation mode H_1 is characterized by the formation of one large-scale vortical structure per acoustic oscillation period in each of the bottom and the top shear layers. In particular, at the time instant shown in Figure 4.3, a negative (clockwise) vortex was forming immediately downstream of the leading edge of the cavity in the bottom shear layer.

At the same time, a fully-formed, large-scale positive (counter-clockwise) vortex in the top shear layer was approaching the downstream edge of the cavity. This instantaneous position of the vortices indicates that the vortex formation in the top and bottom shear layers occurred with a phase shift of 180°.

In the range of the inflow velocities 78 m/s $\leq U \leq$ 100 m/s, the flow tone shifted to the fourth diametral acoustic mode of the cavity (f_4 = 2,891 Hz), which resonated with the second hydrodynamic mode H_2. The pressure amplitudes in this range of velocities were between 139.2 dB and 170.7 dB, with the maximum value attained at U = 93.5 m/s.

Flow patterns corresponding to the second hydrodynamic mode at U = 91.5 m/s (St = 0.8) are shown in Figure 4.4. In this flow regime, two large-scale vortices were formed in each of the bottom and the top shear layers during a typical acoustic oscillation cycle. In other words, at any instant, two vortices can exist in a shear layer. At the time instant shown in Figure 4.4, two positive vortices can be observed in the top shear layer near the corners of the cavity, while a single vortex was located near the middle of the cavity opening in the bottom shear layer. Thus, similar to the flow regime shown in Figure 4.3, the second hydrodynamic mode also exhibited asymmetric flow oscillation, or out-of-phase formation of vortices in the top and the bottom shear layers.

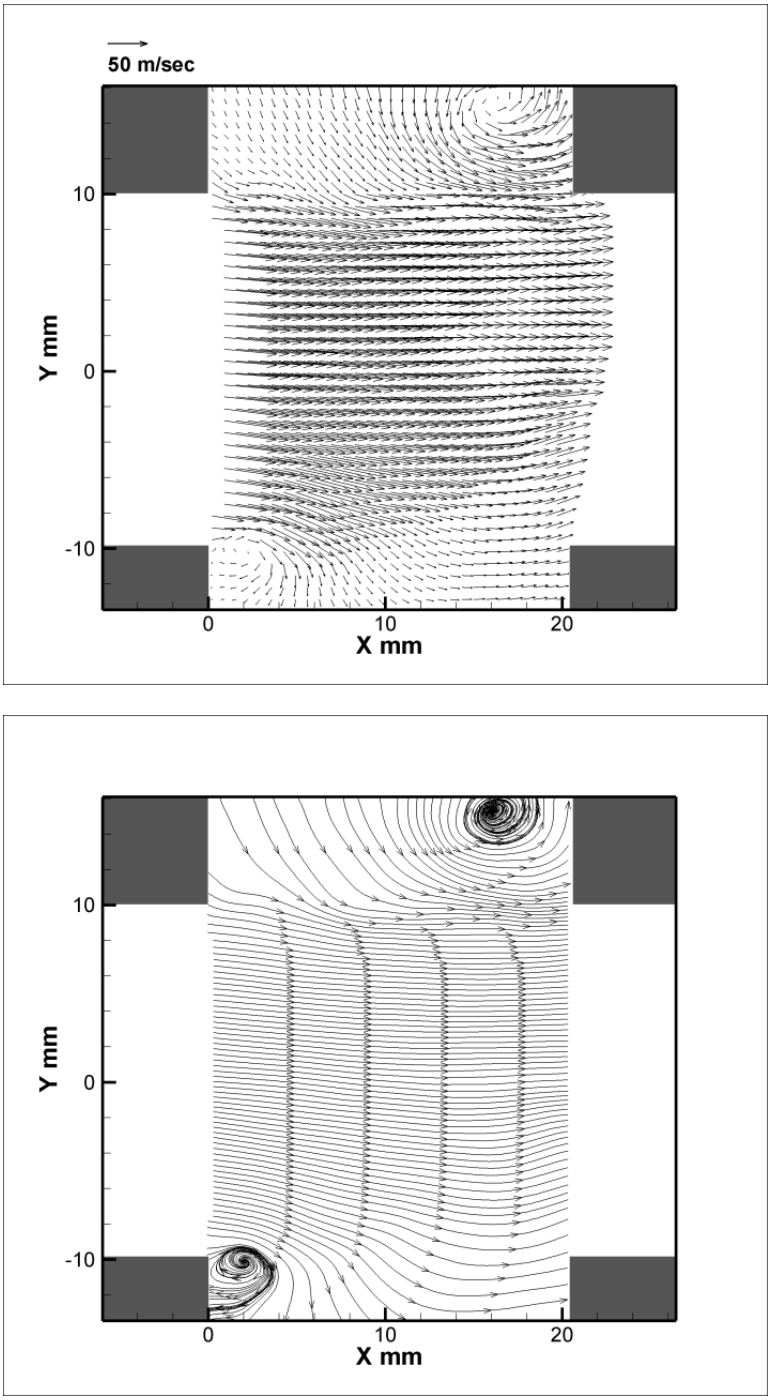

Figure 4.3: Patterns of instantaneous (a) velocity, (b) streamlines corresponding to the first hydrodynamic mode at U = 67 m/s.

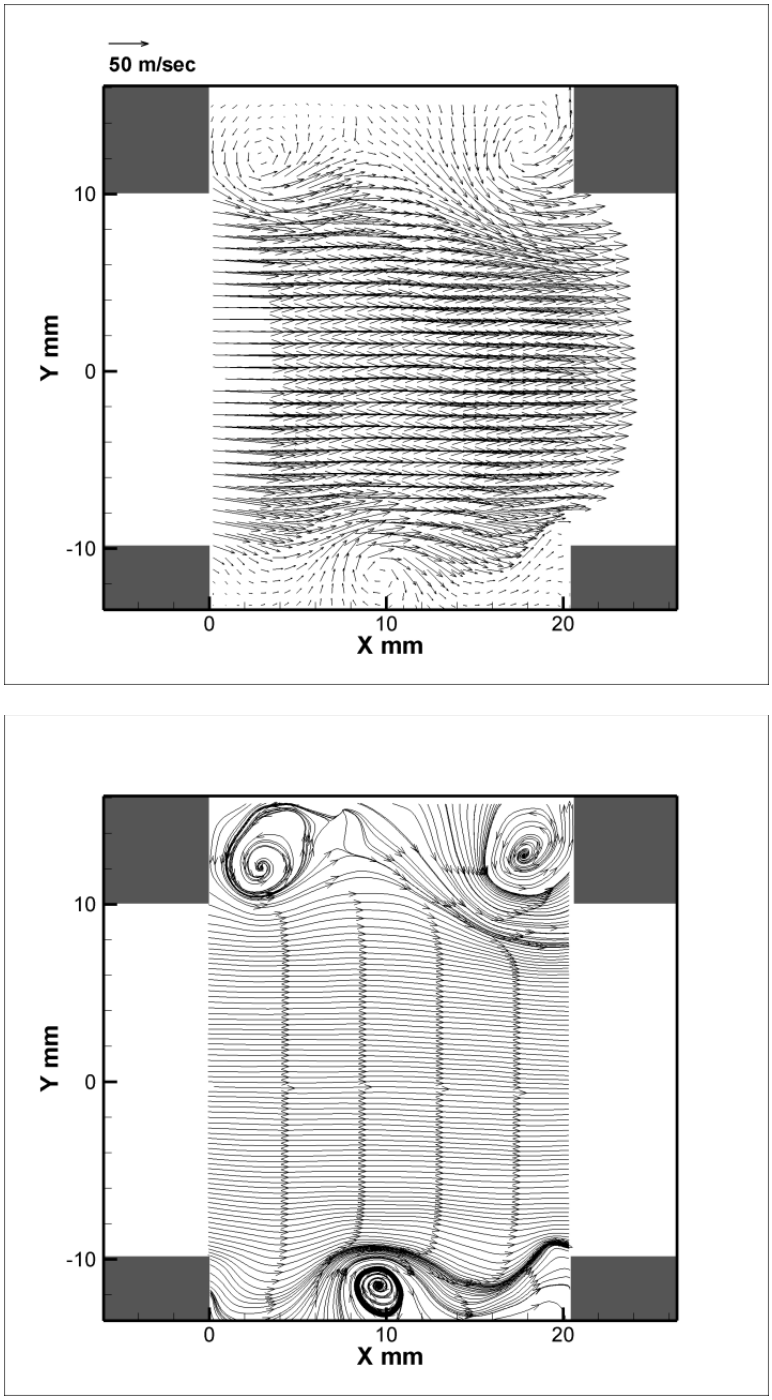

Figure 4.4: Patterns of instantaneous (a) velocity, (b) streamlines corresponding to the second hydrodynamic mode at U = 91.5 m/s.

The tenth diametral acoustic mode (f_{10} = 6,328 Hz) was excited by the third hydrodynamic mode H_3 in a narrow range of the inflow velocities approximately centered at U = 119 m/s. As the inflow velocity continued to increase, the flow tone lock-on got shifted to both a lower frequency (f_7 = 4,618 Hz) and a lower hydrodynamic mode, H_2. The corresponding maximum pressure amplitude of 185.6 dB was observed at U = 142.5 m/s. The plots of Figure 4.2 also indicate simultaneous strong excitation of the seventh (f_7 = 4,618 Hz) and the fifteenth (f_{15} = 9,152 Hz) diametral acoustic modes, which were excited in the range 137 m/s $\leq U \leq$ 149 m/s.

4.2.2 Case 2: Symmetric chamfers

4.2.2.1 Acoustic response in the case of L_C = 1.27 mm

One of the objectives of the present study is to investigate the influence of the hydrodynamic flow characteristics, specifically the flow conditions in the vicinity of the nominal separation and the impingement points of the shear layer, indicated as A and B, respectively, in Figure 2.4. In order to alter shear layer characteristics in these regions, chamfers of the angle α = 15° and of the length L_C ranging from 1.27 mm to 10.16 mm were machined into the upstream and the downstream edges of the cavity.

Variation of the pressure amplitude as a function of the oscillation frequency f and the inflow velocity U in the case of the modified cavity geometry with the chamfer length L_C = 1.27 mm is illustrated in Figure 4.5. The acoustic response of the cavity-pipeline system shares several common features with that of the reference case of the cavity with 90° edges (without chamfer). In particular, the single mode locked-on states corresponding to the first, the fourth and the seventh diametral acoustic modes produced the dominant peaks of pressure

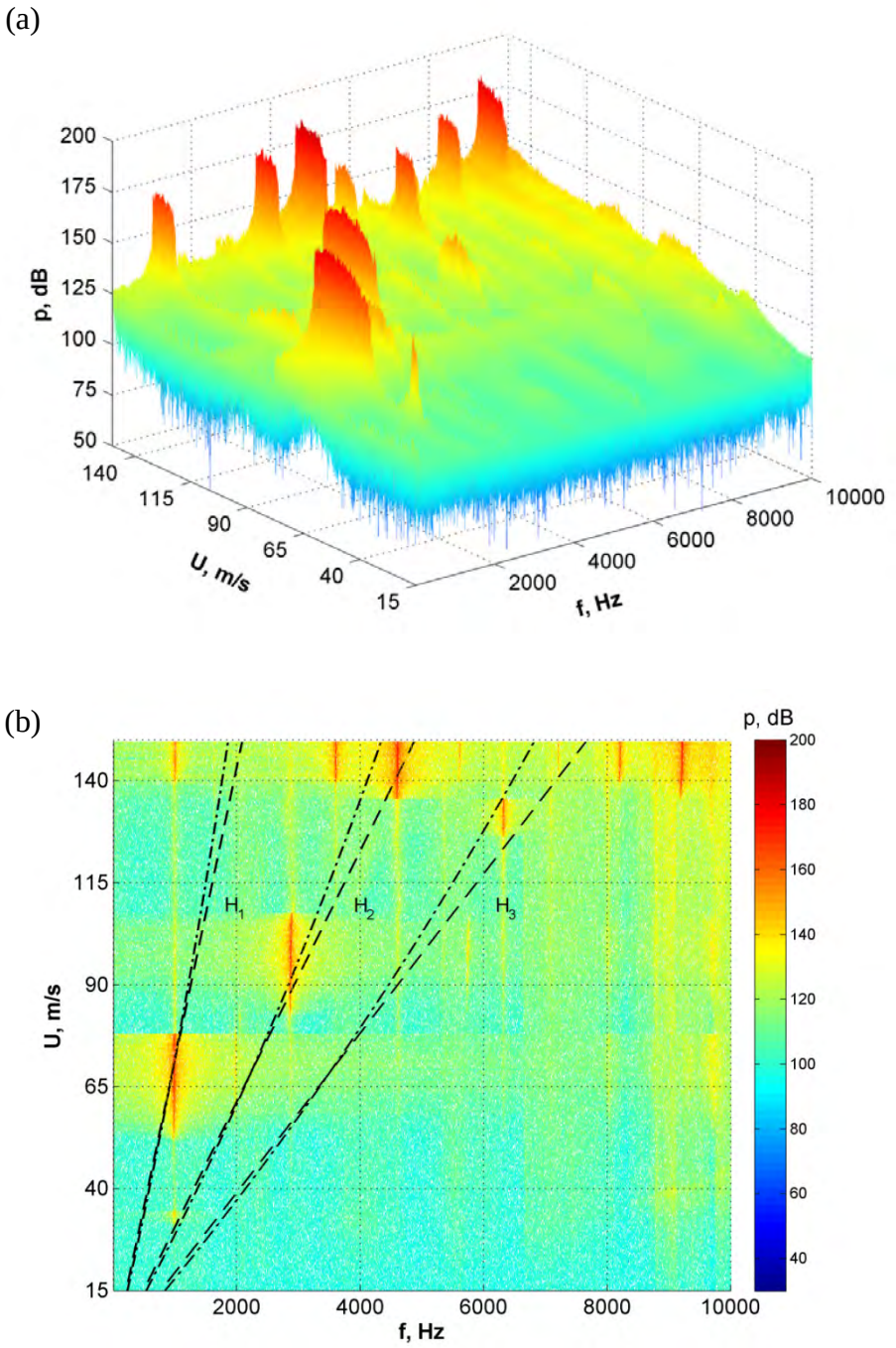

Figure 4.5: Pressure amplitude as a function of the frequency f and the inflow velocity U for the case of the symmetric chamfer with chamfer length L_C = 1.27 mm: (a) waterfall plot, (b) contour plot. Shear layer oscillation modes: $---\ \frac{f_n L}{U} = 0.52(n - 1/4)$, $-\cdot-\cdot\ \frac{f_n L}{U} = \frac{n - 1/4}{0.58 + M}$.

amplitude. Moreover, the ranges of the inflow velocity corresponding to these locked-on states were similar to those in the reference case, which is shown in Figure 4.2.

In contrast to the reference case, however, the modified cavity with L_C = 1.27 mm exhibited simultaneous excitation, at different acoustic pressure levels, of the diametral acoustic modes number 1 through 15 (f_1 = 992 Hz, f_5 = 3,449 Hz, f_7 = 4,618 Hz, f_{12} = 8,189 Hz, f_{15} = 9,152 Hz) in the range of the inflow velocities 140 m/s ≤ U ≤ 149 m/s. Typically, higher order acoustic modes are less prone to generating locked-on states, as the acoustic energy associated with them dissipates relatively quickly, compared to the lower order modes. The observed excitation of higher order modes is likely associated with the relatively deep cavity, which has a greater degree of confinement compared to other shallow cavity systems.

It should be pointed out that in the present case the acoustic energy generated in the system is distributed over multiple acoustic modes. The plot of Figure 4.5(b) also suggests that the acoustic modes are coupled to different hydrodynamic modes of the shear layer oscillation. This condition, although it is associated with relatively high peak pressure levels, is expected to result in an intermittent flow patterns in the vicinity of the cavity opening due to the presence of vortical structures of different scales, which are associated with the different hydrodynamic oscillation modes (Oshkai et al., 2005). Moreover, introduction of the chamfers changes the effective length of the cavity. Thus, the corresponding expression for the cavity length L in Equations (1.2) and (1.3)becomes:

$$L = L + \left(L_C^{Up} + L_C^{Down}\right), \tag{4.1}$$

where L_C^{Up} and L_C^{Down} are the lengths of the chamfers at the upstream and the downstream cavity edges, respectively. Since the shear layer oscillations occur at a constant Strouhal number,

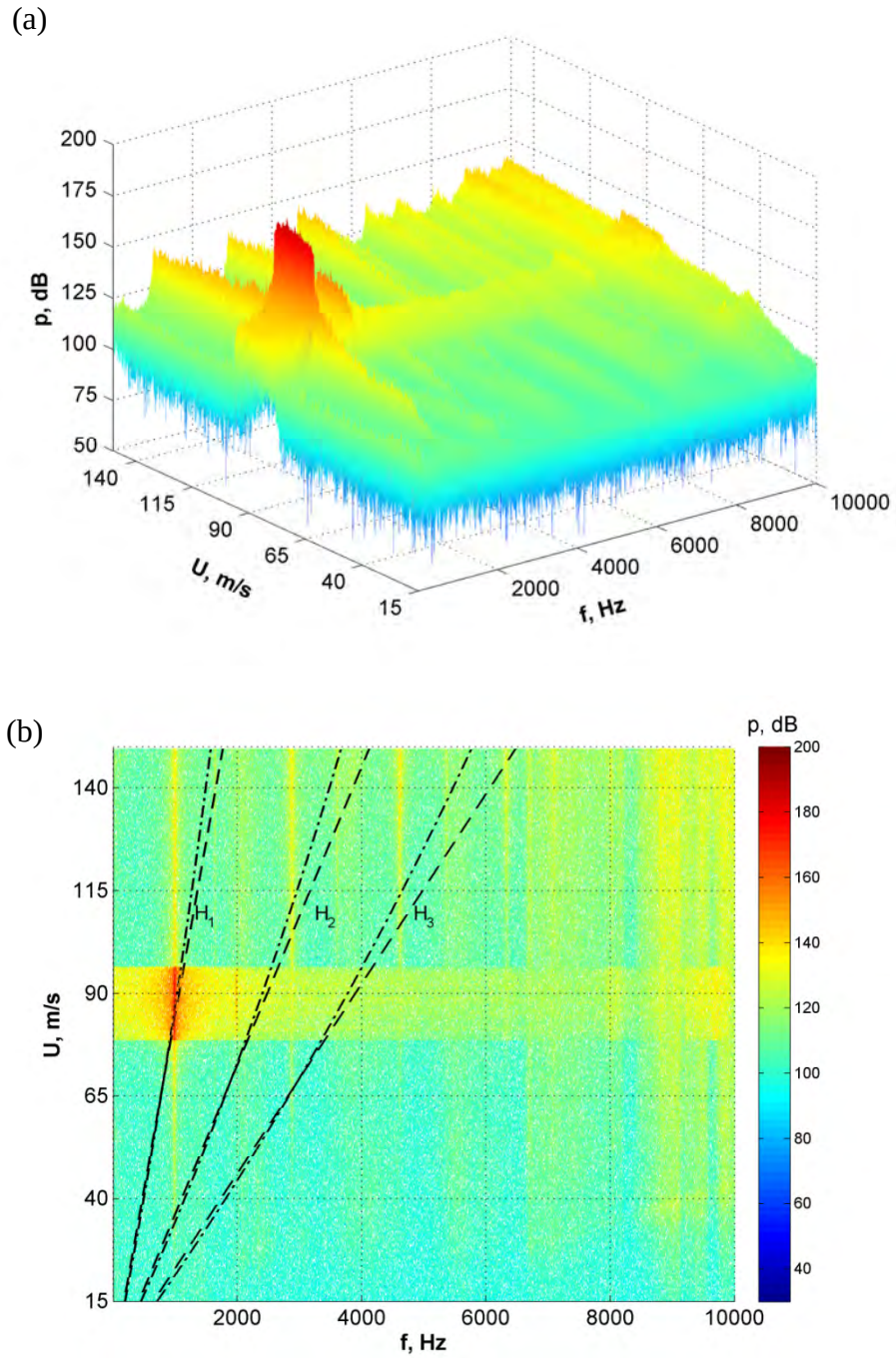

Figure 4.6: Pressure amplitude as a function of the frequency f and the inflow velocity U for the case of the symmetric chamfer with chamfer length L_C = 3.81 mm: (a) waterfall plot. (b) contour plot. Shear layer oscillation modes: $---\ \frac{f_n L}{U} = 0.52(n - 1/4), -\cdot-\cdot\ \frac{f_n L}{U} = \frac{n - 1/4}{0.58 + M}$.

introducing the chamfers to the cavity edges effectively shifts the locked-on flow regime to higher inflow velocities. It should be noted that (Bruggeman et al., 1991) concluded that in the case of a cavity formed by the side branches of a gas transport system, the effective cavity length is reduced to: $L = L + L_C^{Up}$. Only the upper chamfer was relevant in his experiments. This has been confirmed by experiments on Helmholtz resonators by (Dequand et al., 2003). One of the goals of this dissertation was to verify the above findings in the case of the deep, circular, axisymmetric cavity.

4.2.2.2 Acoustic response in the case of L_C = 3.81 mm

Further increase in the length of the 15° chamfers of the cavity edges resulted in a significant change in the acoustic response of the pipeline-cavity system. In the case of the L_C = 3.81 mm, shown in Figure 4.6(a), a single locked-on flow tone corresponding to the first diametral acoustic mode (f_1 = 992 Hz) was generated. Simultaneous excitation of the second acoustic diametral mode (f_2 = 1,642 Hz), although at a much lower amplitude, was also observed. This resonant state was achieved at higher values of the inflow velocity (73.5 m/s ≤ U ≤ 106.5 m/s), compared to the reference case (no chamfers). Figure 4.6(b) shows that the theoretical models of Equations (1.2) and (1.3) provide a rather good prediction for the values of the inflow velocity for the locked-on state. This mainly accounts to the inclusion of the chamfered edges of the cavity, which resulted in the increase of the effective cavity length.

Moreover, the amplitude of the dominant pressure peak in the case of the L_C = 3.81 mm was equal to 191.2 dB at 91.5 m/s, which constitutes a substantial increase compared to p = 178.8 dB generated in the reference case at U = 66 m/s shown in Figure 4.2. This increase in the pressure amplitude of the locked-on acoustic mode is directly related to substantially higher value of the inflow velocity, compared to the reference case with no chamfers.

4.2.2.3 Acoustic response in the case of L_C = 10.16 mm

The acoustic response of the pipeline-cavity system in the case of the longest chamfer of the cavity edges considered in the present study (L_C = 10.16 mm) is presented in Figure 4.7. The plots of acoustic pressure amplitude show broadband excitation of multiple resonant frequencies over a very wide range of the inflow velocities ($U \geq 30$ m/s).

While the locked-on flow states were completely eliminated within the current velocity range, this phenomenon can be attributed to a combination of two factors: (a) increased acoustic radiation into the main pipeline due to the modified geometry of the cavity and (b) increased vorticity thickness (Chapter 6) of the separated shear layer across the cavity, which interfered with formation of coherent vortical structures. It should be also pointed out that small chamfers, by effectively increasing the characteristic cavity length, shift the lock-on flow states to higher inflow velocities, as discussed in Section 4.2.2.1. In practical applications, pipeline systems operate within a certain velocity range. Hence, the ability to shift the locked-on flow states beyond the operating range of the particular system is viewed as a viable passive control strategy.

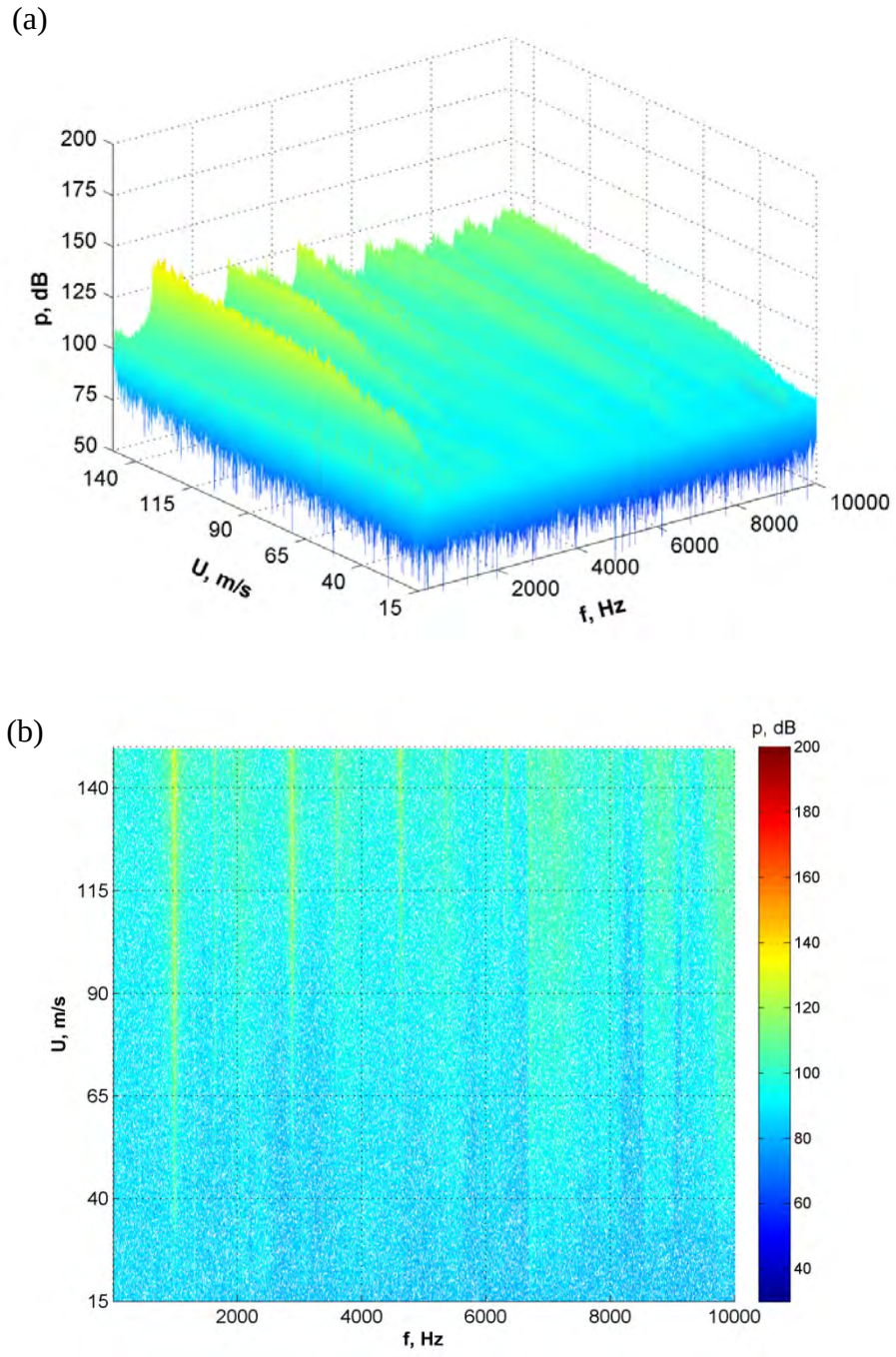

Figure 4.7: Pressure amplitude as a function of the frequency f and the inflow velocity U for the case of the symmetric chamfer with chamfer length L_C = 10.16 mm: (a) waterfall plot. (b) contour plot.

4.3 EFFECT OF DOWNSTREAM CORNER CHAMFER LENGTH VARIATION

In Figure 4.8 through Figure 4.10 one can see the waterfall plot of the pressure spectra as a function of the inflow velocity, along with the contour plot of the pressure amplitude as a function of the pressure oscillation frequency *f* and the inflow velocity *U*. In the results shown in those figures, the introduction of the chamfered edges, with associated chamfer length of L_C = 1.27 mm, 3.81 mm and 10.16 mm, to the downstream corner of the cavity produced little effect on the acoustic response of the system. In fact, the acoustic response shown in Figure 4.8 through Figure 4.10 is approximately the same as that of the cavity with unaltered edges. A possible explanation for this fact is that the separated shear layer remains unaffected at the upstream edge of the cavity.

At the downstream edge, where the transverse velocity of the shear layer is typically larger then that at the upstream edge, the interaction of the shear layer with the cavity edge is directly affected by the size of the chamfers, as it influences the feedback mechanism, one of the main components of which is the interaction of the perturbed velocity field with the impingement edge (Naudascher and Rockwell, 2005).

Since the size of the chamfers introduced at the downstream cavity edge was smaller than the length scale of the impinging vortices, these geometric changes were relatively ineffective and resulted only in a slight decrease in the pressure amplitude. These observations are consistent with the results obtained for two-dimensional open cavity reported in (Franke and Carr, 1975).

(a)

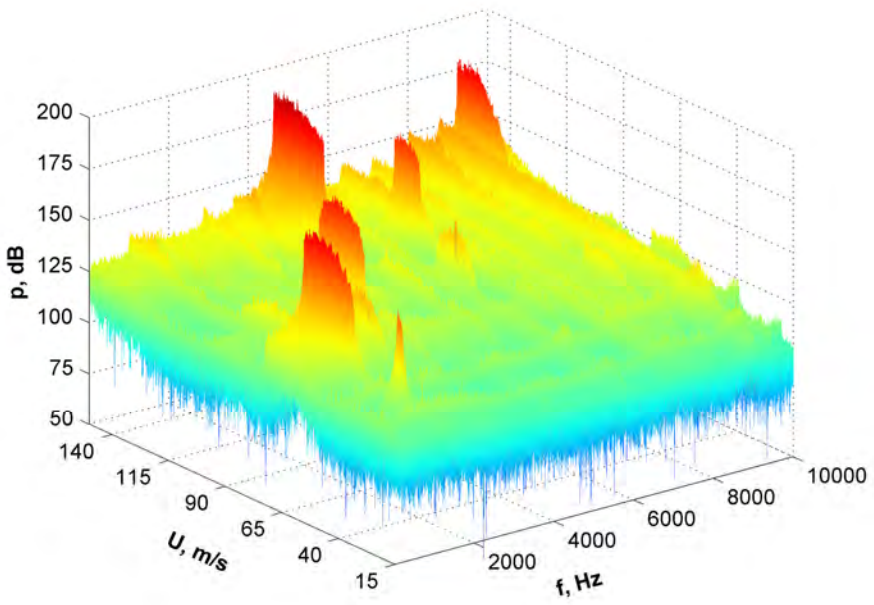

(b)

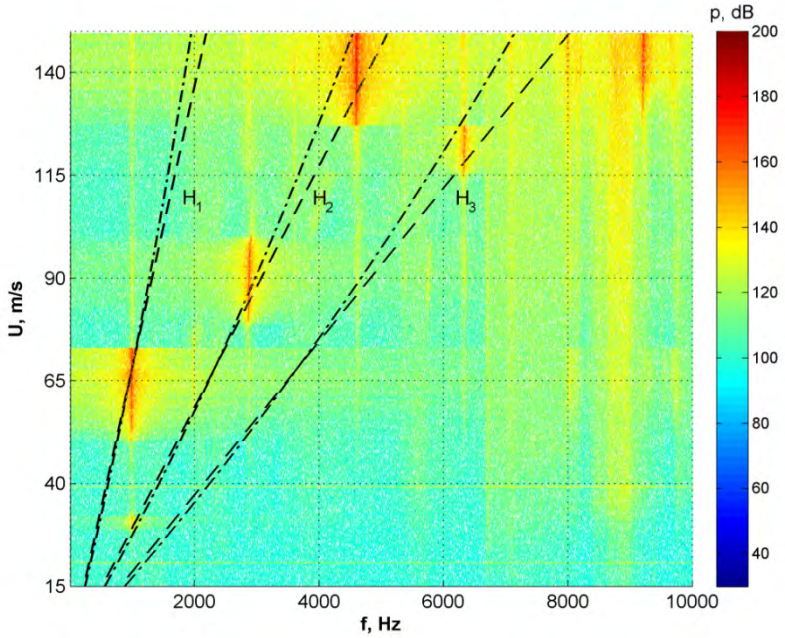

Figure 4.8: Pressure amplitude as a function of the frequency f and the inflow velocity U for the case of the downstream chamfer length L_C = 1.27 mm: (a) waterfall plot, (b) contour plot. Shear layer oscillation modes:

$$---\ \frac{f_n L}{U} = 0.52(n - 1/4), -\cdot-\cdot\ \frac{f_n L}{U} = \frac{n - 1/4}{0.58 + M}.$$

(a)

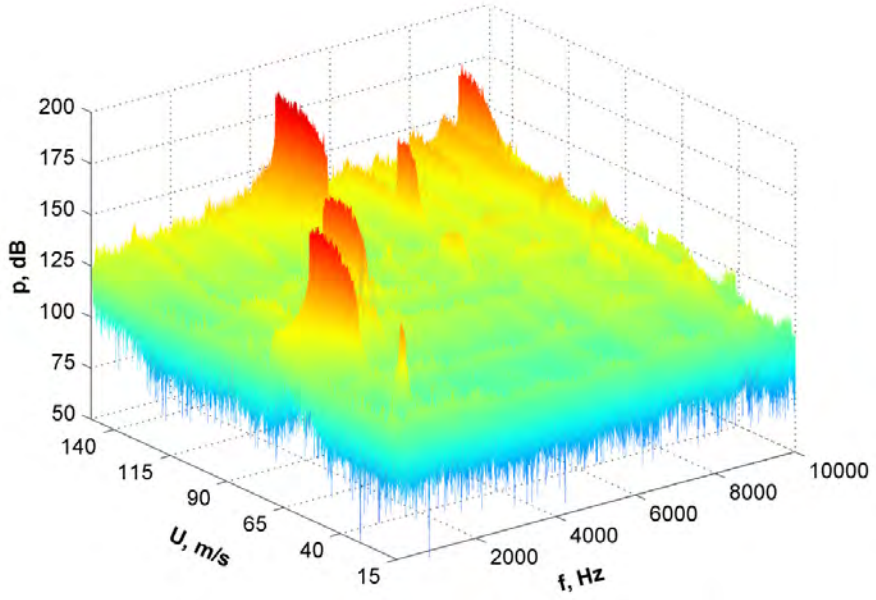

(b)

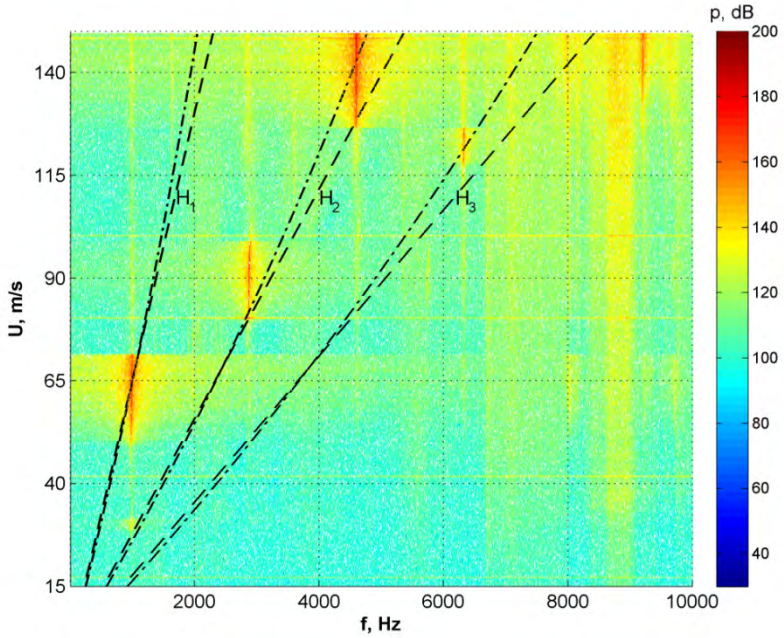

Figure 4.9: Pressure amplitude as a function of the frequency f and the inflow velocity U for the case of the downstream chamfer length L_C = 3.81 mm: (a) waterfall plot, (b) contour plot. Shear layer oscillation modes:

$$---\ \frac{f_n L}{U} = 0.52(n - 1/4), -\cdot-\cdot\ \frac{f_n L}{U} = \frac{n - 1/4}{0.58 + M}.$$

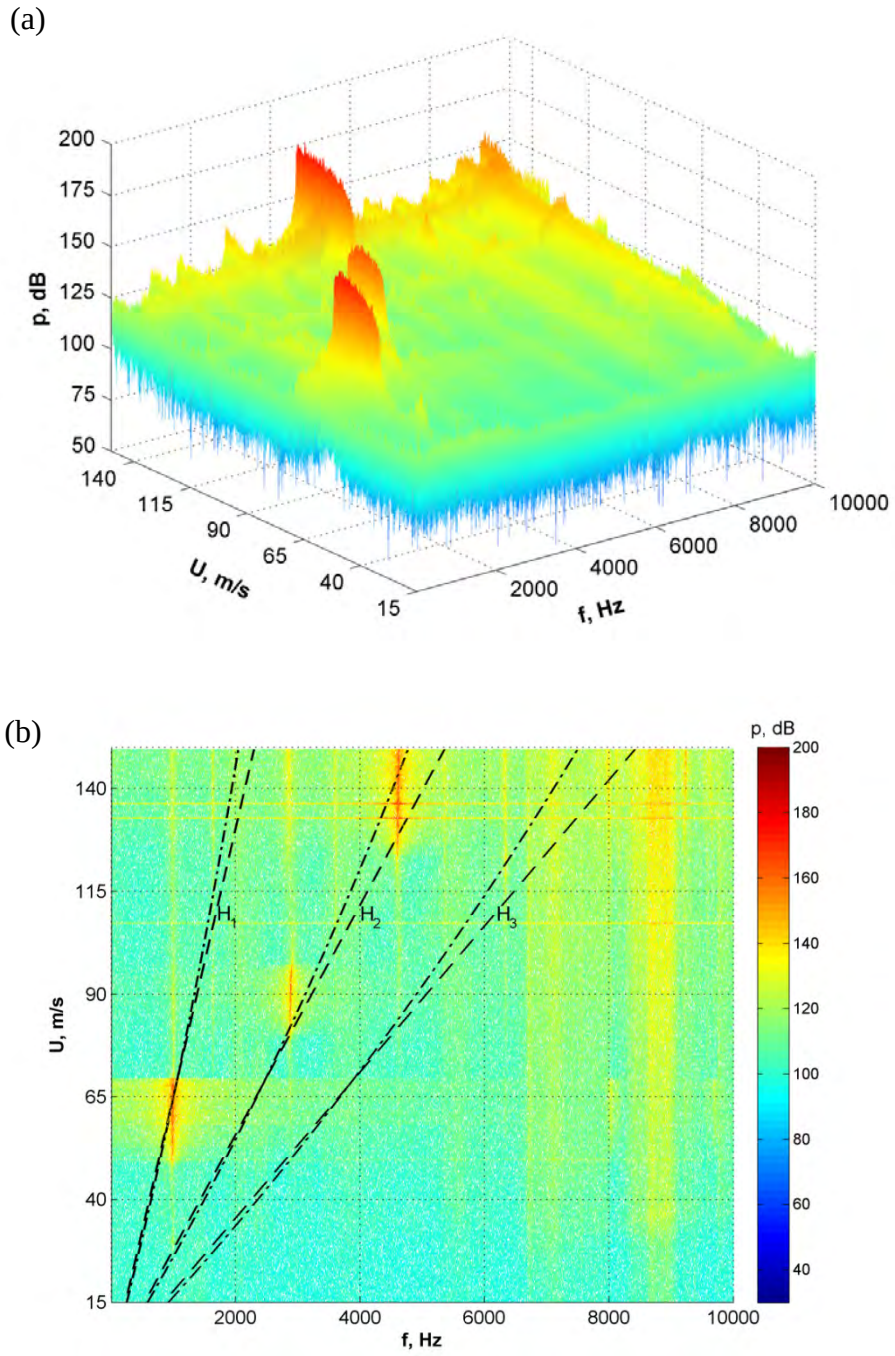

Figure 4.10: Pressure amplitude as a function of the frequency f and the inflow velocity U for the case of the downstream chamfer length L_C = 10.16 mm: (a) waterfall plot, (b) contour plot. Shear layer oscillation modes: $---\ \frac{f_n L}{U} = 0.52(n - 1/4)$, $-\cdot-\cdot\ \frac{f_n L}{U} = \frac{n - 1/4}{0.58 + M}$.

4.4 EFFECT OF CHAMFER LENGTH VARIATION AT THE UPSTREAM CORNER

In this section, three chamfered cavity configurations, with associated chamfer length of L_C = 1.27 mm, 3.81 mm and 10.16 mm at the upstream edge were tested. The effectiveness of the geometric modifications is discussed below.

4.4.1 Acoustic response in the case of L_C = 1.27 mm

The acoustic response of the system with the shortest upstream chamfer is shown in Figure 4.11. The locked-on states presented herein were similar to those in the cavity with symmetric upstream and downstream chamfers, with associated chamfer length of L_C = 1.27 mm. As in the cavity geometry with the chamfer length L_C = 1.27 mm, illustrated in Figure 4.5, the large amplitude pressure oscillations corresponded to the first, the fourth and the seventh diametral acoustic modes. In addition, the acoustic response of the system indicated excitation of higher order diametral acoustic modes (f_5 = 3,449 Hz, f_{10} = 6,328 Hz, f_{12} = 8,189 Hz, f_{15} = 9,152 Hz) of smaller amplitudes in the range of the inflow velocities 137 m/s ≤ U ≤ 149 m/s. These higher order diametral acoustic modes were not as pronounced as in the symmetric chamfer case. In Figure 4.11 one can also see that the introduction of the upstream chamfer to the cavity edge resulted in the slight shift of the lock-on intervals to the higher ranges of the inflow velocity. This shift is due to the increase in of effective cavity length, which was discussed in Section 4.2.1.

4.4.2 Acoustic response in the case of L_C = 3.81 mm

The results illustrated in Figure 4.12 indicate that by increasing the length of the chamfer at the upstream edge of the cavity one can noticeably change the acoustic response of the system. In general, the results follow the trend for the case of the symmetrical chamfers with L_C = 3.81 mm, shown in Figure 4.6, where a single locked-on flow tone corresponding to the first diametral acoustic mode (f_1 = 992 Hz) was observed in the range of the inflow velocity of 73 m/s $\leq U \leq$ 101 m/s. In addition to the first acoustic diametral mode, the simultaneous excitation of the second acoustic diametral mode (f_2 = 1,642 Hz), although at a much lower amplitude, was observed. The amplitude of the dominant pressure peak in the case of the L_C = 3.81 mm was equal to 191.9 dB, which is comparable to p = 191.2 dB generated in the symmetric case shown in Figure 4.6.

(a)

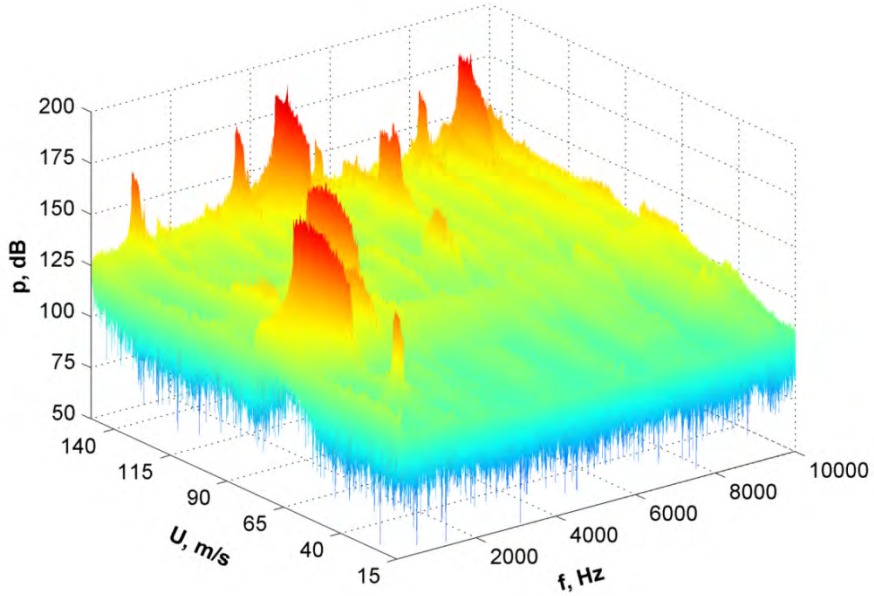

(b)

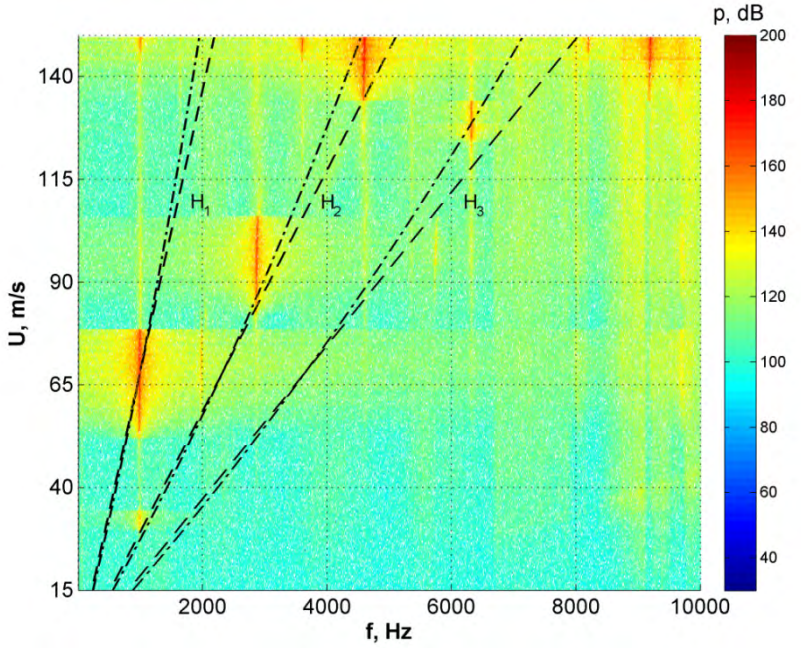

Figure 4.11: Pressure amplitude as a function of the frequency f and the inflow velocity U for the case of the upstream chamfer length L_C = 1.27 mm: (a) waterfall plot, (b) contour plot. Shear layer oscillation modes:

$$---\ \frac{f_n L}{U} = 0.52(n - 1/4), -\cdot-\cdot\ \frac{f_n L}{U} = \frac{n - 1/4}{0.58 + M}.$$

(a)

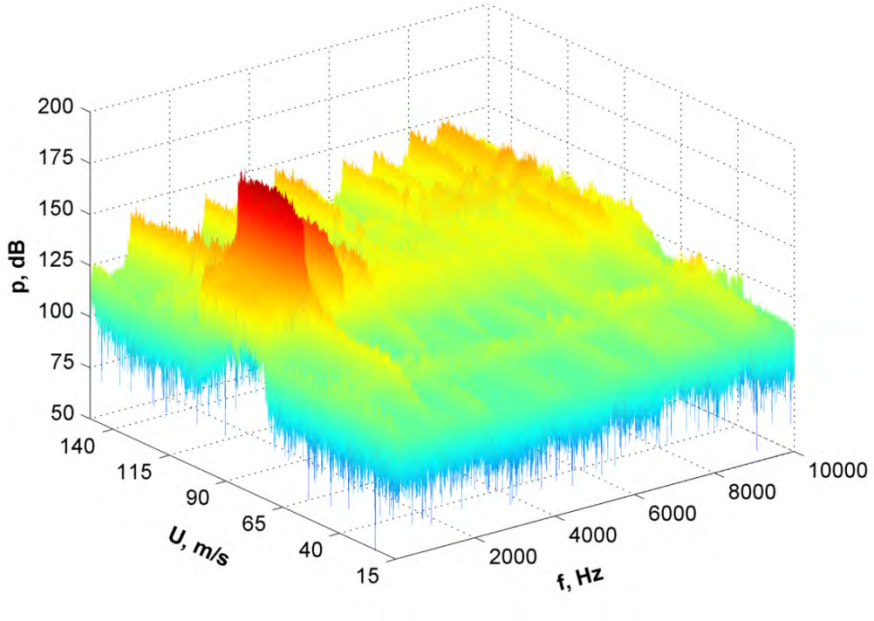

(b)

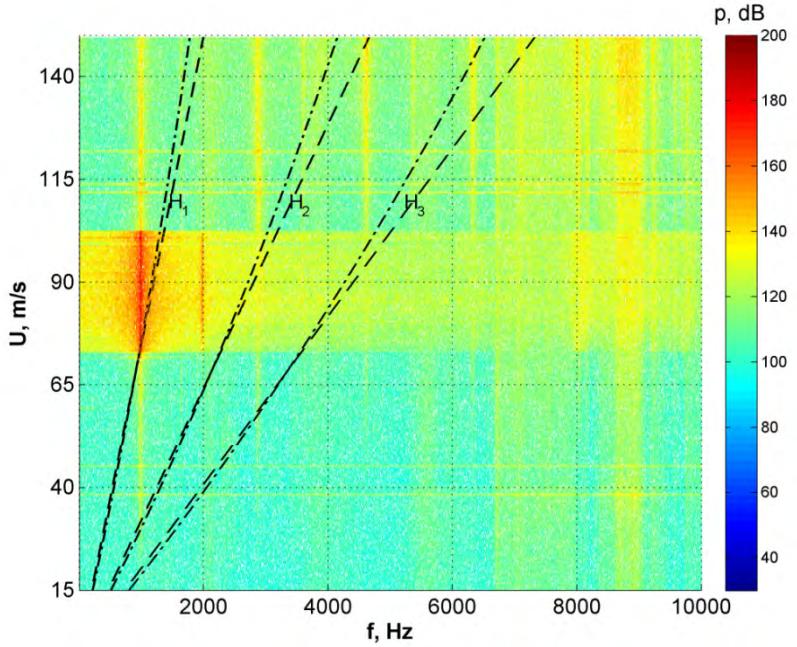

Figure 4.12: Pressure amplitude as a function of the frequency f and the inflow velocity U for the case of the upstream chamfer length L_C = 3.81 mm: (a) waterfall plot, (b) contour plot. Shear layer oscillation modes:

$$---\ \frac{f_n L}{U} = 0.52(n - 1/4), -\cdot-\cdot\ \frac{f_n L}{U} = \frac{n - 1/4}{0.58 + M}.$$

(a)

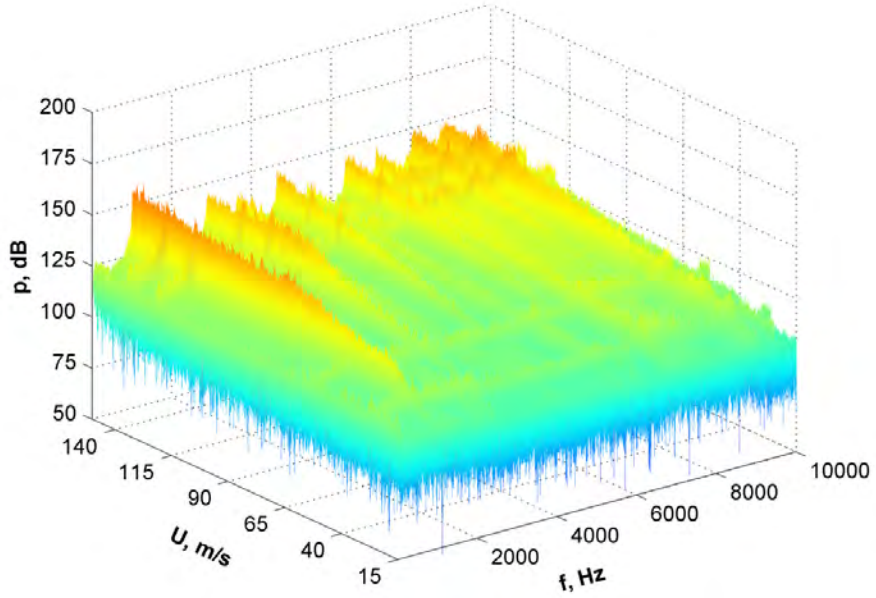

(b)

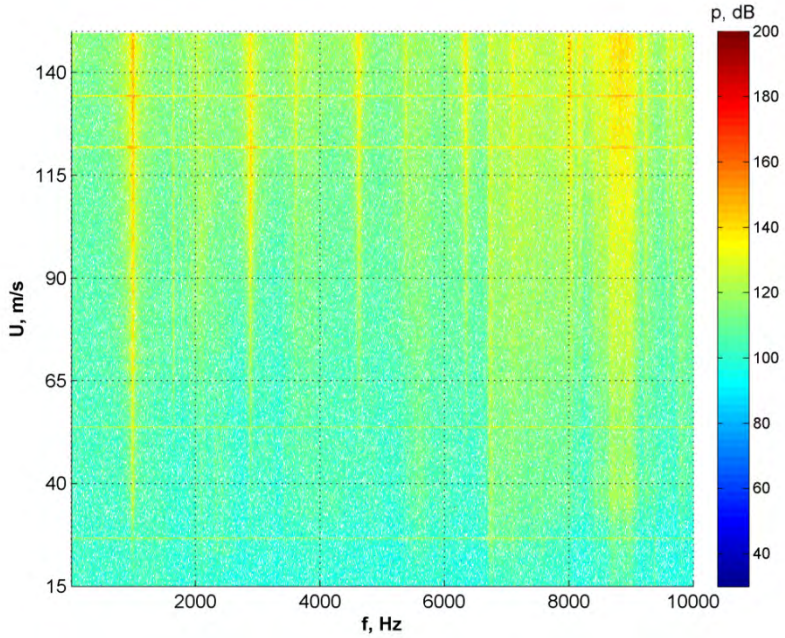

Figure 4.13: Pressure amplitude as a function of the frequency *f* and the inflow velocity *U* for the case of the upstream chamfer length L_C = 10.16 mm: (a) waterfall plot, (b) contour plot.

4.4.3 Acoustic response in the case of L_C = 10.16 mm

In Figure 4.13, one can see the acoustic response of the system in the case of the longest chamfer of the cavity edges (L_C = 10.16 mm). As in the corresponding case of the longest symmetrical chamfers, the plots of acoustic pressure amplitude show broadband excitation of multiple resonant frequencies over a very wide range of the inflow velocities ($U \geq$ 30 m/s). While the locked-on flow states were completely eliminated, the overall level of broadband pressure spectrum was higher than that of the corresponding case of symmetrical chamfers, illustrated in Figure 4.7. This particular result indicates that the presence of the downstream and the upstream chamfered edges is more effective in suppression of the in-cavity pressure oscillations. The presence of the additional chamfer at the downstream edge in the symmetrical case resulted in additional decrease of the pressure amplitude, by influencing the interaction mechanism of the impinging shear layer with the downstream edge of the cavity.

CHAPTER 5

SPINNING BEHAVIOUR OF DIAMETRAL ACOUSTIC MODES IN DEEP AXISYMMETRIC CAVITIES WITH CHAMFERED EDGES

5.1 AZIMUTHAL CHARACTERISTICS OF THE ACOUSTIC DIAMETRAL MODES

A typical mode shape for the first diametral mode has the form shown in Figure 5.1 (a) where black circles indicate the physical position of the pressure transducers. Each pressure transducer is separated from one another by a 45º angle, and it was assumed that maximum pressure was attained at P_1. The amplitude variation of the pressure along the circumference of the cavity follows the sine curve, which is schematically shown in Figure 5.1 (b). The acoustic diametral modes, following classification established in (Aly and Ziada, 2011), can be either: (i) spinning, (ii) stationary, or (iii) partially spinning. The particular type of the acoustic diametral mode can be determined by analyzing the data obtained from the pressure transducers.

The main characteristics of the spinning acoustic mode, when one is looking at the data simultaneously acquired from pressure transducers P_1, P_2, and P_3 is the presence of constant phase shift, as shown in Figure 5.2.

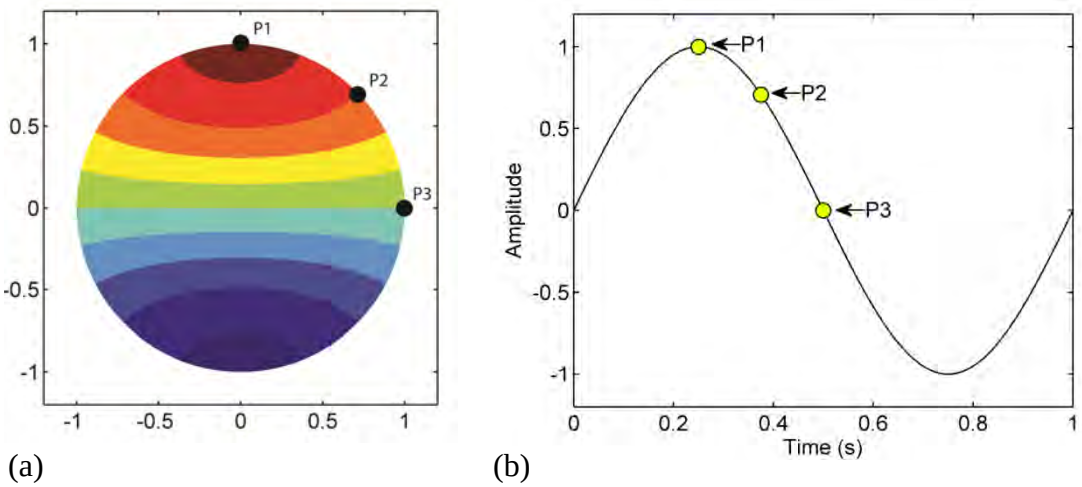

(a) (b)

Figure 5.1: (a) First spinning diametral mode, (b) Pressure variation of the spinning diametral acoustic mode recorded simultaneously from transducers P_1, P_2, and P_3

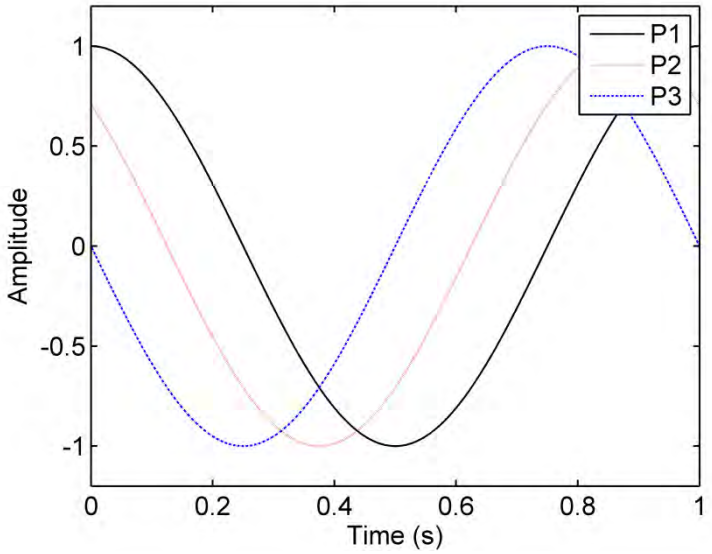

Figure 5.2: Pressure variation of spinning diametral acoustic modes recorded at the same time from transducers P_1, P_2, and P_3

Under ideal conditions, the phase shift between pressure data, illustrated in Figure 5.2, corresponds to the physical angle Θ that separates each pressure transducer from one another in the case of the first acoustic diametral mode, and to the product $n\Theta$, where n is the mode number, in the case of the higher order acoustic diametral modes. In addition to that, each

pressure transducer will record pressure variation with exactly the same amplitude over a period of oscillation of the particular diametral acoustic mode.

Contrary to spinning diametral acoustic modes, the stationary diametral acoustic modes do not preserve the amplitude of the pressure variation. The data acquired from pressure transducers show either 0º or 180º phase shift. This phase shift can be explained from Figure 5.3. In particular, each point in the acoustic pressure field is oscillating at the frequency of the first acoustic diametral mode. Since the mode is stationary, and assuming the pressure distribution shown in Figure 5.3 (a), each pressure transducer P_1 and P_2 will acquire a sinusoidal pressure variation where the maximum (minimum) amplitude is determined by the physical location of the pressure transducer. As it can be seen from Figure 5.3, the pressure data acquired by pressure transducers P_1 and P_2 have the same phase and different amplitude. In fact, the pressure amplitude is proportional to the physical location of the pressure transducer. On the other hand, the pressure data recorded by pressure transducer P_3 are 180º out of phase from the pressure data recorded by pressure transducers P_1 and P_2.

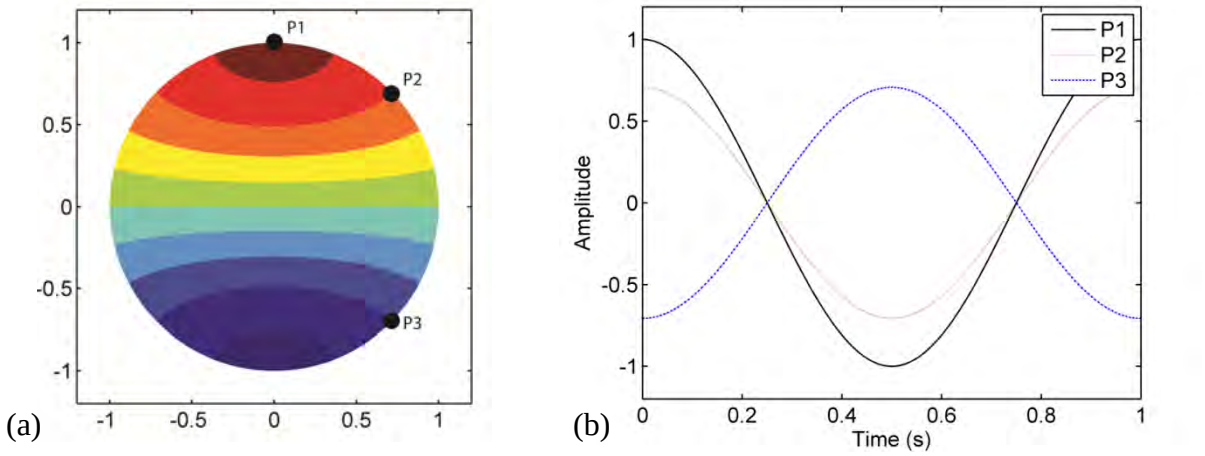

Figure 5.3: (a) First stationary diametral mode, (b) Pressure variation of the stationary diametral acoustic mode recorded simultaneously from transducers P_1, P_2, and P_3

5.2 MATHEMATICAL INTERPRETATION OF THE SPINNING NATURE OF THE ACOUSTIC DIAMETRAL MODES

The propagation of the sound wave through the fluid medium is accompanied by cyclic displacement of the fluid particles from their equilibrium position and simultaneous increase and decrease of the pressure. The general distribution of the sound pressure in a cylindrical cavity associated with the excitation frequency ω is represented by the following expression (Aly and Ziada, 2011):

$$p_{mn}(x,r,\theta,t) = p_{mn} J_m(k_{mn} r)\, \mathrm{e}^{i(\omega t \pm m\theta) - d_\omega x} \tag{5.1}$$

here, $J_m(k_{mn} r)$ is the Bessel function of the first kind, *m* and *n* are diametral and radial mode numbers, *t* is time, $\omega = 2\pi f$ is the angular frequency, θ is a phase angle, and d_ω is a decay factor, which is a function of the ratio between the trapped mode frequency and the corresponding main duct cut-off frequency. The general azimuthal behavior of the trapped acoustic diametral modes can be represented by a superposition of two orthogonal stationary modes, phase-shifted by 90° in time (Aly and Ziada, 2011, Hein and Koch, 2008). Following this concept, the general expression for the azimuthal behavior of acoustic diametral mode in terms of two stationary modes is given by (Aly and Ziada, 2011):

$$p_{mn}(x,r,\theta,t) = (A\cos(m\theta) + iB\sin(m\theta)) J_m(k_{mn} r)\, \mathrm{e}^{i\omega t - d_\omega x} \tag{5.2}$$

here, *A* and *B* are the amplitudes of two stationary modes. The outcome of the Equation (5.2) is a stationary mode whenever *A* or *B* is zero, a spinning mode when *A* = *B*, and a partially spinning mode when $A \neq B$.

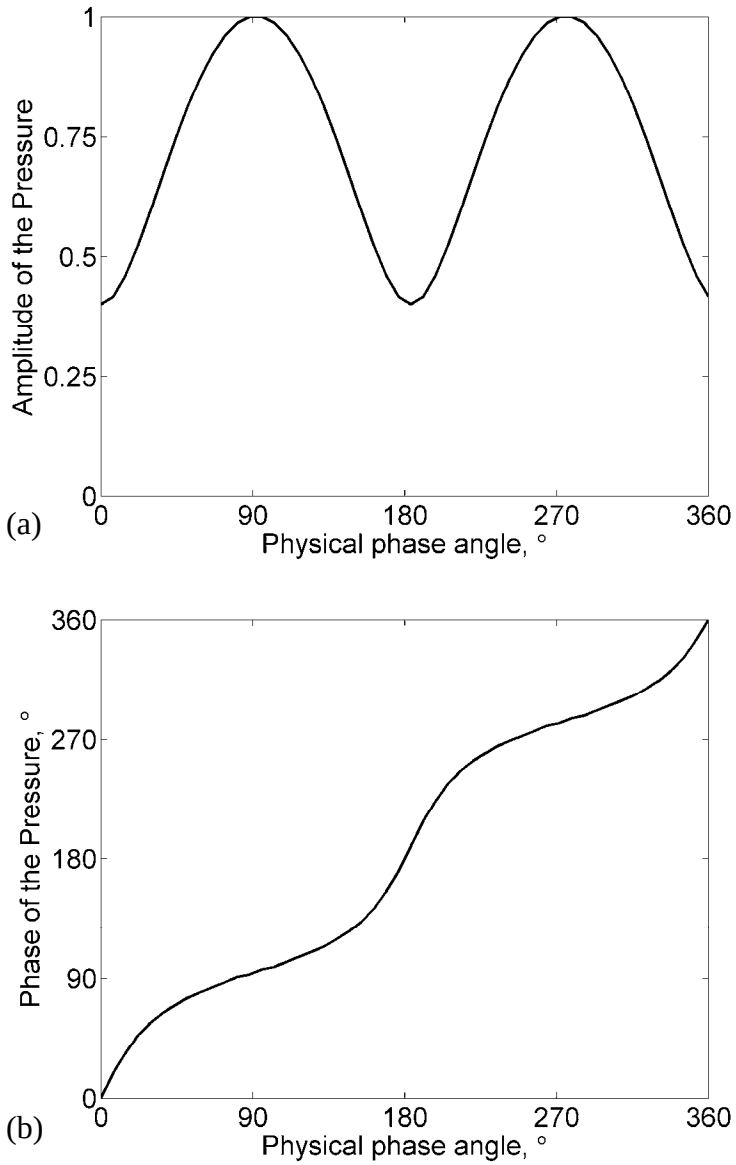

Figure 5.4: (a) Amplitude of the circumferential pressure for a partially spinning mode with $A/B < 1$, (b) Phase of the circumferential pressure for a partially spinning mode with $A/B < 1$.

Using Equation (5.2) and following previously established methodology (Aly and Ziada, 2011), one can illustrate the features of the partially spinning acoustic diametral modes that stand somewhat between those of the spinning and stationary acoustic diametral modes. Specifically, as it can be seen from Figure 5.4 (a), the normalized amplitude of the pressure

varied from 0.4 to 1, following a non-sinusoidal distribution. However, as the azimuthal behavior of the acoustic diametral mode approaches the one of a stationary mode, the graph in Figure 5.4 (a), in return, approaches a sinusoidal distribution. On the other hand, as the azimuthal behavior of the acoustic diametral mode approaches the one of a spinning mode, the graph in Figure 5.4 (a) approaches a constant value.

In addition to the azimuthal distribution of the pressure amplitude, the variation of the pressure phase over the outer perimeter of the cavity for a partially spinning acoustic diametral mode is very specific. It is illustrated in Figure 5.4 (b). One can see that the rate of change of the pressure phase varied with the location of the minimum pressure amplitude. In particular, the rate of change in pressure phase is increased around to point where the pressure amplitude attained its minimum, as was shown in (Aly and Ziada, 2011). This behavior illustrate that while the physical angle between pressure transducer is fixed, one can expect to observe different values of the relative phase difference between pairs of pressure transducers at different locations over the outer perimeter of the cavity. This phenomenon was observed in the current study.

5.3 INTERPRETATION OF THE EXPERIMENTAL DATA

In this Section, the methodology developed in (Aly and Ziada, 2011) was applied to experimental data, represented by pressure signals simultaneously measured by the pressure transducers P_1, P_2 and P_3. The concept of two orthogonal modes was used to interpret the azimuthal characteristics of acoustic diametral modes. The cavity modes were defined as: 1) *primary acoustic mode,* which amplitude corresponds to the maximum amplitude attained during the time cycle of pressure oscillation, and which azimuthal orientation corresponds to

the orientation at which the maximum amplitude was observed, and 2) *secondary acoustic mode,* orthogonal to the primary acoustic mode. The pressure signals were filtered by a narrow-band filter with a bandwidth of 50 Hz in order to isolate the frequency of the locked-on acoustic diametral mode from a wider bandwidth signal that typically contains low-frequency oscillations along with other acoustic diametral modes of the cavity. Assuming sinusoidal distribution of the pressure over the cavity wall and taking the pressure data collected from pressure transducers P_1, P_2 and P_3 the time dependent pressure amplitude $A(t)$ can be obtained from (Aly and Ziada, 2011):

$$p_k(\theta,t) = A(t)\cdot\cos(\theta-\varphi(t)), \tag{5.3}$$

here, $p_k(\theta,t)$, k = 1,2 is the acoustic pressure measured by pressure transducer P_2 or P_3, $A(t)$ is the maximum pressure attained over the cavity wall, θ is the physical angle of pressure transducer p_k relative to the pressure transducer P_1, and $\varphi(t)$ is the orientation of the maximum pressure amplitude relative to that of P_1. The maximum value of $A(t)$ and the orientation at which it occurs was taken as that of the primary acoustic mode of this cycle.

5.4 CHARACTERISTICS OF THE SPINNING MODES

5.4.1 Symmetric chamfers

The plots of Figure 5.5 show the relative phase difference between pressure signals measured by the pressure transducers P_1, P_2 and P_2, P_3 as a function of the inflow velocity for the case of symmetric chamfers. The corresponding evolution of the locked-on flow states as a function of the inflow velocity is presented in Figure 5.6. Figure 5.6 also shows theoretical approximations to the first three modes of the transverse shear layer oscillations (the Strouhal

modes), which are labeled H_1, H_2 and H_3, respectively. The dashed lines represent a simplified semi-empirical model of the Strouhal modes defined in Equation (1.3).

The plots in Figure 5.5 show strong correlation between the locked-on states and relative phase difference between pressure signals. Specifically, in the case of L_C = 0 mm, one can see that as the inflow velocity increased to U = 30 m/s, the values of the relative phase difference φ between the pressure signals P_1, P_2 and P_2, P_3 aggregate mostly around φ = 55°. The amplitude of unsteady pressure fluctuations at this value of inflow velocity is approximately 155 dB, as it was reported in (Oshkai and Barannyk, 2013), which corresponds only to the initial stage of the flow tone lock-on. As such, following the classification established earlier, the excited acoustic diametral mode can be classified as a partially spinning mode, resulted from superposition of two orthogonal modes with the temporal phase shift of 90° and an amplitude ratio A/B < 1, as defined in Equation (5.2).

For the range of the inflow velocities 50 ≤ U ≤ 71 m/s, the locked-on state corresponds to the first diametral mode of the cavity (f_1 = 992 Hz) and the first hydrodynamic mode H_1. In this range, as one can see in Figure 5.5 (a), the values of the relative phase difference φ between the pressure signals P_1, P_2 and P_2, P_3 aggregate around φ = 45°. The amplitude ratio A/B in this range of inflow velocities was approximately equal to 1, which indicates that the superposition of two orthogonal modes with a temporal phase shift of 90° resulted in a spinning acoustic diametral mode, as per established classification. As the range of inflow velocity increased, as it was shown in Figure 5.6, the predominant locked-on state shifted to the second hydrodynamic mode H_2 coupled with the 4th acoustic mode f_4 = 2891 Hz (for 78.5 ≤ U ≤ 100 m/s), the third hydrodynamic mode H_3 coupled with the 10th acoustic mode f_{10} = 6328 Hz (for 113.5 ≤ U ≤ 126.5 m/s) and again the second hydrodynamic mode H_2 coupled

with f_7 = 4618 Hz (for $118 \leq U \leq 149$ m/s). The corresponding relative phase difference φ between the pressure signals P_1, P_2 and P_2, P_3 fell in the range of $43° \leq \varphi \leq 76°$ for the case of f_4 = 2891 Hz and $20° \leq \varphi \leq 60°$ for the case of f_7 = 4618 Hz, respectively. In both cases, the resulting modes can be classified as partially spinning.

The cases of f_4 = 2891 Hz and f_7 = 4618 Hz exhibit a distinct similarity in terms of the variation of the relative phase difference φ. Specifically, in the first half of their respective ranges of the inflow velocity, the values of φ are different from $\varphi = 45°$. However, as the inflow velocity increases, the values of φ converge to $\varphi = 45°$. This trend indicates the tendency of the system to lock the relative phase difference between signals measured by the pressure transducers P_1, P_2 and P_2, P_3 to the value $\varphi = 45°$, which corresponds to the physical separation azimuthal angle between pressure transducers, contrary to the results reported in (Aly and Ziada, 2011). Thus, these diametral modes are classified as partially spinning.

Figure 5.5 also shows the influence of the symmetric chamfers on the spinning behaviour of acoustic diametral modes of the cavity. As it can be seen in Figure 5.5 (b), introduction of a symmetric chamfer with L_C = 1.27 mm lead to noticeable changes in the distribution of relative phase difference φ between the pressure signals P_1, P_2 and P_2, P_3. Specifically, at the range of the inflow velocities of $50 \leq U \leq 71$ m/s, where acoustic modes showed fully spinning behaviour in Figure 5.5 (a), the presence of chamfered edges resulted in a deviation of relative phase difference from $\varphi = 45°$, which is indicative of the partially spinning state.

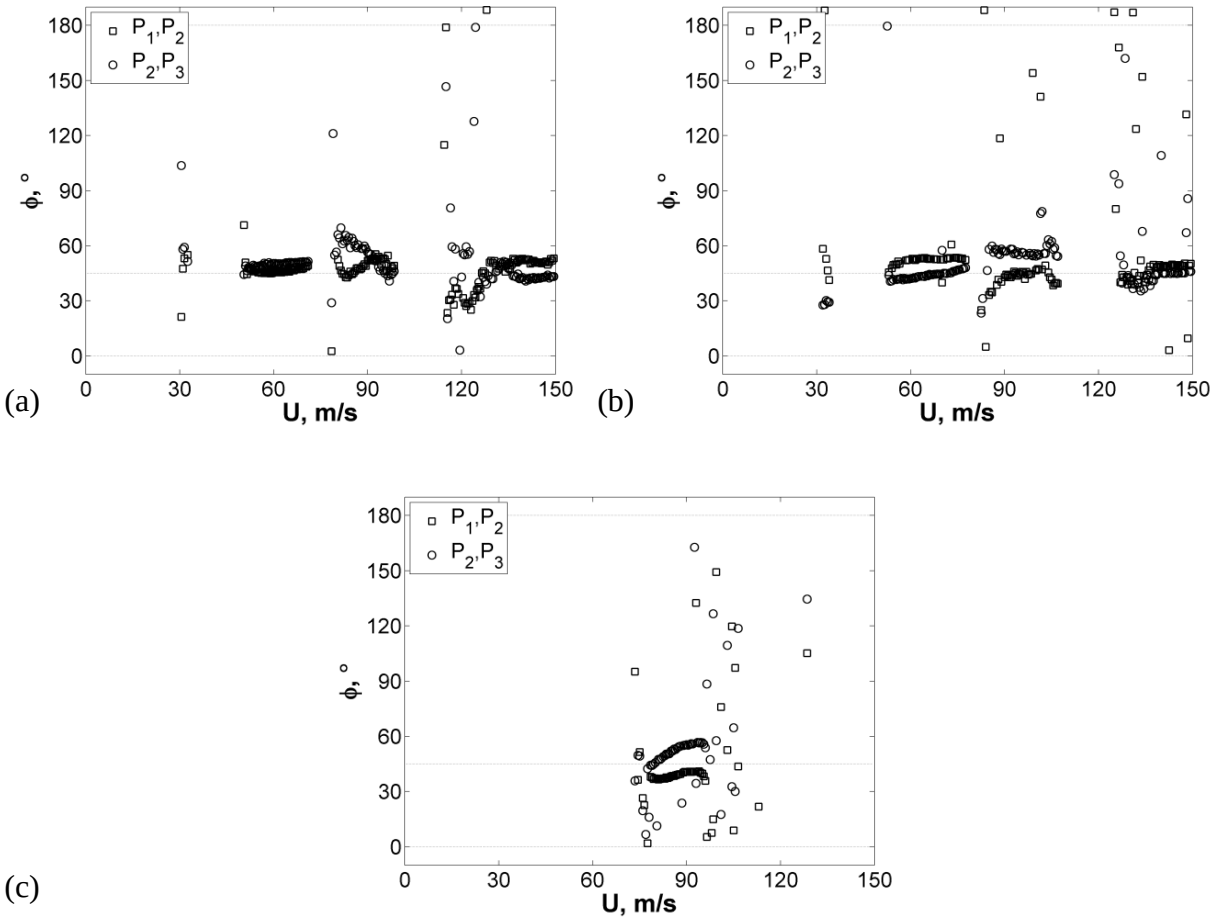

Figure 5.5: Relative phase difference between pressure signals obtained by different transducers as a function of the inflow velocity for the case of symmetric chamfers: (a) L_C = 0, (b) L_C = 1.27 mm, (c) L_C = 3.81 mm.

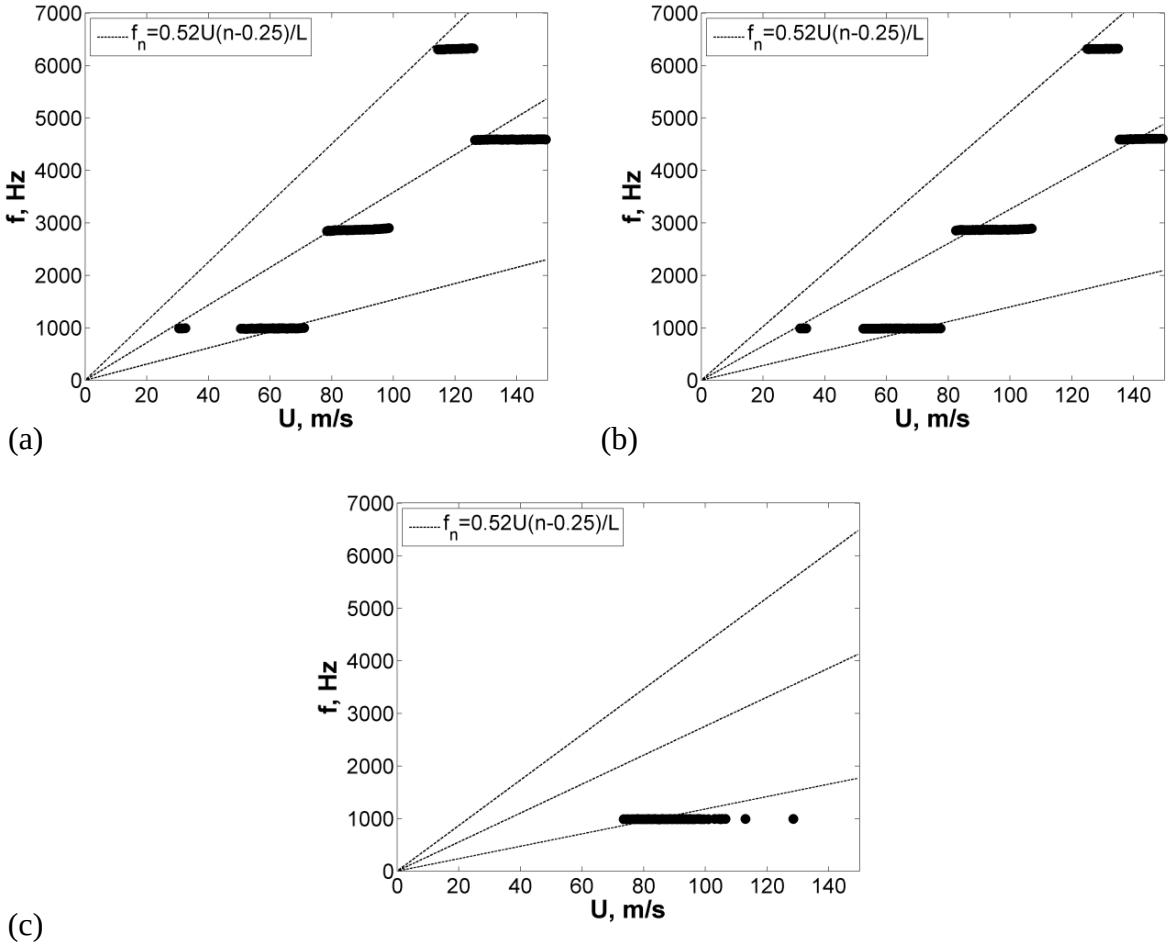

(a) (b)

(c)

Figure 5.6: Frequency of the acoustic pressure as a function of flow velocity for the case of symmetric chamfers: (a) L_C = 0, (b) L_C = 1.27 mm, (c) L_C = 3.81 mm.

A similar trend was observed in the range of the inflow velocities of $78.5 \leq U \leq 100$ m/s, where the hydrodynamic mode H_2 was coupled with the acoustic mode $f_4 = 2891$ Hz. On the other hand, in the range of the inflow velocities of $126 \leq U \leq 149$ m/s, which corresponds to the case of the hydrodynamic mode H_2 coupled with the acoustic mode $f_7 = 4618$ Hz, one can see that the values of φ converged to $\varphi = 45°$, indicating, as in the case of $L_C = 0$ mm, the partially spinning state.

Finally, as the chamfer length increased to $L_C = 3.81$ mm, complete convergence of the relative phase difference φ between the pressure signals P_1, P_2 and P_2, P_3 to the value of $\varphi = 45°$ was not achieved, although φ values clustered in the vicinity of $\varphi = 45°$ in the range of the inflow velocities of $75 \leq U \leq 95$ m/s, as can be seen in Figure 5.5 (c).

It can be concluded that introduction of symmetric chamfers at the upstream and the downstream edges of the cavity can change the temporal behaviour of the acoustic diametral modes of the cavity from spinning to a partially spinning for the lower order modes, while not affecting the higher order modes. This effect becomes more pronounced as the length of the chamfers is increased.

5.4.2 Chamfers of the upstream edge of the cavity

In Figure 5.7, one can see the plots of relative phase difference φ between the pressure signals P_1, P_2 and P_2, P_3 as a function of the inflow velocity, corresponding to the upstream chamfers of $L_C = 1.27$ mm and $L_C = 3.81$ mm. The corresponding evolution of the locked-on flow states as a function of inflow velocity is presented in Figure 5.8.

As can be seen from Figure 5.7 (a), introduction of the upstream chamfer with $L_C = 1.27$ mm resulted in a different effect on φ, compared to the case of symmetric chamfers, illustrated in Figure 5.5 (b). Qualitatively, the upstream chamfer led to a larger deviation of the

temporal behaviour of the acoustic modes from the spinning state, which is illustrated by a divergence of the φ values from $\varphi = 45°$ shown in Figure 5.7 (a). In particular, this effect was observed for the first diametral mode of the cavity (f_1 = 992 Hz) over the entire range of the inflow velocities where this mode was coupled with the hydrodynamic mode H_1. In addition, partially spinning behaviour of the higher order modes f_4 = 2891 Hz and f_7 = 4618 Hz (corresponding to $\varphi = 45°$) was observed over a more narrow range of the inflow velocities, compared to the case of symmetric chamfers.

In contrast to the previously described cases, introduction of a long upstream chamfer (L_C = 3.81 mm) resulted in a well-defined spinning temporal behaviour of the acoustic modes, corresponding to $\varphi = 45°$. An insight into the physics manifested by this result can be obtained from (Oshkai and Barannyk, 2013), where it was shown that a change in the downstream edge of the cavity can weaken the feedback mechanism of the self-sustained shear layer oscillations, one of the main components of which is the interaction of the perturbed velocity field with the impingement edge (Franke and Carr, 1975, Naudascher and Rockwell, 2005). In turn, the change in the upstream feedback affects the amplitude of the acoustic particle velocity of the coupled acoustic mode. In the case of the upstream chamfer, the downstream cavity edge remained sharp, while in the case of the symmetric chamfers, the interaction between the downstream edge and the velocity field was affected.

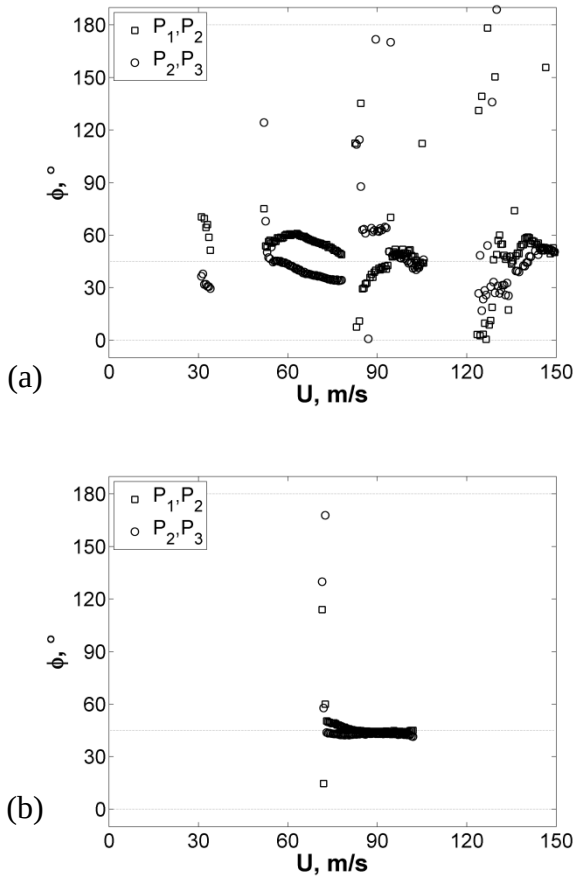

Figure 5.7: Relative phase difference between pressure signals obtained by different transducers as a function of the inflow velocity for the case of the upstream chamfer: (a) L_C = 1.27 mm, (b) L_C = 3.81 mm.

5.4.3 Chamfers of the downstream edge of the cavity

Figure 5.9 shows the evolution of the relative phase difference φ between the pressure signals as a function of the inflow velocity, for the case of the chamfers at the downstream edge of the cavity. The corresponding evolution of locked-on flow states is presented in Figure 5.12.

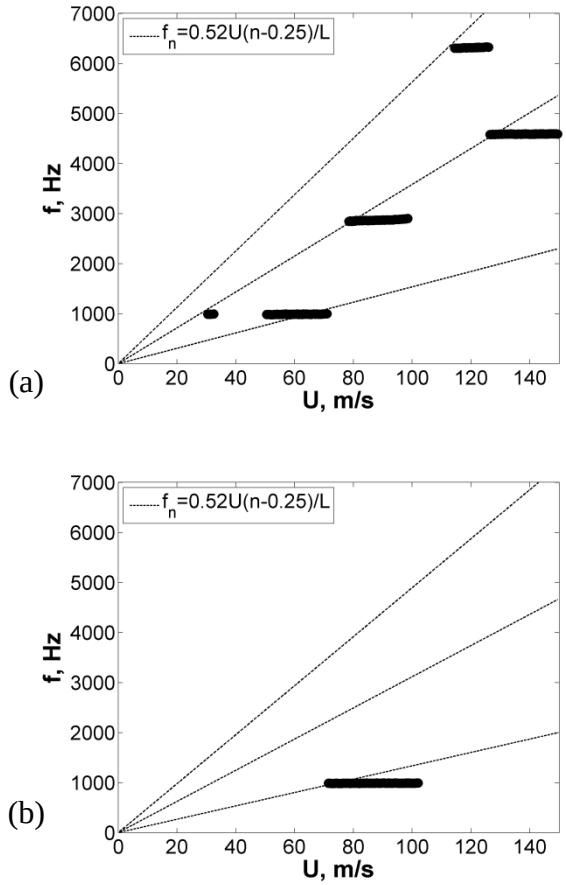

Figure 5.8: Frequency of the acoustic pressure as a function of flow velocity of the acoustic diametral modes for the case of upstream chamfer: (a) L_C = 1.27 mm, (b) L_C = 3.81 mm.

For both values of the chamfer length L_C shown in Figure 5.9, the distribution of the relative phase difference φ between the pressure signals P_1, P_2 and P_2, P_3 was qualitatively similar to the case of the symmetric chamfers, illustrated in Figure 5.5. In particular, the presence of the chamfered downstream edge resulted in a deviation of the φ values from φ = 45°, when the hydrodynamic mode H_2 was coupled with the acoustic modes f_4 = 2891 Hz or f_7 = 4618 Hz.

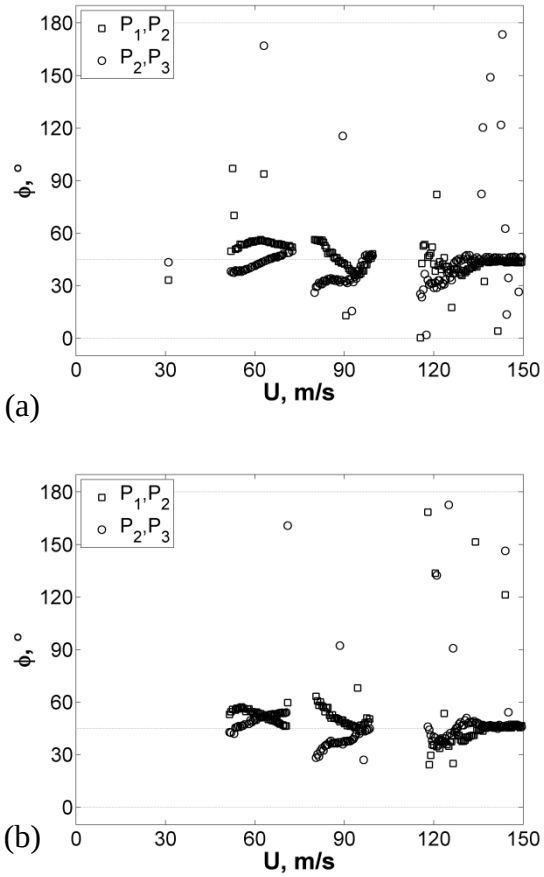

Figure 5.9: Relative phase difference between pressure signals obtained by different transducers as a function of the inflow velocity for the case of the downstream chamfer: (a) L_C = 1.27 mm, (b) L_C = 3.81 mm.

This result agrees with the evolution of the pressure amplitude as a function of the inflow velocity, discussed in (Oshkai and Barannyk, 2013), and indicates that modification (weakening) of the feedback mechanism at the downstream corner of the cavity can change the azimuthal behaviour of the acoustic diametral mode from spinning to a partially spinning by decreasing the contribution from the acoustic particle velocity.

5.5 EFFECT OF SPLITTER PLATE ON THE ROTATIONAL BEHAVIOUR OF THE ACOUSTIC DIAMETRAL MODE

For the next set of experiments, a horizontal splitter plate of two different length (L_S = 57.15 mm, L_S = 81.4 mm) was inserted into the cavity, as it was illustrated in Figure 1 (c). The acoustic mode shapes and the resonant frequencies, associated with the cavity-splitter plate arrangement, were calculated numerically using the finite-element package Comsol 4.2a.

Similarly to the results reported in (Aly and Ziada, 2011), in the case of the first acoustic mode, the numerical simulations revealed the presence of two acoustic diametral modes, which orientation was locked on the splitter plate, with one mode, denoted as f_A, being perpendicular to it (when looking at the nodal diameter with respect to the plate's orientation), and the other mode, denoted as $f_{B,}$ being almost parallel to the plate with its mode shape being noticeably affected by the presence of the splitter plate, which is illustrated in Figure 5.10. In the case of shorter and longer splitter plates the following identity holds: $f_A > f_B$. Besides that, in the current experimental system the frequency of the acoustic mode f^A_i was noticeably higher than that of the acoustic mode f^B_i, for i = 1,4,7,10, as it can be seen in Figure 5.10. This differences, however, are most likely attributed to the different L/D = 0.3 ratio of the current cavity geometry compared to the one used in (Aly and Ziada, 2011), and because of the larger length of the splitter plate used in the present study, which amplified cavity asymmetry and significantly changed the mode shapes and associated with them resonant frequencies. The effect of cavity asymmetry was especially pronounced in the higher order modes.

Table 5.1: Pairs of resonant frequencies obtained numerically and associated with acoustic diametral modes with preferred orientation imposed by a splitter plate.

	Short splitter plate		Long splitter plate	
	f_A, Hz	f_B, Hz	f_A, Hz	f_B, Hz
A_1	1001	842	998	713
A_4	2887	2583	2882	2582
A_7	4659	4365	4659	4365
A_{10}	6413	6119	6408	6117

In order to investigate this shift in the frequency, the data from three pressure transducers was further evaluated. In Figure 5.11, one can see the evolution of resonant frequencies of the acoustic pressure as a function of inflow velocity, obtained from three pressure transducers, for the case of unmodified cavity corners. In this figure, three different colors, black, red and yellow, represent the frequency measured by pressure transducers P_1, P_2, and P_3 respectively.

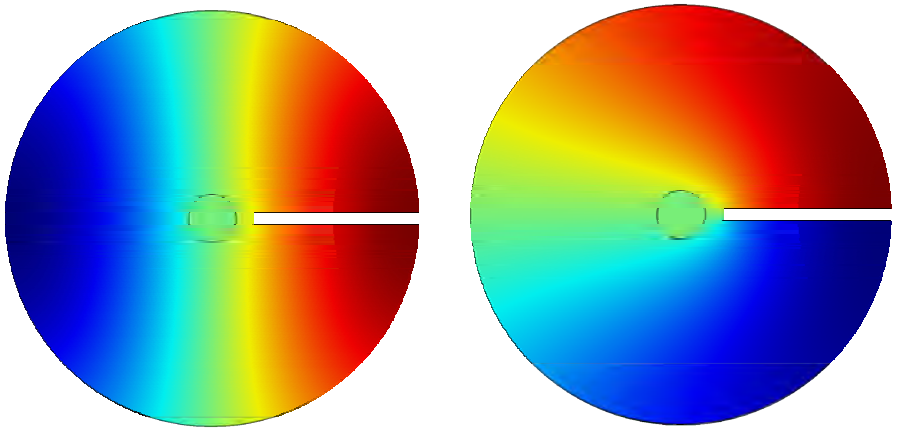

Figure 5.10: The mode shapes of the first acoustic diametral mode in the presence of the long splitter plate (L_S = 81.4 mm): (a) f^A_4 = 998 Hz, (b) f^B_4 = 713 Hz.

In the case of the short splitter plate, which is shown in Figure 5.11(a), it can be seen that over the four regions of the inflow velocity: 1) $53.5 \leq U \leq 64.5$ m/s, 2) $75 \leq U \leq 98$ m/s, 3) $113.5 \leq U \leq 124$ m/s, 4) $129.5 \leq U \leq 149$ m/s, all three pressure transducers showed a single frequency of approximately f^A_i , where i = 1,4,7,10.

In the case of the long splitter plate, illustrated in Figure 5.11(b), one can see that for the range of the inflow velocities $53.5 \leq U \leq 64.5$ m/s, all three pressure transducers show a single frequency of the acoustic mode which nodal diameter was perpendicular to the plate, of approximately $f^A_1 = 998$ Hz.

In contrast to the case of short splitter plate, as the range of the inflow velocities increased to $75 \leq U \leq 98$ m/s, one can see three distinct ranges of the frequency of acoustic pressure. In particular, for $75 \leq U \leq 82.5$ m/s, all three pressure transducers showed a single frequency of approximately $f^X_4 = 2710$ Hz, for $83 \leq U \leq 85$ m/s the pressure transducers P_1 and P_2 showed the frequency of approximately $f^A_4 = 2882$ Hz, while the pressure transducer P_3 indicated the presence of the frequency of approximately $f^X_4 = 2710$ Hz. Finally, for $85.5 \leq U \leq 98$ m/s, all three pressure transducers showed a single frequency of $f^A_4 = 2882$ Hz.

Further increase of the range of the inflow velocities led to the following observations. For $113.5 \leq U \leq 124$ m/s, which corresponded to the excitation of the tenth acoustic mode, the pressure transducers P_1 and P_2 showed the frequency of approximately $f^A_{10} = 6408$ Hz, while the pressure transducer P_3 indicated the presence of a different frequency of approximately $f^X_{10} = 6297$ Hz.

Finally, for $124.5 \leq U \leq 149$ m/s, three different ranges of the frequency of the acoustic pressure were observed. Specifically, for $124.5 \leq U \leq 129$ m/s, all three pressure transducers showed a single frequency of approximately $f^X_7 = 4531$ Hz. For $129.5 \leq U \leq 143$ m/s, the

pressure transducers P_1 and P_2 show the frequency about f^A_7 = 4659 Hz, while the pressure transducer P_3 indicated the presence of a different frequency of approximately f^X_7 = 4531 Hz. In addition, for $143.5 \leq U \leq 149$ m/s, all three pressure transducers showed a single frequency of f^A_7 = 4659 Hz.

Based on the results obtained for the long splitter plate, it can be seen that the resonant frequencies f^X_i, where i = 4,7,10, are different from the frequencies f^B_i, reported in (Aly and Ziada, 2011). These results lead to the conclusion that the singularity represented by the splitter plate, not only introduced a substantial frequency shift between the pair of acoustic diametral modes, but also did not allow the simultaneous excitation of the pair of acoustic diametral modes, as it was shown in (Aly and Ziada, 2011). These results also showed the presence of other acoustic modes with resonant frequencies f^X_i, where i = 4,7,10 and indicated a simultaneous excitation of multiple acoustic diametral modes by different azimuthal portions of the cavity shear layer (corresponding to the different locations of the pressure transducers), confirming similar results reported in (Aly and Ziada, 2011).

The results reported above introduced the following constraint on the evaluation of phase difference between pressure signals obtained by different transducers. Figure 5.13 illustrates the effect of splitter plate on the acoustic response of the pipeline-cavity system without chamfers. The plots shown in Figure 5.13 (a) and (b) correspond to the cases of the short splitter plate (L_S = 57.15 mm) and the long plate (L_S = 81.4 mm), respectively.

In the case of the short splitter plate, since all three pressure transducers showed excitation of the single frequency over its respective velocity regions, the distribution of the relative phase difference φ between the pressure signals illustrated in Figure 5.13 (a) shows convergence of the φ values to $\varphi = 0°$ when the first diametral acoustic mode of the cavity (f_1 =

992 Hz) was excited by the first hydrodynamic mode H_1, indicating stationary (non-spinning) behaviour of this acoustic mode.

In the case of the long splitter plate, the distribution of the relative phase difference φ between the pressure signals is shown in Figure 5.13 (b). The velocity regions that correspond to the presence of resonant flow states were adjusted based on the results shown in Figure 5.11(b), and the velocity sub-regions where simultaneous excitation of multiple acoustic diametral modes was observed is not shown. As it can be seen in Figure 5.13 (b), the φ values converged to $\varphi = 0°$ when the first (f_1 = 998 Hz), the fourth (f_4 = 2882 Hz) and the seventh (f_7 = 4659 Hz) diametral acoustic modes were excited by locked on the hydrodynamic modes H_1 and H_2. The decrease in the maximum pressure amplitude was accompanied by a noticeable change in the azimuthal behaviour of the acoustic diametral modes.

These results indicate that due to the presence of the splitter plate, the azimuthal behaviour of the diametral acoustic modes can switch from spinning or partially spinning to stationary. In addition, the decrease in the maximum pressure amplitude indicate that the spinning modes are capable of producing more energy compared to stationary modes, as it was indicated in (Aly and Ziada, 2011).

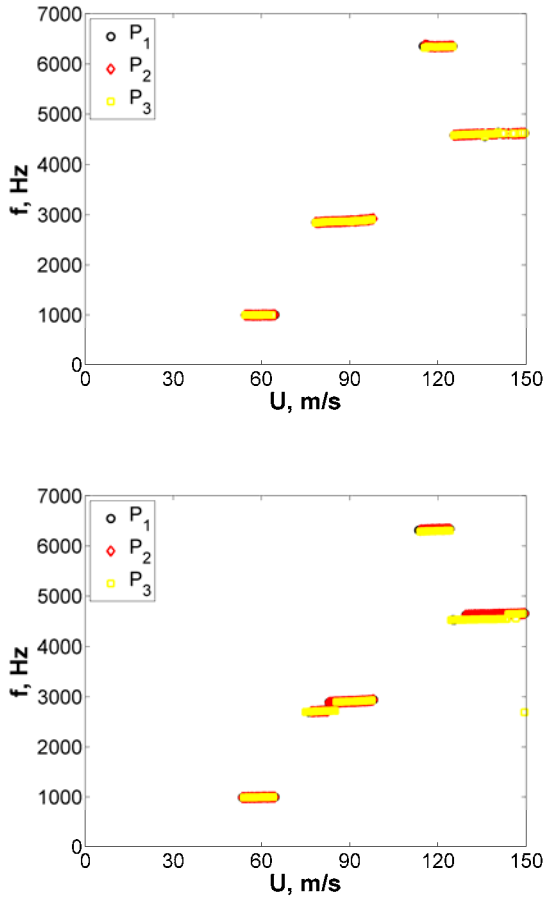

Figure 5.11: Frequency of the acoustic pressure as a function of flow velocity of the acoustic diametral modes, obtained from three pressure transducers, for the case of unmodified cavity corners (no chamfers): (a) Short splitter plate (L_S = 57.15 mm), (b) Long splitter plate (L_S = 81.4 mm).

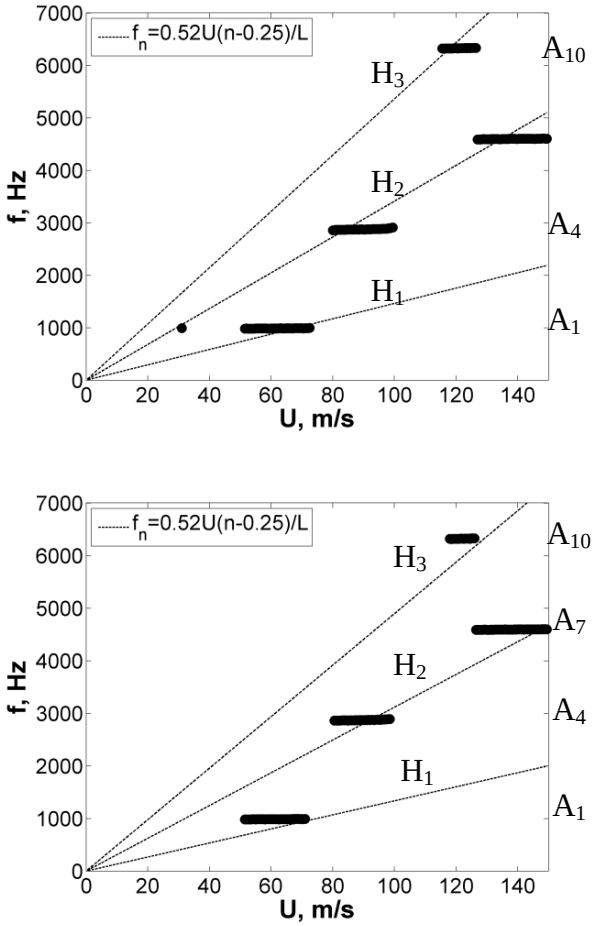

Figure 5.12: Frequency as a function of flow velocity of the acoustic diametral modes for the case of down-stream chamfer: (a) L_C = 1.27 mm, (b) L_C = 3.81 mm.

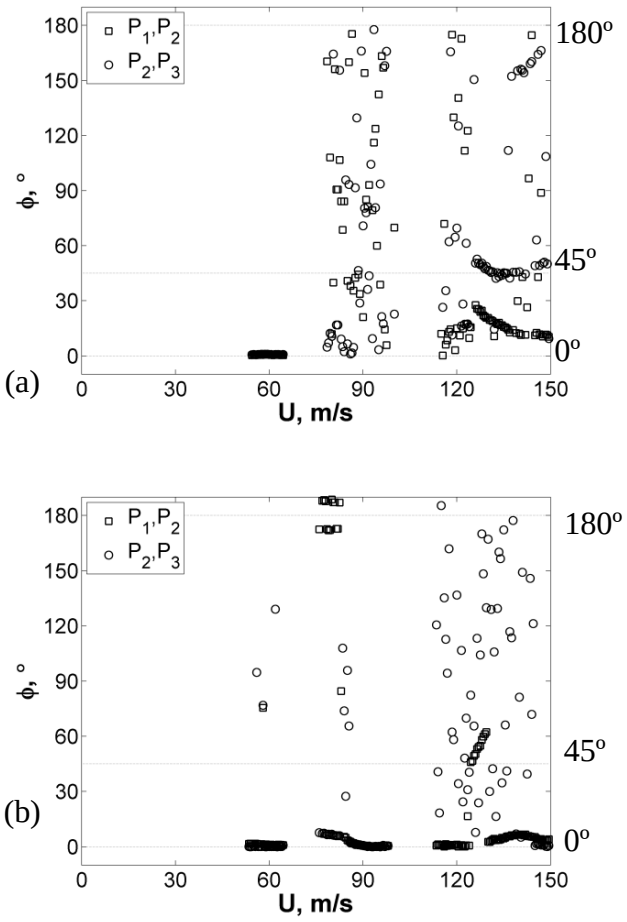

Figure 5.13: Effect of splitter plate on the rotational behaviour of the acoustic diametral mode for the case of symmetric L_C = 0 mm: (a) Short splitter plate (L_S = 57.15 mm), (b) long splitter plate (L = 81.4 mm).

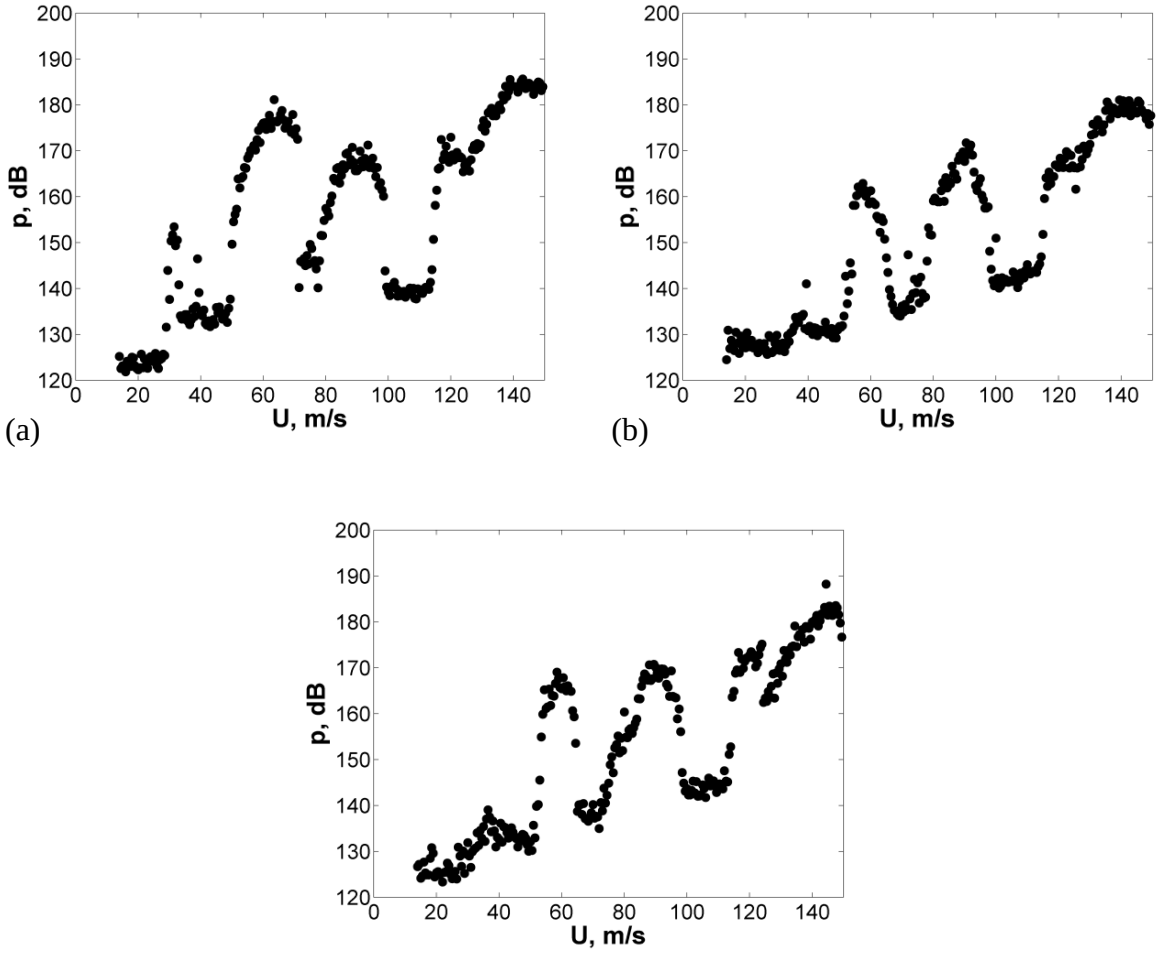

Figure 5.14: Effect of splitter plate on the pressure amplitude of the acoustic diametral mode for the case of symmetric L_C = 0 mm: (a) No splitter plate, (b) Short splitter plate (L_S = 57.15 mm), (c) Long splitter plate (L_S = 81.4 mm).

CHAPTER 6

QUANTITATIVE VISUALIZATION OF UNSTABLE, ACOUSTICALLY COUPLED SHEAR LAYERS IN DEEP AXISYMMETRIC CAVITIES

This Chapter illustrates the evolution of fully turbulent, acoustically coupled shear layers that form across the deep, axisymmetric cavity shown in Figure 2.4. Effects of geometric modifications of the cavity edges, indicated in Figure 2.4 (b), on the separated flow structure were investigated using digital particle image velocimetry (PIV). The internal flow was non-intrusively accessed by means of a borescope, which allowed illumination and optical recording of flow tracers inside the cavity. Due to strong reflections from the inside surface of the inlet pipe, the region right near the upstream edge of the cavity was masked out in order to avoid error propagation in the vorticity calculation. Instantaneous, phase- and time-averaged patterns of out-of-plane vorticity, root-mean-square values of the streamwise u and transverse v velocity fluctuations, u_{rms}/U, v_{rms}/U and their correlations $\langle u'v' \rangle / U^2$, provided insight into the flow physics during flow tone generation and noise suppression by the geometric modifications.

6.1 INSTANTANEOUS FLOW PATTERNS

Figure 6.1 shows patterns of the instantaneous out-of-plane vorticity corresponding to the first H_1, second H_2 and third H_3 hydrodynamic modes of cavity shear layer oscillation for

the case L_C = 0 mm. In Figure 6.1 (a), the first hydrodynamic mode was coupled with the first acoustic mode of the cavity (f_1 = 992 Hz) at U = 67 m/s, which corresponds to the Strouhal number St = fL/U = 0.37. The area of the plots represents the opening of the cavity. The flow in the main pipeline is from left to right, and the cavity extends in the vertical direction. Two shear layers formed between the fast flow in the middle of the pipeline and slowly moving flow inside the cavity. The first hydrodynamic oscillation mode H_1 is characterized by the formation of one large-scale vortical structure per acoustic oscillation period in each of the bottom and the top shear layers. In particular, at the time instant shown in Figure 6.1 (a), a positive (counter-clockwise) vortex was forming immediately downstream of the leading edge of the cavity in the upper shear layer.

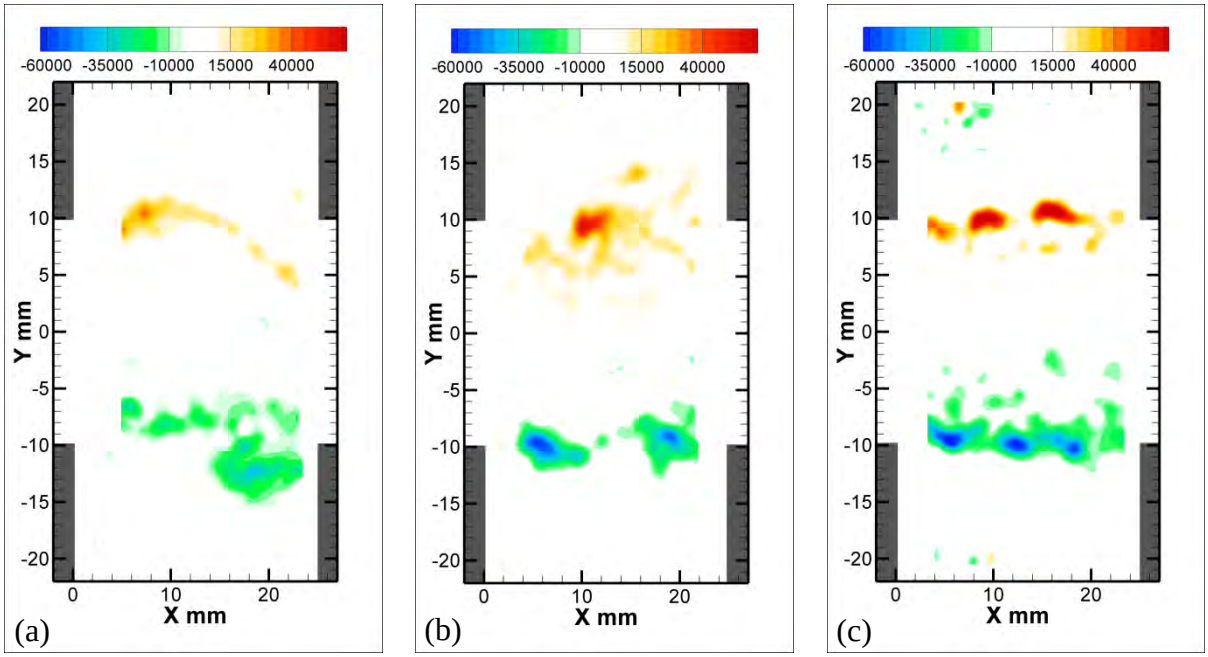

Figure 6.1: Patterns of instantaneous out-of-plane vorticity (s^{-1}) corresponding to the (a) first (St = 0.37, U = 67m/s), (b) second (St = 0.8, U = 91.5 m/s), and (c) third (St = 1.32, U = 121 m/s) hydrodynamic mode for the case L_C = 0 mm. Flow is from left to right.

At the same time, a fully formed, large-scale negative (clockwise) vortex in the bottom shear layer was approaching the downstream edge of the cavity. This instantaneous position of the vortices indicates that the vortex formation in the top and bottom shear layers occurred with a phase shift of 180°.

In Figure 6.1 (b), the instantaneous patterns of out-of-plane vorticity correspond to the inflow velocity of U = 91.5 m/s (St = 0.8). In this case, the flow tone represented by the fourth acoustic mode of the cavity (f_4 = 2,891 Hz) resonated with the second hydrodynamic mode H_2. In this flow regime, two large-scale vortices were formed in each of the bottom and the top shear layers during a typical acoustic oscillation cycle. In other words, at any instant, two vortices can exist in a shear layer. At the time instant shown in Figure 6.1 (b), two negative vortices can be observed in the bottom shear layer near the corners of the cavity, while a single positive vortex was located approximately near the middle of the cavity opening in the top shear layer. Thus, similar to the flow regime shown in Figure 6.1 (a), the second hydrodynamic mode also exhibited asymmetric flow oscillation, or out-of-phase formation of vortices in the top and the bottom shear layers.

Flow patterns of instantaneous out-of-plane vorticity, shown in Figure 6.1 (c), are associated with the flow regime during which the tenth acoustic mode of the cavity (f_{10} = 2,891 Hz) resonated with the third hydrodynamic mode H_3 at an inflow velocity of U = 121 m/s (St = 1.32). In this case, three large-scale vortices were formed in each of the bottom and the top shear layers during a typical acoustic oscillation cycle. Similar to the flow regimes shown in Figure 6.1 (a,b), the third hydrodynamic mode exhibited asymmetric flow oscillation and formation of vortices in the top and the bottom shear layers. The overall amplitude of these flow oscillations is substantially lower than that of the flow regime shown

in Figure 6.1 (a), which is most likely attributed to the stationary behaviour of the tenth acoustic mode of the cavity. As it was shown in Chapter 5, at U = 67 m/s and U = 91.5 m/s the first and the fourth acoustic modes behaved as a spinning and partially spinning modes, respectively, as such enforcing the asymmetric flow oscillation of the cavity shear layer.

From the analysis of the flow patterns illustrated in Figure 6.1 one can see that patterns of out-of-plane vorticity show the tendency to form a large-scale structure in the top and bottom shear layers, with the highest levels of vorticity located near the center of the cluster of large-scale structure. Another noticeable feature of the vorticity plots in Figure 6.1 is the difference in the shape of the associated shear layers. In particular, the amplitude of shear layer oscillation corresponding to the first H_1 hydrodynamic mode is substantially higher than that of H_2 and especially of H_3, where the oscillation of the shear layer is less pronounced.

6.2 TIME-AVERAGED FLOW PATTERNS

6.2.1 No chamfers

6.2.1.1 Average vorticity

Figure 6.2 through Figure 6.6 show the patterns of time-averaged out-of-plane vorticity, root-mean-square values of the streamwise u and transverse v velocity fluctuations u_{rms}/U and v_{rms}/U respectively, and contours of Reynolds stress correlations $\langle u'v' \rangle / U^2$, obtained for the case L_C = 0 mm of the first hydrodynamic mode of the cavity locked on the first trapped acoustic mode, second hydrodynamic mode of the cavity locked on the fourth trapped acoustic mode, and the third hydrodynamic mode of the cavity locked on the tenth trapped acoustic mode. For correct representation of the time-averaged patterns in Figure 6.2, the procedure outlined in Section 2.2.5 was implemented. A total number of 200 consecutive PIV re-

cordings taken continuously at time intervals Δt and with constant mean flow conditions were used for the averaging.

As it can be seen from Figure 6.2, for the case H_1A_1 the maximum level of time-averaged out-of-plane vorticity $\langle \omega_z \rangle$ of 21800 s^{-1} was attained at (4.9 mm, 8.9 mm) and it decreases in a streamwise direction to a substantially lower value of 4170 s^{-1}. For the case H_2A_4, the level of out-of-plane vorticity close to the upstream edge of the cavity has the maximum value of 28000 s^{-1} at (4.5 mm, 8.9 mm) and it decreases to the value of 12600 s^{-1} at the downstream edge of the cavity. Finally, for the case H_3A_{10}, the level of vorticity decreases from the maximum value of 52000 s^{-1} at (4.2 mm, 8.9 mm) to the value of 19900 s^{-1} at the downstream edge location of the cavity.

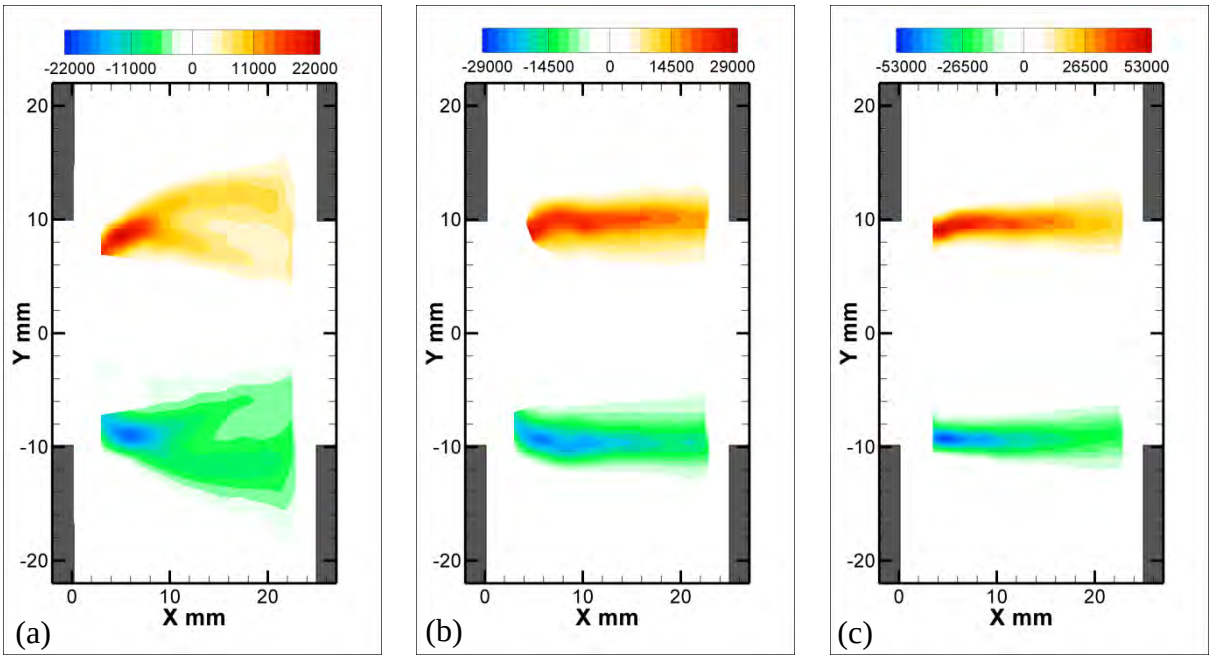

Figure 6.2: Patterns of time-averaged out-of-plane vorticity (s^{-1}) corresponding to the (a) first (St = 0.37, U = 67 m/s), (b) second (St = 0.8, U = 91.5 m/s), and (c) third (St = 1.32, U = 121 m/s) hydrodynamic mode for the case L_C = 0 mm.

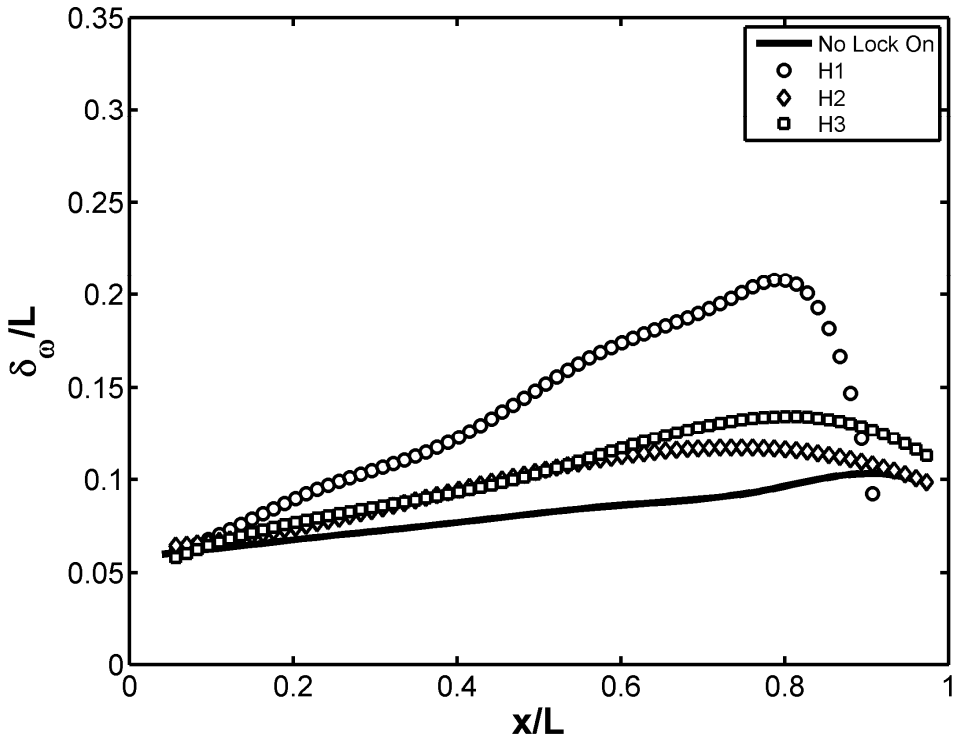

Figure 6.3: Growth of the vorticity thickness across the cavity for the case L_C = 0 mm.

The location of peak levels of time-averaged out-of-plane vorticity is associated with the location of flow separation near the upstream edge of the cavity.

Another feature of the patterns of time-averaged out-of-plane vorticity $\langle \omega_z \rangle$ shown in Figure 6.2 is a noticeable change in the vorticity growth rate, which decreases with the increase of the hydrodynamic mode number. This phenomenon can be quantitatively assessed by introducing vorticity thickness, defined as (Schlichting, 1955),

$$\delta_\omega = \frac{U_1 - U_2}{\left[\frac{d\langle u \rangle}{dy}\right]_{max}} \tag{6.1}$$

where U_1 and U_2 are the centerline velocity and free-stream velocity at the lower side of the shear layer, respectively.

Figure 6.3 illustrates the distribution of the normalized vorticity thickness δ_ω/L across the cavity opening for the case of no chamfers (L_C = 0). Four characteristic flow regimes were considered: no flow tone lock-on as well as the resonant shear layer oscillations corresponding to the first three hydrodynamic modes, H_1, H_2 and H_3. These hydrodynamic modes were coupled to the acoustic modes f_1 = 992 Hz, f_4 = 4,618 Hz and f_{10} = 6,328 Hz, respectively. The wavelength and scale of the vortices in the shear layer are expected to increase as the vorticity thickness increases (Monkewitz and Huerre, 1982). Thus, the plot of Figure 6.3 indicates that, in all cases, small-scale vortices were forming in the vicinity of the upstream cavity corner, and that their scale increased at locations downstream from the flow separation point. In the non-resonant flow regime, the vorticity thickness increased approximately linearly along with a rate of $d\delta_\omega/dx$ = 0.046 until x/L = 0.9, at which point the values of δ_ω/L rapidly decreased indicating the shear layer impingement at the downstream edge of the cavity. In the resonant cases, the vorticity thickness increases more rapidly with the downstream distance. The first hydrodynamic oscillation mode H_1 exhibits the highest growth rate of $d\delta_\omega/dx$ = 0.235, while the second and the third modes H_2 and H_3 correspond to approximately equal growth rates of $d\delta_\omega/dx$ = 0.11. These results indicate that among the first three hydrodynamic oscillation modes, mode H_1 is associated with the most rapid development of the large-scale vortices in the separated shear layer, which in turn leads to the most pronounced transverse velocity fluctuations and the most effective coupling with the standing waves of the acoustic pressure in the cavity. This observation is consistent with the results reported in (Oshkai and Barannyk, 2013), which demonstrated that the highest amplitude of pressure pulsations in the deep circular cavity were associated with the first hydrodynamic mode of the shear layer oscillations.

6.2.1.2 *Velocity correlation*

In Figure 6.4 through Figure 6.6, one can see the patterns of the normalized velocity fluctuations and their correlation, presented in terms of u_{rms}/U and v_{rms}/U respectively, and contours of Reynolds stress $<u'v'>/U^2$.

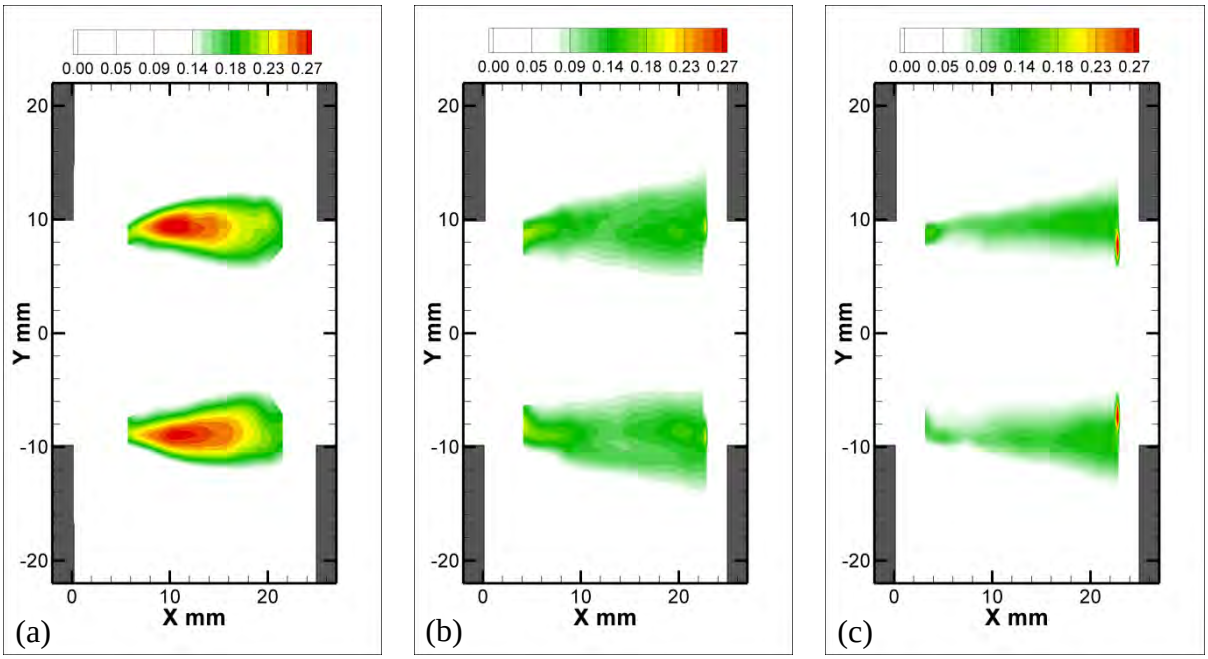

Figure 6.4: Patterns of time-averaged u_{rms}/U corresponding to the (a) first (St = 0.37, U = 67m/s), (b) second (St = 0.8, U = 91.5 m/s), and (c) third (St = 1.32, U = 121 m/s) hydrodynamic mode for the case L_C = 0 mm.

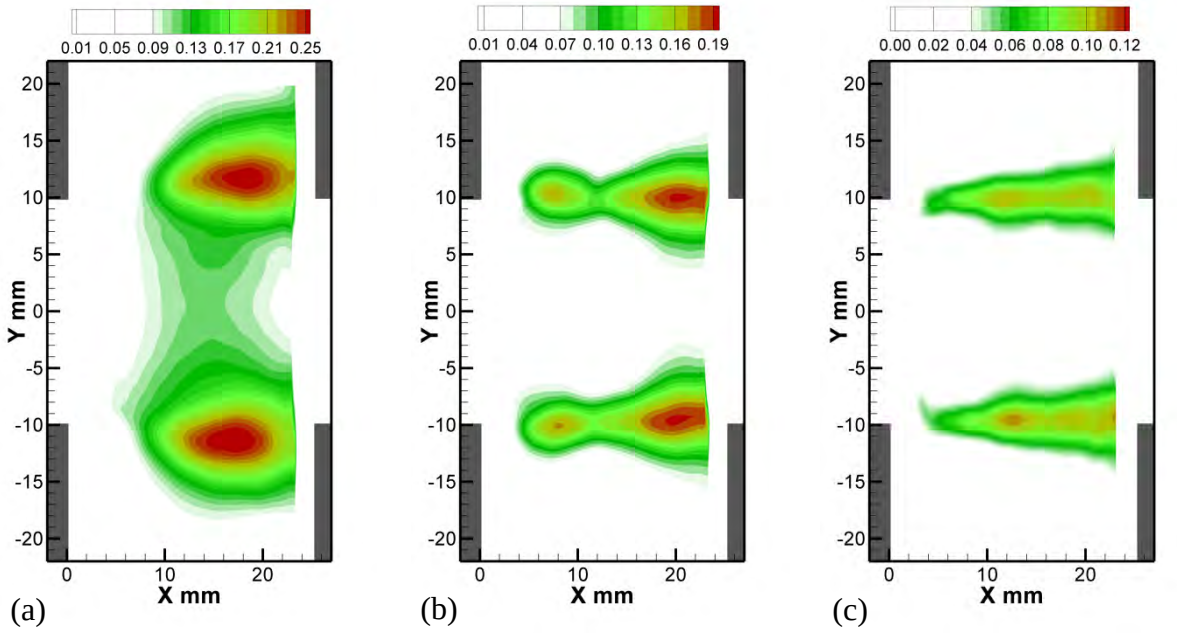

Figure 6.5: Patterns of time-averaged v_{rms}/U corresponding to the (a) first (St = 0.37, U = 67m/s), (b) second (St = 0.8, U = 91.5 m/s), and (c) third (St = 1.32, U = 121 m/s) hydrodynamic mode for the case L_C = 0 mm.

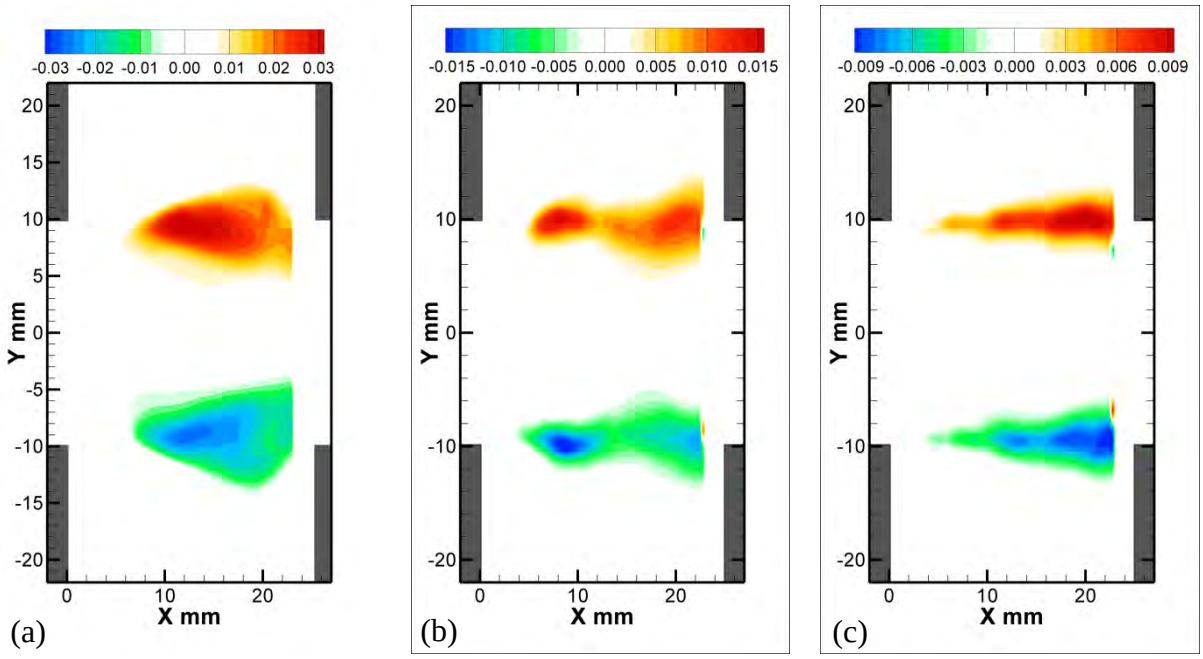

Figure 6.6: Patterns of time-averaged $<u'v'>/U^2$ corresponding to the (a) first (St = 0.37, U = 67m/s), (b) second (St = 0.8, U = 91.5 m/s), and (c) third (St = 1.32, U = 121 m/s) hydrodynamic mode for the case L_C = 0 mm.

The common feature among the flow patterns shown in Figure 6.4 through Figure 6.6 is the presence of one, two and three peaks of velocity correlations u_{rms}/U, v_{rms}/U and contours of Reynolds stress $<u'v'>/U^2$, which are associated with the nature of the particular hydrodynamic mode of the cavity present in each case, i.e. the number of vortices shed per cycle.

As can be seen from Figure 6.4, the peak values of u_{rms}/U occur in the separated shear layer, with the maximum value u_{rms}/U = 0.267, was attained downstream of the leading edge of the cavity, at X = 10.3 mm for the case (a), u_{rms}/U = 0.2, was attained downstream of the leading edge of the cavity, at X = 21.7 mm for the case (b). Finally, u_{rms}/U = 0.15, was attained downstream of the leading edge of the cavity, at X = 21.4 mm for the case (c). At the downstream edge of the cavity the contours of u_{rms}/U expand, indicating movement and distortion of large-scale vortical structures through this region. In Figure 6.5, one can also see that the peak values of v_{rms}/U = 0.26, 0.19, 0.11 were mostly prevalent close to the trailing edge of the cavity at X = 16.7 mm, 19.4 mm, 22.7 mm for the cases (a), (b), (c), respectively, in the area associated with the formation of large-scale vortical structures. The latter statement is supported by the corresponding instantaneous images in Figure 6.1 where the appearance of large-scale vortical structures is aligned with the regions of peak values of velocity fluctuations u_{rms}/U and v_{rms}/U respectively, illustrated in Figure 6.4. At the same time, the noticeably low values of streamwise and transverse velocity fluctuations at the upstream edge of the cavity are associated with the initial region of the shear layer development where the large-scale, organized formation of the vortical structures has not happened yet, which is also evident in Figure 6.1.

Figure 6.6 show the contours of Reynolds stress $<u'v'>/U^2$. It can be seen that noticeably high levels of Reynolds stress of the opposite sign were generated in the top and bot-

tom separated shear layer of the cavity. It is evident that the sign depends on relative strengths of positive and negative contributions. The peak values of the velocity correlations $<u'v'>/U^2$ = -0.026, 0.03 were observed at X = 11.3 mm, for the cases shown in Figure 6.6 (a), $<u'v'>/U^2$ = -0.014, 0.015 at X = 8.6 mm, for the cases shown in Figure 6.6 (b), and $<u'v'>/U^2$ = -0.009, 0.009 at X = 20.4 mm, for the cases shown in Figure 6.6 (c).

For all three types of velocity correlations discussed above, their respective peak values decreased with the increase of hydrodynamic mode number. Substantially higher values of velocity correlations in the case of H_1A_1 were associated with the development of vortical structures of much larger scale, compared to the case of H_2A_4 and H_3A_{10}. In addition to that, as it was shown in Section 4.2.2, the amplitude of the unsteady pressure fluctuations in the case of H_2A_4 and H_3A_{10} indicated weaker locked-on regimes associated with organized vortex development of noticeable smaller scales, as it was shown in Figure 6.1 (b,c).

6.2.2 Effect of the edge geometry

6.2.2.1 Average vorticity

In this Section, the influence of cavity edge geometry on the flow characteristics was investigated during the locked-on state, in the vicinity of the nominal separation and the impingement points of the shear layers indicated in Section 2.1.2. As shown in Section 4.2.2, the first resonant case H_1A_1 resulted in the highest amplitude of pressure pulsations within the cavity, compared to other resonant cases. As such, the effect of cavity edge geometry was investigated only for the case H_1A_1. Shear layer characteristics at the upstream and the downstream edges of the cavity were altered by means of chamfers of the angle α = 15° and of the length L_C ranging from 1.27 mm to 10.16 mm, illustrated in Figure 2.4. In Section 4.3 it was shown that introduction of chamfers at the downstream corner of the cavity slightly

decreased the overall amplitude of the self-sustained oscillations but did not lead to the suppression the locked-on flow tones. Based on that result, it was decided to limit current investigation to the case of symmetric chamfers, which were introduced at the upstream and downstream edge of the cavity, and to the case of a chamfer introduced only at the upstream edge of the cavity. The overall effect was analyzed from the set of time-averaged flow patterns of time-averaged out-of-plane vorticity $\langle \omega_z \rangle$ and time-averaged, normalized velocity correlations u_{rms}/U, v_{rms}/U, $\langle u'v' \rangle / U^2$. Due to the qualitative similarity between the flow patterns in the case of symmetric and upstream chamfers, only the case for symmetric chamfers will be illustrated in this Section. The images of flow patterns that correspond to the upstream chamfer were moved to APPENDIX A:.

In Figure 6.7, one can see the contours of time-averaged out-of-plane vorticity $\langle \omega_z \rangle$ for the case of the symmetric chamfer with chamfer length: (a) L_C = 1.27 mm, (b) L_C = 3.81 mm, (b) L_C = 10.16 mm. Within the region of separated shear layer, which was extended from the upstream to the downstream edge of the cavity, one can see that the peak levels of out-of-plane vorticity are concentrated close to the upstream edge of the cavity. A summary of peak values of out-of-plane vorticity for cases investigated in this section is given in Table 6.1. In the region of high vorticity, the flow drastically changes its behaviour from attached to fully separated.

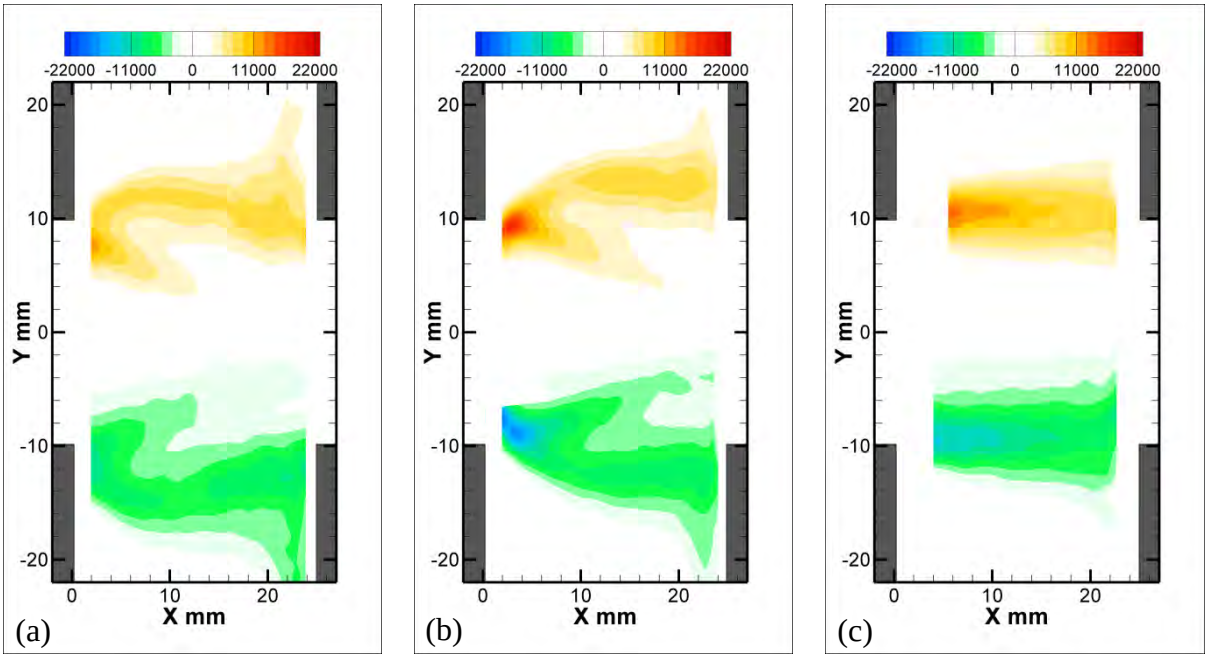

Figure 6.7: Patterns of time-averaged out-of-plane vorticity (s^{-1}) corresponding to the case of the symmetric chamfer with chamfer length: (a) L_C = 1.27 mm, (b) L_C = 3.81 mm, (c) L_C = 10.16 mm.

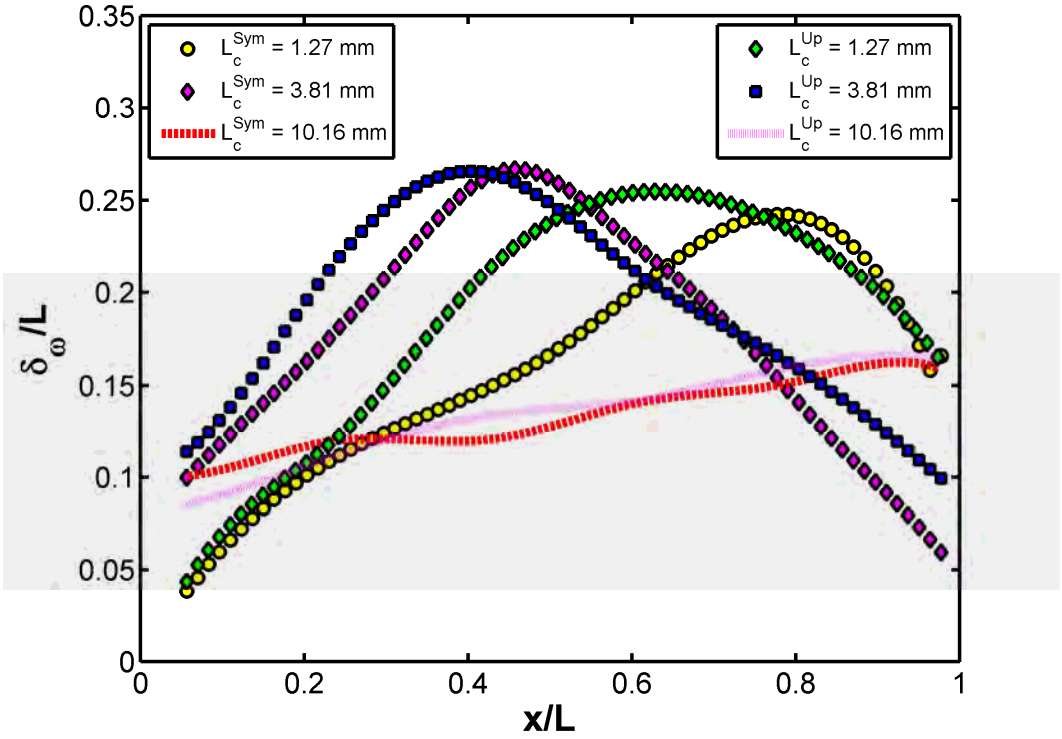

Figure 6.8: Growth of the vorticity thickness across the cavity corresponding to the case of the symmetric and upstream chamfer with chamfer length: L_C = 1.27 mm, L_C = 3.81 mm, L_C = 10.16 mm.

Table 6.1: Peak values of time-averaged out-of-plane vorticity for the case of symmetric and upstream chamfer length.

Symmetric, mm	**Max($\langle\omega_z\rangle$),s^{-1}**	***X*, mm**	**Min($\langle\omega_z\rangle$),s^{-1}**	***X*, mm**
L_C = 1.27	20700	3.89	-19300	2.86
L_C = 3.81	17400	2.86	-13300	2.86
L_C = 10.16	11000	3.87	-9900	4.19
Upstream, mm	**Max($\langle\omega_z\rangle$),s^{-1}**	***X*, mm**	**Min($\langle\omega_z\rangle$),s^{-1}**	***X*, mm**
L_C = 1.27	20000	3.19	-16100	3.53
L_C = 3.81	16000	2.86	14800	2.86
L_C = 10.16	12000	3.87	11300	4.2

As shown in Chapter 4, between three chamfer lengths L_C that were investigated in this study the highest amplitude of pressure pulsation was attained in the case (b) L_C = 3.81 mm with the lock-on flow states being completely eliminated in the case (c) L_C = 10.16 mm. These results are supported by the patterns of out-of-plane vorticity $\langle\omega_z\rangle$ in Figure 6.7. Specifically, in the absence of locked-on flow state, in the case of L_C = 10.16 mm, shown in Figure 6.7 (c), one can see that the top and bottom shear layers develop linearly from the upstream to the downstream edge of the cavity at a steady growth rate, without noticeably, high amplitude oscillations. In contrast, the separated shear layers in Figure 6.7 (a,b) that corresponds to the presence of lock-on flow state, were represented by a wedge-like structure, which indicates the presence of high amplitude oscillation in the shear layer. Another noticeable feature in the patterns of out-of-plane vorticity in Figure 6.7 (a,b) is the pitchfork shape of the separated shear layers. The development of the inner part of this pitchfork is due to the

presence of number of small-scale vortical structures within the shear layer, which is also evident from the patterns of instantaneous out-of-plane vorticity in Figure 6.1.

A further comparison between cases of symmetric and upstream chamfer variation was performed from the streamwise variation of vorticity thickness, shown in Figure 6.8, where the data plotted correspond to shallow chamfers (α = 15°) and three values of the chamfer length L_C = 1.27 mm, 3.81 mm and 10.16 mm. It should be noted that while the upstream and the symmetric chamfer arrangements were similar in terms of the acoustic response of the pipeline-cavity system (Oshkai and Barannyk, 2013), the associated growth of the shear layers was substantially different.

The distribution of the normalized vorticity thickness δ_ω/L was analyzed for three types of chamfer length (a) L_C = 1.27 mm, (b) L_C = 3.81 mm, and (c) L_C = 10.16 mm for both symmetric and upstream chamfers. In the case of the short chamfers (L_C = 1.27 mm), the growth rate of the vorticity thickness was equal to $d\delta_\omega/dx$ = 0.35 and $d\delta_\omega/dx$ = 0.26 for the upstream and the symmetric chamfers, respectively.

This result indicates that the large-scale vortical structures develop more rapidly in the case of the upstream chamfers. Moreover, the maximum values of the vorticity thickness occurred at x/L = 0.59 and x/L = 0.78 for the upstream and the symmetric chamfers, respectively. This observation supports the hypothesis that introduction of the downstream chamfers changes the effective cavity length by postponing the interaction of the large-scale vortical structures with the downstream corner, thus altering the feedback mechanism of the self-sustained shear layer oscillations.

In the case of the intermediate chamfer length (L_C = 3.81 mm), the growth rate of the vorticity thickness was equal to $d\delta_\omega/dx$ = 0.48 and $d\delta_\omega/dx$ = 0.46 with maximum values of the

vorticity thickness occurred at x/L = 0.45 and x/L = 0.37 for the upstream and the symmetric chamfers, respectively.

In the case of the long chamfers (L_C = 10.16 mm), the resonant shear layer oscillations were effectively eliminated by both the upstream and the symmetric chamfers, and the corresponding growth rate was equal to $d\delta_\omega/dx$ = 0.09 and $d\delta_\omega/dx$ = 0.084 for the upstream and the symmetric chamfers, respectively. As will be shown in the following Section, the local increase in the growth rate of vorticity thickness as a function of the downstream distance at x/L = 0.38 for the case of L_C = 0, x/L = 0.5 for the case of L_C = 1.27 mm and x/L = 0.2 for the case of L_C = 3.81 mm correspond to the location where discrete large-scale vortices initially form in the separated shear layers. It follows that introduction of chamfers to the upstream and downstream corners of the cavity not only effectively shifted the locked-on flow states, as it was shown in Chapter 4, but also effectively influenced the process at which the large scale vortical structure was detached from the separated shear layer by shifting the separation point closer to the upstream edge of the cavity by approximately $\Delta x/L$ = 0.38.

The difference in the growth rate of the vorticity thickness between the cases with symmetric chamfers (lower) and those with only upstream chamfers (higher), as it can be seen in Figure 6.8, supports the results discussed in Chapter 4. At the downstream cavity edge the transverse velocity of the shear layer is typically larger then that at the upstream edge. As such, any change at the downstream edge of the cavity directly influences the behavior of the large scale vortices at that location. In fact, the introduction of the chamfer at the downstream edge disturbs and consequently weakens the feedback mechanism, one of the main components of which is the interaction of the perturbed velocity field with the impingement edge.

6.2.2.2 Velocity correlation

In Figure 6.9 through Figure 6.11 one can see the time-averaged distribution of velocity fluctuations and their correlation, presented in terms of u_{rms}/U and v_{rms}/U and contours of Reynolds stress $<u'v'>/U^2$ respectively. As in the case of time-averaged patterns of vorticity, due to the qualitative similarity between the flow patterns in the case of symmetric and upstream chamfers, only the case for symmetric chamfers will be illustrated in this Section. The images of flow patterns that correspond to the upstream chamfer were moved to APPENDIX A:. The peak values for all cases were summarized in the Table 6.2.

Comparison of streamwise velocity fluctuations u_{rms}/U between the three cases is illustrated in Figure 6.9. It can be seen that case (a) L_C = 1.27 mm and case (b) L_C = 3.81 mm differ drastically from the case (c) L_C = 10.16 in terms of locations of peak values of u_{rms}/U and the size of the area they occupy. Specifically, the peak values of u_{rms}/U occur downstream of the leading edge of the cavity in the separated shear layer with the maximum attained at X = 6.9 mm, 4.2 mm, for the cases (a), (b), and at X = 10.6 mm, at the downstream edge of the cavity, for the case (c), respectively. Out of three cases illustrated here for symmetric chamfers and analogous cases for upstream chamfers, it can be deduced that peak values of u_{rms}/U in case (b) L_C = 3.81 mm extended over substantially larger domain, compared to the case (a) L_C = 1.27 mm. In addition to that, the location of peak values of streamwise velocity fluctuation in the cases (a), (b) is associated with the region of initial roll-up and subsequent growth and detachment of large scale vortical structures. In the case of (c) L_C = 10.16 mm, as it can be observed in Figure 6.9 (c), the peak values of u_{rms}/U were located way downstream and were mainly due to the interaction of shear layer with the downstream edge of the cavity.

Table 6.2: Peak values of root-mean-square of the streamwise (u_{rms}/U) and transverse (v_{rms}/U) velocity fluctuations and velocity correlation $<u'v'>/U^2$ for symmetric and upstream cavity chamfers.

Symmetric	u_{rms}/U	**X, mm**	v_{rms}/U	**X, mm**	**Max($<u'v'>/U^2$)**	**X, mm**	**Min($<u'v'>/U^2$)**	**X, mm**
L_C = 1.27	0.29	6.9	0.3	15.7	0.03	8.3	-0.03	10
L_C = 3.81	0.32	4.2	0.35	11	0.05	4.2	-0.05	4.5
L_C = 10.16	0.2	10.6	0.11	19.3	0.01	18.3	-0.01	19.4
Upstream	u_{rms}/U	**X, mm**	v_{rms}/U	**X, mm**	**Max($<u'v'>/U^2$)**	**X, mm**	**Min($<u'v'>/U^2$)**	**X, mm**
L_C = 1.27	0.31	7.24	0.31	15	0.03	9.6	-0.03	8.9
L_C = 3.81	0.33	4.56	0.32	11.7	0.04	6.3	-0.04	7.9
L_C = 10.16	0.22	4.2	0.11	20.4	0.01	20.7	-0.01	20.4

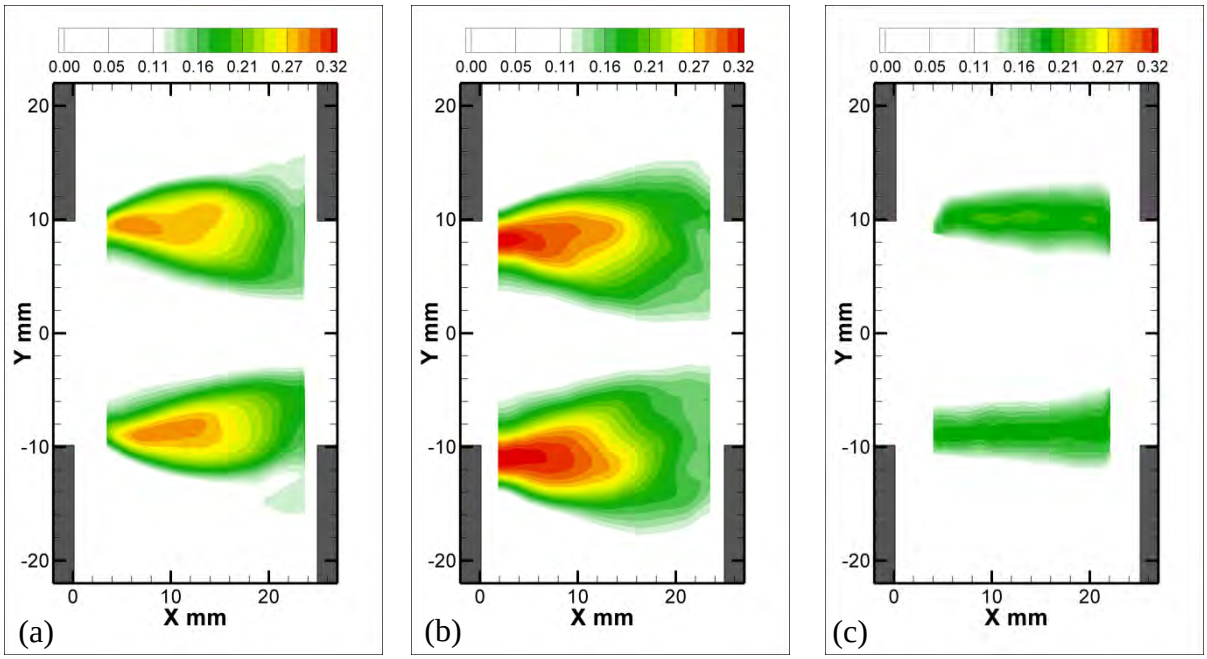

Figure 6.9: Patterns of time-averaged u_{rms}/U corresponding to the case of the symmetric chamfer with chamfer length: (a) L_C = 1.27 mm, (b) L_C = 3.81 mm, (c) L_C = 10.16 mm.

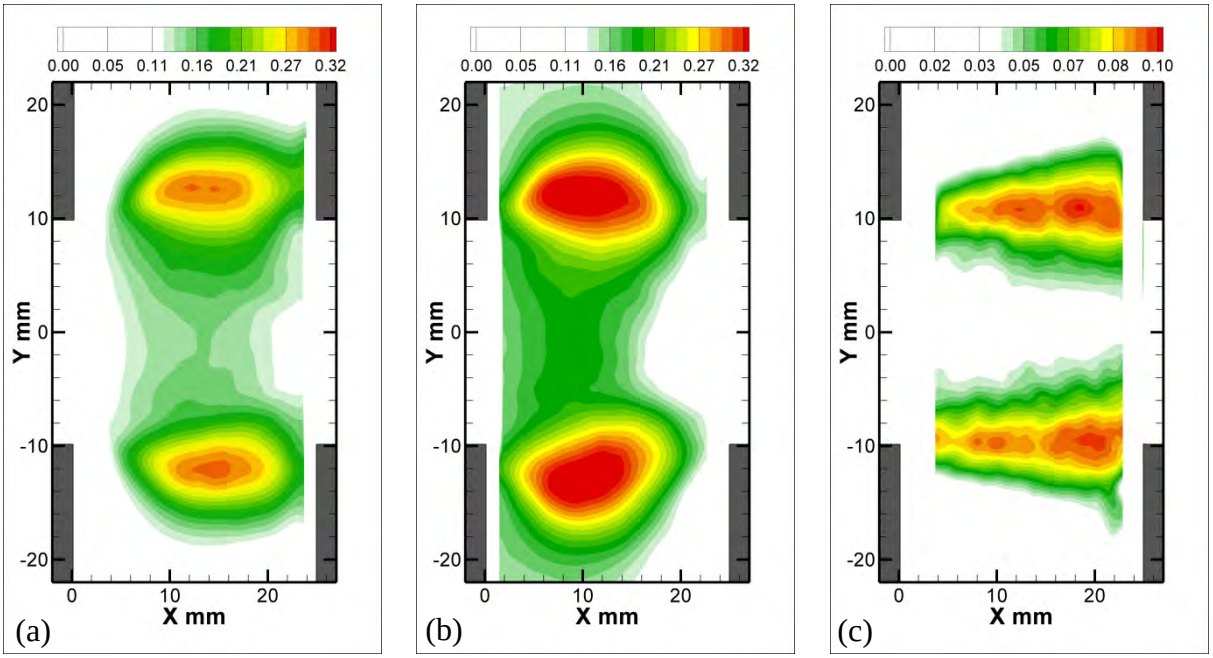

Figure 6.10: Patterns of time-averaged v_{rms}/U corresponding to the case of the symmetric chamfer with chamfer length: (a) L_C = 1.27 mm, (b) L_C = 3.81 mm, (c) L_C = 10.16 mm.

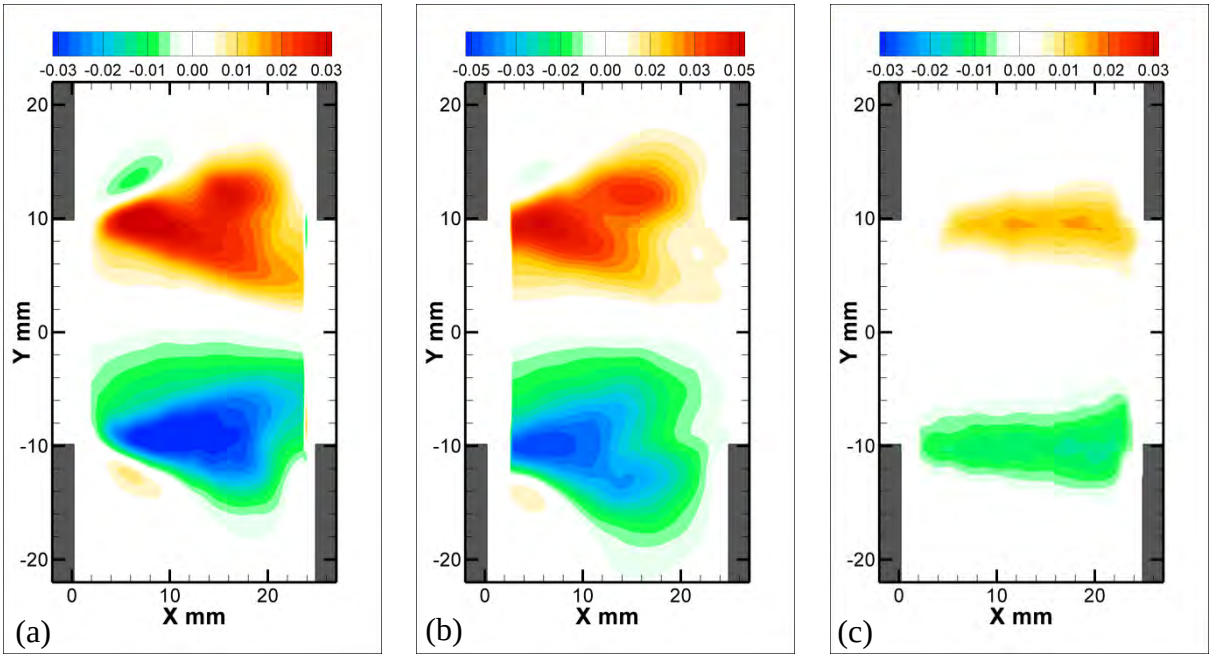

Figure 6.11: Patterns of time-averaged $<u'v'>/U^2$ corresponding to the case of the symmetric chamfer with chamfer length: (a) L_C = 1.27 mm, (b) L_C = 3.81 mm, (c) L_C = 10.16 mm.

Corresponding patterns of the transverse velocity fluctuations, v_{rms}/U are shown in Figure 6.10. One can see some degree of similarly to the patterns of u_{rms}/U. In particular, the elevated levels of v_{rms}/U that occur within shear layer, downstream of the upstream edge of the cavity in the case (b) L_C = 3.81 mm, occupy a well-defined area, which is noticeably wider compared to the case (c) L_C = 10.16 mm, although comparable to the case (a) L_C = 1.27 mm. The main difference, however, between cases (a) and (b) that correspond to the presence of a locked-on flow tone, and the case (c) without one is in the spatial distribution of the elevated levels of v_{rms}/U. It can be seen that in (a) and (b) cases, elevated levels of v_{rms}/U were concentrated around X = 15 mm, 10 mm respectively which suggest the presence of isolated acoustic noise structure at that location, while in case (c) the elevated levels of v_{rms}/U demonstrated a continuous growth in a streamwise direction with peak levels, as in the case of u_{rms}/U, right at the downstream edge of the cavity. These observations, combined with the ones in the case of u_{rms}/U indicate that the quite extensive domain of peak values of u_{rms}/U and v_{rms}/U suggests movement and distortion of large-scale vortical structures through this region.

Figure 6.11 illustrates time-averaged distribution of $<u'v'>/U^2$. It was found that the substantially high levels of $<u'v'>/U^2$ of opposite sign were generated in the top and bottom separated shear layer of the cavity and were concentrated around X = 15 mm, 10 mm for case (a) and (b) respectively, and were extended over the cavity length with maximum value attained at approximately X = 20 mm for case (c). Combining these observations with the similar ones for u_{rms}/U and v_{rms}/U allow concluding that the region of elevated peaks of velocity fluctuations and their correlation is associated with severe and rapid flow distortion and highlight the presence of self-sustained oscillations due to lock-on flow tones.

For all three types of velocity correlations discussed above, their respective peak values depended on value of L_C and attained their respective global maximums for L_C = 3.81 mm, similarly to the results of Chapter 4, where the global maximum in the amplitude of unsteady pressure oscillations was achieved for the case of L_C = 3.81 mm, which allowed to make the following conclusion. The introduction of chamfers to cavity edges effectively shifted the lock-on flow states, beyond the operation range of the system to higher velocities. As a side effect, in the intermediate case of L_C = 3.81 mm, the introduced chamfers led to noticeably higher values in the amplitude of unsteady pressure oscillations, accompanied by a substantial increase in the vorticity growth rate.

6.3 PHASE-AVERAGED FLOW PATTERNS

Figure 6.12 and Figure 6.13 illustrate phase averaged patterns of out-of-plane vorticity $\langle \omega_z \rangle$, which were used to analyze the flow physics observed in three case: (a) L_C = 0 mm, (b) L_C = 1.27 mm, (c) L_C = 3.81 mm. In Figure 6.12, the first and second rows correspond to the value of phase (φ) of 36° and 180°, respectively. Accordingly, in Figure 6.13, the first and second rows correspond to the value of phase (φ) of 252° and 324°. In the present study, φ = 0° corresponded to the instant when the acoustic pressure changed sign from negative to positive. The images of flow patterns that correspond to the rest of the phases were moved to APPENDIX B:. In each case, the corresponding flow patterns were ensemble-averaged from up to 100 PIV images, corresponding to the same phase of the acoustic pressure oscillating cycle.

The patterns of phase-averaged out-of-plane vorticity illustrate a number of important features. Specifically, in all three cases shown in Figure 6.12 and Figure 6.13, the magnitude of the out-of-plane vorticity and the cross-stream location of the shear layer fluctuate significantly in the region between upstream and downstream edges of the cavity. In the early phase, one can see the initial deflection of the lower shear layer, at the beginning of new vortex formation. This deflection of the shear layer is due to the dominance of transverse component of acoustic velocity, directed downwards, compared to its streamwise component. At the upper part of the cavity, a fully developed shear layer is evident with a fully formed, large vortical structure close to the downstream edge of the cavity.

Combining the results from phase-averaged patterns of out-of-plane vorticity with those of vorticity growth rate, illustrated in Figure 6.3 and Figure 6.8, one can make the following observations. In the case of L_C = 0 mm, in the interval $x/L \in [0.05, 0.37]$ the patterns of out-of-plane vorticity show little variations in the vorticity magnitude and no significant movement of the shear layer in the cross-stream direction due to the presence of relatively small-scale structures involved in separation from the upstream edge of the cavity. However, at x/L = 0.38 one can observe a rapid transformation of previously formed small-scale vortical structures into large scale vortex, accompanied by the local increase in the growth rate of vorticity thickness as a function of the downstream distance. Further downstream (x/L > 0.55), as it can be observed in Figure 6.3, Figure 6.12 and Figure 6.13, the vorticity agglomerated into a large-scale vortical structure, which eventually gets carried away into the pipeline by the flow. Similar observation can be made for the rest of the cases. Specifically, the local increase in the growth rate of vorticity thickness as a function of the downstream distance occurred at x/L = 0.5 for the case of L_C = 1.27 mm and at x/L = 0.2 for the case of L_C = 3.81 mm corre-

spond to the location where discrete large-scale vortices initially form in the separated shear layers.

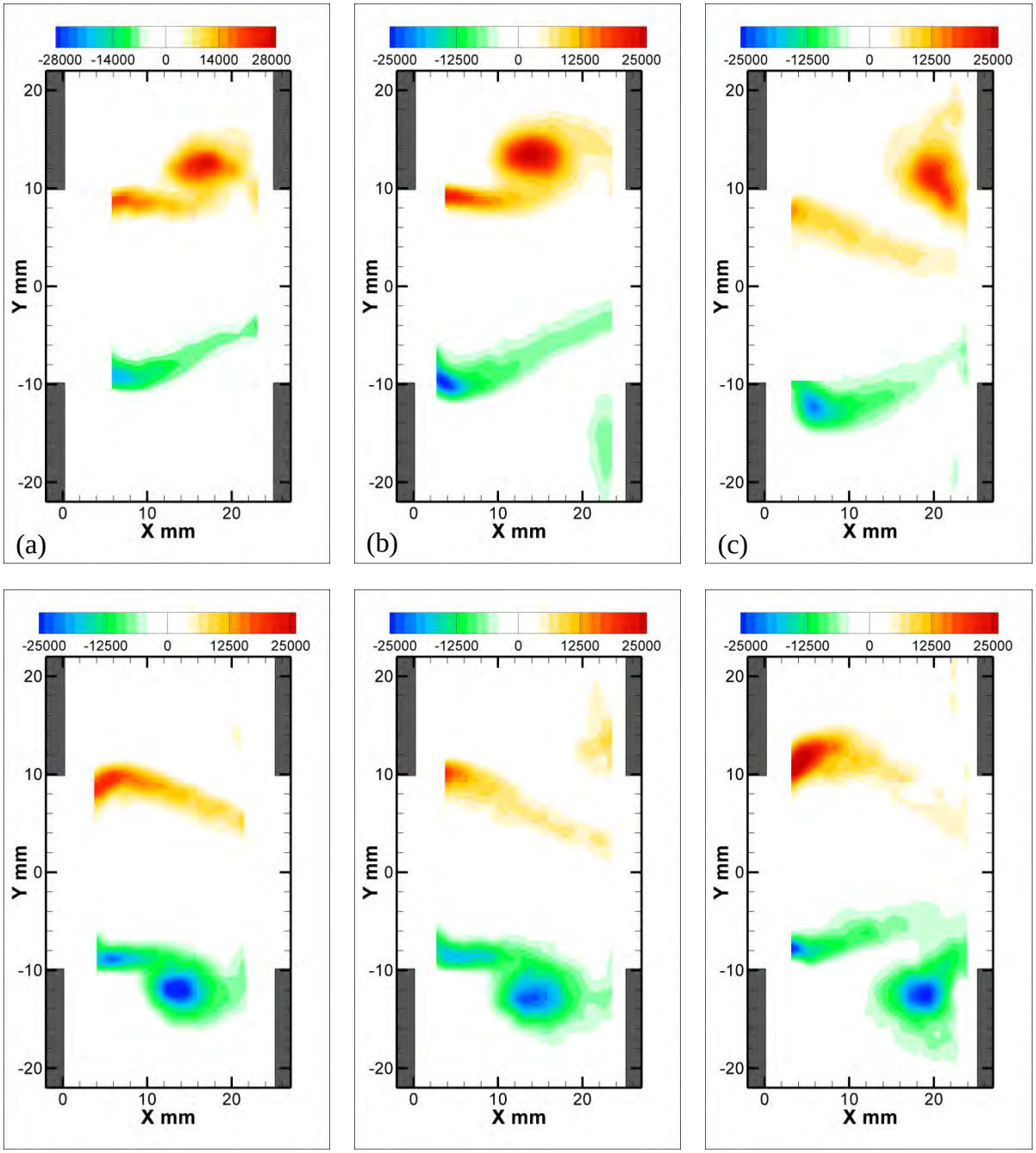

Figure 6.12: Patterns of phase-averaged out-of-plane vorticity (s^{-1}) corresponding to the (a) L_C = 0 (St = 0.37, U = 67m/s), (b) L_C = 1.27 mm (St = 0.36, U = 70 m/s), and (c) L_C = 3.81 mm (St = 0.29, U = 87 m/s) at φ = 36° and 180°.

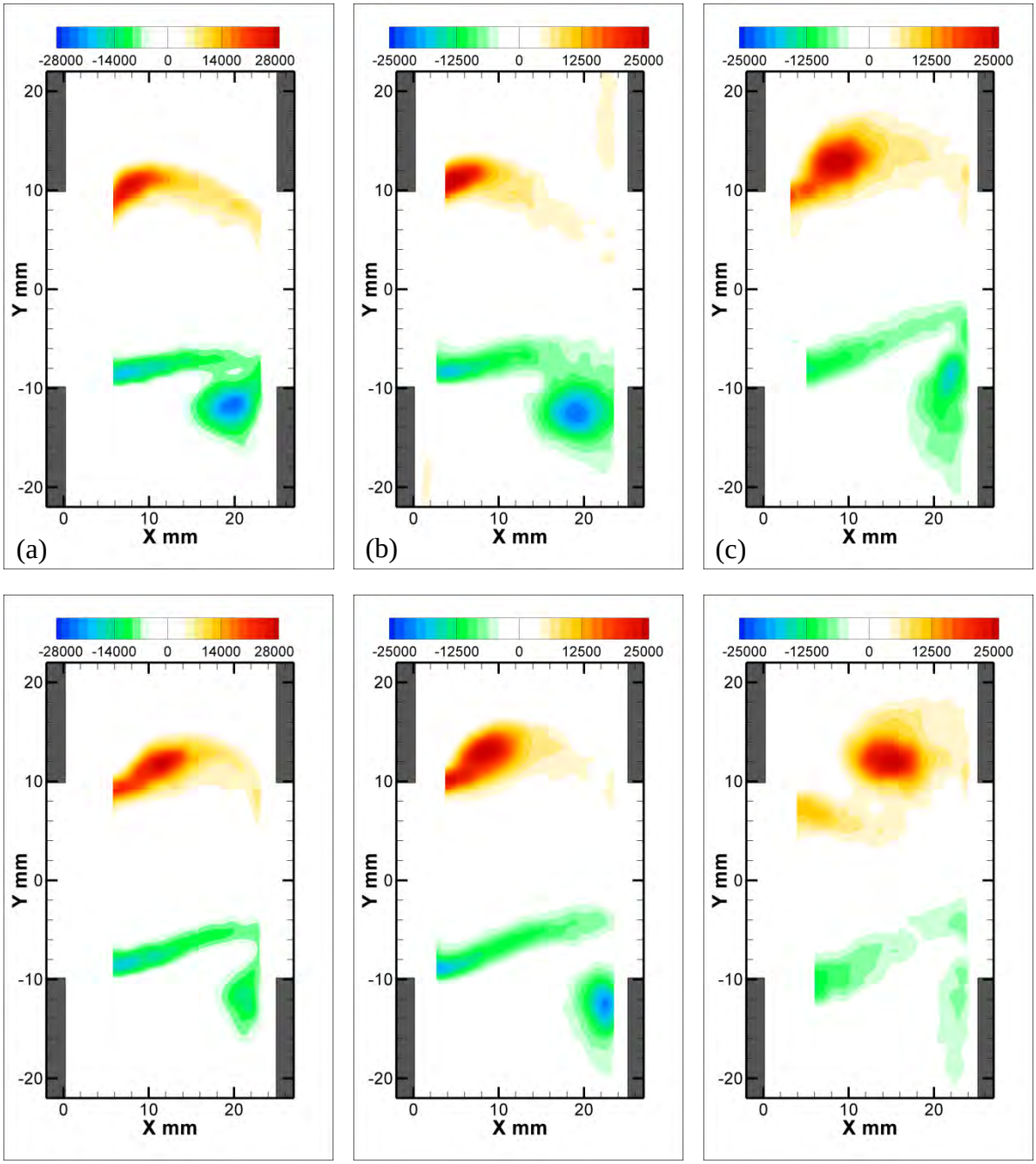

Figure 6.13: Patterns of phase-averaged out-of-plane vorticity (s^{-1}) corresponding to the symmetric cases (a) L_C = 0 (St = 0.37, U = 67m/s), (b) L_C = 1.27 mm (St = 0.36, U = 70 m/s), and (c) L_C = 3.81 mm (St = 0.29, U = 87 m/s) at φ = 252° and 324°.

The patterns of phase-averaged out-of-plane vorticity, shown in Figure 6.12 and Figure 6.13 allow one to compare the experimental results with those that can be obtained by the help of several theoretical models. The currently available models of the vorticity field can be categorized into two distinctive groups. In the first group, referred to as a vortex sheet model, it is assumed that the flow is represented by a perturbed vortex sheet (Chatellier et al., 2004, Elder, 1978, Howe, 1981). In these models, the cross-stream distribution of the vorticity is neglected and the shear flow is represented by an infinitely thin vortex sheet. The location of the vortex sheet in the cross-stream direction is assumed to be periodic in time with the shape of the sheet being governed by the set of eigenfunctions. The advantage of this model is that it provides an analytical formulation that can be solved in order to determine the natural instability characteristics of the shear layer.

In the second group, which is categorized as a discrete vortex model, the vorticity at the vicinity of the upstream entrance to the cavity is rolled up into a single vortex core, which convects over the cavity (Bruggeman et al., 1989, Kook and Mongeau, 2002, Mast and Pierce, 1995, Nelson et al., 1983). The main advantage of this model is that it is easy to implement and it allows one to include the effect of unsteady forcing, such as hydrodynamic forcing considered by (Kook and Mongeau, 2002) as a result of a discrete vortex convected over the cavity in a given period of the oscillation.

The flow patterns of Figure 6.12 and Figure 6.13 suggest that the two types of models can be combined to achieve improved analytical representation of the phenomenon of flow-acoustic coupling. In particular, in the vicinity of the upstream corner of the cavity, the shear layer oscillations can be effectively approximated by an oscillating thin sheet of vorticity,

while farther downstream, the shear layer can be represented by discrete vortical structures, which convect across the cavity opening and eventually impinge on the downstream corner.

6.4 HYDRODYNAMIC CONTRIBUTIONS TO ACOUSTIC POWER INTEGRAL

The very nature of the free shear layer formed along the mouth of the cavity is that it can be excited over a large range of resonant modes, which are naturally present in the cavity, as shown in Chapter 4. Coupling of the shear layer oscillations with the acoustic cavity modes, during which the frequency of the resonant mode of the cavity corresponds to the frequency of excitation of the separated shear layer, often results in generation of flow tones. Because of the inherent instability of the free shear layer, small disturbances at the upstream edge of the cavity result in the formation of large-scale vortices in the shear layer over the cavity. Each vortex will convect downstream until it impinges on the downstream edge of the cavity where it causes a pressure perturbation. This pressure perturbation will then be acoustically transmitted back to the upstream edge where it can initiate the formation of another vortex.

The process described above will eventually reach its steady state, at which point it can be described according to the concept of Howe's acoustic power integral (Howe, 1975, Howe, 1980):

$$P = -\rho_0 \iiint_V (\boldsymbol{\omega} \times \boldsymbol{V}) \cdot \boldsymbol{u}_{ac} dV \,, \tag{6.2}$$

where ρ_0 is the fluid density, $\boldsymbol{V}$ is the fluid velocity and $\boldsymbol{u}_{ac}$ is the acoustic particle velocity. The integral in Equation (6.2) models the excitation mechanism of acoustically-coupled flow,

in which vorticity, as a source of sound, is related to the generation of acoustic power. The essential components of the integral in Equation (6.2) are the vorticity, naturally present in the vortical structures, velocity fluctuations of the hydrodynamic field, and velocity fluctuations of the acoustic field. As such, the acoustic power is efficiently generated only when there is a proper relationship between the vortical structure at the downstream edge of the cavity, and the phase and direction of the acoustic particle velocity in that region (Howe, 1980, Oshkai et al., 2005, Yang et al., 2009).

In order to establish the proper relationship between flow patterns and acoustic power integral, one can decompose the integrant of Equation (6.2) along the streamwise and transverse direction of the flow as follows (Geveci et al., 2003),

$$\left\{\left[\left\langle\boldsymbol{\omega}\right\rangle_p\times\left\langle\boldsymbol{V}\right\rangle_p\right]_x\boldsymbol{i}+\left[\left\langle\boldsymbol{\omega}\right\rangle_p\times\left\langle\boldsymbol{V}\right\rangle_p\right]_y\boldsymbol{j}\right\}\cdot\left\{\left[\boldsymbol{u}_a\right]_x\boldsymbol{i}+\left[\boldsymbol{u}_a\right]_y\boldsymbol{j}\right\}, \tag{6.3}$$

where $\boldsymbol{i}$ and $\boldsymbol{j}$ are the unit vectors in the streamwise and transverse directions, respectively. In order to determine the hydrodynamic contributions to the acoustic power integral the vector field defined by $\boldsymbol{\omega}\times\boldsymbol{V}$ along with its components in the streamwise and transverse directions $\left[\left\langle\boldsymbol{\omega}\right\rangle_p\times\left\langle\boldsymbol{V}\right\rangle_p\right]_x$, $\left[\left\langle\boldsymbol{\omega}\right\rangle_p\times\left\langle\boldsymbol{V}\right\rangle_p\right]_y$, respectively, will be considered.

Due to the qualitative similarity between patterns of phase-averaged vorticity, investigated in Section 6.3, only the case of $L_C = 0$ will be discussed here.

In Figure 6.14, one can see the evolution of the flow patterns of phase-averaged hydrodynamic contribution to the acoustic power along with transverse and streamwise projections of the magnitude of the hydrodynamic contribution to the acoustic power integral at φ = 36° and 180°.

It can be seen in Figure 6.14 (a) that the component of the vector field $\boldsymbol{\omega}\times\boldsymbol{V}$ that is transverse to the mean flow is dominant, and it reaches its maximum close to the downstream edge of the cavity, at around X = 17 mm. The streamwise location of the aggregations of large, transversely oriented vectors corresponds to the two major regions within the cavity: (1) the region associated with the presence of relatively small-scale vortical structures involved in separation from the upstream edge of the cavity, and (2) the region where the large-scale vortical structures being present, as can be seen in Figure 6.12 (a). From the patterns of transverse projections of the hydrodynamic contribution to the acoustic power integral, which are illustrated in Figure 6.14 (b), one can see that similar to the vectors in Figure 6.14 (a), the concentration of elevated peaks of vorticity can be associated with the elevated levels of transverse projections of the hydrodynamic contribution to the acoustic power integral. In addition, values of transverse projections of the hydrodynamic contribution to the acoustic power integral preserve the sign within their shear layer. Finally, the patterns of phase-averaged streamwise projections of the hydrodynamic contribution to the acoustic power integral are shown in Figure 6.14 (c). One can see that a large concentration of elevated levels of $\left[\langle\boldsymbol{\omega}\rangle_p\times\langle\boldsymbol{V}\rangle_p\right]_x$, which contrary to the values of $\left[\langle\boldsymbol{\omega}\rangle_p\times\langle\boldsymbol{V}\rangle_p\right]_y$ can have alternating signs within their shear layer, is located at the downstream edge of the cavity. At the same time, as in the previous cases patterns of $\left[\langle\boldsymbol{\omega}\rangle_p\times\langle\boldsymbol{V}\rangle_p\right]_x$ can be also observed at the upstream edge of the cavity, although at noticeably low level. As such, the location of the elevated levels of phase-averaged $\left[\langle\boldsymbol{\omega}\rangle_p\times\langle\boldsymbol{V}\rangle_p\right]_x$ can be associated with the large-scale vortical structures. The overall evolution of the maximum positive and negative values in the phase-averaged patterns at φ = 252° and 324° are generally similar.

In order to determine the overall effect from transverse and streamwise hydrodynamic contributions to the generation of acoustic power, governed by Equation (6.2), one would need to analyze the complete integrand $(\boldsymbol{\omega}\times\boldsymbol{V})\cdot\boldsymbol{u}_{ac}$, which determines the effectiveness of the acoustic power generation (Geveci et al., 2003) and involves streamwise and transverse components of acoustic particle velocity. However, based on current experimental observations and on the previously obtained results (Oshkai and Velikorodny, 2013, Aly and Ziada, 2012), at certain phases of the acoustic oscillating cycle, one can assume that in the vicinity of upstream and downstream edges of the cavity, the transverse component of acoustic particle velocity dominates the streamwise component. The direction of hydrodynamic contributions will be aligned with that of transverse component of acoustic particle velocity, at the upstream and downstream region of the cavity, which will lead to the significant contribution to the acoustic power integral.

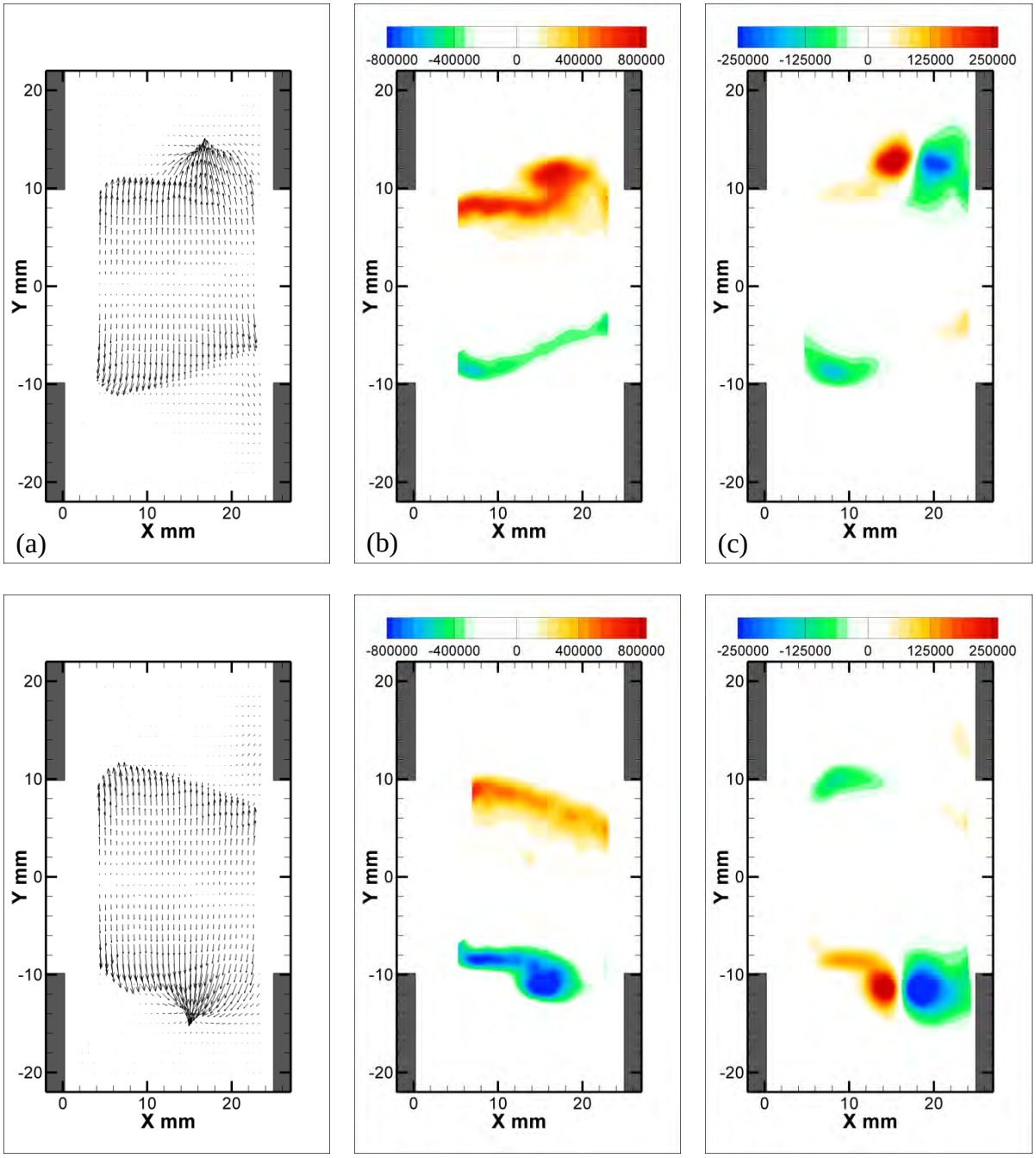

Figure 6.14: Patterns of phase-averaged (a) hydrodynamic contribution to the acoustic power (b) transverse (*Y*-direction) projections of the magnitude of the hydrodynamic contribution to the acoustic power integral, (c) streamwise (*X*-direction) projections of the magnitude of the hydrodynamic contribution to the acoustic power integral at φ = 36° and 180°.

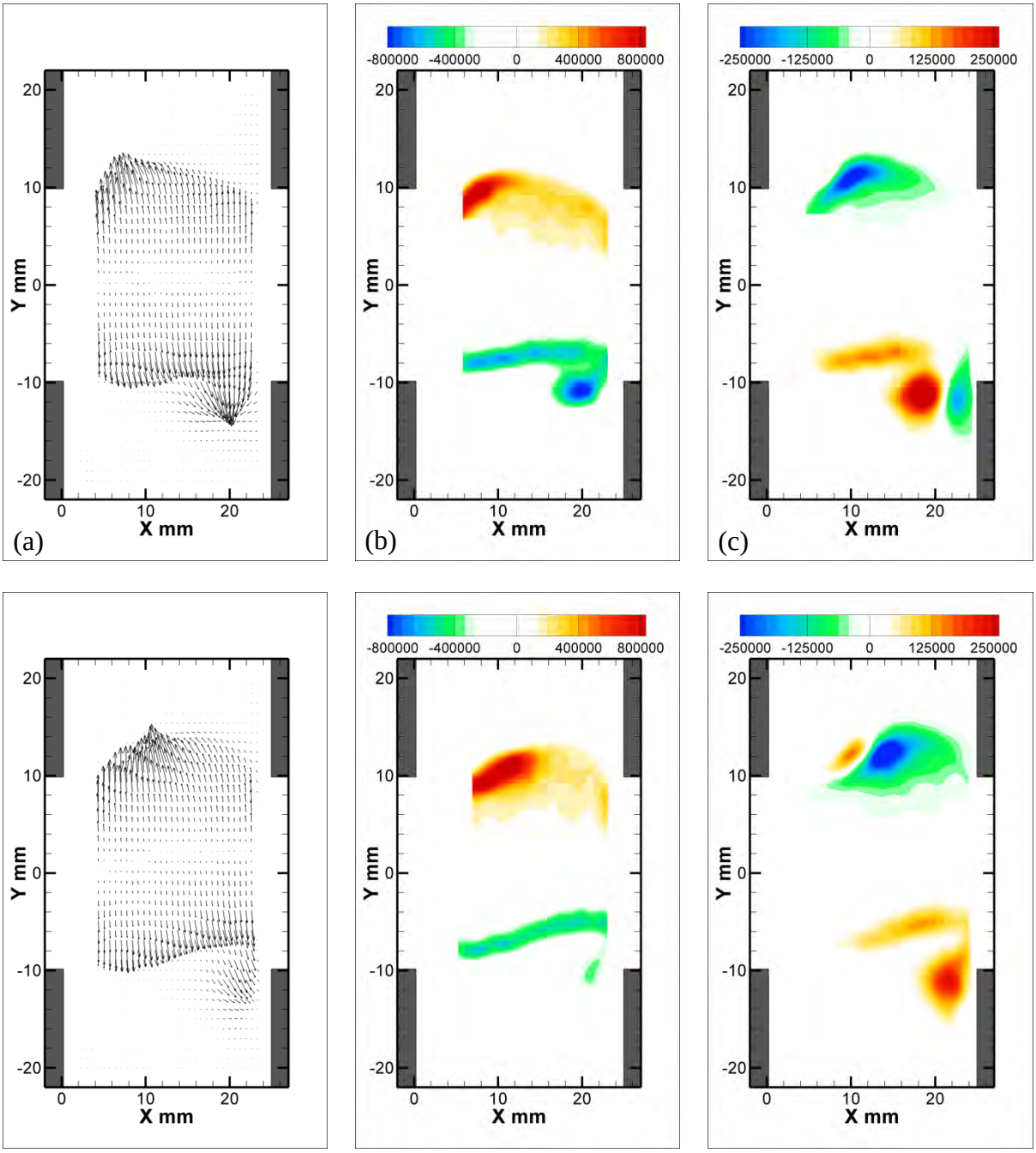

Figure 6.15: Patterns of phase-averaged (a) hydrodynamic contribution to the acoustic power (b) transverse (*Y*-direction) projections of the magnitude of the hydrodynamic contribution to the acoustic power integral, (c) streamwise (*X*-direction) projections of the magnitude of the hydrodynamic contribution to the acoustic power integral at φ = 252° and 324°.

CHAPTER 7

SHEAR LAYER INSTABILITIES IN THE CARDIOVASCULAR SYSTEM

In this Chapter, qualitative and quantitative flow visualization study was conducted for the case of a biomimetic pulsatile flow through an artificial heart valve placed into a physiologically accurate model of an aortic root with sinuses of Valsalva. Phase-averaged velocity measurements as well as the associated turbulent statistics were analyzed in tandem to investigate the evolution and the structure of the shear layers formed at the edges of the leaflets of a prototype trileaflet polymeric valve. During evaluation of the experimental data, it was found that elevated levels of turbulent shear stresses and potential for thrombus formation due to activated platelets were only observed at the peak systole (acceleration) phase of the cardiac cycle when $t/T = 0.13$. As such, in this Chapter, only this phase of the cardiac cycle will be investigated in detail. The peak values of respective flow quantities as well as visual representation of the rest of the phases of the cardiac cycle were moved to APPENDIX C: and APPENDIX D:.

7.1 FLOW CHARACTERISTICS DOWNSTREAM OF THE VALVE

During the systole phase of the cardiac cycle, the typical nature of the flow through the polymeric valve was characterized by the presence of the central orifice jet due to the opening of valve leaflets. The nominal diameter of the jet was approximately 14 mm, meas-

ured across the edges of the leaflets of the valve. The maximum forward velocity, which is shown in Figure 7.1, of the central orifice jet was greater than 2 m/s, and the overall velocity profile gradually changed from flat top at the leading edge of the valve leaflets to a parabolic velocity profile between 40 mm and 50 mm downstream from the valve, depending on the case and the viewing plane, as it can be seen in Figure 7.1.

As expected, due to different expansion ratios of each of the geometries, summarized in , the maximum forward velocity was higher for the case of geometry resulted from severe valve insufficiency. The geometry caused by valve stenosis was characterized by slightly lower maximum forward velocities. Finally, the lowest value of the maximum forward velocity was found in the case of the normal geometry. During the acceleration phase, formation of the central orifice jet was accompanied by the creation of a vortex ring inside of the aortic sinuses region. The creation of the vortex ring resulted from flow separation occurring at the edge of the orifice formed by the leaflets of the opened valve.

In the case of the severe stenosis geometry, the vortex ring was not substantially confined by the aortic walls. The propagation of central orifice jet in the case of the normal geometry was accompanied by minor vortex stretching at the point where the aortic sinuses transitioned to the straight part of the aortic root.

Table 7.1: Peak values of velocity at t/T = 0.13 and location of reattachment points in three experimental cases.

	Plane 1		Plane 2	
	V_{max} (m/s)	Reattachment point (X,Y) mm	V_{max} (m/s)	Reattachment point (Z,Y) mm
Normal	2.37	(-14,40)	2.45	(-16,32) (14,44)
Severe Stenosis	2.51	(-16,64)	2.5	(-16,56)
Severe Insufficiency	2.64	(-14,34) (14,52)	2.53	(-14,28) (14,38)

The vortex stretching was identified based on Kelvin's theorem and by looking at the change in the cross-sectional area of the vortex ring at a particular location. In the essence, any shrinking of the cross-sectional area must be accompanied by a longitudinal stretching. Finally, in the case of the severe insufficiency geometry, the flow was substantially confined, which resulted in strong interaction between the vortex ring and the aortic walls in and immediately downstream of the sinuses.

The propagation of the central orifice jet was also accompanied by formation of recirculation zones between shear layers and the walls of the aortic root. Flow reattachment points were strongly influenced by the aortic root geometry. The mean positions of primary reattachment L_1 and L_2 (defined in Figure 7.1 (a)) on both aortic root side walls were evaluated at the locations where the mean streamwise velocity component changes sign. The reattachment was determined by extrapolating the PIV data up to the wall. The locations of the reattachment points at $t/T = 0.13$ are presented in Table 7.1. Out of three test cases, the reattachment points closest to the base of the valve were observed for geometry associated severe insufficiency. On the other hand, the severe stenosis geometry resulted in the location of the reattachment points farthest from the valve among all three cases. The difference in Y coordinates of the reattachment points, observed for each of three cases, was due to the asymmetry of the jet, caused by the aortic root geometry, and in particular, by the differences in the depth and the width of the aortic sinuses. Out of three test cases, the reattachment points closest to the base of the valve were observed for geometry associated severe insufficiency. On the other hand, the severe stenosis geometry resulted in the location of the reattachment points farthest from the valve among all three cases.

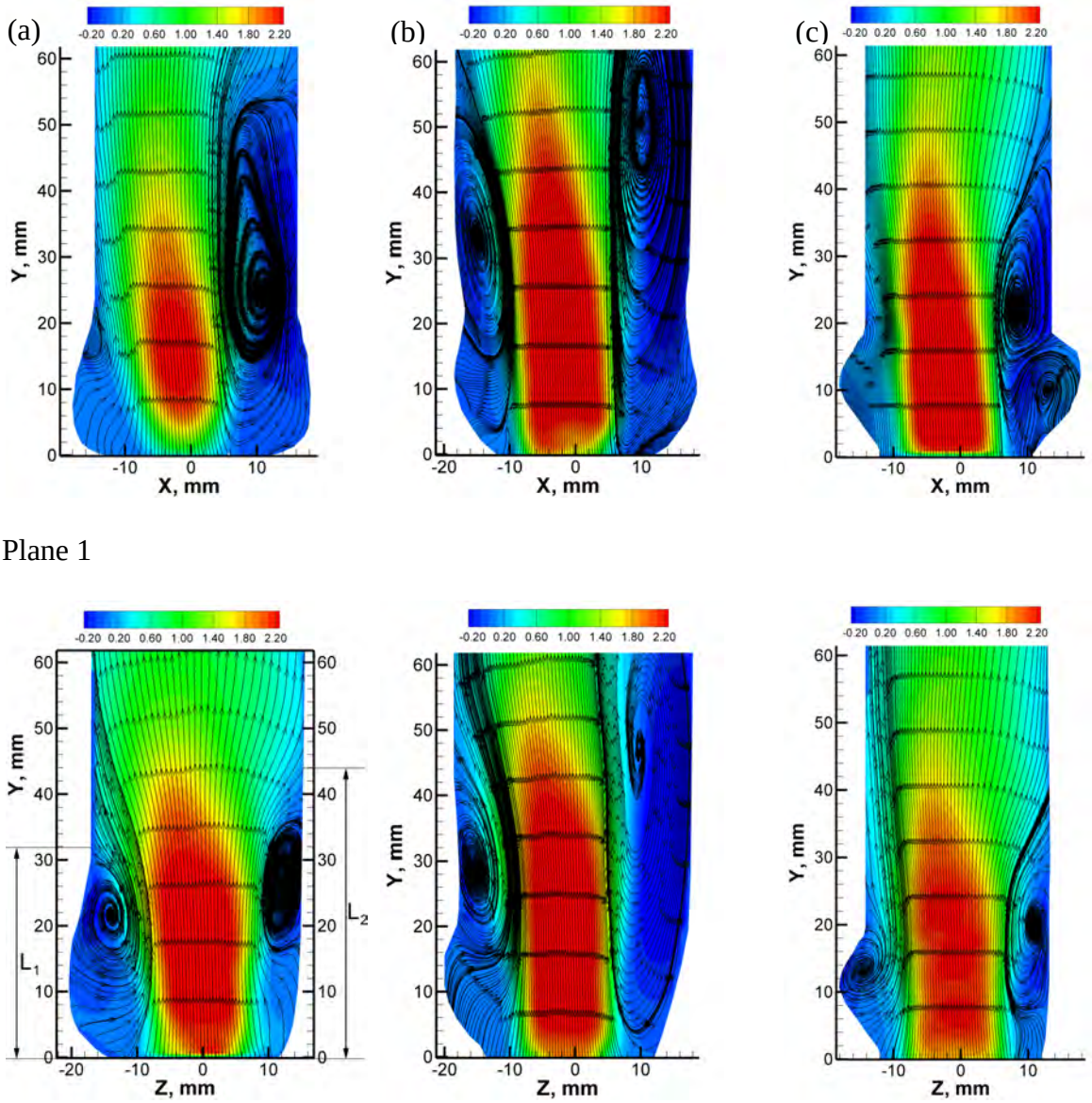

Figure 7.1: Streamline patterns and contours of velocity magnitude (V_{avg}, m/s) at t/T = 0.13. (a) Normal geometry, (b) Severe stenosis, (c) Severe insufficiency.

The difference in *Y* coordinates of the reattachment points, observed for each of three cases, was due to the asymmetry of the jet, caused by the aortic root geometry, and in particular, by the differences in the depth and the width of the aortic sinuses. In each case, flow recirculation zones were observed. The largest recirculation zone was produced by the severe

stenosis geometry, while the smallest recirculation zone was present in the severe insufficiency geometry, as shown in Figure 7.1.

7.2 TURBULENT CHARACTERISTICS OF THE FLOW

In this section, turbulent characteristics of the flow are summarized. The patterns of Reynolds shear stress (RSS), defined in Section 2.2.8, are shown in Figure 7.2, and the peak values of RSS, as well as the axial and the transverse turbulence intensities u_{rms} and v_{rms}, measured in Plane 1, are presented in Table 7.2. While evaluating the peak values from two planes is not sufficient in order to accurately describe the 3D flow-structure interaction, it is, however, believed that variation of RSS, u_{rms} and v_{rms} values in two orthogonal planes and the respective location of those planes allows one to follow a general trend throughout the particular phase of the cardiac cycle.

7.2.1 Normal geometry

When the aortic root is not affected by a valve disease, which corresponds to the normal geometry case, the following observations were made throughout the selected phases of the cardiac cycle.

After the valve opened at t/T = 0.01(not shown here), the central orifice jet emerged from the opening created by the valve leaflets. At this time, shear layers were formed at the trailing edge of the valve leaflets. Consequently, detectable levels of the RSS appeared in these high-shear regions.

As the jet developed through the systole phase, its direction of propagation was influenced by the asymmetry of the aortic root and by the dynamics of the leaflets during valve opening.

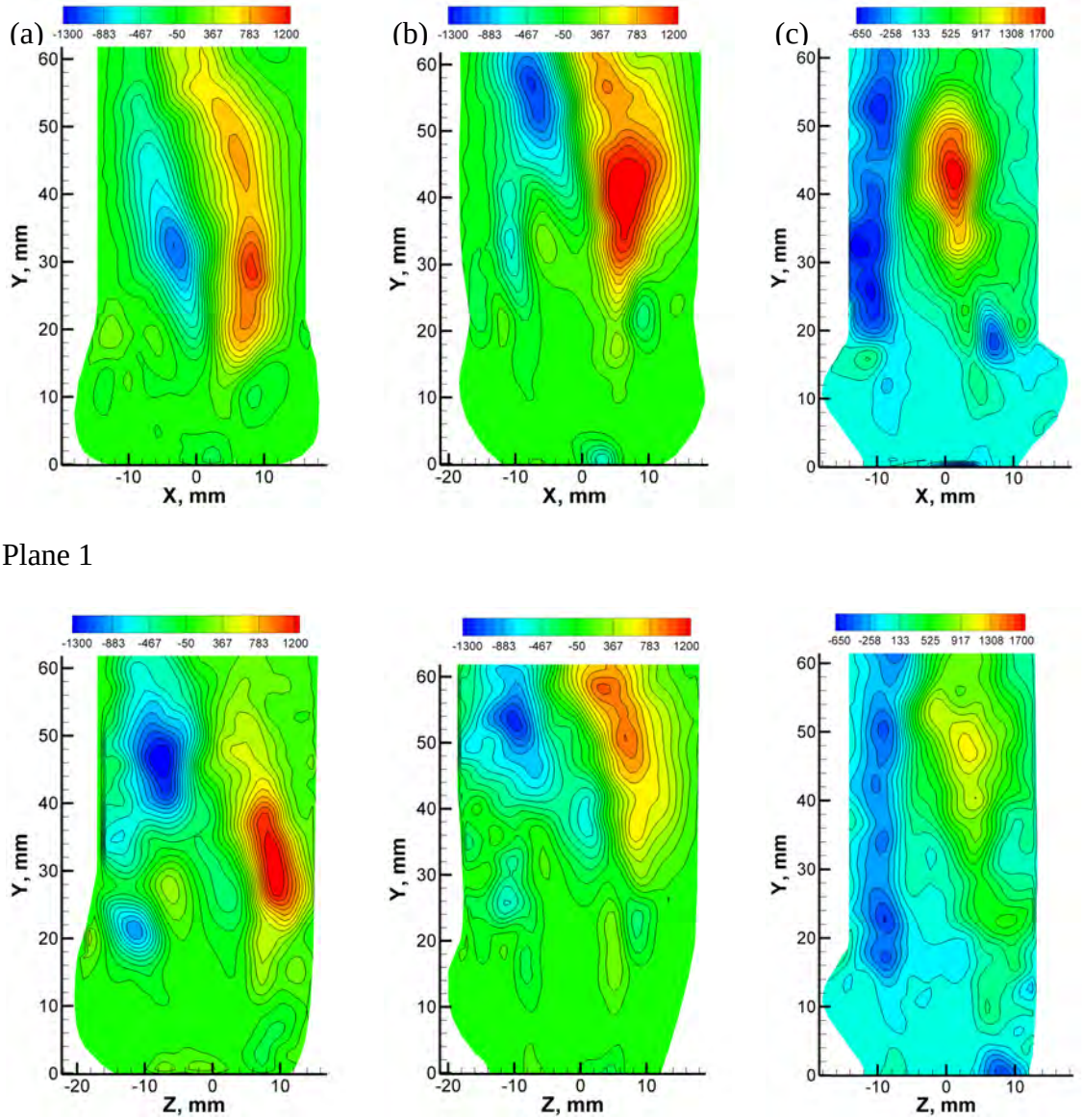

Figure 7.2: Contours of RSS (dyne/cm^2) at t/T = 0.13; (a) Normal geometry, (b) Severe stenosis, (c) Severe insufficiency.

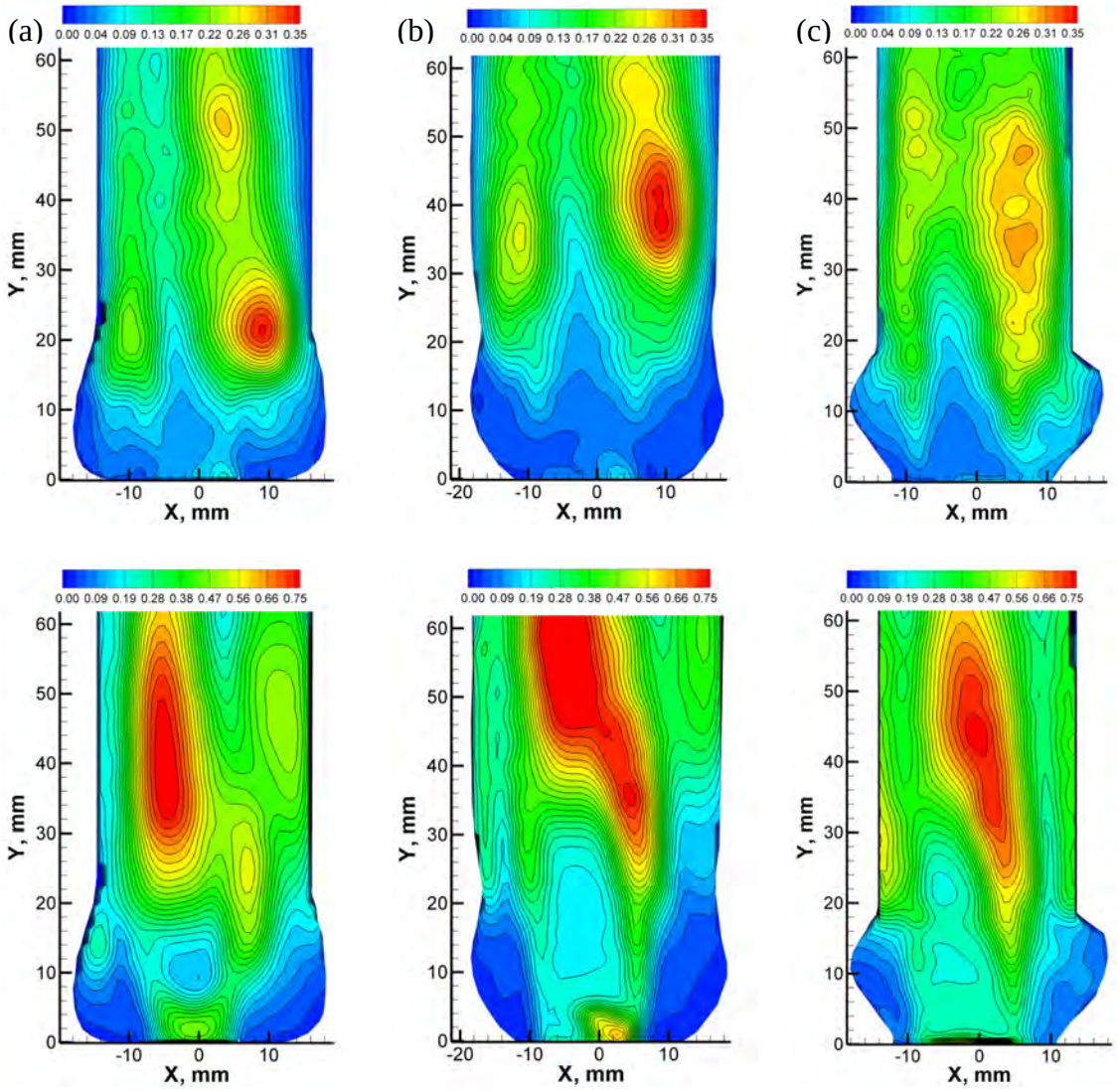

Figure 7.3: Contours of u_{rms} (top column) and v_{rms} (bottom column) in Plane 1 at t/T = 0.13; (a) Normal geometry, (b) Severe stenosis, (c) Severe insufficiency.

As the result, as it can be seen in Figure 7.1, the jet was forced towards left wall (in Plane 1) of the aortic root geometry. The consequence of this change of direction is the appearance of a high-shear region. At t/T = 0.05, the largest peak of the RSS in this zone were observed to be -873 dyne/cm^2 at X = -5.8 mm, Y = 16.2 mm (Figure 7.2).

At the peak systole phase, t/T = 0.13, large recirculation zone developed at the right wall, when looking at Plane 1, which is shown in Figure 7.1. As the center of this recirculation zone interacted with periphery of the jet, the region of high shear appeared at X = 8.2 mm, Y = 31.0 mm, with the peak value of the RSS equal to 1294 dyne/cm^2. At t/T = 0.22, the recirculation cell moved upstream towards the valve, with a central vortex been at X = 4.5 mm, Y = 18.2 mm. As a result, a region of elevated RSS developed, with a peak value of 520 dyne/cm^2. During the diastole phase magnitude of RSS diminished to 11 dyne/cm^2.

7.2.2 Severe aortic valve stenosis

As the flow gradually progressed through the acceleration phase, two recirculation zones had developed on both sides of the central orifice jet, as seen in Figure 7.1 (b). These recirculation zones influenced the propagation of the jet and resulted in high-shear regions near the periphery of the jet.

At t/T = 0.05, the peak RSS was equal to 1047 dyne/cm^2 at X = 5.3 mm, Y = 19.4 mm (Figure 7.1 (b)). As the flow reached the peak systole phase, t/T = 0.13, the peak value of the RSS equal to 1373 dyne/cm^2 appeared at X = 6.1 mm, Y = 42 mm. At t/T = 0.22, one of the recirculation areas was pushed upstream, with a central vortex located at X = 4.2 mm, Y = 32 mm. An additional recirculation zone appeared in one of the sinus cavities. Peak value of the RSS equal to 574 dyne/cm^2 was measured at X = 1.6 mm, Y = 55 mm. After flow transitioned to the diastole phase, peak values of RSS dropped to 14 dyne/cm^2.

7.2.3 Severe aortic valve insufficiency

The beginning of the acceleration phase was accompanied by the development of two recirculation zones on both sides of the central orifice jet, and one additional recirculation cell in the sinus cavity, as can be seen in Figure 7.1. These recirculation zones resulted in high-shear regions near the periphery of the jet and at the walls of the aortic root.

At t/T = 0.05, the peak RSS was equal to -1227 dyne/cm^2 at X = -6.5 mm, Y = 17.3 mm. At the peak systole phase, t/T = 0.13, two recirculation zones induced elevated levels of RSS -638, 1718 dyne/cm^2 as indicated in Figure 7.1. The locations of the peak value of the RSS was at X = 1 mm, Y = 43.5mm. At t/T = 0.22, one of the recirculation zones moved up-stream, with a central vortex located at X = 7.2 mm, Y = 19 mm. An additional recirculation zone appeared in one of the sinus cavities. The peak value of the RSS equal to -435 dyne/cm^2 were observed at X = -8.1 mm, Y = 46.7 mm. During the diastole phase, the peak values of the RSS decreased further to -5 dyne/cm^2.

7.2.4 Turbulent intensities

Figure 7.3 shows patterns of u_{rms} and v_{rms} corresponding to the three considered ge-ometries of the aortic root at t/T = 0.13. In Table 7.2 and Table 7.3, the peak values of u_{rms} and v_{rms} are shown in selected phases along the cardiac cycle, indicated by circular symbols in Figure 2.8. The highest values of v_{rms}, concentrated at the valve leaflets, were observed during the acceleration phase, at t/T=0.05. These high values of v_{rms} can be attributed to the valve design and the resulting shear layers that exhibited fluctuations in the transverse direction.

Table 7.2: Elevated levels of u_{rms}, v_{rms} and RSS at various phases of the cardiac cycle.

Phase		Plane1		
		u_{rms} (m/s)	v_{rms} (m/s)	RSS (dyne/cm^2)
t/T = 0.05	Normal	0.20	0.73	-873, 817
	Severe Stenosis	0.24	0.88	-940, 1047
	Severe Insufficiency	0.23	0.92	-1227, 1104
t/T = 0.13	Normal	0.28	0.72	-527, 1294
	Severe Stenosis	0.34	0.87	-1115, 1373
	Severe Insufficiency	0.29	0.74	-638, 1718
t/T = 0.22	Normal	0.17	0.31	-242, 520
	Severe Stenosis	0.20	0.39	-392, 574
	Severe Insufficiency	0.15	0.33	-435, 334
t/T = 0.29	Normal	0.15	0.28	-184, 365
	Severe Stenosis	0.16	0.34	-182, 392
	Severe Insufficiency	0.13	0.28	-236, 232
t/T = 0.69	Normal	0.04	0.06	-14, 11
	Severe Stenosis	0.06	0.08	-16, 14
	Severe Insufficiency	0.04	0.05	-5, 10

Table 7.3: Elevated levels of u_{rms}, v_{rms} and RSS at various phases of the cardiac cycle.

Phase		Plane2		
		u_{rms} (m/s)	v_{rms} (m/s)	RSS (dyne/cm^2)
t/T = 0.05	Normal	0.26	0.84	-1044, 1090
	Severe Stenosis	0.30	0.88	-1053, 1008
	Severe Insufficiency	0.20	0.79	-896, 1054
t/T = 0.13	Normal	0.34	0.63	-869, 1224
	Severe Stenosis	0.40	0.75	-1154, 1029
	Severe Insufficiency	0.30	0.60	-495, 1601
t/T = 0.22	Normal	0.17	0.30	-263, 341
	Severe Stenosis	0.20	0.37	-296, 563
	Severe Insufficiency	0.15	0.27	-210, 247
t/T = 0.29	Normal	0.14	0.27	-212, 300
	Severe Stenosis	0.18	0.32	-186, 391
	Severe Insufficiency	0.12	0.27	-153, 148
t/T = 0.69	Normal	0.05	0.07	-14, 11
	Severe Stenosis	0.06	0.08	-14, 15
	Severe Insufficiency	0.04	0.05	-4, 5

After the values of v_{rms} reached its maximum, and as the central orifice jet undergoes through the systole phase, the peak values of v_{rms} stayed concentrated at the upper part of the central orifice jet, which can be seen in Figure 7.3, in the region where the jet becomes highly unstable and breakdown of the shear layers occurred.

7.3 THE EFFECT OF AORTIC ROOT GEOMETRY ON POTENTIAL THROMBUS FORMATION

One of the goals of this work was to establish how a deformation in the aortic root geometry leads to the elevated levels of the Reynolds shear stresses.

It was shown in (Lu et al., 2001, Leverett et al., 1972, Goncalves et al., 2005) that elevated levels of the RSS, caused by an artificial heart valve, can impose damage on blood elements. In particular, it was reported that the breakage of a red blood cell's membrane, called hemolysis, can occur for peak values of the RSS in the range from 400 dyne/cm^2 to 5,600 dyne/cm^2 with exposure time as low as 10 ms (Sallam and Hwang, 1984).

In addition to hemolysis, the levels of the RSS in the range between 100 to 1000 dyne/cm^2 can lead to the activation of platelets, which when activated, aggregate together and lead to formation of blood clots. The blood clot can eventually detach from the aggregation site and form a free floating blood clot, which is extremely dangerous as it is capable of blocking an artery in the brain, disrupt the blood supply and cause a stroke.

In all of the studied geometries, the elevated levels of the RSS were higher than 400 dyne/cm^2 and within the range for polymeric valves, published in (Leo et al., 2006). These abnormally high levels of the RSS were typically present in the regions of interaction of recirculation zones with the periphery of the central orifice jet.

At the peak acceleration phase, at $t/T = 0.13$, the levels of RSS were the highest in the geometry resulted from severe aortic valve insufficiency, and the lowest in the normal geometry. These results indicated that implanting a heart valve without taking into consideration changes in the aortic root geometry caused by valve diseases might result in sub-lethal and/or lethal damage to blood elements and platelet activation.

CHAPTER 8

CONCLUSIONS AND RECOMMENDATIONS

8.1 LINKS BETWEEN TWO MAIN RESEARCH FOCUSES IN THE DISSERTATION

In this dissertation, two research focuses in the general area of unsteady shear flows were investigated experimentally. The primary research focus is the pipe-cavity flows, and the associated flow-acoustic coupling. The secondary research focus is the flow through the heart valve, and the associated regions of elevated Reynolds shear stresses. The direct links between the two flows are: (i) shear layer instabilities and dynamics, which are predominant in both flows; (ii) flow-acoustic coupling phenomena that are mainly present in the first part of the dissertation, but are also applicable to second part as a nonintrusive method of diagnostics of the heart valve problems.

The results of this dissertation indicate that the unstable disturbances in the shear layers can be effectively amplified not only by the presence of the acoustic mode of the system, which is in charge of sustaining the oscillations at the upstream edge of the cavity in the model of the gate valve, but also by the pulsatile upstream forcing, resulted from the c of the heart, that initiated strong flow-induced oscillations and amplification of the unstable disturbances in the shear layers formed at the trailing edges of the heart valve leaflets. In the latter

case, the flexible walls of the aorta can also undergo displacement that is large enough to exert feedback on the shear layers.

In both parts of this dissertation, the unstable disturbances in the shear layers were associated with a certain type of the destructive aftermath, although on a very different scale. In the case of pipe-cavity flows, the flow-acoustic coupling in the gate valve caused severe vibration, high noise levels, and, in certain cases wear and fracture of the components of the pipe-cavity flow system. The disturbances associated with the pipe-cavity flows act on the macro scale. In the case of the flow through the heart valve, the presence of strong flow-induced oscillations and amplification of the unstable disturbances in the shear layers at the trailing edges of the heart valve leaflets led to the appearance of the regions of elevated Reynolds shear stresses. The shear forces, induced by unstable shear layers, can act destructively on the blood elements such as platelets and, in certain cases can induce a hemolysis and/or lead to thrombus formation. The disturbances associated with the flow through the heart valve act on the micro scale, comparable to the size of red blood cells or platelets.

The flow-acoustic coupling, phenomena predominately present in the first part of the dissertation is also applicable in the context of the heart valve as one of the main tools used to detect heart valve problems and showing the interrelationship of the various cardiac sounds and murmurs (Johnson et al., 1973, Dimond and Benchimol, 1961). The operation of the normal heart is associated with the generation of two sounds referred as the first and the second heart sounds (Dimond and Benchimol, 1961). The first sound is due to the closure of mitral and tricuspid valves. Typically, a loud, sharp and delayed first sound implies the presence of a good, flexible and mobile valve, while a small, muffled first sound in common to the patients with unquestionable mitral stenosis and indicates the presence of rigid, nonflexible and

calcified cusps. Conduction defect, either right or left bundle branch block, is also capable in delaying closure of the tricuspid or mitral valves (Dimond and Benchimol, 1961).

In contrast to the first sound, a careful analysis of the second sound provides very useful information regarding hemodynamic factors in the pulmonary circulation. Specifically, the valve rigidity and the low diastolic pressure in the pulmonary artery with pulmonary stenosis are factors responsible for the delay in the closure of the pulmonary valve (Dimond and Benchimol, 1961).

The methodology for investigation of azimuthal characteristics of the acoustic modes of the cavity, developed in this dissertation, can be potentially employed in appraisal of congenital heart disease, associated with the presence of rotational flow, and pulmonary hypertension because it reflects the duration of right ventricular systoles.

In the following Sections, the major findings of this dissertation are summarized.

8.2 SHALLOW CIRCULAR AXISYMMETRIC CAVITY

It was confirmed that flow across a shallow axisymmetric cavity can strongly excite the acoustic diametral modes of the cavity. The broadband excitation of the flow tones was observed for a range of inflow velocities up to 30 m/s. It was shown that the predominant acoustic response corresponded to the partially trapped second diametral acoustic mode of the cavity. Simultaneous excitation of the longitudinal acoustic modes of the main pipeline was also observed.

The acoustic response of the system showed qualitative similarity for all values of the angle of the convergence-divergence of the pipeline section in the vicinity of the cavity. In particular, the predominant mode switching from the diametral acoustic modes of the cavity

to the longitudinal acoustic modes of pipeline was observed at low inflow velocities. At the higher inflow velocities, simultaneous excitation of both the diametral and the longitudinal acoustic modes was observed.

As the convergence-divergence angle of the pipeline section increased, a substantial decrease in the maximum pressure values was achieved. This drop in the peak pressure levels corresponded to a decrease in the degree of confinement of the diametral modes. The increased radiation of acoustic energy into the main pipeline could be effectively prevented by increasing the length of the constant-diameter section of the pipe immediately upstream and downstream of the cavity.

8.3 DEEP CIRCULAR AXISYMMETRIC CAVITY

Flow-acoustic coupling in a deep, circular cavity mounted in a pipeline was investigated using a combined approach that involved numerical simulation of the resonant acoustic mode shapes, measurements of acoustic pressure and quantitative flow imaging using PIV.

The acoustic response of the cavity-pipeline system manifested as high-amplitude, self-sustained pressure oscillations corresponding to the first, the fourth and the seventh diametral acoustic modes of the cavity, which were excited by the first three hydrodynamic oscillation modes of the separated shear layers that formed across the cavity opening. In addition, simultaneous excitation of the higher order diametral acoustic modes were observed in a few cases in the higher end of the range of the inflow velocities, from 137 m/s $\leq U \leq$ 149 m/s.

Introduction of symmetric chamfers to the upstream and downstream corners of the cavity effectively shift the lock-on flow states to higher inflow velocities. In this study, the angle of the chamfers was kept constant, while several values of the chamfer length were considered. As the chamfer length increased to L_C = 10.16 mm, resonant acoustic response was completely eliminated.

Introduction of chamfers at the downstream corner of the cavity slightly decreased the overall amplitude of the self-sustained oscillations but did not lead to suppression of the locked-on flow tones. In particular, the shape of the downstream edge does not influence much the critical Strouhal number for oscillation nor the pulsation amplitude. On the other hand, the presence of the chamfers at the upstream corner of the cavity allowed eliminating the lock-on flow states at L_C = 10.16 mm but exhibited higher amplitude of the overall level of broadband pressure spectrum, compared to the case with symmetric chamfers, indicating the importance of having both upstream and downstream chamfers for more effective suppression of the pressure oscillations.

Introduction of shallow chamfers to the upstream and downstream edges of the cavity resulted in changes of azimuthal orientation and spinning behaviour of the acoustic modes. In addition, introduction of splitter plates in the cavity led to pronounced change in the spatial orientation and the spinning behaviour of the acoustic modes and to a decrease in the maximum pressure amplitude. The short splitter plates changed the behaviour of the dominant acoustic modes from partially spinning to stationary, while the long splitter plates enforced the stationary behaviour across all resonant acoustic modes.

Flow-acoustic coupling in a deep, circular cavity mounted in a pipeline was also investigated using a quantitative flow imaging approach. Introduction of symmetric chamfers to

the upstream and downstream corners of the cavity not only effectively shifted the locked-on flow states, as it was shown earlier, but also influenced the process at which the large scale vortical structures were detached from the separated shear layer by shifting the separation point closer to the upstream edge of the cavity.

Introduction of chamfers at the downstream corner of the cavity slightly decreased the overall amplitude of the self-sustained oscillations and consequently weakened the feedback mechanism, one of the main components of which is the interaction of the perturbed velocity field with the impingement edge, indicating the importance of having both upstream and downstream chamfers for more effective elimination of the pressure oscillations.

8.4 CARDIOVASCULAR SYSTEM

The PIV technique was employed to investigate the flow through a polymeric heart valve implanted in patients that had developed certain types of valve diseases prior to the valve replacement. Those valve diseases led to the pathological deformation of the aortic root.

The locations of flow regions with elevated levels of the RSS and high velocity gradients were identified for each of the cases. As the peak levels of RSS were substantially higher than the recognized dangerous threshold, it was concluded that these regions of high fluid stresses may contribute to the platelet activation and to the formation of blood clots. The results suggest that the type of the replacement valve should be considered in conjunction with the aortic root geometry, as the improper choice of the latter might lead to the elevated levels of the RSS.

BIBLIOGRAPHY

AAZAMI, M. & SCHÄFERS, H.-J. 2003. Advances in Heart Valve Surgery. *Journal of Interventional Cardiology,* 16**,** 535-541.

ADRIAN, R. J. 2005. Twenty years of particle image velocimetry. *Experiments in Fluids,* 39**,** 159-169.

ADRIAN, R. J. & WESTERWEEL, J. 2011. *Particle Image Velocimetry,* New York, Cambridge University Press.

ALY, K. & ZIADA, S. 2010. Flow-excited resonance of trapped modes of ducted shallow cavities. *Journal of Fluids and Structures,* 26**,** 92-120.

ALY, K. & ZIADA, S. 2011. Azimuthal behaviour of flow-excited diametral modes of internal shallow cavities. *Journal of Sound and Vibration,* 330**,** 3666-3683.

ALY, K. & ZIADA, S. 2012. Effect of mean flow on the trapped modes of internal cavities. *Journal of Fluids and Structures,* 33**,** 70-84.

ARTHURS, D., ZIADA, S. & BRAVO, R. 2007. Flow induced acoustic resonances of an annular duct with co-axial side branches. Proceedings of the ASME Pressure Vessels and Piping Conference 2007 Vancouver, BC, Canada. 135-145.

BARANNYK, O., KARRI, S. & OSHKAI, P. 2013. In Vitro Study of The Influence of the Aortic Root Geometry on Flow Characteristics of a Prosthetic Heart Valve. Proceedings of the ASME Pressure Vessels & Piping Conference, 2013 Paris, France.

BARANNYK, O. & OSHKAI, P. 2014a. Effect of the edge geometry on flow-acoustic coupling in a deep axisymmetric cavity. *Journal of Fluids and Structures*.

BARANNYK, O. & OSHKAI, P. 2014b. Investigation of diametral acoustic modes in a model of a steam control gate valve. *Journal of Pressure Vessel Technology*.

BARANNYK, O. & OSHKAI, P. Spinning Behaviour of Diametral Acoustic Modes in Deep Axisymmetric Cavities with Chamfered Edges. Proceedings of the ASME 2014 Pressure Vessels & Piping Division Conference, 2014c Anaheim, California, USA. ASME.

BELLHOUS.BJ 1972. Fluid mechanics of a model mitral-valve and left ventricle. *Cardiovascular Research,* 6**,** 199-&.

BILANIN, A. J. & COVERT, E. E. 1973. Estimation of Possible Excitation Frequencies for Shallow Rectangular Cavities. *AIAA Journal,* 11**,** 347-351.

BLEVINS, R. D. 1979. *Formulas for natural frequency and mode shape,* Van Nostrand Reinhold.

BLEVINS, R. D. 1985. The Effect of Sound on Vortex Shedding from Cylinders. *Journal of Fluid Mechanics,* 161**,** 217-237.

BLEVINS, R. D. 1990. *Flow-induced vibration,* New York, Van Nostrand Reinhold Co.

BOLDUC, M., ELSAYED, M. & ZIADA, S. Effect of Upstream Edge Geometry on the Trapped Mode Resonance of Ducted Cavities. *In:* ASME, ed. Proceedings of the ASME 2013 Pressure Vessels and Piping Conference, 2013 Paris, France.

BRUCKER, C., STEINSEIFER, U., SCHRODER, W. & REUL, H. 2002. Unsteady flow through a new mechanical heart valve prosthesis analysed by digital particle image velocimetry. *Measurement Science & Technology,* 13**,** 1043-1049.

BRUGGEMAN, J. C., HIRSCHBERG, A., DONGEN, M. E. H. V., WIJNANDS, A. P. J. & GORTER, J. 1989. Flow Induced Pulsations in Gas Transport Systems: Analysis of the Influence of Closed Side Branches. *Journal of Fluids Engineering,* 111**,** 484-491.

BRUGGEMAN, J. C., HIRSCHBERG, A., VAN DONGEN, M. E. H., WIJNANDS, A. P. J. & GORTER, J. 1991. Self-sustained aero-acoustic pulsations in gas transport systems: Experimental study of the influence of closed side branches. *Journal of Sound and Vibration,* 150**,** 371-393.

CATTAFESTA, L., WILLIAMS, D. R., ROWLEY, C. W. & ALVI, F. 2003. Review of active control of flow-induced cavity resonance. *In:* AIAA (ed.) *AIAA Fluid Dynamics Conference.*

CHATELLIER, L., LAUMONIER, J. & GERVAIS, Y. 2004. Theoretical and experimental investigations of low Mach number turbulent cavity flows. *Experiments in Fluids,* 36**,** 728-740.

DASI, L. P., GE, L., SIMON, H. A., SOTIROPOULOS, F. & YOGANATHAN, A. P. 2007. Vorticity dynamics of a bileaflet mechanical heart valve in an axisymmetric aorta. *Physics of Fluids,* 19.

DEQUAND, S., HULSHOFF, S., KUIJK, H. V., WILLEMS, J. & HIRSCHBERG, A. 2003. Helmholtz-Like Resonator Self-Sustained Oscillations, Part 2: Detailed Flow Measurements and Numerical Simulations. *AIAA Journal,* 41**,** 416-423.

DIMOND, E. G. & BENCHIMOL, A. 1961. Phonocardiography. *California Medicine,* 94**,** 139-146.

DUAN, Y. T., KOCH, W., LINTON, C. M. & MCIVER, M. 2007. Complex resonances and trapped modes in ducted domains. *Journal of Fluid Mechanics,* 571**,** 119-147.

ELDER, S. A. 1978. Self-Excited Depth-Mode Resonance for a Wall-Mounted Cavity in Turbulent-Flow. *Journal of the Acoustical Society of America,* 64**,** 877-890.

ERDEM, D., ROCKWELL, D., OSHKAI, P. & POLLACK, M. 2003. Flow tones in a pipeline-cavity system: effect of pipe asymmetry. *Journal of Fluids and Structures,* 17**,** 511-523.

ETHEMBABAOGLU, Ş. 1973. *On the fluctuating flow characteristics in the vicinity of gate slots.* Licentiatus Technicae in Civil Engineering, The University of Trondheim.

EVANS, D. V., LINTON, C. M. & URSELL, F. 1993. Trapped mode frequencies embedded in the continuous-spectrum. *Quarterly Journal of Mechanics and Applied Mathematics,* 46**,** 253-274.

FOMIN, V., KOSTAREV, V. & REINSCH, K. Elimination of Chernobyl NPP Unit 3 Power Output Limitation Associated with High Main Steam Piping Flow Induced Vibration. Proceedings of the 16th International Conference on Structural Mechanics in Reactor Technology, 2001 Washington, DC, USA. IASMIRT, NC State University and EC, 1375-1383.

FRANKE, M. & CARR, D. 1975. *Effect of geometry on open cavity flow-induced pressure oscillations,* American Institute of Aeronautics and Astronautics.

FUNDER, J. A., FROST, M. W., RINGGAARD, S., KLAABORG, K. E., WIERUP, P., HJORTDAL, V., NYGAARD, H. & HASENKAM, J. M. 2010. In-Vivo Blood Velocity and Velocity Gradient Profiles Downstream of Stented and Stentless Aortic Heart Valves. *Journal of Heart Valve Disease,* 19**,** 292-303.

GE, L., DASI, L. P., SOTIROPOULOS, F. & YOGANATHAN, A. P. 2008. Characterization of hemodynamic forces induced by mechanical heart valves: Reynolds vs. viscous stresses. *Annals of Biomedical Engineering,* 36**,** 276-297.

GEVECI, M., OSHKAI, P., ROCKWELL, D., LIN, J. C. & POLLACK, M. 2003. Imaging of the self-excited oscillation of flow past a cavity during generation of a flow tone. *Journal of Fluids and Structures,* 18**,** 665-694.

GIJRATH, J. W. M., VERHAAR, B. T. & BRUGGEMAN, J. C. Prediction model for broadband noise in bends. *In:* ZIADA, S. & STAUBLI, T., eds. Proceedings of the 7th international Conference on Flow Induced Vibration, 2000 Lucerne, Switzerland. 623-627.

GONCALVES, I., NESBITT, W. S., YUAN, Y. P. & JACKSON, S. P. 2005. Importance of temporal flow gradients and integrin alpha(IIb)beta(3) mechanotransduction for shear activation of platelets. *Journal of Biological Chemistry,* 280**,** 15430-15437.

GRANT, I. 1997. Particle image velocimetry: A review. *Proceedings of the Institution of Mechanical Engineers Part C-Journal of Mechanical Engineering Science,* 211**,** 55-76.

HALL, J. W., ZIADA, S. & WEAVER, D. S. 2003. Vortex-shedding from single and tandem cylinders in the presence of applied sound. *Journal of Fluids and Structures,* 18**,** 741-758.

HARIHARAN, P., GIARRA, M., REDDY, V., DAY, S. W., MANNING, K. B., DEUTSCH, S., STEWART, S. F. C., MYERS, M. R., BERMAN, M. R., BURGREEN, G. W., PATERSON, E. G. & MALINAUSKAS, R. A. 2011. Multilaboratory Particle Image Velocimetry Analysis of the FDA Benchmark Nozzle Model to Support Validation of Computational Fluid Dynamics Simulations. *Journal of Biomechanical Engineering-Transactions of the ASME,* 133.

HARIHARAN, P., MYERS, M. R., ROBINSON, R. A., MARUVADA, S. H., SLIWA, J. & BANERJEE, R. K. 2008. Characterization of high intensity focused ultrasound transducers using acoustic streaming. *Journal of the Acoustical Society of America,* 123**,** 1706-1719.

HART, D. P. 2000. PIV error correction. *Experiments in Fluids,* 29**,** 13-22.

HEIN, S. & KOCH, W. 2008. Acoustic resonances and trapped modes in pipes and tunnels. *Journal of Fluid Mechanics,* 605**,** 401-428.

HELLER, H. H., HOLMES, D. G. & COVERT, E. E. 1971. Flow-induced pressure oscillations in shallow cavities. *Journal of Sound and Vibration,* 18**,** 545.

HELLMICH, B. & SEUME, J. R. 2008. Causes of acoustic resonance in a high-speed axial compressor. *Journal of Turbomachinery-Transactions of the ASME,* 130.

HIRAHARA, H., KAWAHASHI, M., KHAN, M. U. & HOURIGAN, K. 2007. Experimental investigation of fluid dynamic instability in a transonic cavity flow. *Experimental Thermal and Fluid Science,* 31**,** 333-347.

HOWE, M. S. 1975. Contributions to theory of aerodynamic sound, with application to excess jet noise and theory of flute. *Journal of Fluid Mechanics,* 71**,** 625-673.

HOWE, M. S. 1980. The dissipation of sound at an edge. *Journal of Sound and Vibration,* 70**,** 407-411.

HOWE, M. S. 1981. The influence of mean shear on unsteady aperture flow, with application to acoustical diffraction and self-sustained cavity oscillations. *Journal of Fluid Mechanics,* 109**,** 125-146.

HUANG, H., DABIRI, D. & GHARIB, M. 1997. On errors of digital particle image velocimetry. *Measurement Science & Technology,* 8**,** 1427-1440.

IDE, M., IRIE, S., MATSUO, N., ODA, A., TANAKA, S. & ITOH, S. 2010. *Research about Pulverization of Rice using Underwater Shock Wave by Electric Discharge,* New York, ASME.

ISO 2013. *Cardiovascular implants - Cardiac valve prostheses*

IUNG, B., BARON, G., BUTCHART, E. G., DELAHAYE, F., GOHLKE-BARWOLF, C., LEVANG, O. W., TORNOS, P., VANOVERSCHELDE, J. L., VERMEER, F., BOERSMA, E., RAVAUD, P. & VAHANIAN, A. 2003. A prospective survey of patients with valvular heart disease in Europe: The Euro Heart Survey on Valvular Heart Disease. *European Heart Journal,* 24**,** 1231-1243.

JANZEN, V. P., SMITH, B. A. W., LULOFF, B. V., POZSGAI, J., DIETRICH, A. R., BOUVIER, J. M. & ERRETT, A. J. 2008. *Acoustic noise reduction in large-diameter steam-line gate valves,* San Antonio, TX, USA.

JOHNSON, M. L., HOLMES, J. H. & PATON, B. C. 1973. Echocardiographic Determination of Mitral Disc Valve Excursion. *Circulation,* 47**,** 1274-1280.

KARADOGAN, H. & ROCKWELL, D. 1983. Toward Attenuation of Self-Sustained Oscillations of a Turbulent Jet Through a Cavity. *Journal of Fluids Engineering,* 105**,** 335-340.

KARRI, S. & VLACHOS, P. P. 2010. Time-Resolved DPIV Investigation of Pulsatile Flow in Symmetric Stenotic Arteries Effects of Phase Angle. *Journal of Biomechanical Engineering-Transactions of the ASME,* 132.

KEANE, R. D. & ADRIAN, R. J. 1990. Optimization of Particle Image Velocimeters .1. Double Pulsed Systems. *Measurement Science & Technology,* 1**,** 1202-1215.

KEGERISE, M. A., SPINA, E. F., GARG, S. & CATTAFESTA, L. N. 2004. Mode-switching and nonlinear effects in compressible flow over a cavity. *Physics of Fluids,* 16**,** 678-687.

KELLER, J. J. & ESCUDIER, M. P. 1983. Flow-excited resonances in covered cavities. *Journal of Sound and Vibration,* 86**,** 199-226.

KOOK, H. & MONGEAU, L. 2002. Analysis of the periodic pressure fluctuations induced by flow over a cavity. *Journal of Sound and Vibration,* 251**,** 823-846.

KRIESELS, P. C., PETERS, M. C. A., HIRSCHBERG, A., WIJNANDS, A. P. J., IAFRATI, A., RICCARDI, G., PIVA, R. & BRUGGEMAN, J. C. 1995. High amplitude vortex-induced pulsations in a gas transport system. *Journal of Sound and Vibration,* 184**,** 343-368.

LAFON, P., CAILLAUD, S., DEVOS, J. P. & LAMBERT, C. 2003. Aeroacoustical coupling in a ducted shallow cavity and fluid/structure effects on a steam line. *Journal of Fluids and Structures,* 18**,** 695-713.

LEO, H. L., DASI, L. P., CARBERRY, J., SIMON, H. A. & YOGANATHAN, A. P. 2006. Fluid dynamic assessment of three polymeric heart valves using particle image velocimetry. *Annals of Biomedical Engineering,* 34**,** 936-952.

LEVERETT, L. B., LYNCH, E. C., ALFREY, C. P. & HELLUMS, J. D. 1972. Red blood-cell damage by shear-stress. *Biophysical Journal,* 12**,** 257-&.

LIM, W. L., CHEW, Y. T., CHEW, T. C. & LOW, H. T. 1994. Particle image velocimetry in the investigation of flow past artificial-heart valves. *Annals of Biomedical Engineering,* 22**,** 307-318.

LIM, W. L., CHEW, Y. T., CHEW, T. C. & LOW, H. T. 1998. Steady flow dynamics of prosthetic aortic heart valves: a comparative evaluation with PIV techniques. *Journal of Biomechanics,* 31**,** 411-421.

LIM, W. L., CHEW, Y. T., CHEW, T. C. & LOW, H. T. 2001. Pulsatile flow studies of a porcine bioprosthetic aortic valve in vitro: PIV measurements and shear-induced blood damage. *Journal of Biomechanics,* 34**,** 1417-1427.

LINTON, C. M. & MCIVER, M. 1998. Trapped modes in cylindrical waveguides. *Quarterly Journal of Mechanics and Applied Mathematics,* 51**,** 389-412.

LINTON, C. M., MCIVER, M., MCIVER, P., RATCLIFFE, K. & ZHANG, J. 2002. Trapped modes for off-centre structures in guides. *Wave Motion,* 36**,** 67-85.

LU, P. C., LAI, H. C. & LIU, J. S. 2001. A reevaluation and discussion on the threshold limit for hemolysis in a turbulent shear flow. *Journal of Biomechanics,* 34**,** 1361-1364.

MAST, T. D. & PIERCE, A. D. 1995. Describing-function theory for flow excitation of resonators. *Journal of the Acoustical Society of America,* 97**,** 163-172.

MCDONALD, D. A. 1974. *Blood Flow in Arteries,* London, Edward Arnold.

MELLING, A. 1997. Tracer particles and seeding for particle image velocimetry. *Measurement Science & Technology,* 8**,** 1406-1416.

MICHAUD, S., ZIADA, S. & PASTOREL, H. 2001. Acoustic fatigue of a steam dump pipe system excited by valve noise. *Journal of Pressure Vessel Technology-Transactions of the ASME,* 123**,** 461-468.

MONKEWITZ, P. A. & HUERRE, P. 1982. Influence of the velocity ratio on the spatial instability of mixing layers. *Physics of Fluids,* 25**,** 1137-1143.

NAUDASCHER, E. & ROCKWELL, D. 2005. *Flow-induced vibrations: An engineering guide,* Mineola, New York, Dover Publications, Inc.

NELSON, P. A., HALLIWELL, N. A. & DOAK, P. E. 1983. Fluid-dynamics of a flow excited resonance .2. Flow acoustic interaction. *Journal of Sound and Vibration,* 91**,** 375-402.

OSHKAI, P. & BARANNYK, O. Experimental Investigation of Flow-Acoustic Coupling in a Deep Axisymmetric Cavity. *In:* ASME, ed. Proceedings of the ASME 2013 Pressure Vessels and Piping Conference, 2013 Paris, France. ASME.

OSHKAI, P. & BARANNYK, O. Quantitative Visualization of Unstable, Acoustically Coupled Shear Layers in Deep Axisymmetric Cavities. Proceedings of the ASME 2014 Pressure Vessels & Piping Division Conference, 2014 Anaheim, California, USA. ASME.

OSHKAI, P., GEVECI, M., ROCKWELL, D. & POLLACK, M. 2005. Imaging of acoustically coupled oscillations due to flow past a shallow cavity: Effect of cavity length scale. *Journal of Fluids and Structures,* 20**,** 277-308.

OSHKAI, P. & VELIKORODNY, A. 2013. Flow-acoustic coupling in coaxial side branch resonators with rectangular splitter plates. *Journal of Fluids and Structures,* 38**,** 22-39.

PETERS, M. C. A. M. 1993. *Aeroacoustic sources in internal flows.* Technical University of Eindhoven.

POWELL, A. 1964. Theory of Vortex Sound. *Journal of the Acoustical Society of America,* 36**,** 177-&.

PRANDTL, L. Uber Flussigkeitsbewegung bei sehr kleiner Reibung (On the Motion of Fluid with Very Little Friction). Third International Mathematics Congress 1904 Heidelberg.

RAFFEL, M., WILLERT, C. E., WERELEY, S. T. & KOMPENHANS, J. 2007. *Particle Image Velocimetry: A Practical Guide,* London, Springer.

RAJU, N. & MEIBURG, E. 1995. The accumulation and dispersion of heavy particles in forced two-dimensional mixing layers. Part 2: The effect of gravity. *Physics of Fluids (1994-present),* 7**,** 1241-1264.

REUL, H., VAHLBRUCH, A., GIERSIEPEN, M., SCHMITZRODE, T., HIRTZ, V. & EFFERT, S. 1990a. The geometry of the aortic root in health, at valve disease and after valve-replacement. *Journal of Biomechanics,* 23**,** 181-&.

REUL, H., VAHLBRUCH, A., GIERSIEPEN, M., SCHMITZRODE, T., HIRTZ, V. & EFFERT, S. 1990b. The geometry of the aortic root in health, at valve disease and after valve-replacement. *Journal of Biomechanics,* 23**,** 181-&.

ROCKWELL, D. & KNISELY, C. 1979. The organized nature of flow impingement upon a corner. *Journal of Fluid Mechanics,* 93**,** 413-432.

ROCKWELL, D., LIN, J. C., OSHKAI, P., REISS, M. & POLLACK, M. 2003. Shallow cavity flow tone experiments: onset of locked-on states. *Journal of Fluids and Structures,* 17**,** 381-414.

ROCKWELL, D. & NAUDASCHER, E. 1978. Review: Self-sustaining oscillations of flow past cavities. *Journal of Fluids Engineering-Transactions of the ASME,* 100**,** 152-165.

ROSSITER, J. E. 1964. Wind-Tunnel Experiments on the Flow over Rectangular Cavities at Subsonic and Transonic Speeds. *Aerodyn Res Counc Rep Memo 3438.*

ROSZELLE, B. N., DEUTSCH, S. & MANNING, K. B. 2010. Flow Visualization of Three-Dimensionality Inside the 12 cc Penn State Pulsatile Pediatric Ventricular Assist Device. *Annals of Biomedical Engineering,* 38**,** 439-455.

SALLAM, A. M. & HWANG, N. H. C. 1984. Human red blood-cell hemolysis in a turbulent shear-flow - contribution of Reynolds Shear Stresses. *Biorheology,* 21**,** 783-797.

SCHLICHTING, H. 1955. *Boundary-layer theory*, New York: McGraw-Hill.

SENSIAU, C., NICOUD, F. & POINSOT, T. 2009. A tool to study azimuthal standing and spinning modes in annular combustors. *International Journal of Aeroacoustics,* 8**,** 57-67.

SMITH, B. A. W. & LULOFF, B. V. 2000. The effect of seat geometry on gate valve noise. *Journal of Pressure Vessel Technology-Transactions of the ASME,* 122**,** 401-407.

TAM, C. K. W. & BLOCK, P. J. W. 1978. On the tones and pressure oscillations induced by flow over rectangular cavities. *Journal of Fluid Mechanics,* 89**,** 373-399.

TANG, L., WEN, F., YANG, Y., CROWE, C. T., CHUNG, J. N. & TROUTT, T. R. 1992. Self-organizing particle dispersion mechanism in a plane wake. *Physics of Fluids a-Fluid Dynamics,* 4**,** 2244-2251.

TONON, D., HIRSCHBERG, A., GOLLIARD, J. & ZIADA, S. 2011. Aeroacoustics of pipe systems with closed branches. *International Journal of Aeroacoustics,* 10**,** 201-275.

VAKILI, A. D. & GAUTHIER, C. 1994. Control of cavity flow by upstream mass-Injection. *Journal of Aircraft,* 31**,** 169-174.

VELIKORODNY, A., YAN, T. & OSHKAI, P. 2010. Quantitative imaging of acoustically coupled flows over symmetrically located side branches. *Experiments in Fluids,* 48**,** 245-263.

VERDUGO, F. R., GUITTON, A. & CAMUSSI, R. 2012. Experimental investigation of a cylindrical cavity in a low Mach number flow. *Journal of Fluids and Structures,* 28**,** 1-19.

VONGPATANASIN, W., HILLIS, L. D. & LANGE, R. A. 1996. Medical progress - Prosthetic heart valves. *New England Journal of Medicine,* 335**,** 407-416.

WEAVER, D. S., ZIADA, S., AY-YANG, M. K., CHEN, S. S., PAIDOUSSIS, M. P. & PETTIGREW, M. J. 2000. Flow-induced vibrations in power and process plant components - Progress and prospects. *Journal of Pressure Vessel Technology-Transactions of the ASME,* 122**,** 339-348.

WESTERWEEL, J. 1997. Fundamentals of digital particle image velocimetry. *Measurement Science & Technology,* 8**,** 1379-1392.

WESTERWEEL, J., DABIRI, D. & GHARIB, M. 1997. The effect of a discrete window offset on the accuracy of cross-correlation analysis of digital PIV recordings. *Experiments in Fluids,* 23**,** 20-28.

WILLERT, C. E. & GHARIB, M. 1991. Digital Particle Image Velocimetry. *Experiments in Fluids,* 10**,** 181-193.

WILLMARTH, W. W., GASPAROVIC, R. F., MASZATICS, J. M., MCNAUGHTON, J. L. & THOMAS, D. J. 1978. Management of turbulent shear layers in separated flow. *Journal of Aircraft,* 15**,** 385-386.

YANG, Y., ROCKWELL, D., CODY, K. L. F. & POLLACK, M. 2009. Generation of tones due to flow past a deep cavity: Effect of streamwise length. *Journal of Fluids and Structures,* 25**,** 364-388.

YOGANATHAN, A. P., CHANDRAN, K. B. & SOTIROPOULOS, F. 2005. Flow in prosthetic heart valves: State-of-the-art and future directions. *Annals of Biomedical Engineering,* 33**,** 1689-1694.

YOGANATHAN, A. P., HE, Z. M. & JONES, S. C. 2004. Fluid mechanics of heart valves. *Annual Review of Biomedical Engineering,* 6**,** 331-362.

ZIADA, S. 2003. Control of fluid-structure-sound interaction mechanisms by means of synthetic jets. *JSME International Journal Series C-Mechanical Systems Machine Elements and Manufacturing,* 46**,** 873-880.

ZIADA, S. 2010. Flow-Excited Acoustic Resonance in Industry. *Journal of Pressure Vessel Technology-Transactions of the ASME,* 132**,** 1-9.

ZIADA, S. & BUHLMANN, E. T. 1992. Self-excited resonances of 2 side-branches in close proximity. *Journal of Fluids and Structures,* 6**,** 583-601.

ZIADA, S. & LAFON, P. 2013. Flow-Excited Acoustic Resonance Excitation Mechanism, Design Guidelines, and Counter Measures. *Applied Mechanics Reviews,* 66**,** 010802-010802.

APPENDIX A: TIME-AVERAGED FLOW PATTERNS

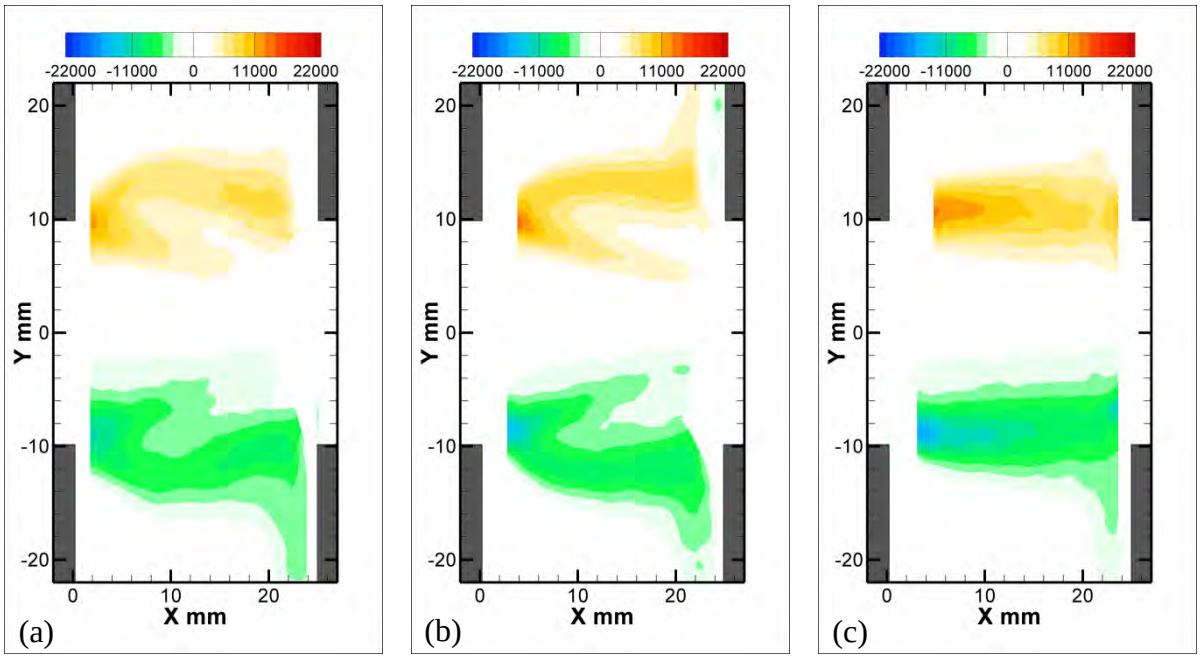

Figure A.1: Patterns of time-averaged out-of-plane vorticity (s^{-1}) corresponding for the case of the upstream chamfer with chamfer length: (a) L_C = 1.27 mm, (b) L_C = 3.81 mm, (c) L_C = 10.16 mm.

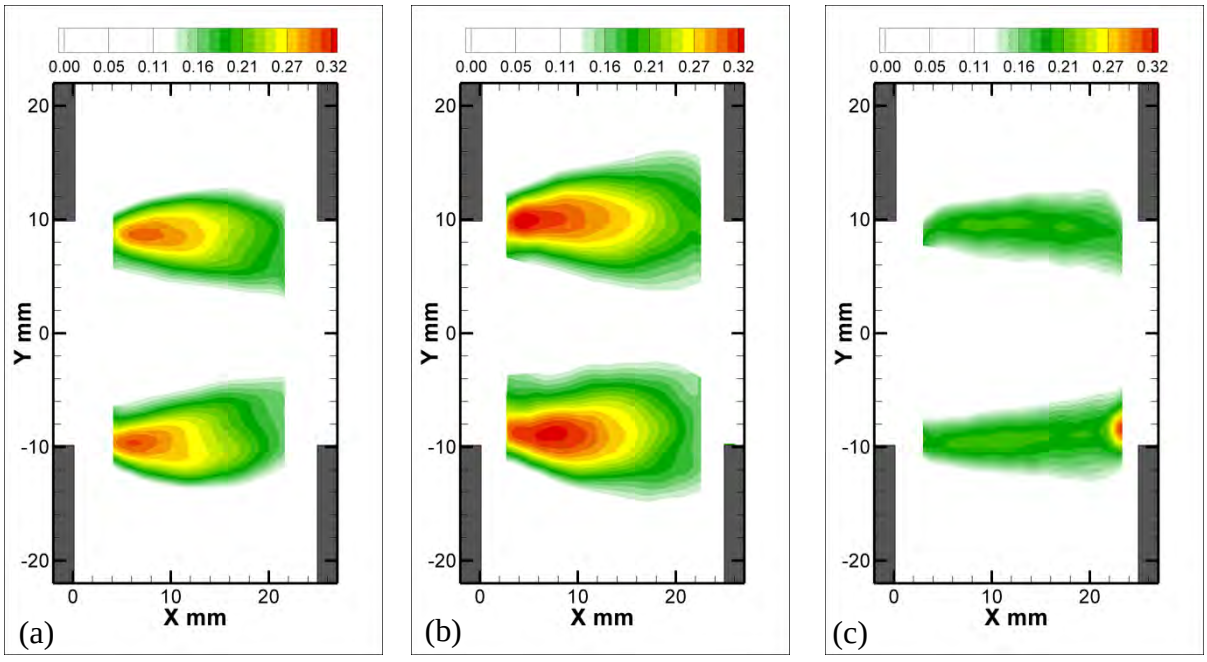

Figure A.2: Patterns of time-averaged u_{rms}/U corresponding to the case of the upstream chamfer with chamfer length: (a) L_C = 1.27 mm, (b) L_C = 3.81 mm, (c) L_C = 10.16 mm.

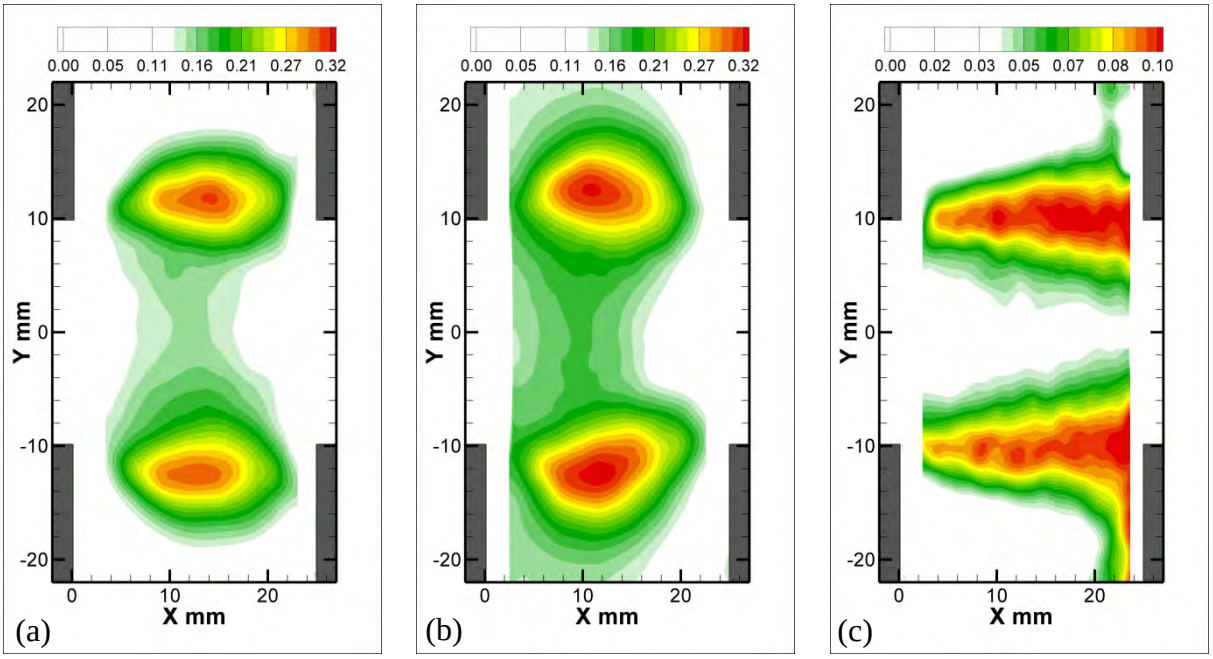

Figure A.3: Patterns of time-averaged v_{rms}/U corresponding to the case of the upstream chamfer with chamfer length: (a) L_C = 1.27 mm, (b) L_C = 3.81 mm, (c) L_C = 10.16 mm.

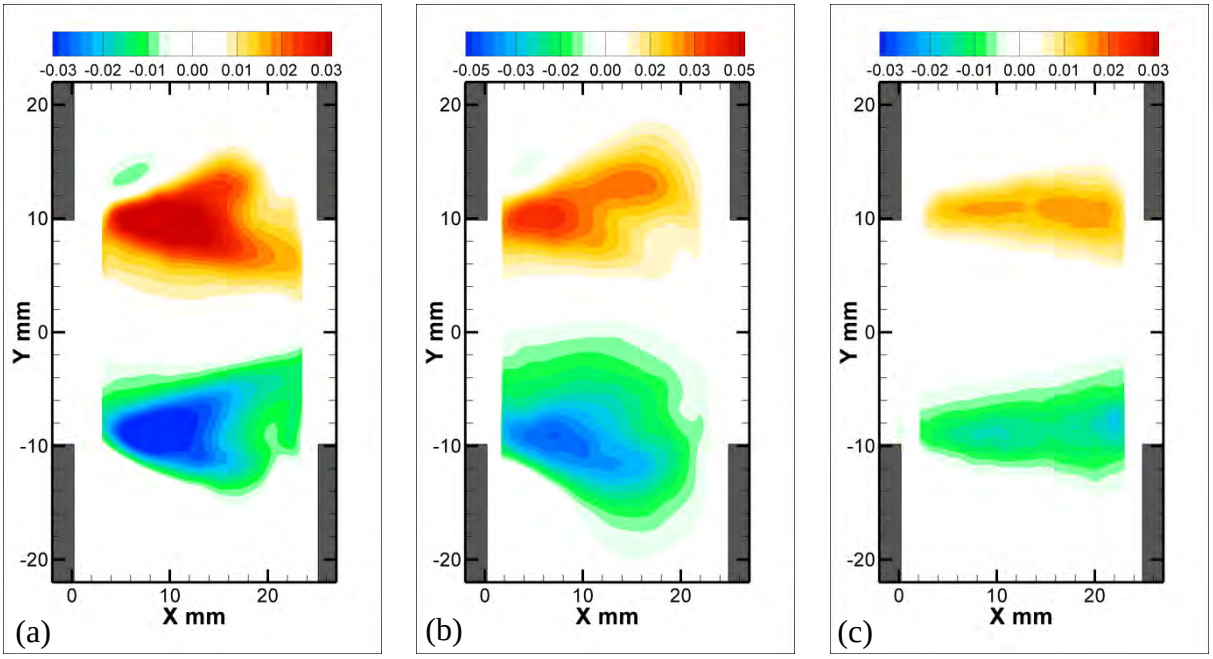

Figure A.4: Patterns of time-averaged Reynolds stress corresponding to the case of the upstream chamfer with chamfer length: (a) L_C = 1.27 mm, (b) L_C = 3.81 mm, (c) L_C = 10.16 mm.

APPENDIX B: PHASE-AVERAGED FLOW PATTERNS

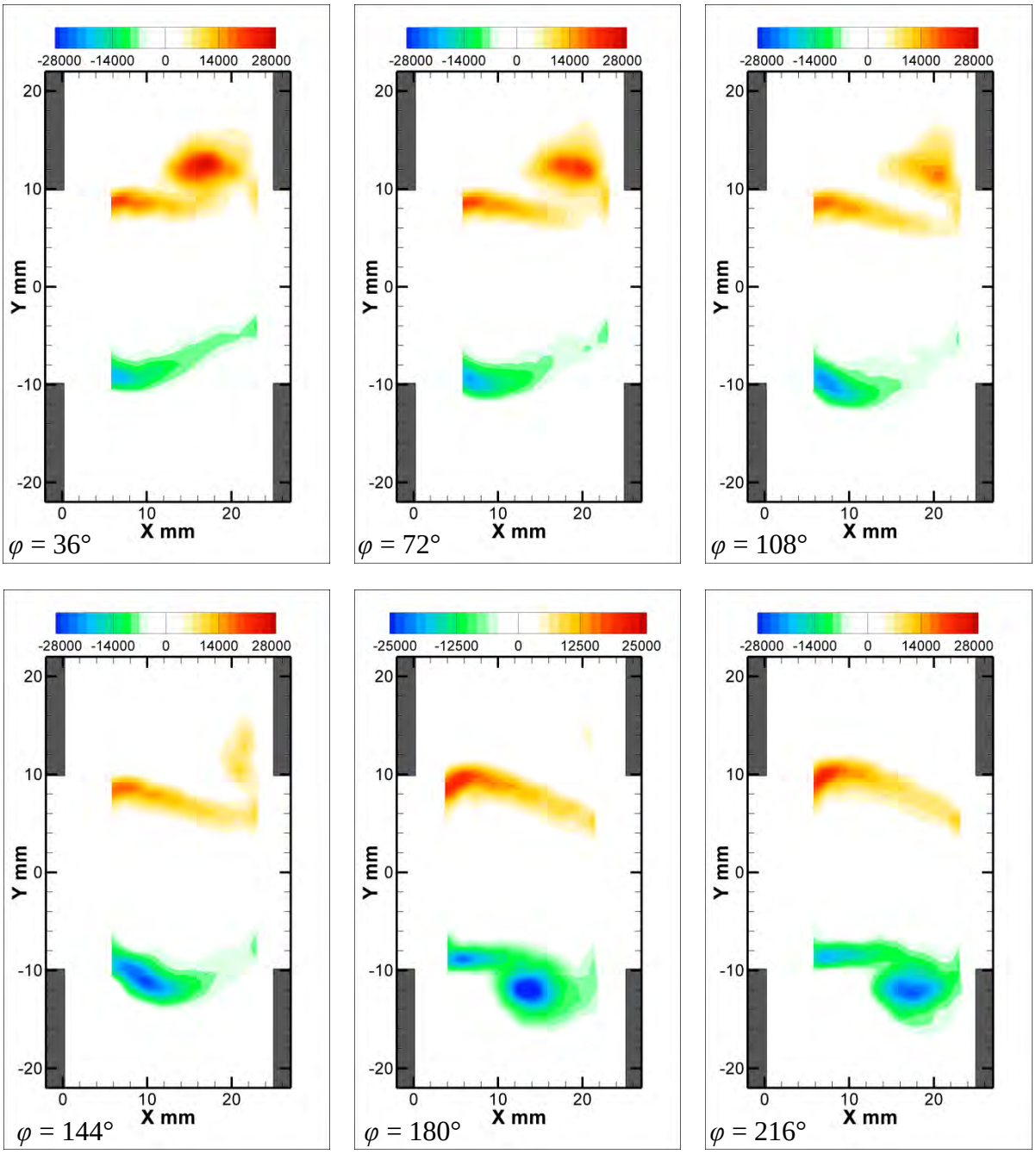

Figure B.1: Patterns of phase-averaged out-of-plane vorticity (s^{-1}) corresponding to the symmetric case $L_C = 0$, φ = 36° through 216°.

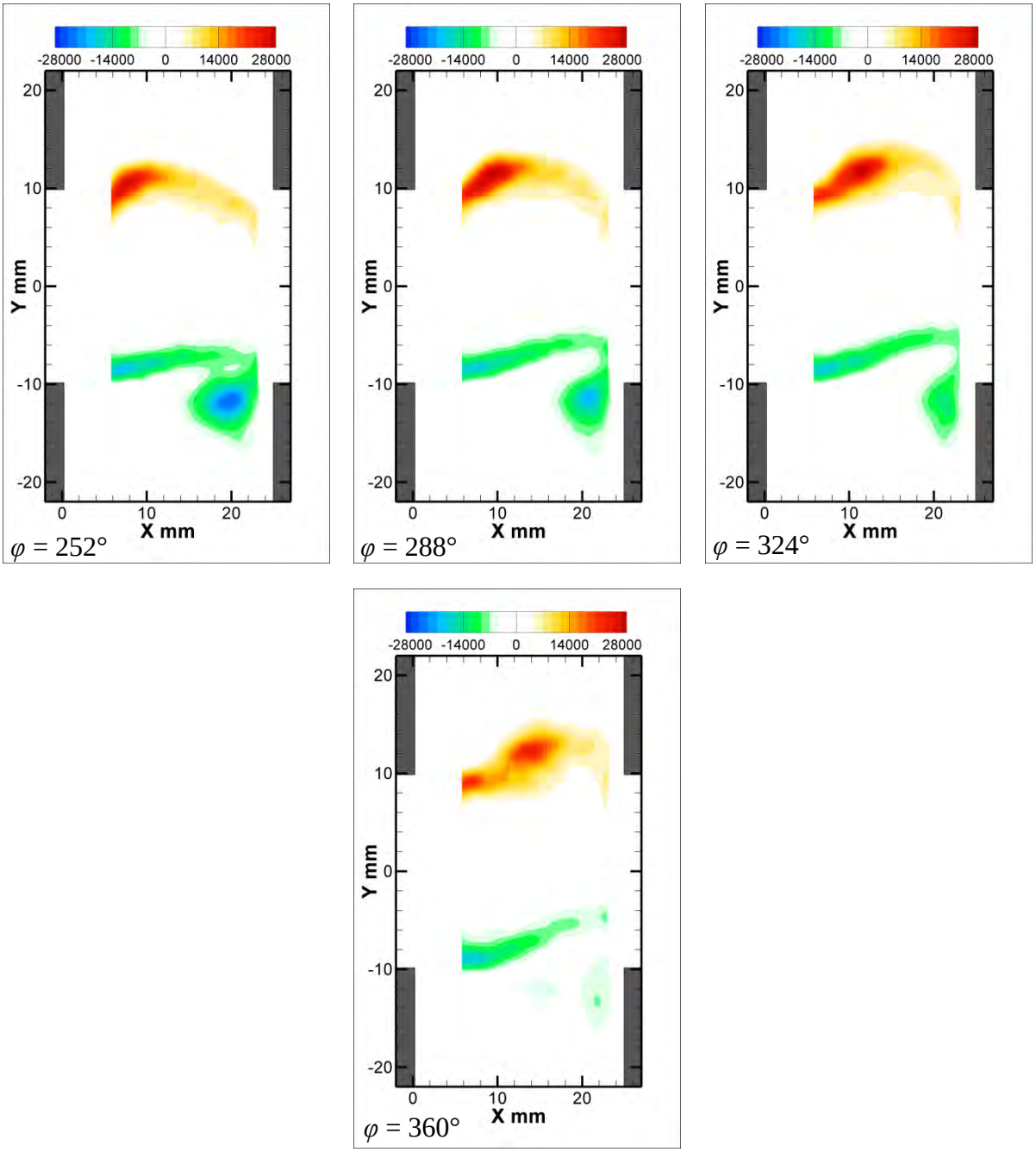

Figure B.2: Patterns of phase-averaged out-of-plane vorticity (s^{-1}) corresponding to the symmetric case $L_C = 0$, $\varphi = 252°$ through 360°.

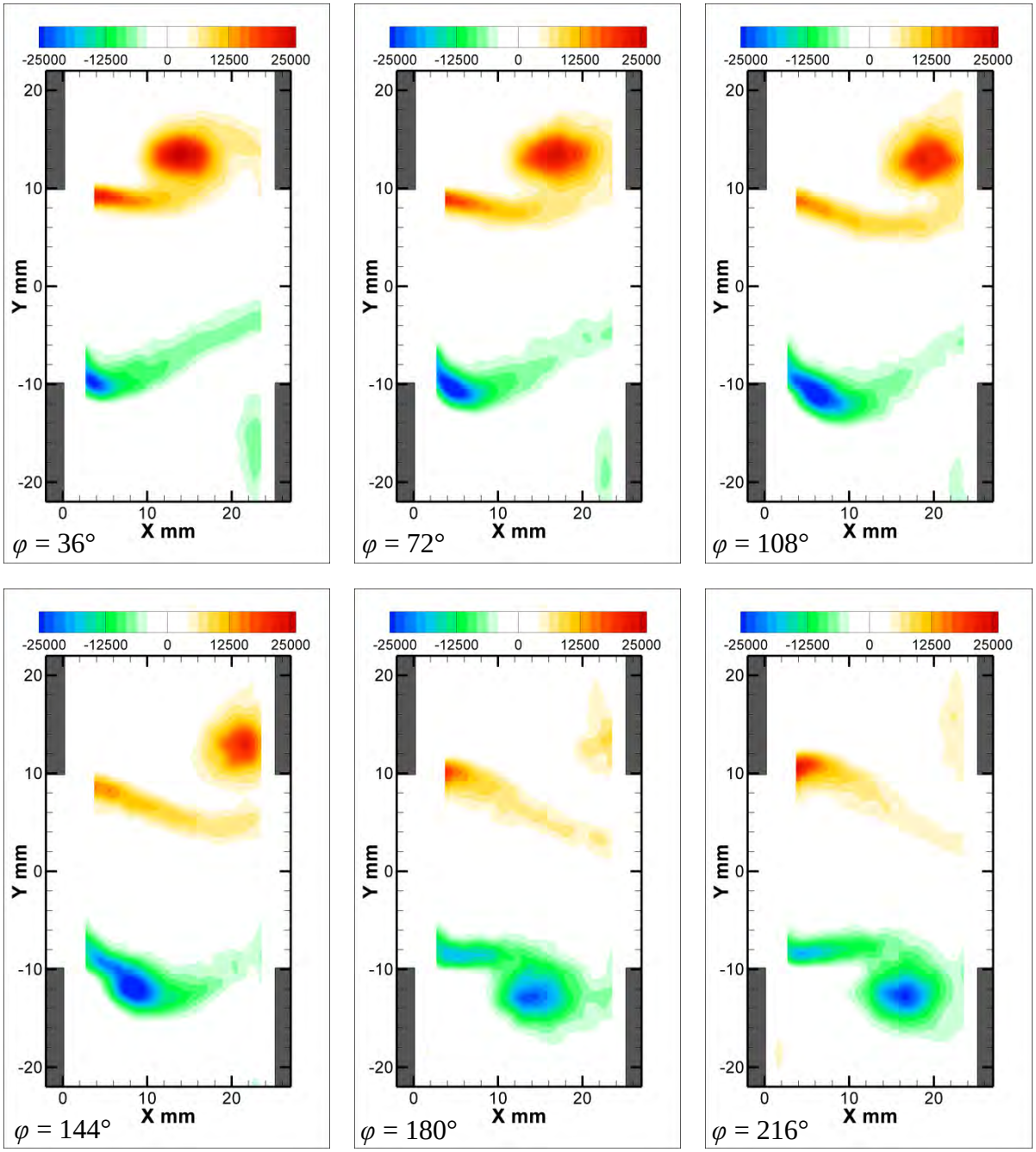

Figure B.3: Patterns of phase-averaged out-of-plane vorticity (s^{-1}) corresponding to the symmetric case L_C = 1.27 mm, φ = 36° through 216°.

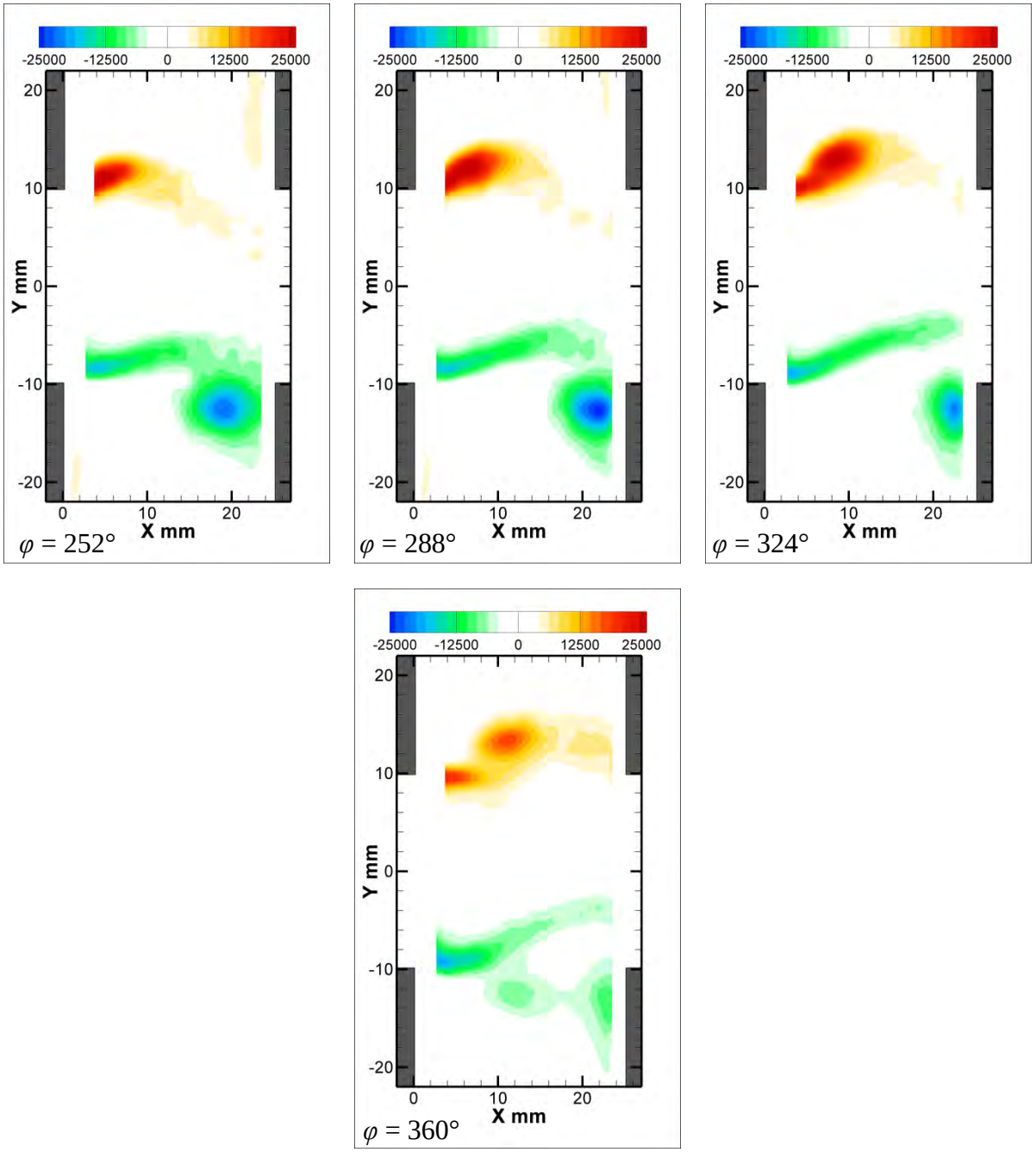

Figure B.4: Patterns of phase-averaged out-of-plane vorticity (s^{-1}) corresponding to the symmetric case L_C = 1.27 mm, φ = 252° through 360°.

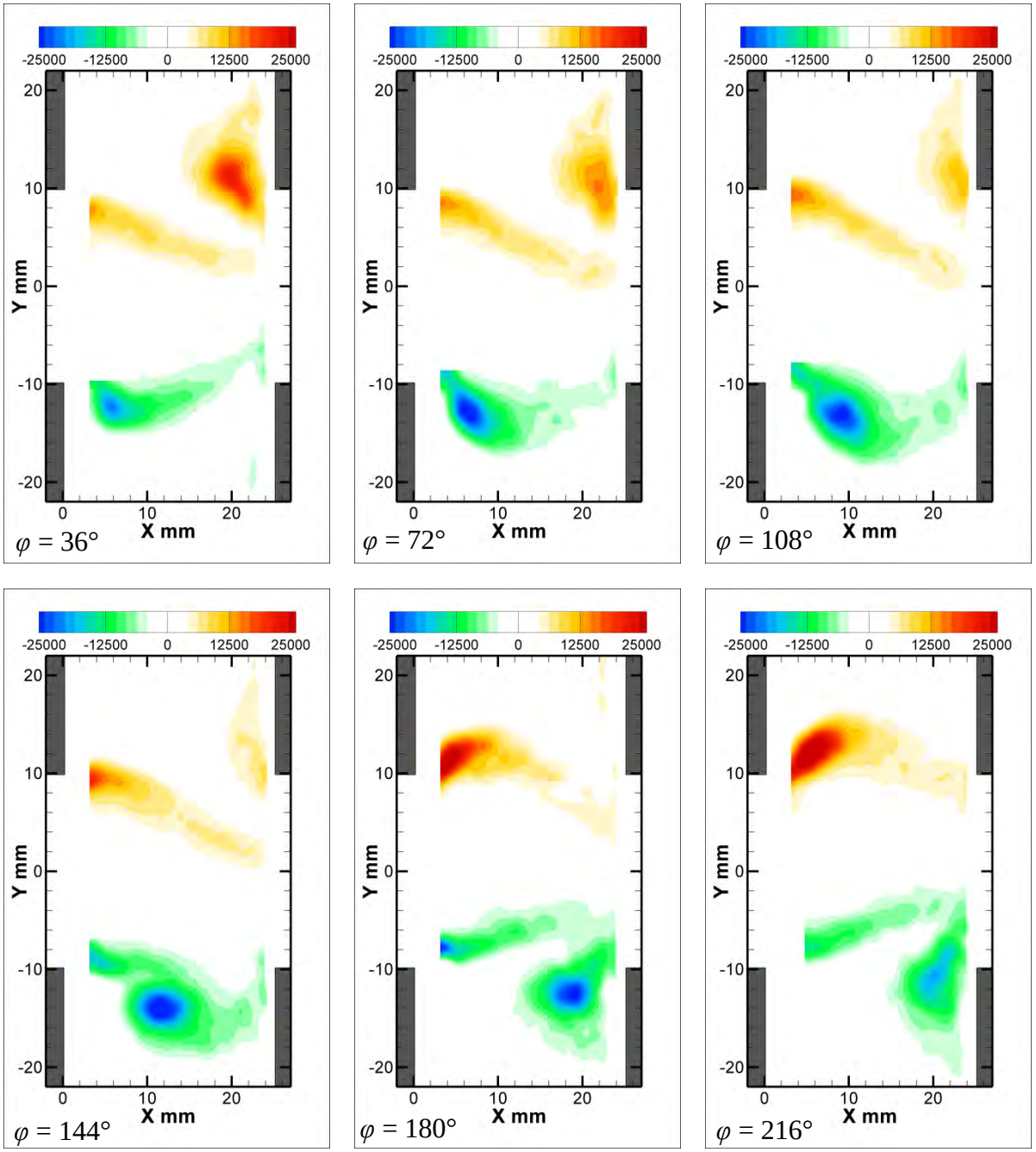

Figure B.5: Patterns of phase-averaged out-of-plane vorticity (s^{-1}) corresponding to the symmetric case L_C = 3.81 mm, φ = 36° through 216°.

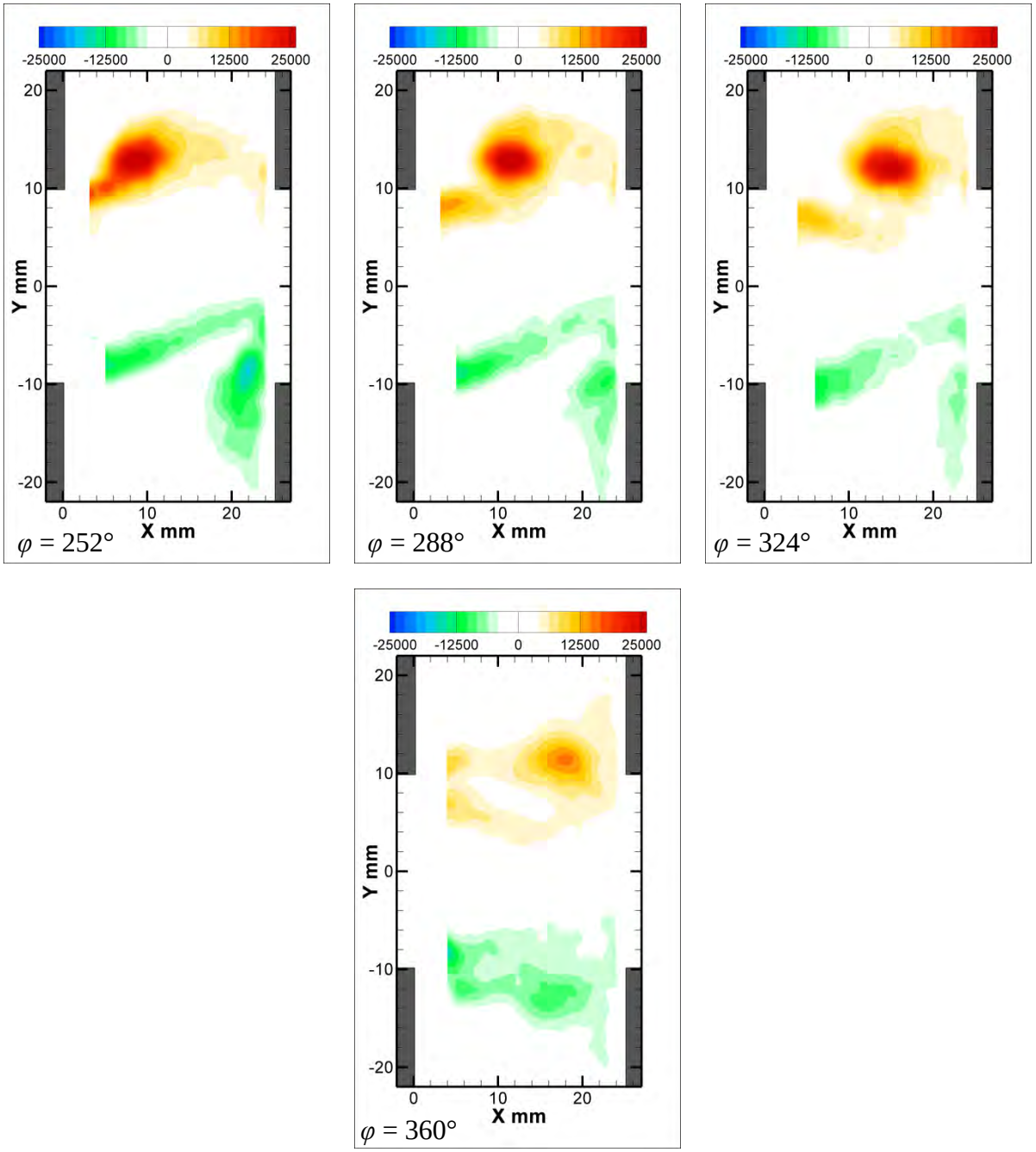

Figure B.6: Patterns of phase-averaged out-of-plane vorticity (s^{-1}) corresponding to the symmetric case L_C = 1.27 mm, φ = 252° through 360°.

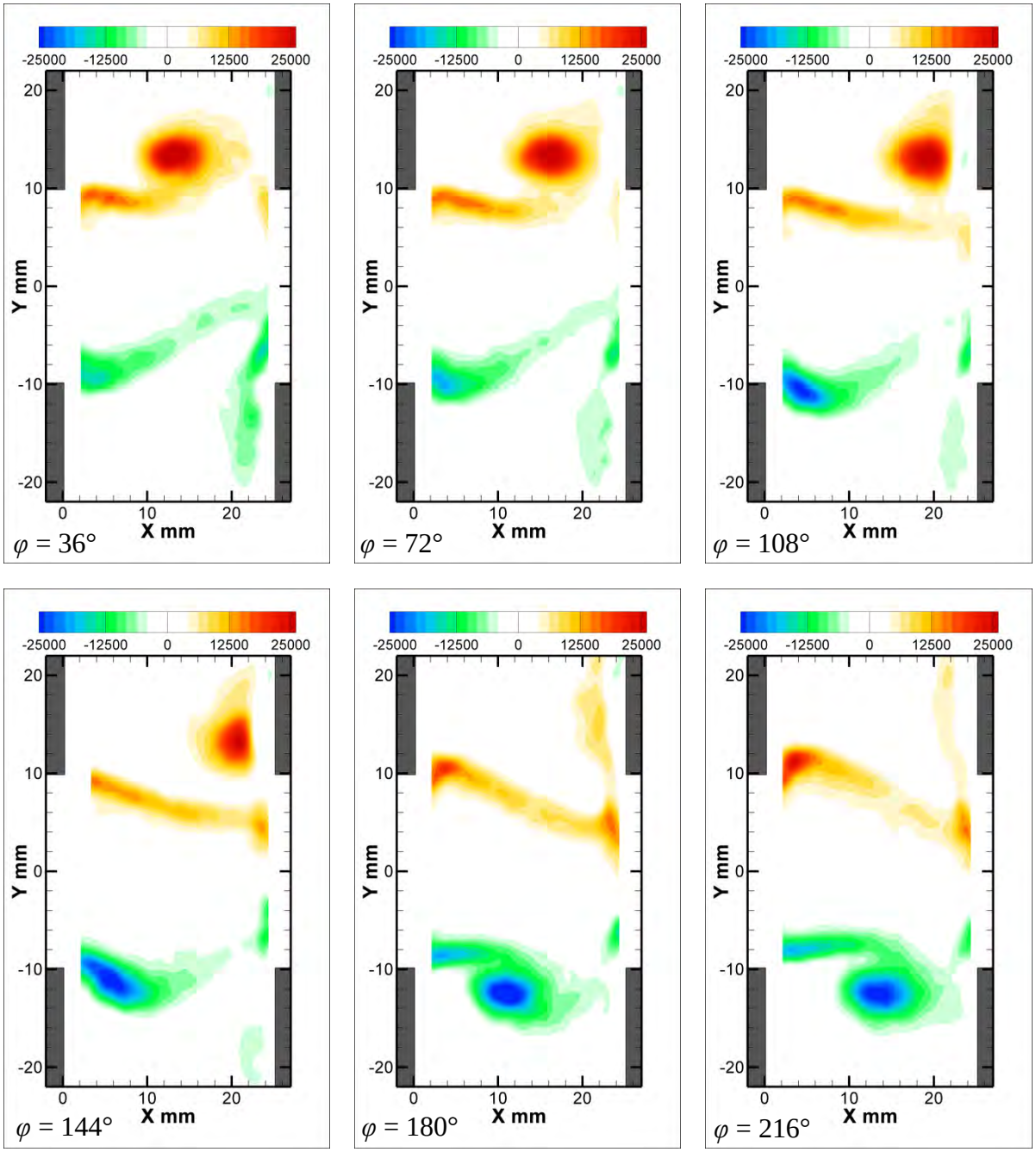

Figure B.7: Patterns of phase-averaged out-of-plane vorticity (s^{-1}) corresponding to the upstream case L_C = 1.27 mm, φ = 36° through 216°.

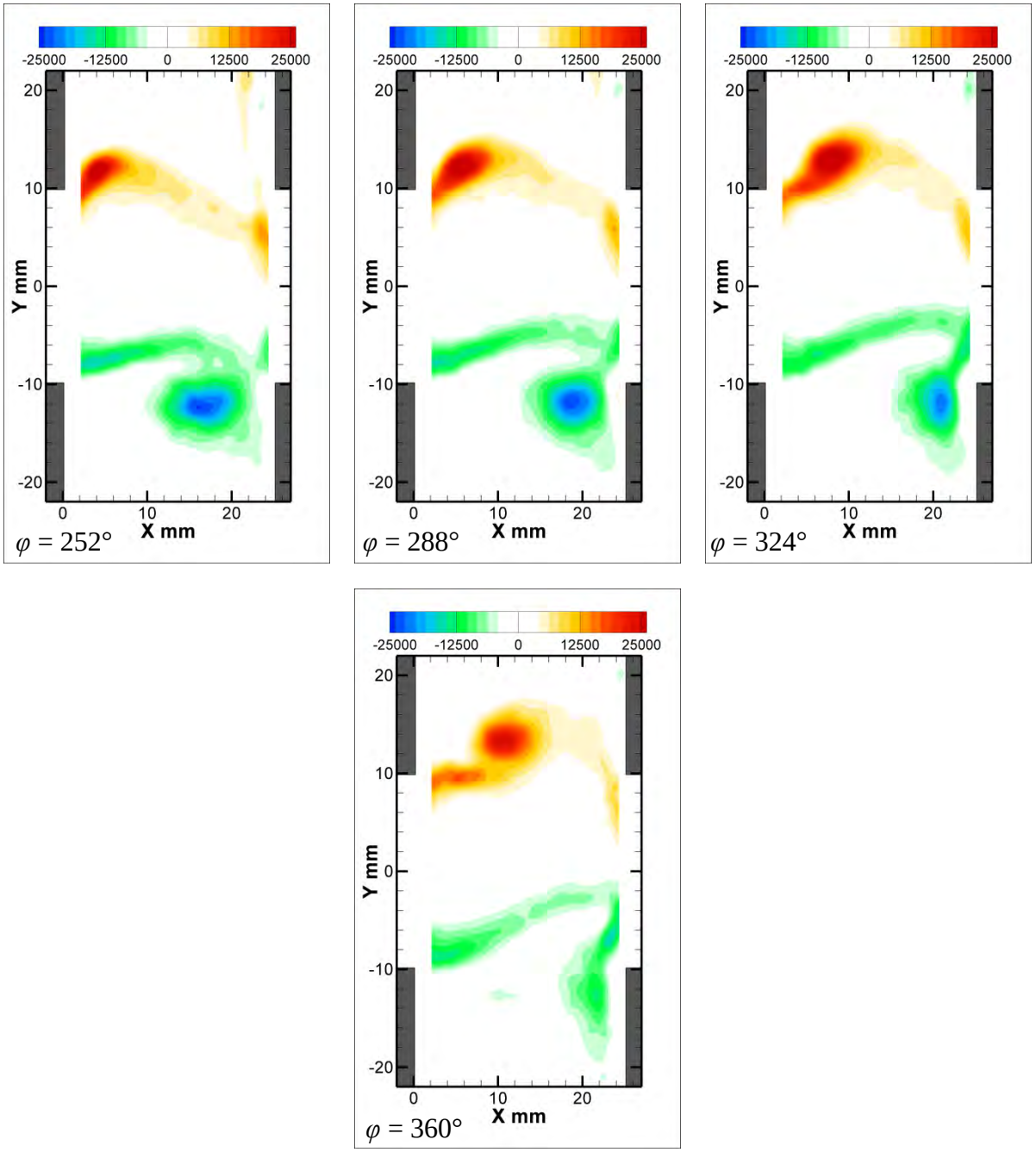

Figure B.8: Patterns of phase-averaged out-of-plane vorticity (s^{-1}) corresponding to the upstream case L_C = 1.27 mm, φ = 252° through 360°.

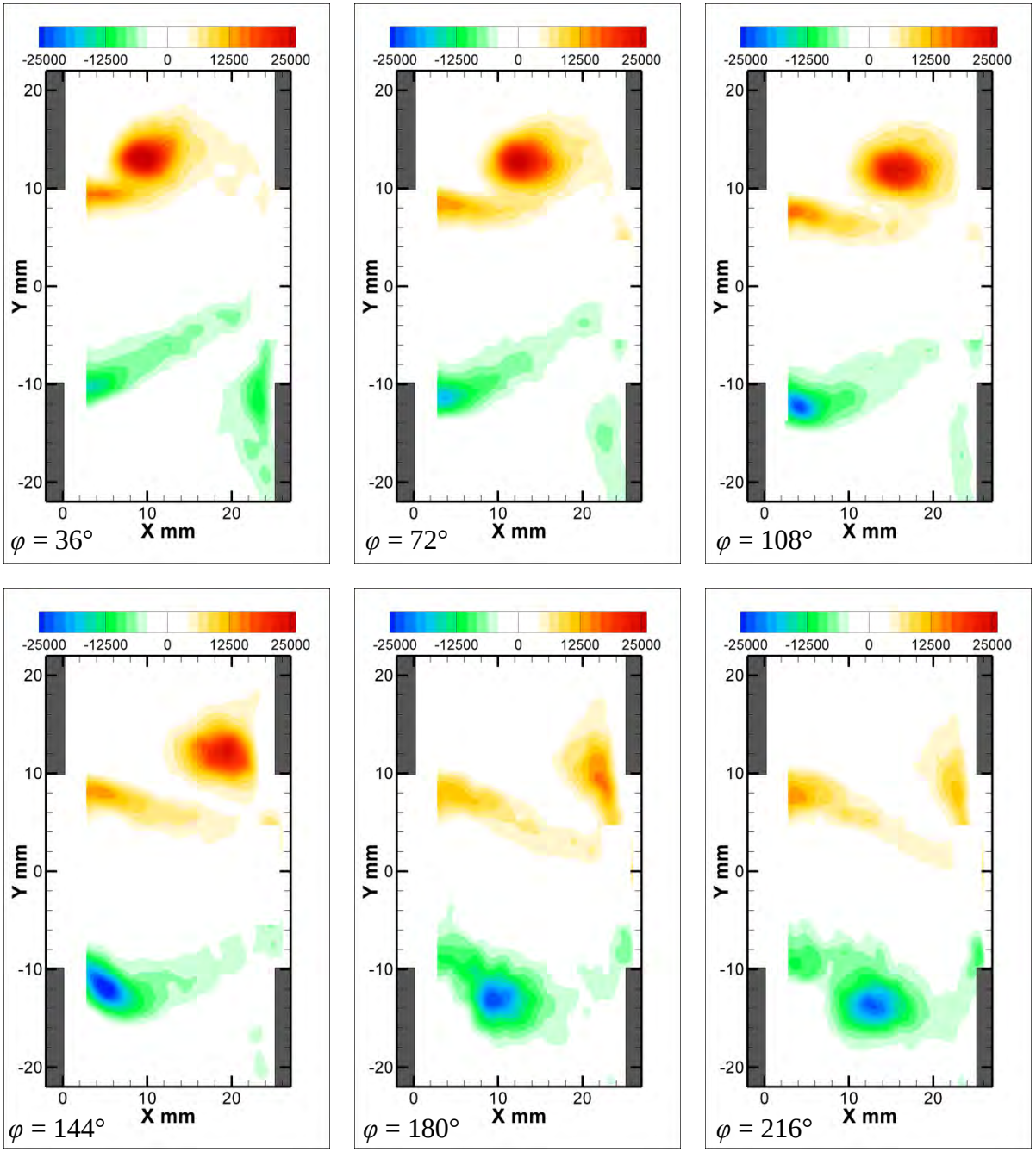

Figure B.9: Patterns of phase-averaged out-of-plane vorticity (s^{-1}) corresponding to the upstream case L_C = 3.81 mm, φ = 36° through 216°.

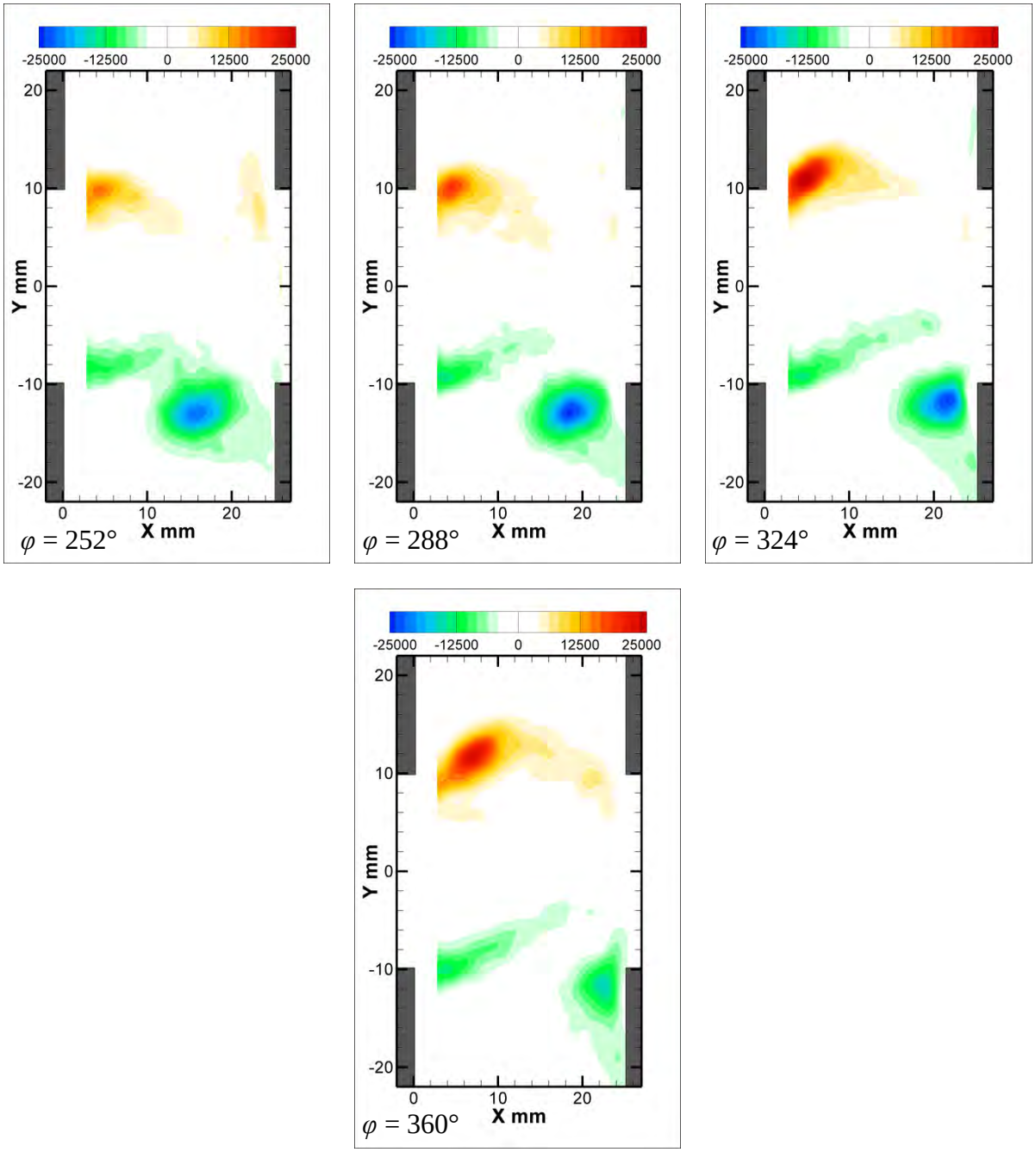

Figure B.10: Patterns of phase-averaged out-of-plane vorticity (s^{-1}) corresponding to the upstream case L_C = 3.81 mm, φ = 252° through 360°.

APPENDIX C: NORMAL GEOMETRY, PHASE-AVERAGED FLOW PATTERNS

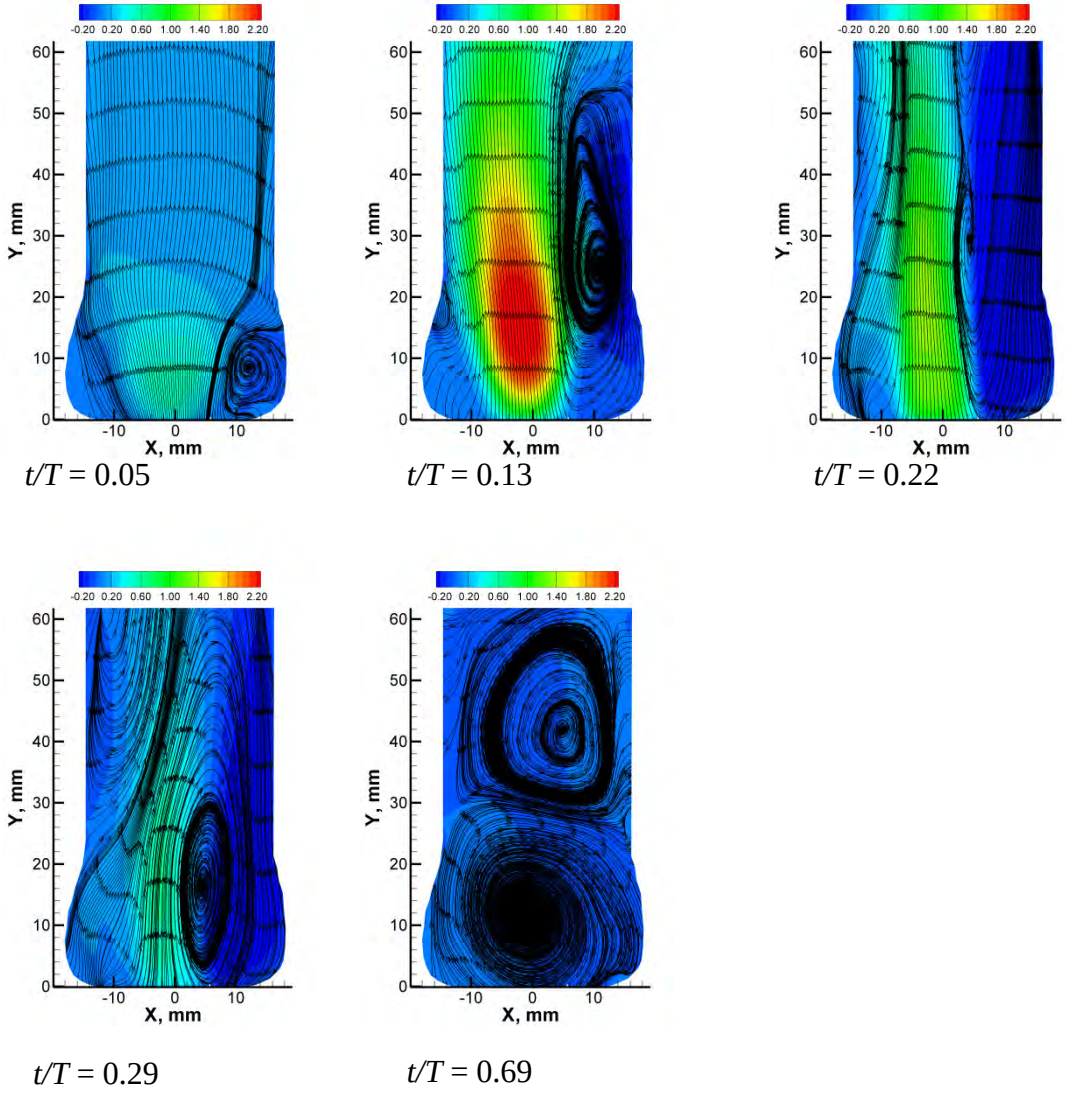

Figure C.1: Streamline patterns and contours of velocity magnitude (V_{avg}, m/s) in Plane 1, Normal geometry.

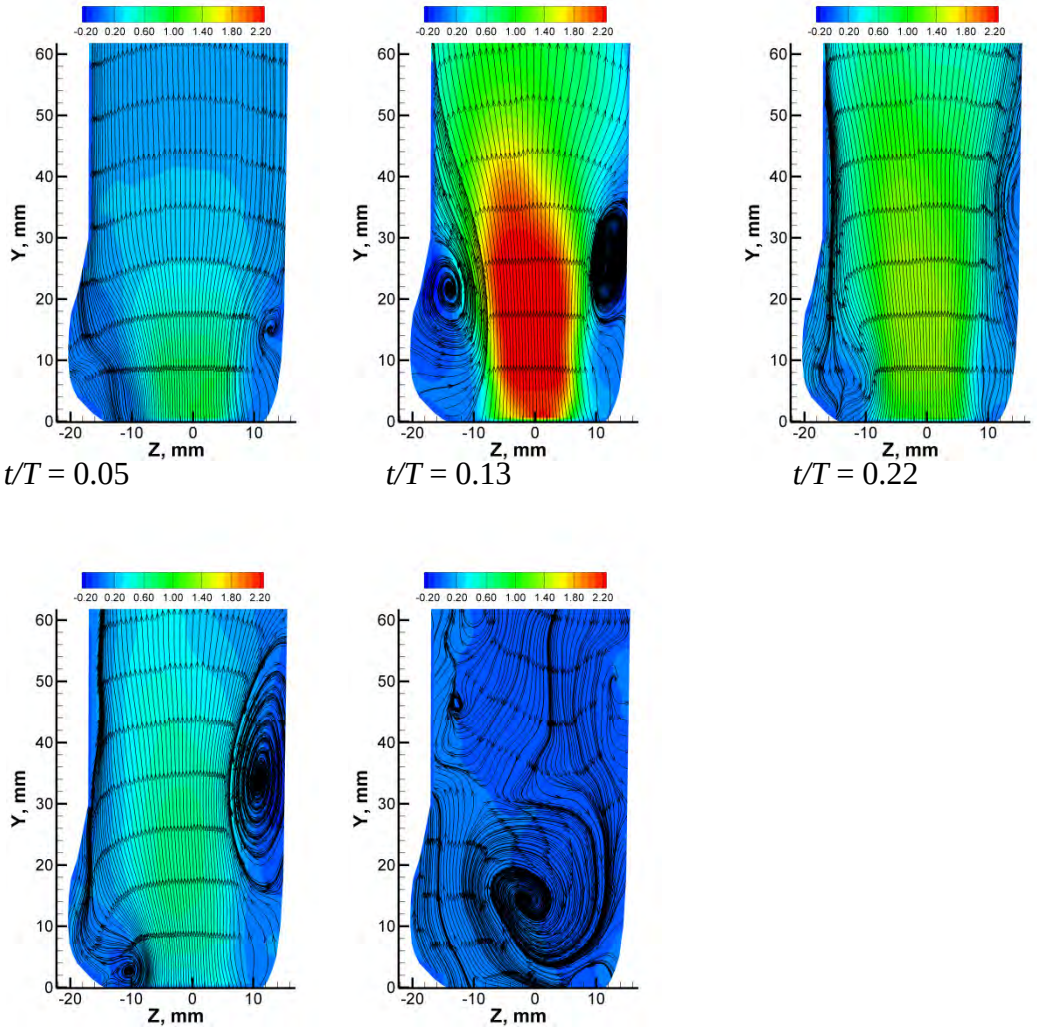

Figure C.2: Streamline patterns and contours of velocity magnitude (V_{avg}, m/s) in Plane 2, Normal geometry.

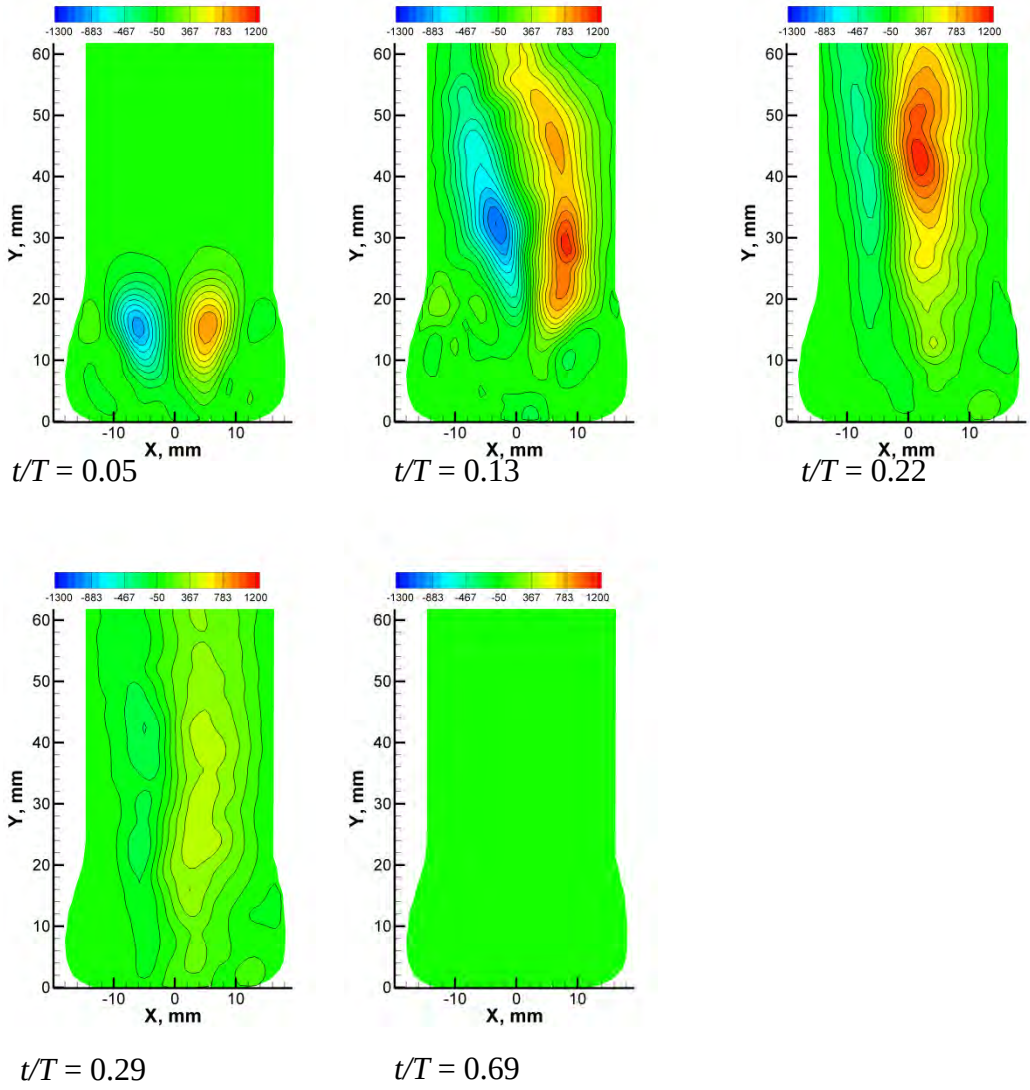

Figure C.3: Contours of RSS (dyne/cm^2) in Plane 1, Normal geometry.

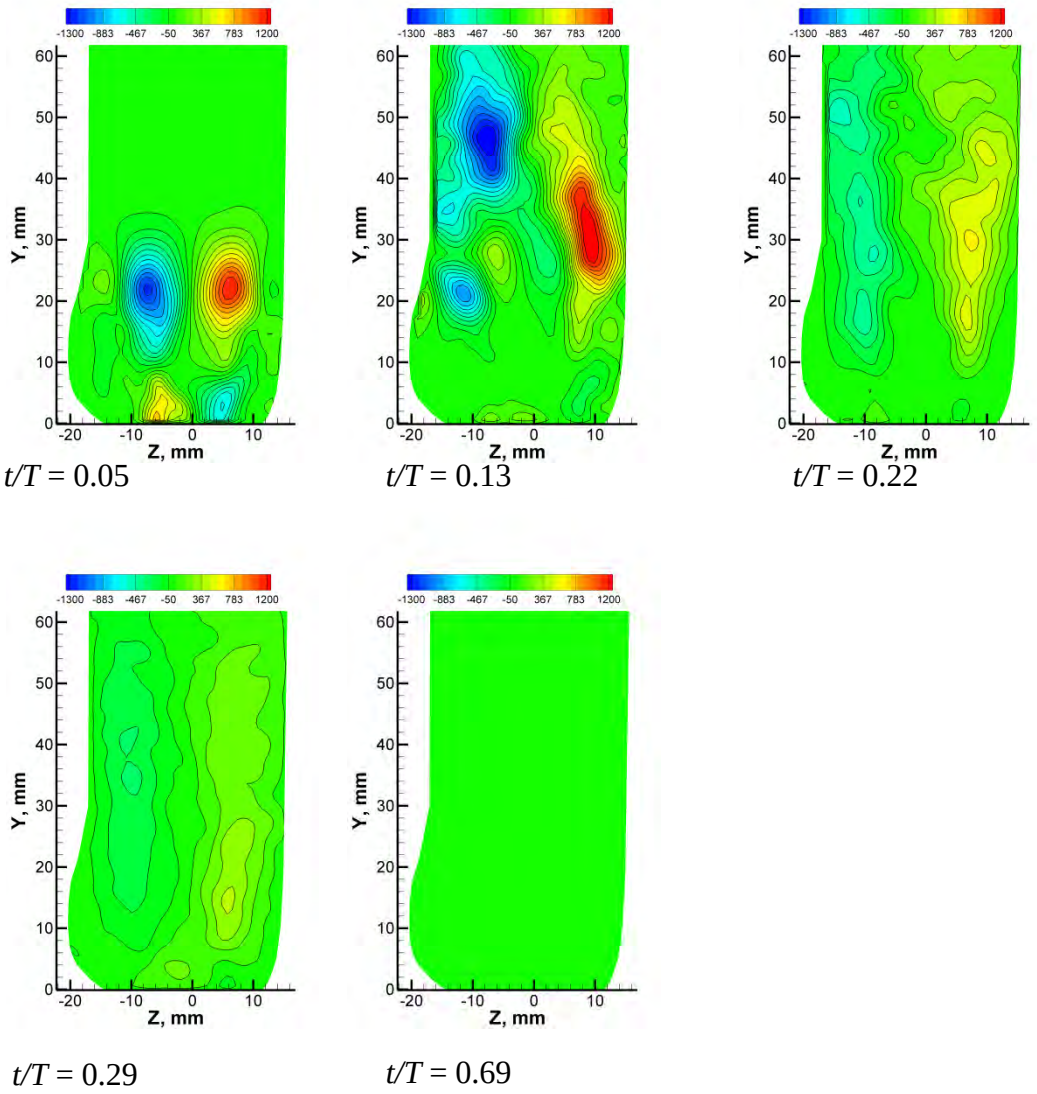

Figure C.4: Contours of RSS (dyne/cm^2) in Plane 2, Normal geometry.

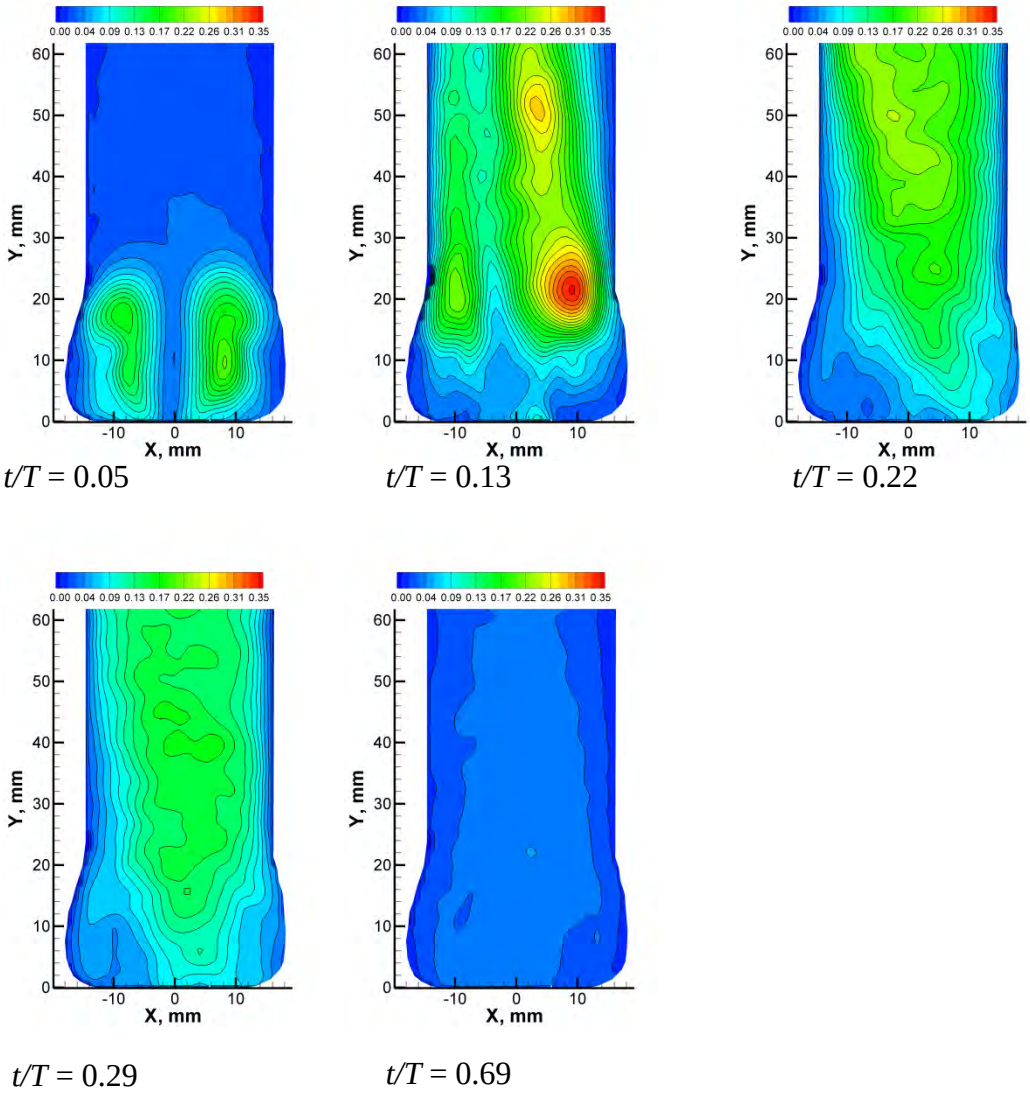

Figure C.5: Contours of u_{rms} (m/s) in Plane 1, Normal geometry.

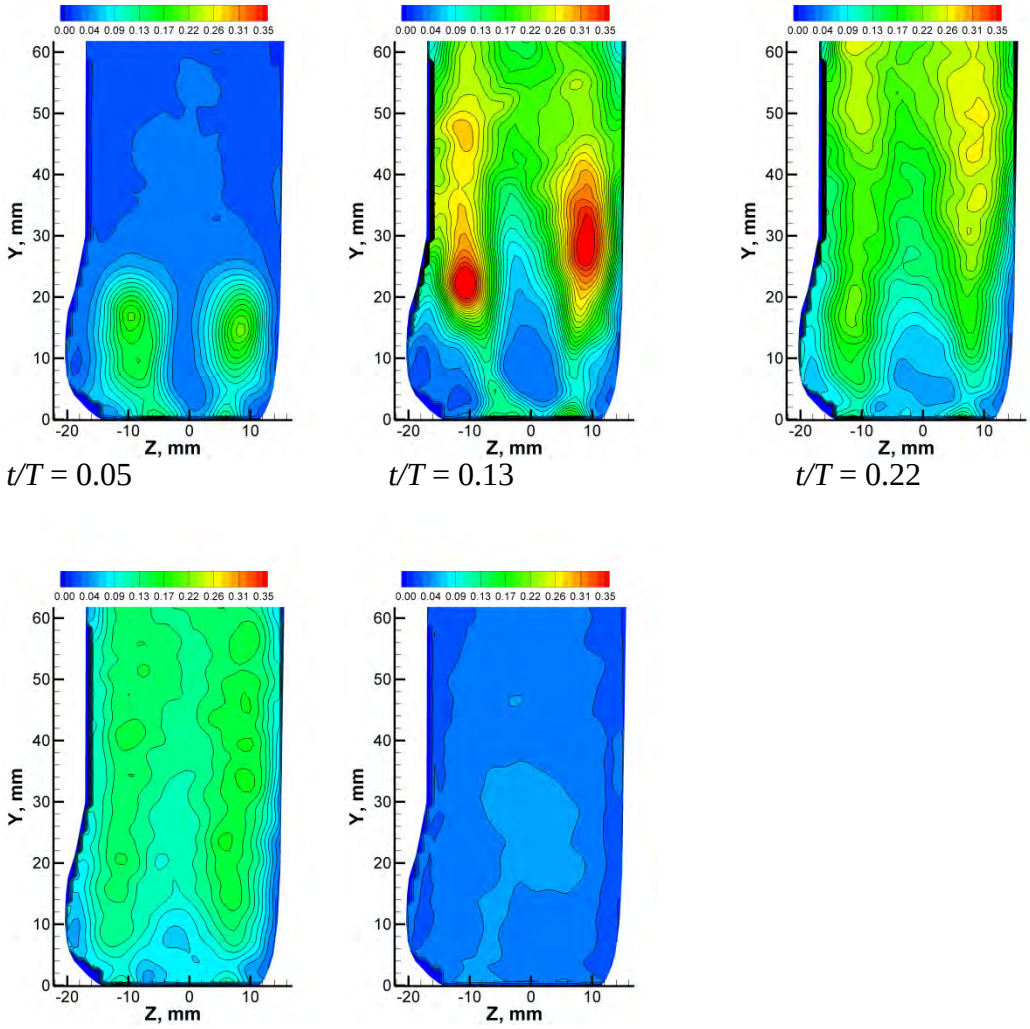

Figure C.6: Contours of u_{rms} (m/s) in Plane 2, Normal geometry.

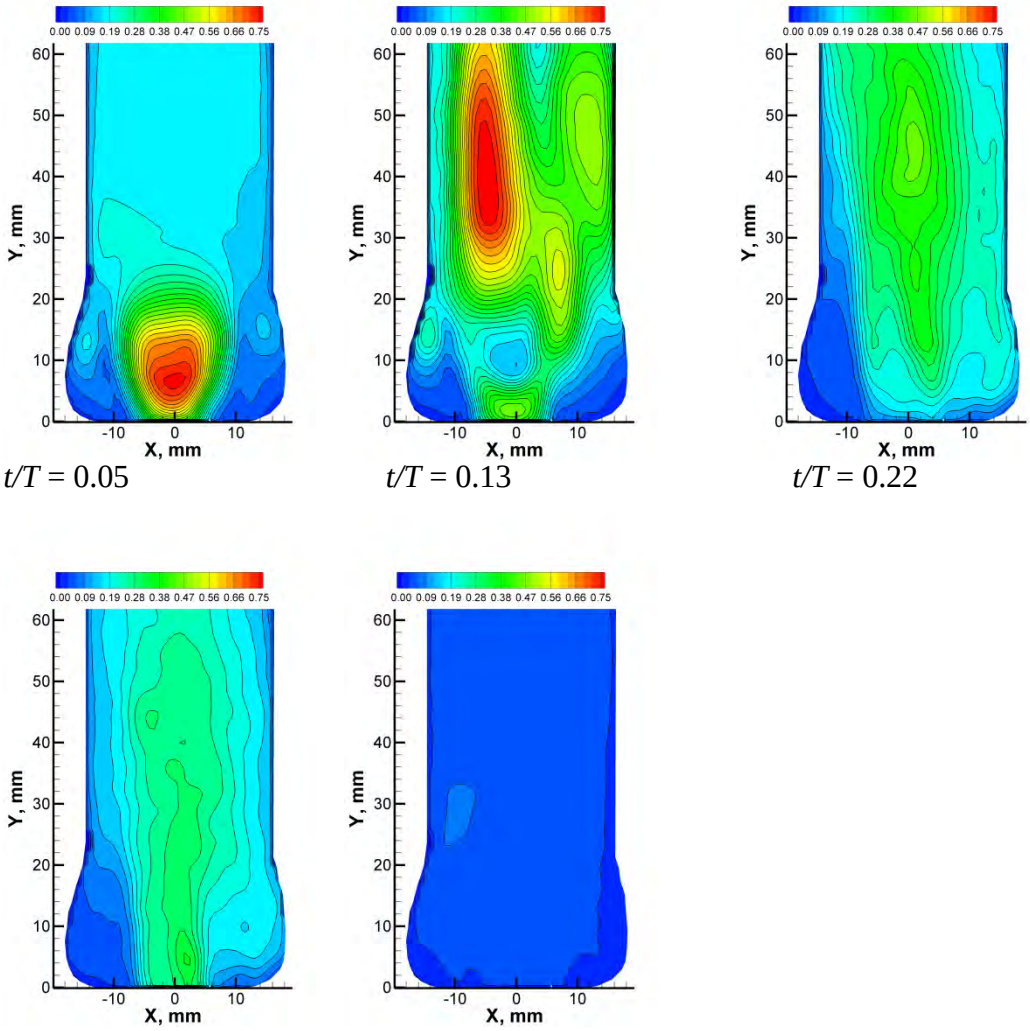

t/T = 0.05 *t/T* = 0.13 *t/T* = 0.22

t/T = 0.29 *t/T* = 0.69

Figure C.7: Contours of v_{rms} (m/s) in Plane 1, Normal geometry.

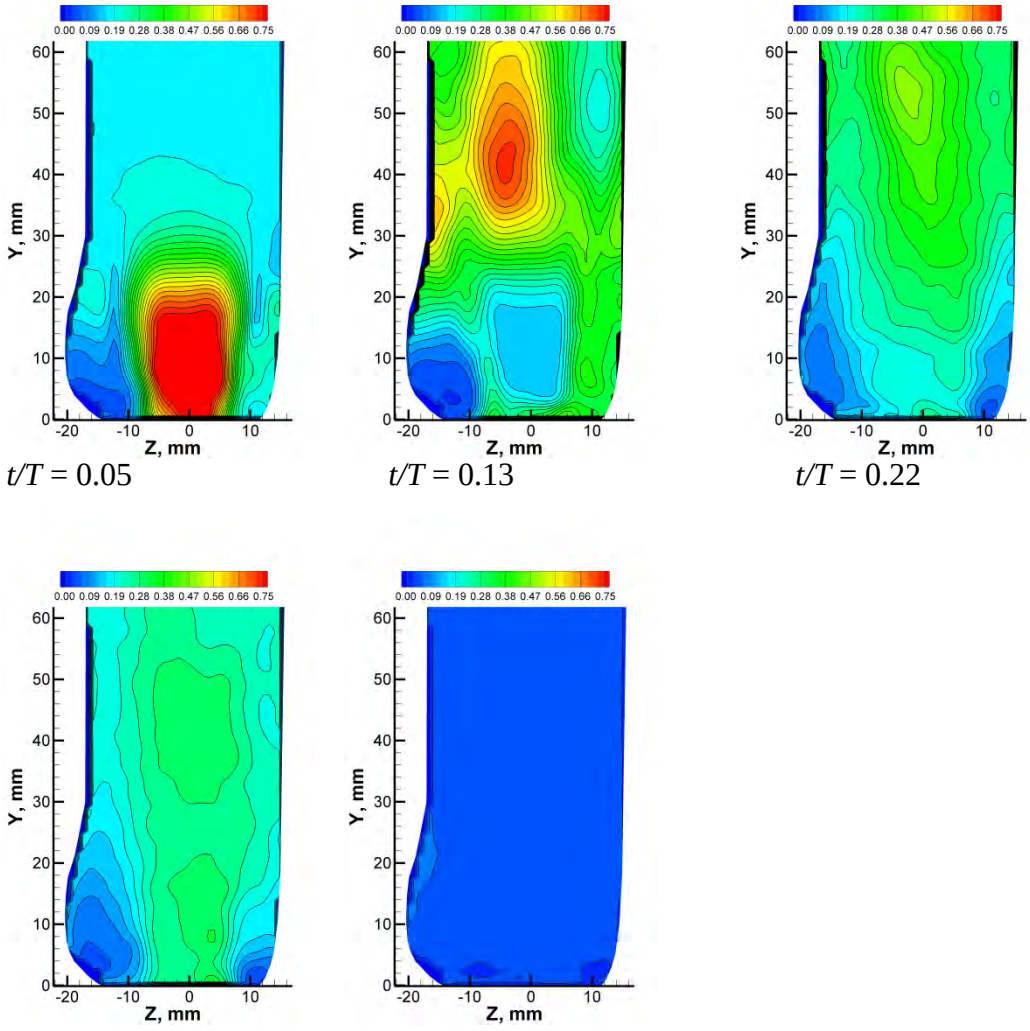

t/T = 0.05 *t/T* = 0.13 *t/T* = 0.22

t/T = 0.29 *t/T* = 0.69

Figure C.8: Contours of v_{rms} (m/s) in Plane 2, Normal geometry.

APPENDIX D: SEVERE STENOSIS, PHASE-AVERAGED FLOW PATTERNS

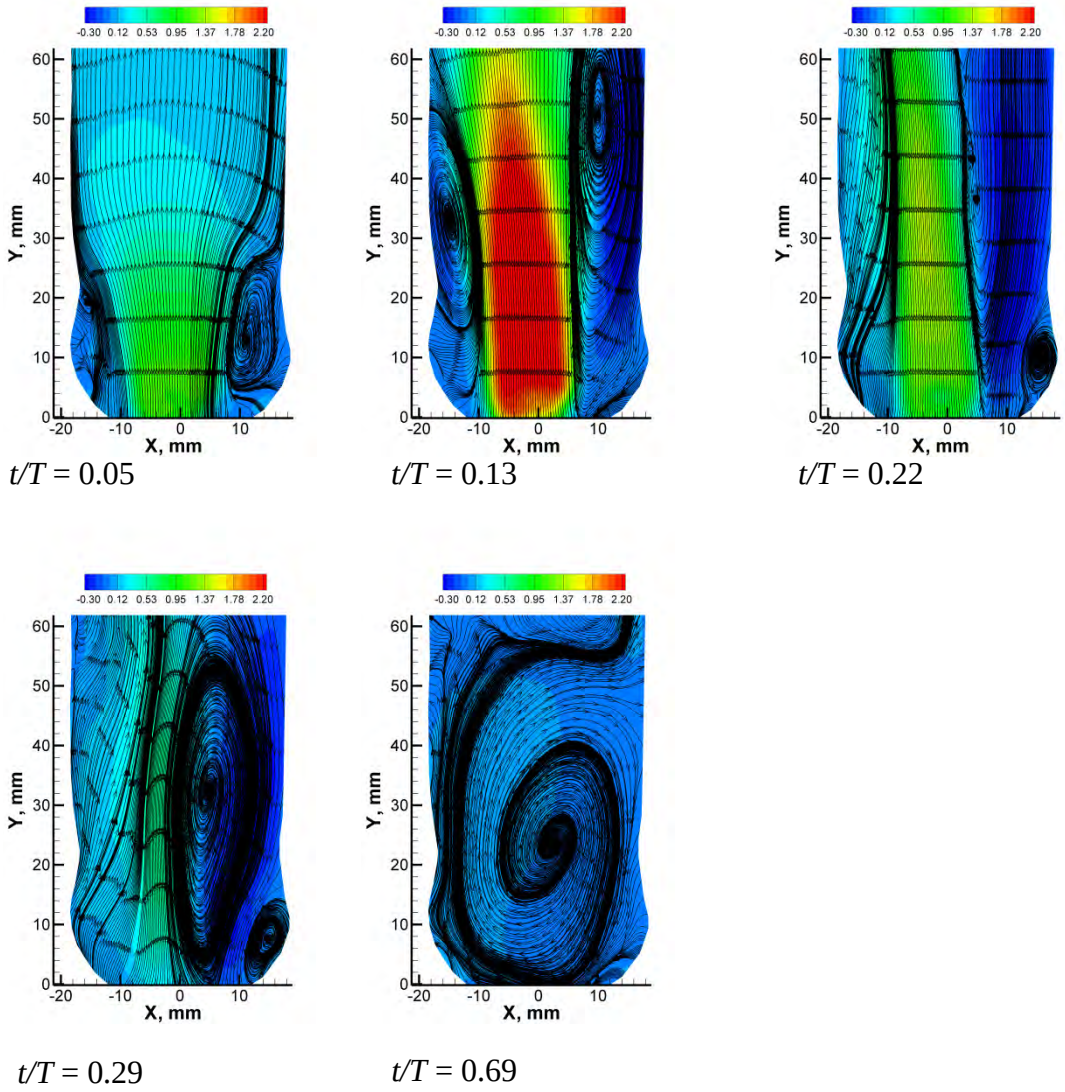

Figure D.1: Streamline patterns and contours of velocity magnitude (V_{avg}, m/s) in Plane 1, Severe stenosis.

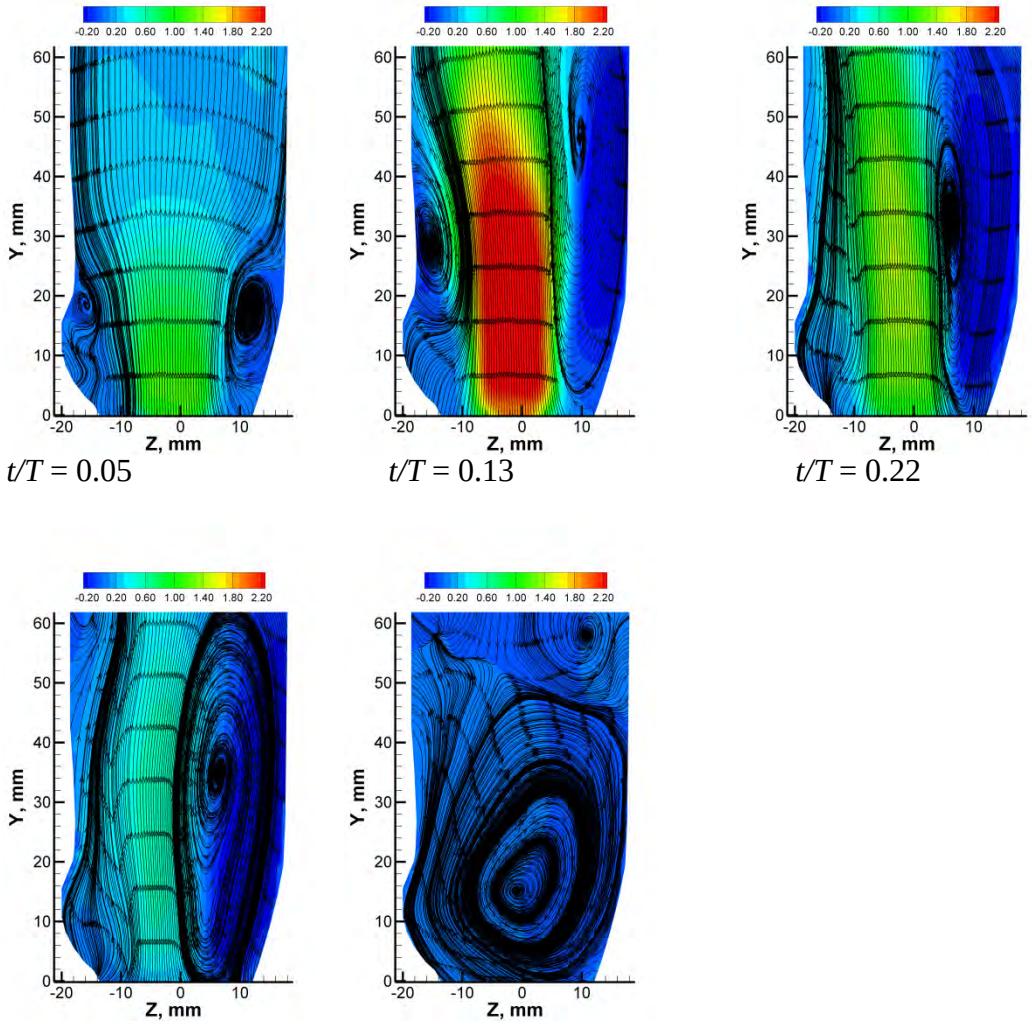

Figure D.2: Streamline patterns and contours of velocity magnitude (V_{avg}, m/s) in Plane 2, Severe stenosis.

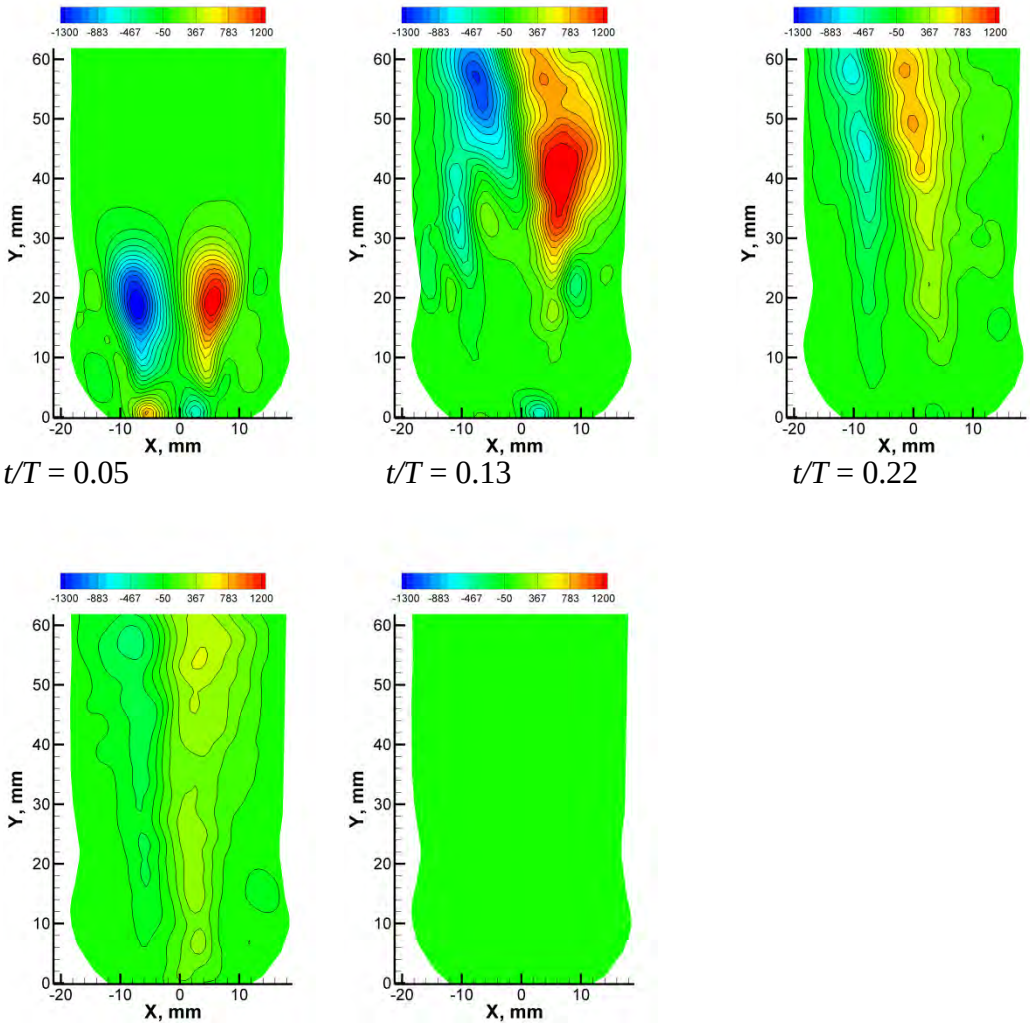

Figure D.3: Contours of RSS (dyne/cm^2) in Plane 1, Severe stenosis.

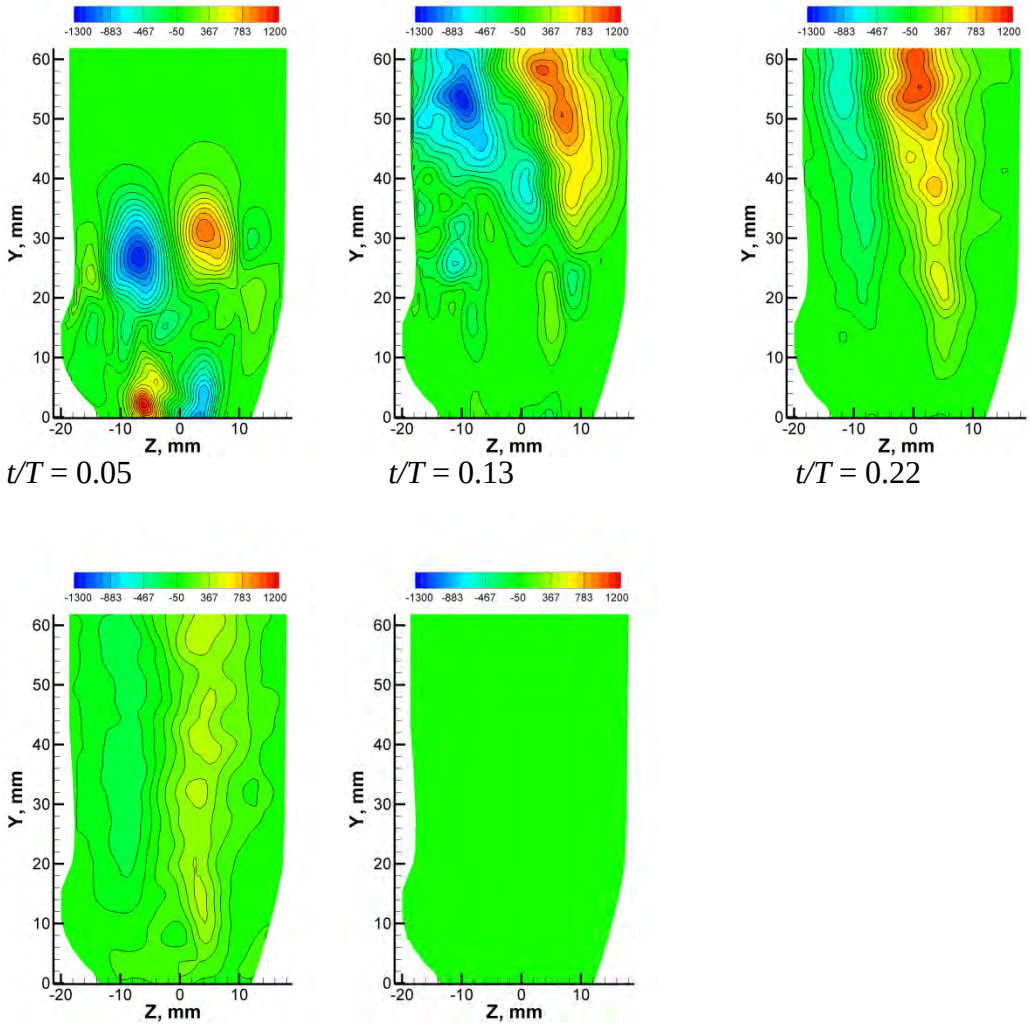

Figure D.4: Contours of RSS (dyne/cm^2) in Plane 2, Severe stenosis.

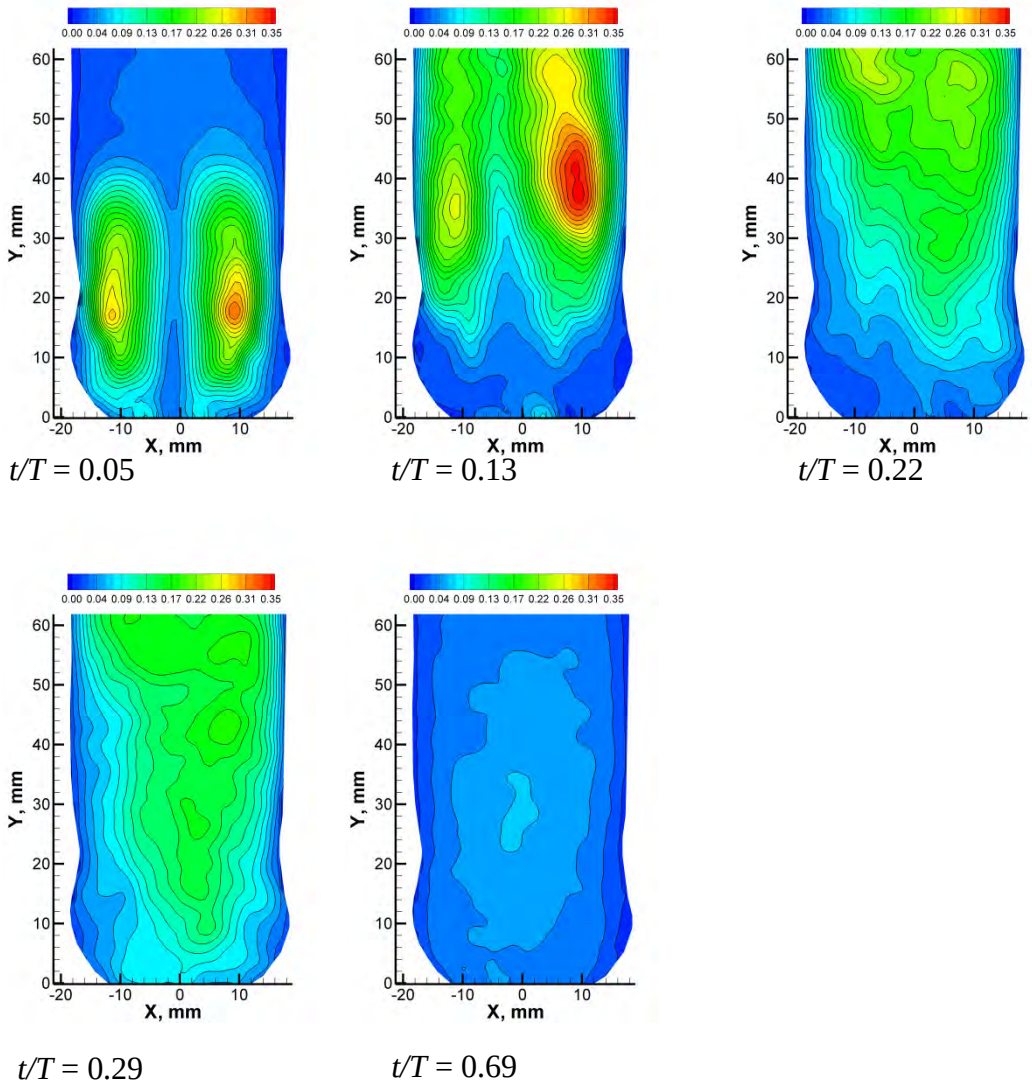

Figure D.5: Contours of u_{rms} (m/s) in Plane 1, Severe stenosis.

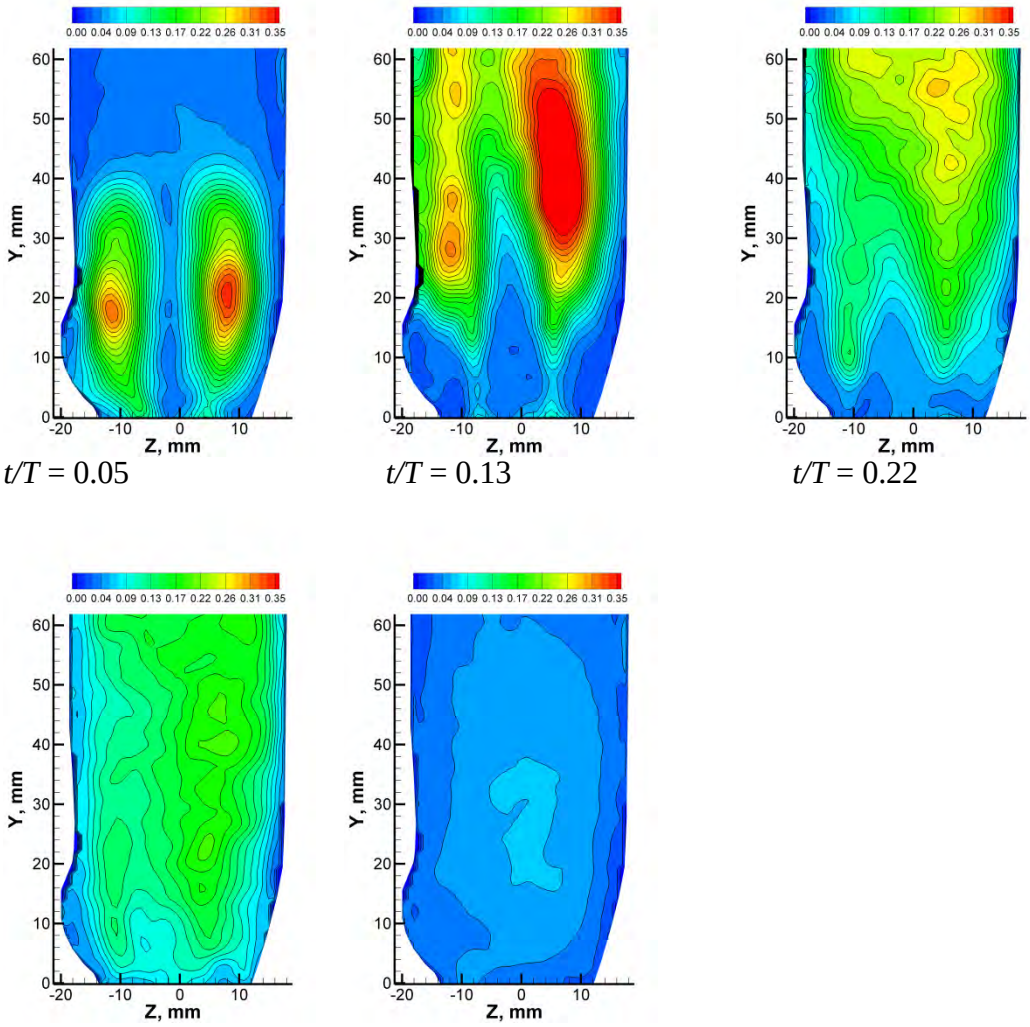

Figure D.6: Contours of u_{rms} (m/s) in Plane 2, Severe stenosis.

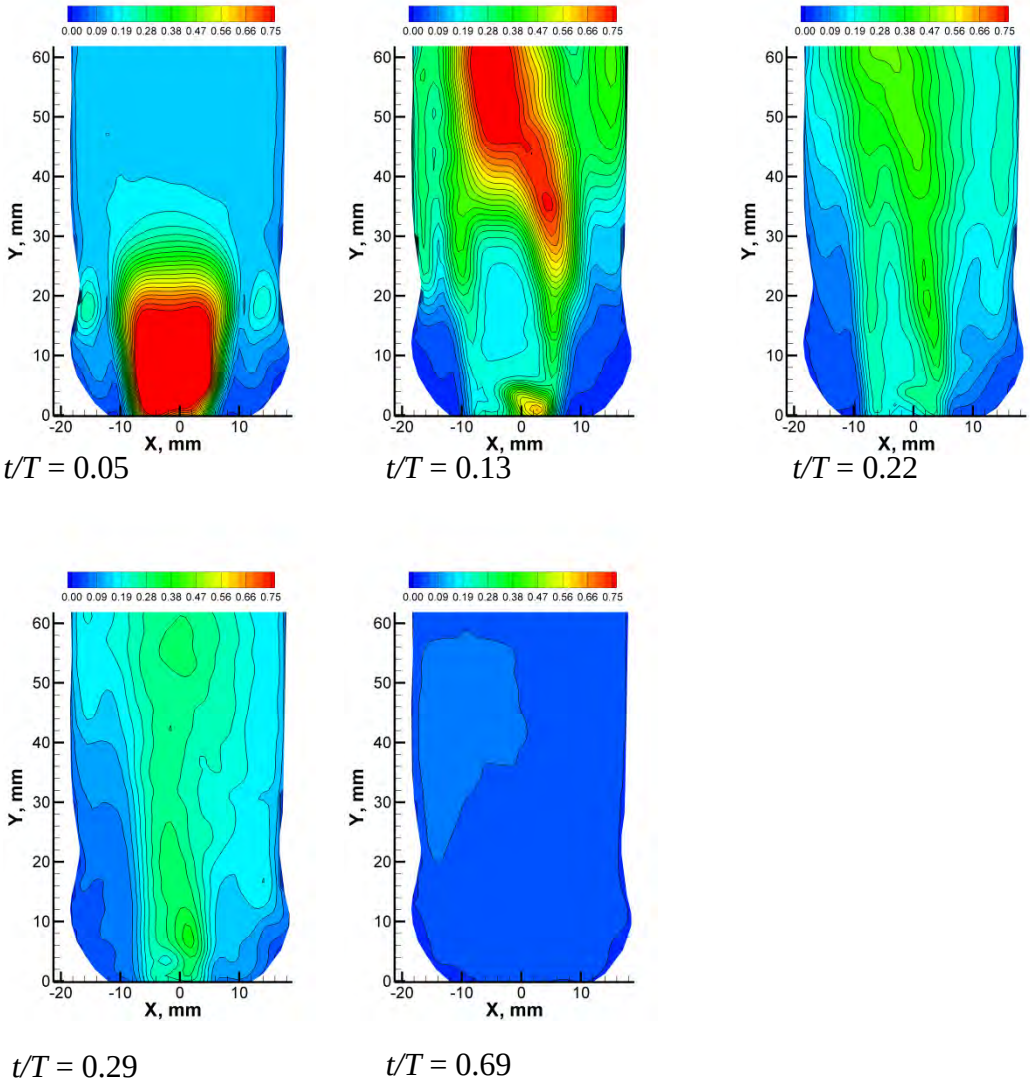

Figure D.7: Contours of v_{rms} (m/s) in Plane 1, Severe stenosis.

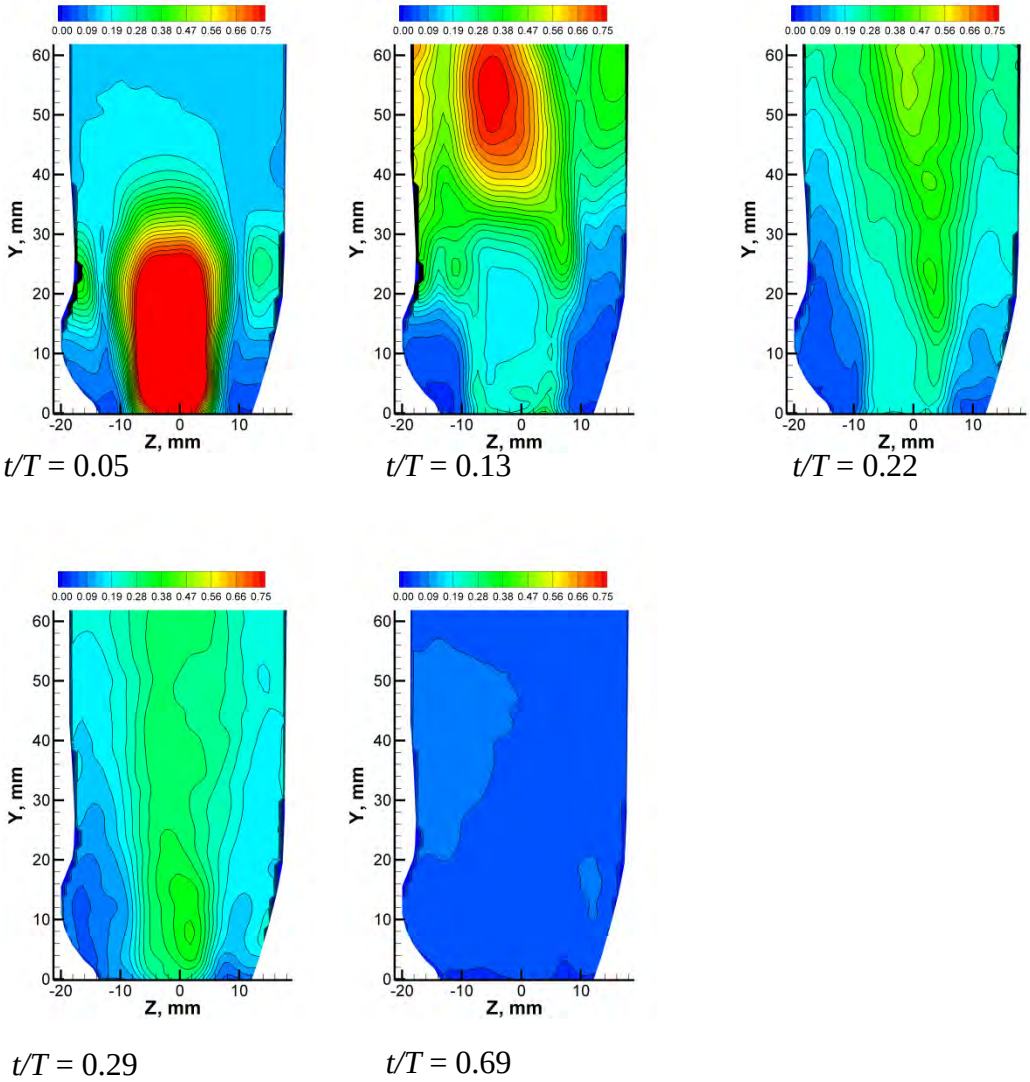

Figure D.8: Contours of v_{rms} (m/s) in Plane 2, Severe stenosis.

APPENDIX E: SEVERE INSUFFICIENCY, PHASE-AVERAGED FLOW PATTERNS

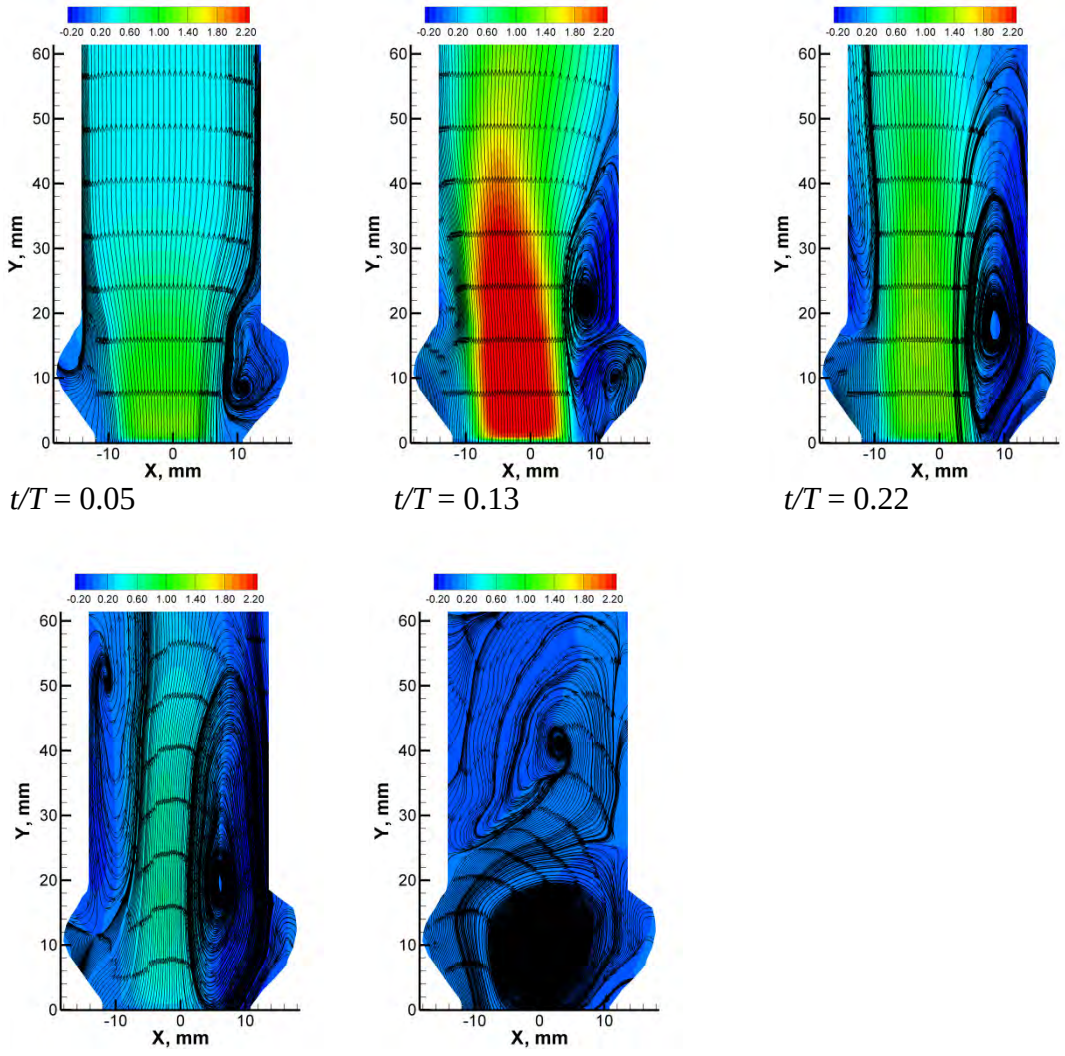

t/T = 0.05 *t/T* = 0.13 *t/T* = 0.22

t/T = 0.29 *t/T* = 0.69

Figure E.1: Streamline patterns and contours of velocity magnitude (V_{avg}, m/s) in Plane 1, Severe insufficiency.

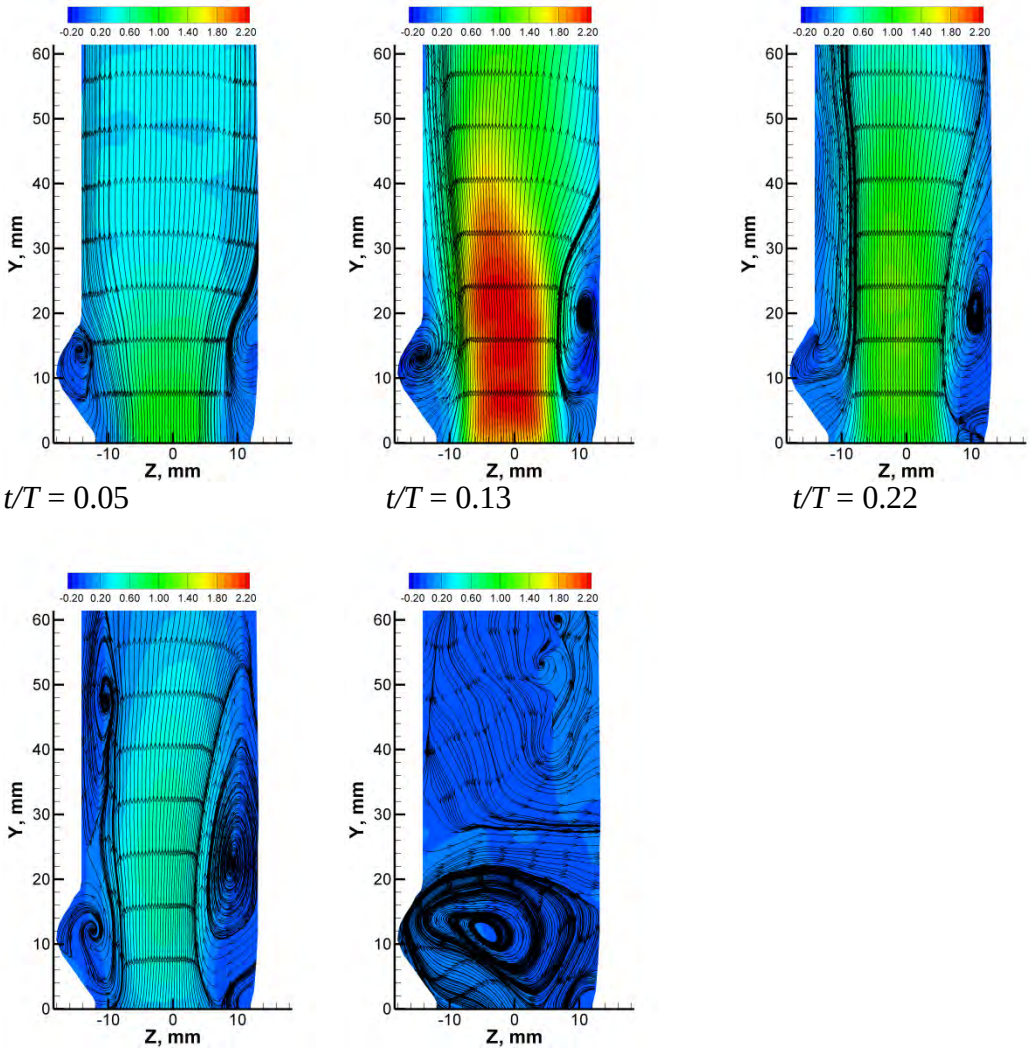

t/T = 0.05 *t/T* = 0.13 *t/T* = 0.22

t/T = 0.29 *t/T* = 0.69

Figure E.2: Streamline patterns and contours of velocity magnitude (V_{avg}, m/s) in Plane 2, Severe insufficiency.

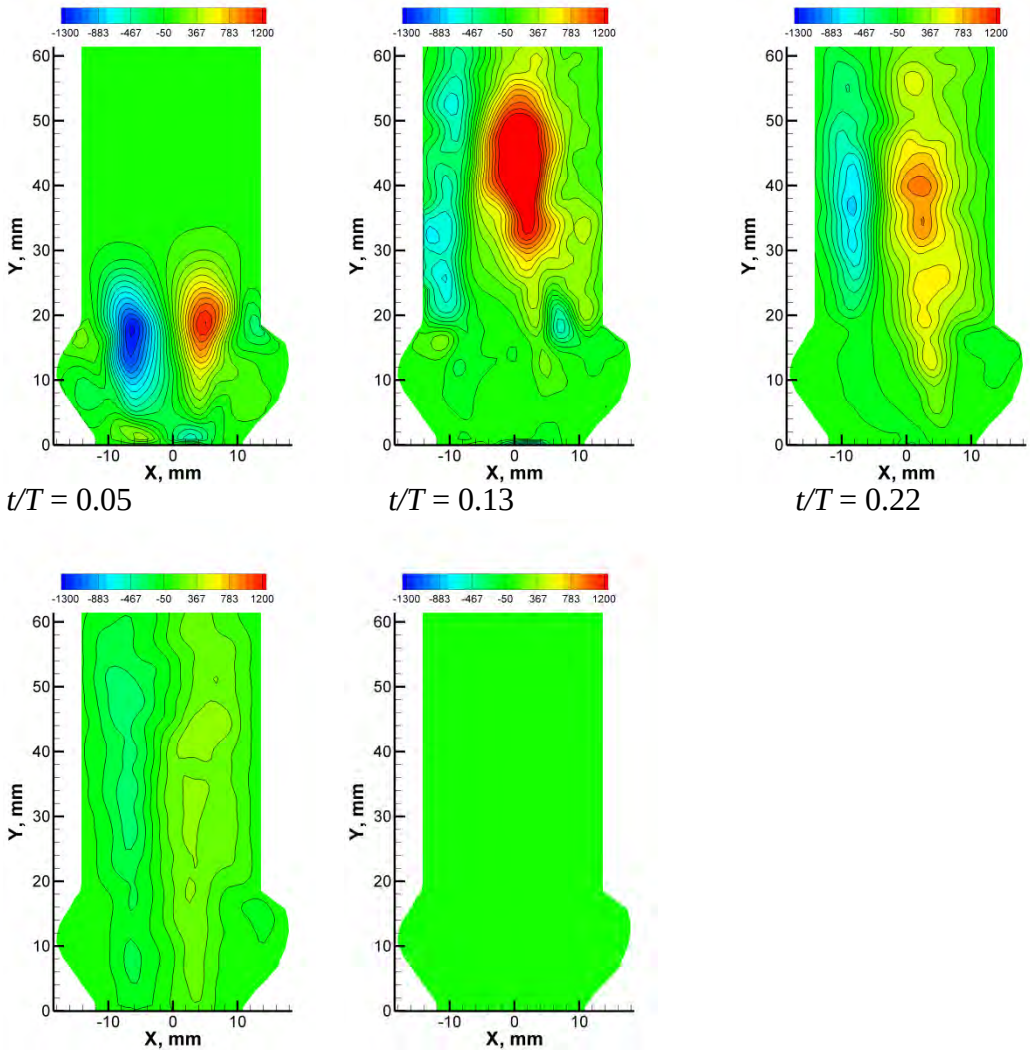

t/T = 0.05 *t/T* = 0.13 *t/T* = 0.22

t/T = 0.29 *t/T* = 0.69

Figure E.3: Contours of RSS (dyne/cm^2) in Plane 1, Severe insufficiency.

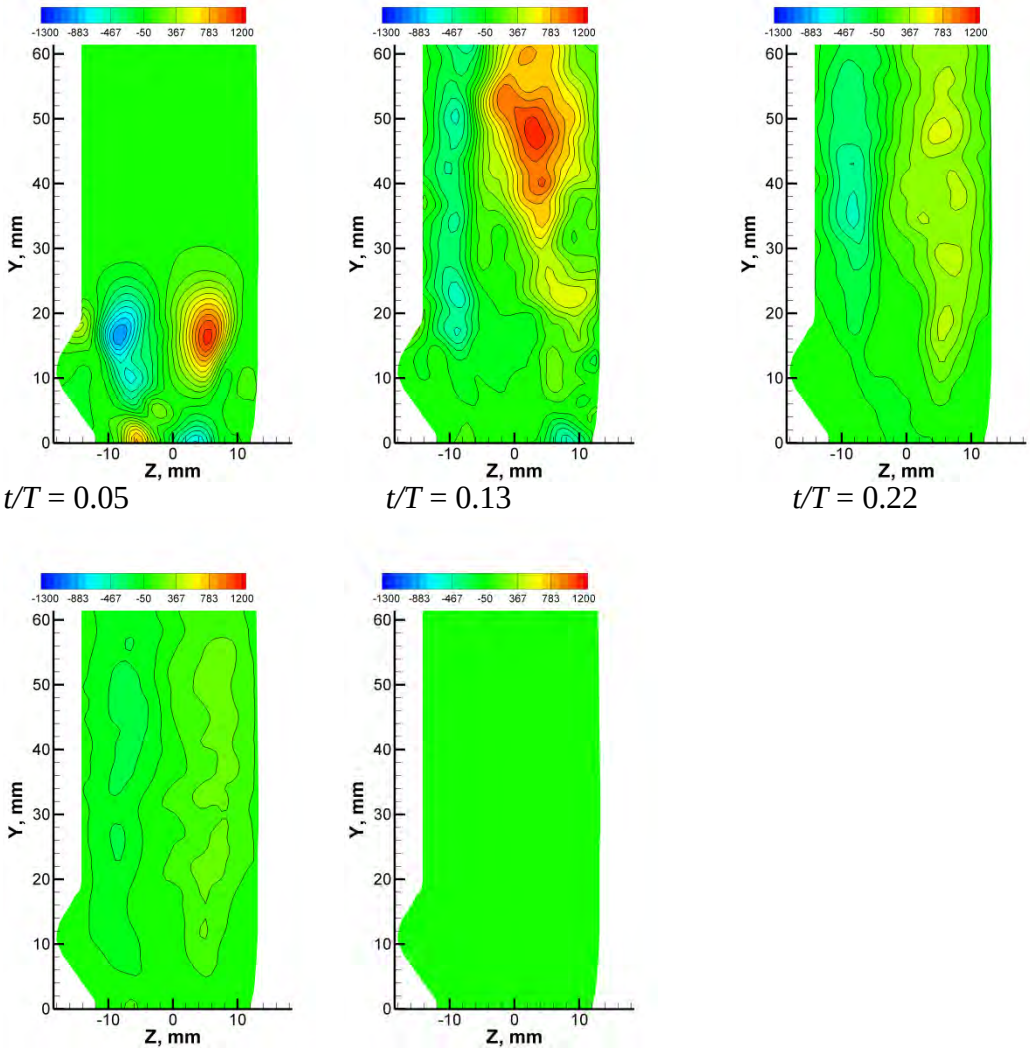

Figure E.4: Contours of RSS (dyne/cm^2) in Plane 2, Severe insufficiency.

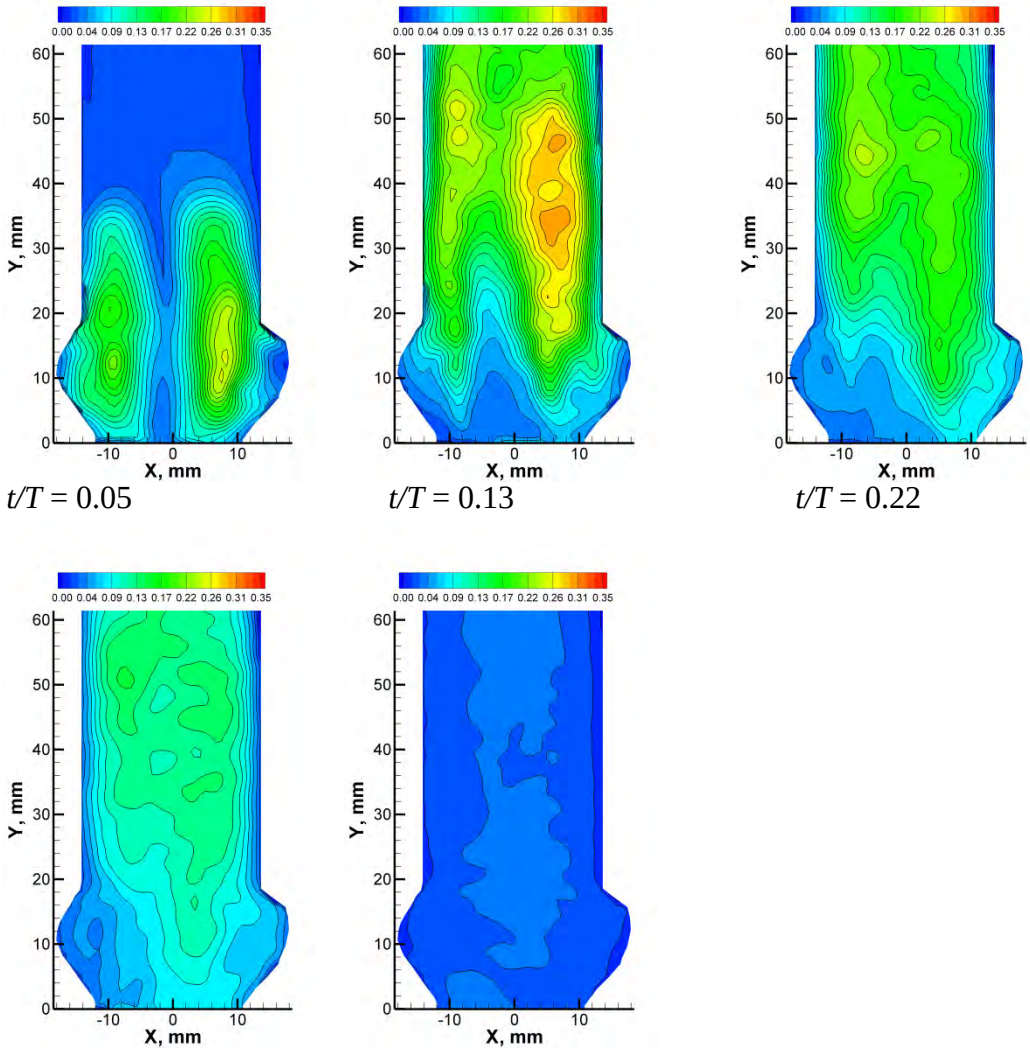

t/T = 0.05 *t/T* = 0.13 *t/T* = 0.22

t/T = 0.29 *t/T* = 0.69

Figure E.5: Contours of u_{rms} (m/s) in Plane 1, Severe insufficiency.

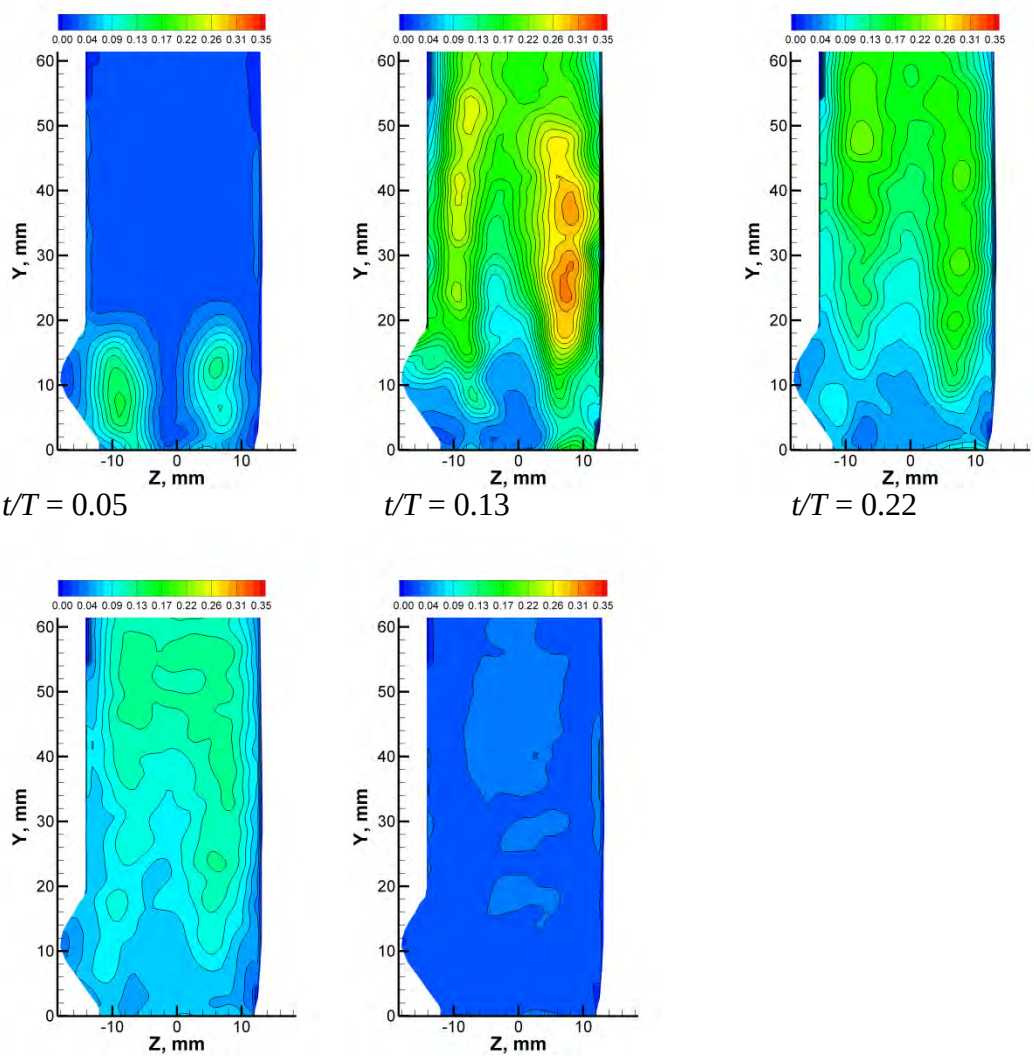

t/T = 0.05 *t/T* = 0.13 *t/T* = 0.22

t/T = 0.29 *t/T* = 0.69

Figure E.6: Contours of u_{rms} (m/s) in Plane 2, Severe insufficiency.

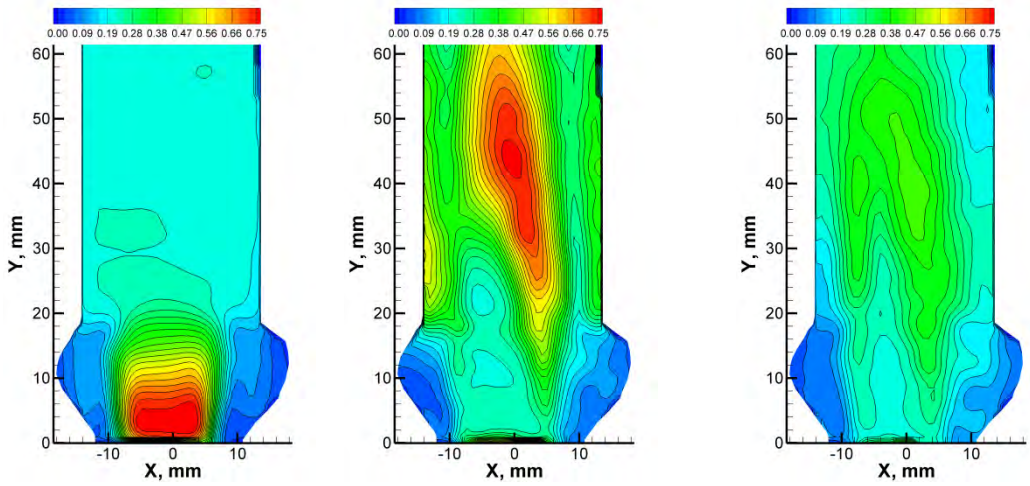

t/T = 0.05 *t/T* = 0.13 *t/T* = 0.22

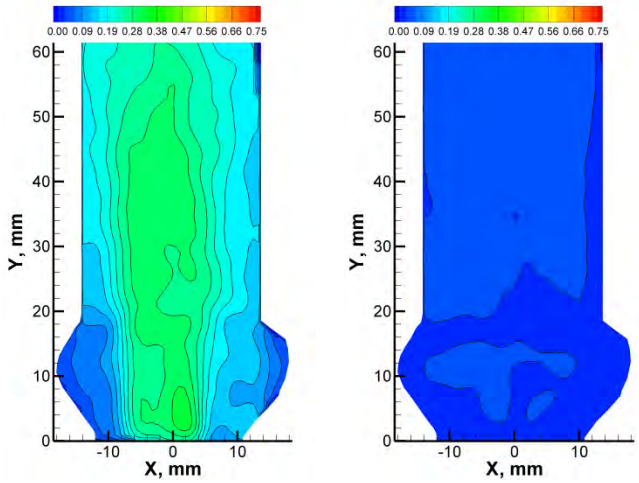

t/T = 0.29 *t/T* = 0.69

Figure E.7: Contours of v_{rms} (m/s) in Plane 1, Severe insufficiency.

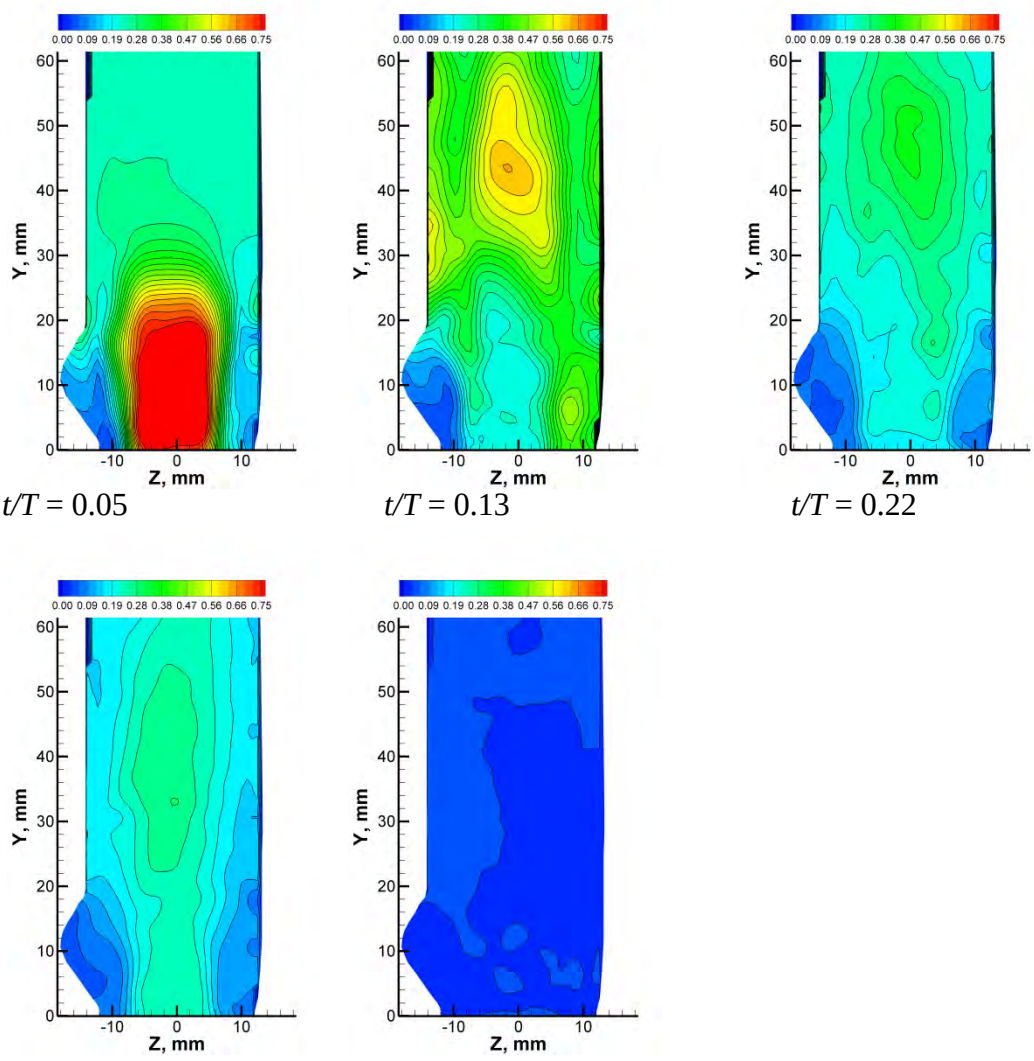

t/T = 0.05 *t/T* = 0.13 *t/T* = 0.22

t/T = 0.29 *t/T* = 0.69

Figure E.8: Contours of v_{rms} (m/s) in Plane 2, Severe insufficiency.

APPENDIX F: ISSUES, LIMITATIONS AND FUTURE WORK

Shallow circular axisymmetric cavity

The size of the experimental apparatus, and, in particular, the diameter of the inflow pipeline imposed a great limitation on the range of inflow velocity. As a result of this limitation the pipeline-cavity system was only tested over the low range of inflow velocity, typically used in the actual power plant. In addition to that, the physical dimensions of the cavity did not allow for any flow visualisation, which in turn limited the current study to the analysis of the acoustic pressure data and finite element numerical simulations.

As a possible extension of this work, one might consider adjusting inflow velocity conditions to match those of the cold-reheat section of the actual power plant. In addition to that, it would be fruitful to analyze the change in the oscillation structural amplitude of the pipeline-cavity system on the route to resonance and test various designs of passive and active vibration isolation systems, as an alternative to geometry modifications of the converging/diverging section of the original pipeline-cavity system.

Deep circular axisymmetric cavity

In this part of the dissertation, the cavity geometry represented an idealized case, related to circular, axisymmetric cavities of the gate valves that are present in the steam delivery system of a power plant. Although the gate valves are typically associated with relatively shallow cavities, the usage of deeper circular cavity allowed increasing the degree of confinement of the diametral modes to the vicinity of the cavity and provide results that might be relevant to annular combustion applications and high speed axial compressors (Hellmich and

Seume, 2008, Sensiau et al., 2009), typically associated with deeper circular cavities. In addition to the limitations induced by the design of experimental apparatus, the following challenges and constrains were experienced:

1) Optical challenges during PIV experiments
    a. Optical access into a highly-constrained geometry
    b. Reflections from the interior cavity walls
    c. Accumulation of the DEHS oil in the cavity and in the inlet/outlet pipelines
2) Presence of out-of-plane particles in the field of view

During the preparation stage of the experiments, it was possible to address some the issues listed above. In particular, the way how constraints associated with item 1) a. and b. were addressed is summarized in Section 2.2.2.

In the case of item 1)c., a routine for regular maintenance of the pipeline-cavity system was adopted, which completely negated the critical accumulation of the oil in the inlet/outlet pipelines and in the cavity itself.

In the case of constraint 2), one deals with a high level of background noise as a result of illumination of out-of-plane particles. In order to overcome this difficulty, it was ensured that the laser sheet thickness was thin enough, typically about 1 mm to avoid spatial averaging of the velocity (Hirahara et al., 2007). In this work, a combination of thin laser sheet in conjunction with very shallow depth of field, introduced by a 50 mm f/1.4 camera lens allowed to reduce the effects from out-of-plane particles to a minimum. Due to strong reflections from the inside surface of the inlet pipe, the region right near the upstream edge of the cavity was masked out in order to avoid error propagation in the vorticity calculation.

In the attempt to experimentally validate the effectiveness of passive control methods on generation of noise and vibration, two different approaches were implemented. The first approach was associated with geometric modifications of the cavity edges and was aimed at controlling the development of fee shear layer at the upstream cavity edge and the way how it interacts with the downstream edge of the cavity. The second approach attempted to control the azimuthal behaviour of acoustic diametral modes of the cavity, by introducing either short or long splitter plate. Both approaches can be successfully extended to a more robust set of passive or active counter measures that can be introduced in the industrial environment. In particular, one can consider the following future extensions of this work:

1. In this work, it was shown the effectiveness of modifying the upstream edge of the cavity in order to shift the development of strong acoustic resonance beyond the operation limits of the system. In addition to that, in one of the earlier works (Bolduc et al., 2013), it was shown that introduction of chevron-shaped spoilers or vortex generators to the upstream edge of the cavity can be very effective when dealing with the same problem. As it was shown in this dissertation, at the highest range of inflow velocity, the system experienced a simultaneous excitation of several acoustic diametral modes, in which case a single geometric modification of the cavity edge might not always be optimal. As an alternative, one can consider development of an active control mechanism, represented by a flexible strip, introduced at the leading edge of the cavity, with variable and controllable mass/stiffness distribution that would allow tuning its natural frequency to an optimal value that would lead to noise and vibration suppression at the full range of inflow velocity.

2. In this dissertation, control on the azimuthal behaviour of acoustic diametral modes of the cavity was attempted by introducing either short or long splitter plate. Only a single plate of each size was used. The natural extension of this work would be to optimize the effective length of the plate and then verify the minimal number of splitter plates required for optimal control of the azimuthal behaviour of acoustic diametral modes of the cavity.
3. This dissertation was aimed for experimental verification of passive noise and vibration control mechanisms. A natural extension of this work would be to develop a model of the vorticity filed, which could achieve good analytical approximation of the experimental results, reported in this work. In particular, at the upstream region of the cavity, the shear layer oscillations can be approximated by a flapping sheet of vorticity, while at the center and close to the downstream edge of the cavity the shear layer can be represented by the formation of a discrete vortical structure, which partially detaches from the rest of the vorticity in the region.

Cardiovascular system

The results presented in this part of the dissertation revealed the dependence of Reynolds shear stress (RSS), and consequently possibility of platelet activation, on the geometry of aortic root. However, the exact mechanism behind rapid increase of RSS, the exposure time of fluid to the elevated levels of RSS, the influence of aortic root compliance on the flow patterns and the effect of aortic arch on the development of flow patterns still need to be ad-

dressed. For that purpose, it is suggested that the material presented in Chapter 7 should be expanded to address the above mentioned questions.

The future extension of the results reported in Chapter 7 will help to answer the following questions:

1. How does aortic root compliance influence hemolysis in polymeric heart valve prostheses? This study would be a natural extension of the current work and would require usage of current models of aortic root connected to the ViVitro Superpump root compliance chambers, along with the same models but made of an elastic material. Compliance reduction due to the aging of patients can be also successfully explored.
2. In this work, the effect of aortic torsion, branching, and curvature on blood flow was not considered, although, as it was shown in Chapter 7, the flow tend to bend towards the upper part of the aortic root, which suggests the helical nature of the flow in that region. Using a physiologically accurate mode of the aorta, one can evaluate the role of the torsion in the formation of the helical flow in the aortic arch and how the later one can be used in order to stabilizing the flow of blood in the aorta, and compensated the adverse effects of the aortic curvature on blood flow, thus reducing risk of atherosclerosis in the ascending aorta and in the aortic arch.

APPENDIX G: PERMISSION LETTERS FOR COPYRIGHTED MATERIAL

ViVitro Labs

Rob Fraser
Biomedical Engineer, MSc.
ViVitro Labs Inc
455 Boleskine Rd
Victoria, BC, V8Z 1E7, Canada
Phone: (250) 940-2429
E-mail: RFraser@vivitrolabs.com

October 10, 2013

Oleksandr Barannyk
Institute for Integrated Energy Systems
Fluid Mechanics Research Group, ELW A248
Department of Mechanical Engineering
University of Victoria
Phone:(250) 853-3182
E-mail: barannyk@uvic.ca

Dear Rob,

I am completing a PhD dissertation at the University of Victoria, British Columbia, Canada, entitled "Shear layer instabilities and flow-acoustic coupling in valves: Application to power plant components and cardiovascular devices." I would like your permission to reprint in my dissertation the following images:

1) PIV Assembly Complete Image
2) PIV Test Section

The requested permission extends to any future revisions and editions of my dissertation, including non-exclusive world rights in all languages, and to the prospective publication of my dissertation by the National Library of Canada and Proquest. Dissertations published at the University of Victoria are also made digitally available on the Internet for public access via the university's Institutional Repository (UVic DSpace). For more information on the UVic DSpace see: https://dspace.library.uvic.ca:8443/dspace/.

These rights will in no way restrict republication of the material in any other form by you or by others authorized by you. Your signing of this letter will also confirm that your company owns the copyright to the above-described material.

If these arrangements meet with your approval, please sign this letter where indicated below and return it to me in the enclosed return envelope. Thank you very much.

Sincerely,

Oleksandr Barannyk

PERMISSION GRANTED FOR THE USE REQUESTED ABOVE:

National Heart, Lung, and Blood Institute; National Institutes of Health; U.S. Department of Health and Human Services.

Dear Mr. Barannyk:

Thank you for your inquiry to the National Heart, Lung, and Blood Institute (NHLBI) Health Information Center about NHLBI's copyright policy.

Unless specified otherwise, the text of and information contained in materials published by the NHLBI are in the public domain. No further permission is required to reproduce or reprint the text in whole or in part. This applies to print publications, graphics, and animations in the NHLBI's Health Topics index as well as documents and content from the NHLBI website. The NHLBI asks only that no changes be made to the content of the materials, and that the material as well any NHLBI Internet links not be used in any direct or indirect product endorsement or advertising. Organizations may add their own logo or name.

Please use the following language to cite the source of the materials: Source: National Heart, Lung, and Blood Institute; National Institutes of Health; U.S. Department of Health and Human Services. Your assistance in making our research and health-related information available to the largest number of people possible is greatly appreciated.

Sincerely,

NHLBI Health Information Center
P.O. Box 30105
Bethesda, MD 20824
Phone: 301-592-8573
Email: nhlbiinfo@nhlbi.nih.gov
Website: http://www.nhlbi.nih.gov

Springer license

TERMS AND CONDITIONS

Dec 16, 2013

This is a License Agreement between Oleksandr Barannyk ("You") and Springer ("Springer") provided by Copyright Clearance Center ("CCC"). The license consists of your order details, the terms and conditions provided by Springer, and the payment terms and conditions. All payments must be made in full to CCC. For payment instructions, please see information listed at the bottom of this form.

License Number 3290940090350

License date Dec 16, 2013

Licensed content publisher Springer

Licensed content

publication

Experiments in Fluids

Licensed content title Digital particle image velocimetry

Licensed content author C. E. Willert

Licensed content date Jan 1, 1991

Volume number 10

Issue number 4

Type of Use Thesis/Dissertation

Portion Figures

Author of this Springer

Article No

Order reference number

Title of your thesis /dissertation

SHEAR LAYER INSTABILITIES AND FLOW-ACOUSTIC COUPLING IN VALVES APPLICATION TO POWER PLANT COMPONENTS AND CARDIOVASCULAR DEVICES

Expected completion date Mar 2014

Estimated size(pages) 200

Total 0.00 CAD

Terms and Conditions

Introduction

The publisher for this copyrighted material is Springer Science + Business Media. By clicking "accept" in connection with completing this licensing transaction, you agree that the following terms and conditions apply to this transaction (along with the Billing and Payment terms and conditions established by Copyright Clearance Center, Inc. ("CCC"), at the time that you opened your Rightslink account and that are available at any time at http://myaccount.copyright.com).

Limited License

With reference to your request to reprint in your thesis material on which Springer Science and Business Media control the copyright, permission is granted, free of charge, for the use indicated in your enquiry. Licenses are for one-time use only with a maximum distribution equal to the number that you identified in the licensing process. This License includes use in an electronic form, provided its password protected or on the university's intranet or repository, including UMI (according to the definition at the Sherpa website: http://www.sherpa.ac.uk/romeo/). For any other electronic use, please contact Springer at (permissions.dordrecht@springer.com or permissions.heidelberg@springer.com).

The material can only be used for the purpose of defending your thesis, and with a maximum of 100 extra copies in paper. Although Springer holds copyright to the material and is entitled to negotiate on rights, this license is only valid, subject to a courtesy information to the author (address is given with the article/chapter) and provided it concerns original material, which does not carry references to other sources (if material in question appears with credit to another source, authorization from that source is required as well). Permission free of charge on this occasion does not prejudice any rights we might have to charge for reproduction of our copyrighted material in the future.

Altering/Modifying Material: Not Permitted

You may not alter or modify the material in any manner. Abbreviations, additions, deletions and/or any other alterations shall be made only with prior written authorization of the author(s) and/or Springer Science + Business Media. (Please contact Springer at (permissions.dordrecht@springer.com or permissions.heidelberg@springer.com) Reservation of

Indemnity

You hereby indemnify and agree to hold harmless Springer Science + Business Media and CCC, and their respective officers, directors, employees and agents, from and against any and all claims arising out of your use of the licensed material other than as specifically authorized pursuant to this license.

No Transfer of License

This license is personal to you and may not be sublicensed, assigned, or ransferred by you to any other person without Springer Science + Business Media's written permission. No Amendment Except in Writing This license may not be amended except in a writing signed by both parties (or, in the case of Springer Science + Business Media, by CCC on Springer Science + Business Media's behalf). Objection to Contrary Terms Springer Science + Business Media hereby objects to any terms contained in any purchase order, acknowledgment, check endorsement or other writing prepared by you, which terms are inconsistent with these terms and conditions or CCC's Billing and Payment terms and conditions. These terms and conditions, together with CCC's Billing and Payment terms and conditions (which are incorporated herein), comprise the entire agreement between you and Springer Science +Business Media (and CCC) concerning this licensing transaction. In the event of any conflict between your obligations established by these terms and conditions and those established by CCC's Billing and Payment terms and conditions, these terms and conditions shall control.

Jurisdiction

All disputes that may arise in connection with this present License, or the breach thereof, shall be settled exclusively by arbitration, to be held in The Netherlands, in accor-

dance with Dutch law, and to be conducted under the Rules of the Netherlands Arbitrage Instituut' (Netherlands Institute of Arbitration).*OR:*

All disputes that may arise in connection with this present License, or the breach thereof, shall be settled exclusively by arbitration, to be held in the Federal Republic of Germany, in accordance with German law.